

Hybridization and crystal-field effects  
in Kondo insulators  
studied by means of core-level spectroscopy

Inaugural-Dissertation  
zur  
Erlangung des Doktorgrades  
der Mathematisch-Naturwissenschaftlichen Fakultät  
der Universität zu Köln

vorgelegt von  
Fabio Strigari  
aus Leverkusen

Köln, 2015

Berichterstatter:

Prof. Dr. P. H. M. van Loosdrecht

Prof. Dr. L. H. Tjeng

Tag der mündlichen Prüfung:

13. April 2015

# Contents

<b>1 Heavy-fermion physics and Kondo insulators</b>	<b>1</b>
1.1 Properties and concepts . . . . .	1
1.2 Non-integer $4f$ occupation . . . . .	8
1.3 Crystalline electric field . . . . .	10
1.4 Scope of the thesis . . . . .	16
<b>2 Spectroscopic techniques: Theoretical and experimental background</b>	<b>19</b>
2.1 Soft x-ray absorption spectroscopy . . . . .	20
2.1.1 Theoretical description . . . . .	22
2.1.2 Atomic full multiplet theory . . . . .	24
2.1.3 Determination of crystal fields . . . . .	26
2.1.4 Experimental aspects . . . . .	29
2.1.5 Light sources and beamlines . . . . .	31
2.2 Hard x-ray photoelectron spectroscopy . . . . .	32
2.2.1 General principle . . . . .	32
2.2.2 Theoretical description . . . . .	33
2.2.3 Full multiplet configuration interaction model . . . . .	35
2.2.4 Experimental aspects . . . . .	38
2.2.5 Light source and beamline . . . . .	40
2.2.6 Addendum: $4f$ spectral weights . . . . .	41
2.3 Synchrotron radiation . . . . .	42
<b>References of Chapter 1 and 2</b>	<b>45</b>
<b>3 Crystal-field ground state of the orthorhombic Kondo insulator <math>\text{CeRu}_2\text{Al}_{10}</math></b>	<b>57</b>
Phys. Rev. B <b>86</b> , 081105(R) (2012)	
3.1 Introduction . . . . .	57
3.2 Experimental and theoretical details . . . . .	58
3.3 Results and discussion . . . . .	60
3.4 Conclusion . . . . .	64
<b>4 Crystal-field ground state of the orthorhombic Kondo semiconductors <math>\text{CeOs}_2\text{Al}_{10}</math> and <math>\text{CeFe}_2\text{Al}_{10}</math></b>	<b>65</b>
Phys. Rev. B <b>87</b> , 125119 (2013)	
4.1 Introduction . . . . .	65
4.2 Experimental and theoretical details . . . . .	66
4.3 Results and discussion . . . . .	67
4.4 Conclusion . . . . .	74

<b>5</b>	<b>Valence and configuration interaction parameters of <math>CeM_2Al_{10}</math> (<math>M = Ru, Os, Fe</math>)</b>	<b>75</b>
	J. Electron Spectrosc. Relat. Phenom. <b>199</b> , 56 (2015)	
5.1	Introduction . . . . .	75
5.2	Experimental details . . . . .	77
5.3	Experimental results . . . . .	78
5.4	Quantitative analysis . . . . .	80
5.4.1	Concept . . . . .	80
5.4.2	Simulation of Ce 3 <i>d</i> spectra . . . . .	81
5.5	Discussion . . . . .	81
5.6	Summary . . . . .	85
5.7	Appendix A: Plasmon properties . . . . .	85
5.8	Appendix B: Consequences of the fm-CI model . . . . .	87
	<b>References of Chapters 3 – 5</b>	<b>91</b>
<b>6</b>	<b>Revisiting the crystal-field ground state in the Kondo semimetal CeNiSn</b>	<b>99</b>
6.1	Introduction . . . . .	99
6.2	Experimental details . . . . .	100
6.3	Theoretical details . . . . .	101
6.4	Results . . . . .	102
6.5	Discussion . . . . .	108
6.6	Conclusion . . . . .	110
	<b>References of Chapter 6</b>	<b>111</b>
<b>7</b>	<b>Correlation between ground state and orbital anisotropy in heavy fermions</b>	<b>115</b>
	Proc. Natl. Acad. Sci. USA <b>112</b> (8), 2348 (2015)	
7.1	Introduction . . . . .	115
7.2	Materials and methods . . . . .	118
7.3	Experimental results . . . . .	119
7.4	Discussion . . . . .	121
7.5	Summary . . . . .	124
	<b>References of Chapter 7</b>	<b>125</b>
<b>8</b>	<b>Conclusions and outlook</b>	<b>129</b>
	<b>References of Chapter 8</b>	<b>135</b>
	<b>Abstract</b>	<b>139</b>
	<b>Kurzzusammenfassung</b>	<b>141</b>
	<b>Acknowledgment</b>	<b>145</b>
	<b>Publications</b>	<b>149</b>

# 1 Heavy-fermion physics and Kondo insulators

Heavy-fermion materials feature an enormous diversity of ground states producing a rich spectrum of fundamental and exotic physical phenomena. The members of this material class are lanthanide- or actinide-based intermetallic compounds, with the main representatives being Ce and Yb systems as well as compounds containing e.g. Pr, Sm, U or Pu [1–3]. Heavy fermions all have in common that their physics is driven by the interaction between the  $4f$  or  $5f$  electrons with the conduction band – which constitutes a system of localized magnetic moments residing in a sea of itinerant conduction electrons. The hybridization of  $f$  and conduction electrons leads to two competing effects: (a) An inter-site interaction where  $f$  electrons at different lattice sites couple with each other via the conduction electrons, favoring a magnetically ordered ground state. This is the so-called Ruderman-Kittel-Kasuya-Yoshida (RKKY) interaction. (b) An on-site interaction where the conduction electrons tend to screen the local moments so that a non-magnetic state forms. This is the so-called Kondo screening. The competition of both effects leads to remarkable magnetic, thermodynamic and electronic characteristics at low temperatures [1, 4, 5]. The properties of such heavy-fermion materials may range from magnetically ordered to Kondo-screened or intermediate valent, and from metallic or (unconventionally) superconducting to Kondo-insulating with quantum critical phenomena and non-Fermi liquid behavior when going from one regime to the other. Kondo insulators, which are investigated in this thesis, have been recently connected with the field of topological insulators because some of them are expected to have non-trivial topologies [6]. Because of its vivid and diversified history, the importance of Kondo and heavy-fermion materials for the field of solid state physics, in particular for strongly correlated electron systems, continuously increased in the last 80 years [3].

## 1.1 Properties and concepts

**Historical outline** The Kondo timeline starts off in **1934** when de Haas *et al.* [7] observed a minimum in the electrical resistivity of ‘dirty’ gold at low temperatures (around 4 K) and a follow-up increase of the resistivity for temperatures below. Other dilute magnetic alloys also showed such a behavior [8], already suggesting a connection to the presence of small amounts of magnetic impurities. A theoretical explanation for this anomaly was provided by Kondo in **1964** [9] on the basis of a microscopic model presented by Anderson three years earlier [10], in which the conditions for the existence of localized magnetic moments had been analyzed and a large on-site Coulomb repulsion was found to lead to an antiferromagnetic exchange interaction with the surrounding conduction sea. By applying third-order perturbation theory, Kondo revealed the importance of the logarithmic contribution in the scattering rate of the electrons of a magnetic moment and found that this log-term increases with decreasing temperature, giving rise to a minimum in the resistivity [9]. In other words, the antiferromagnetic coupling

between localized magnetic impurities and the itinerant conduction electrons forms an additional scattering channel which leads to a divergence of the electrical resistivity at low temperatures. This *Kondo effect* sets in below a characteristic energy scale defining the Kondo temperature  $T_K$ . The conduction electron cloud then screens the local moment and the so-called Kondo singlet state develops.

The next milestone dates back to **1975** when heavy-electron behavior was discovered. Andres *et al.* [11] found the linear specific heat coefficient in  $\text{CeAl}_3$  to be  $\gamma = 1620 \text{ mJ mol}^{-1} \text{ K}^{-2}$  for  $T$  below 150 K, which is about 1000 times larger than the values obtained for typical metals, meaning that the effective mass is significantly enhanced compared to the free electron mass – the material class of heavy fermion compounds was born! Still lacking an explanation for how the heavy quasiparticles exactly form, two years later Doniach suggested the Kondo lattice model to provide the theoretical description of the heavy-fermion behavior [12]. In this model, the periodical arrangement of localized magnetic moments (given by the  $4f$  and  $5f$  electrons of rare earth and actinide systems, respectively) in a crystalline structure is interpreted as a dense Kondo lattice, where at each lattice site the Kondo effect, i.e. the screening of the local moment by the conduction electrons, takes place. The already large interest in heavy fermions gained an additional boost in **1979** when Steglich *et al.* [13] discovered the first example of unconventional superconductivity in the heavy-fermion compound  $\text{CeCu}_2\text{Si}_2$ , thereby proving that magnetism and superconductivity are not disconnected phenomena. In the following years intensive work in the area deepened the theoretical understanding, and experimentally many more heavy-fermion systems and superconductors joined the team [1, 14–16]. The list of exotic physical phenomena happening in heavy-electron compounds became even longer in **1994** with the observation of a zero-temperature quantum phase transition (also known as quantum critical point) in Au-doped  $\text{CeCu}_6$  [17].

**Characteristics of heavy fermions** Heavy fermions (HF) belong to the family of strongly correlated electron systems. In general, one speaks of ‘strong correlations’ whenever electron-electron interactions are large compared to the one-electron band width and govern the physical properties of the system. Transition-metal oxides, Mott-Hubbard insulators and high- $T_c$  cuprate superconductors also fall into this category. Correlated electron systems have a partially filled  $d$  or  $f$  shell for which the charge distribution is far from statistical. The behavior of these electrons can therefore no longer be described by an effective one-electron theory. Instead, a true many-body approach has to be applied to account for the correlated motion of those electrons.

In the case of HF, the strong coupling of the  $f$  electrons to the conduction band is responsible for the partial delocalization of the  $f$  electrons and the formation of heavily-dressed quasiparticles with huge effective masses  $m^*$ . At high temperatures (around room temperature) the local  $f$  moments are only weakly interacting and the magnetic susceptibility is characterized by a Curie-Weiss dependence  $\chi = \frac{M^2}{3T}$  with  $M$  being the magnetic moment of an  $f$  state [3]. When lowering the temperature below a characteristic temperature  $T^*$ , the heavy-electron band forms and the magnetic and electronic properties experience significant qualitative changes. The localized  $f$  moments can be thought of as magnetic impurities situated in a crystalline environment, which at low temperatures become screened by the spins of the conduction

electrons as a part of the Kondo effect. This lattice version of the single-ion Kondo effect is called the *Kondo lattice* [12]. At each Kondo lattice site a Kondo singlet forms and acts as a spinless scattering center, so that initially the electrical resistivity increases with decreasing  $T$ , before at  $T^*$  it suddenly drops as phase coherence develops in the scattering channel [3], i.e. the localized magnetic moments do not act as independent scatterers any more. This coherent Kondo state is a lattice effect arising from the interacting localized spin states in the dense Kondo lattice. Note that  $T^*$  is used here to distinguish the characteristic energy scale in Kondo lattice systems from the single-ion Kondo temperature  $T_K$ . However, in the following we refer to  $T^*$  as  $T_K$  (or Kondo temperature) for simplicity.

When it comes to a theoretical description, Landau's *Fermi liquid* (FL) theory [18] has turned out to be able to explain many properties of some of the HF metals. Within the FL model a non-interacting electron fluid is considered to be adiabatically transformed into a corresponding interacting system, when the electron interactions are slowly 'switched on'. The heavy quasiparticles forming in HFs can be interpreted as Landau quasiparticles, which differ from the 'original' electrons in their dynamical properties (e.g. by showing a renormalized mass and a reduced magnetic moment). Characteristic fingerprints of FL behavior at low temperatures are a linear temperature dependence of the specific heat  $C(T) \propto \gamma T$ , a nearly temperature-independent magnetic susceptibility  $\chi(T)$  usually saturating at an enhanced value (one then speaks of enhanced Pauli paramagnetism), and a  $T^2$ -dependence in the electrical resistivity  $\rho(T)$ . As a further consequence, two scaling laws can be deduced which also are classical signatures of the FL character of HF compounds, namely an approximately constant Wilson (or Sommerfeld) ratio  $\chi/\gamma$  [19] and an approximately constant Kadowaki-Woods [20] quotient  $A/\gamma^2$ , where  $A$  is the coefficient of the quadratic contribution to the electrical resistivity. Another remarkable attribute of HF can be seen when measuring their Fermi surface (FS) geometry and volume in de-Haas-van-Alphen or Shubnikov-de-Haas experiments: The former atomic-like  $f$  electrons turn out to contribute to the FS volume and in some cases band structure calculations are able to reproduce the FS geometry, although the effective electron mass is significantly enhanced [3].

**Anderson model and Kondo lattice** As mentioned above, the periodical version of a Kondo system, as it is formed by the localized magnetic moments in heavy-fermion materials, is called a Kondo lattice. We start with the description of a single magnetic  $f$  impurity interacting with a conduction band host. Following Anderson [10], we have:

$$\begin{aligned} H_{\text{AIM}} &= H_{0f} + H_{ff} + H_{0v} + H_{vf} \\ &= E_f n_f + U n_{f\uparrow} n_{f\downarrow} + \sum_{\mathbf{k}\sigma} \epsilon_{\mathbf{k}} n_{\mathbf{k}\sigma} + \sum_{\mathbf{k}\sigma} V(\mathbf{k}) \left[ c_{\mathbf{k}\sigma}^\dagger f_\sigma + f_\sigma^\dagger c_{\mathbf{k}\sigma} \right] \end{aligned} \quad (1.1)$$

This model is referred to as *Anderson impurity model* (AIM). Here  $n_f$ ,  $n_{f\downarrow}$ ,  $n_{f\uparrow}$  and  $n_{\mathbf{k}\sigma}$  are the number operators. The first two terms  $H_{0f}$  and  $H_{ff}$  render the formation of a local moment in the atomic limit, with  $E_f$  being the energy of the  $f$  state and  $U$  the Coulomb interaction between two electrons in the  $f$  shell. The hybridization coupling between the  $f$  electrons and the conduction band is taken into account via the last two terms  $H_{0v}$  and  $H_{vf}$ , where  $\epsilon_{\mathbf{k}}$  is the momentum-dependent energy dispersion of the conduction band and  $V(\mathbf{k})$  is the hybridization strength given by the orbital overlap between  $f$  and the conduction states. In the mean-field

approximation presented in Ref. [10] the AIM explains the formation of the local moments. Furthermore, by taking into account spin fluctuations which can effectively flip the spin of the magnetic impurity [21], the screening of the impurity can be explained and the Kondo effect is found to produce the so-called *Kondo resonance* state close to the Fermi level  $E_F$  [22, 23]. It reflects the large quasiparticle density of states (DOS) near  $E_F$  due to the singlet ‘bound state’ of the conduction electrons with the localized spins [24]. Experimentally, the Kondo resonance can be observed by x-ray photoemission [25–28] or scanning tunneling spectroscopy [29–31]. Its position and width is proportional to  $T_K$  and its intensity inversely proportional to  $T_K$ .

In order to capture the very special low-temperature physics of heavy-fermion compounds, Doniach proposed the transition to the Kondo lattice model [12]:

$$H_{\text{KL}} = \sum_{\mathbf{k}\sigma} \epsilon_{\mathbf{k}} c_{\mathbf{k}\sigma}^\dagger c_{\mathbf{k}\sigma} + J_{\text{ex}} \sum_i \mathbf{s}_i \mathbf{S}_i \quad (1.2)$$

As in  $H_{\text{AIM}}$  the conduction electrons’ energy dispersion is given by  $\epsilon_{\mathbf{k}}$ .  $S_i$  and  $s_i$  are the spin-density operators of the localized and conduction electron spins, respectively, at every lattice site  $i$ , which are coupled via the exchange interaction  $J_{\text{ex}}$ . The coupling constant  $J_{\text{ex}}$  is the crucial parameter here. On the one hand it is decisive for the Kondo effect and on the other hand it also determines the *RKKY interaction* [32–34]. The RKKY interaction is an inter-site effect and refers to the magnetic coupling between two localized moments via oscillations in the conduction electron spin density, whereas the Kondo interaction is an on-site effect. The strengths of these two interactions – expressed by the Kondo temperature  $T_K$  and the ordering temperature  $T_{\text{RKKY}}$  – depend differently on  $J_{\text{ex}}$  [12]. The Kondo temperature scale is characterized by the exponential dependence  $T_K \propto N(0)^{-1} e^{-1/(N(0) \cdot J_{\text{ex}})}$ , where  $N(0)$  is the density of conduction electron states. The RKKY interaction on the other hand scales quadratically with  $J_{\text{ex}}$ , ergo  $T_{\text{RKKY}} \propto J_{\text{ex}}^2 N(0)$ . Important is that these two interactions compete with each other. While the Kondo interaction stabilizes the formation of effective singlet entities, the RKKY interaction wants to drive the system towards a magnetically ordered state (usually antiferromagnetic). Thus, two relevant and competing energy scales exist: In the case of a small exchange interaction  $J_{\text{ex}}$  the RKKY-scale dominates and antiferromagnetic order with localized spins develops, whereas for large  $J_{\text{ex}}$  the formation of singlet Kondo clouds prevails and a non-magnetic ground state with partially delocalized  $f$  electrons forms. This competition between RKKY and Kondo interactions governs the physics of Kondo lattice materials and is qualitatively summarized in the *Doniach phase diagram*, which is shown in Fig. 1.1. Although Doniach’s original approach assumes a simplified one-dimensional Kondo lattice, the derived phase diagram still generally helps to understand the behavior of many HF compounds.

Depending on whether  $J_{\text{ex}}$  is below or above a critical value  $J_{\text{ex}}^c$ , the system is either in the AFM regime or in a paramagnetic Fermi liquid state, as depicted in Fig. 1.1. The transition between these phases is achieved by tuning the exchange coupling  $J_{\text{ex}}$ , which in a more general picture can be regarded as an adjustable global parameter  $\delta$  that influences the lattice density and thereby the degree of hybridization. In practice, the enhancement of  $\delta$  is realized by external pressure, chemical substitution or a magnetic field, continuously reducing the AFM ordering temperature and migrating from a localized towards a more itinerant regime. Before entering the FL phase, in between the two regimes one often reaches a so-called *quantum critical point* (QCP), which resembles a zero-temperature quantum phase transition. The emergence of quantum

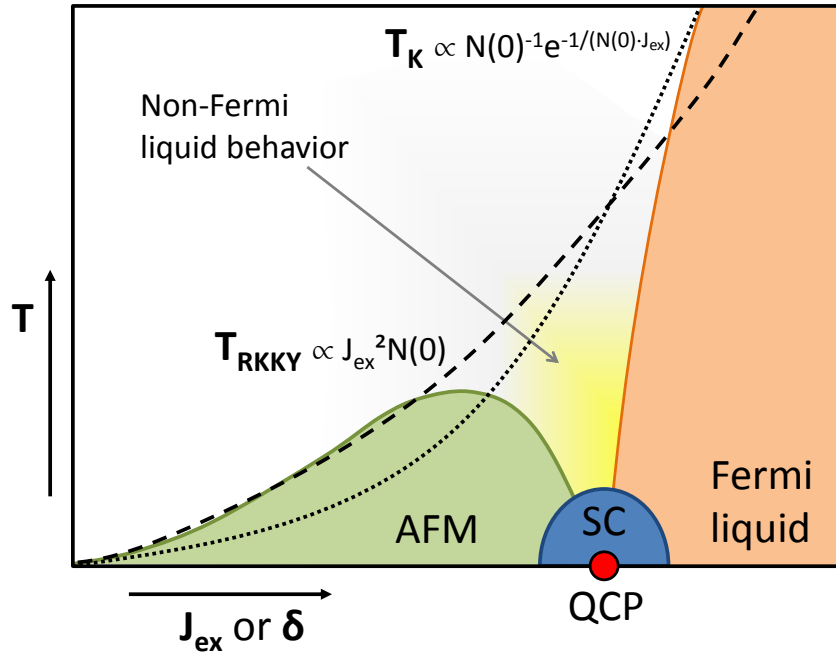


Figure 1.1: Illustration of the Doniach phase diagram (redrawn following Fig. 15 in Ref. [3]), showing the competition between RKKY and Kondo interactions in dependency of the exchange interaction  $J_{\text{ex}}$  or an equivalent control parameter  $\delta$ . For  $T_{\text{RKKY}} > T_{\text{K}}$  an antiferromagnetic ground state forms (localized regime), whereas for  $T_{\text{RKKY}} < T_{\text{K}}$  a paramagnetic Fermi liquid phase develops (delocalized regime). At the boundary of the two phases a quantum critical point can arise, in the vicinity of which (at finite temperatures) non-Fermi liquid behavior can be found which often goes along with the emergence of unconventional superconductivity (SC ‘dome’).

critical behavior in Kondo lattice materials arose particular interest because it goes along with deviations from the FL properties in the phase space close to the QCP [35]. In the case of this *non-Fermi liquid* (NFL) behavior, the above-mentioned signatures of a FL do not hold any more; instead one finds for instance  $\rho(T) \propto T^n$  with  $n$  between 1 and 1.5, or a logarithmic dependence in  $C(T)$ . Magnetic field induced quantum phase transitions can be found for example in  $\text{YbRh}_2\text{Si}_2$  [35] or  $\text{CeCoIn}_5$  [36, 37], and  $\text{CeCu}_{6-x}\text{Au}_x$  is a prominent example where the QCP is reached via chemical substitution [38, 39]. In addition to that, unconventional superconductivity (SC) can occur in the vicinity of a QCP, as for example observed in  $\text{CeIn}_3$  [40],  $\text{CeCoIn}_5$  [41],  $\text{CeCu}_2\text{Si}_2$ ,  $\text{CeCu}_2\text{Ge}_2$  and  $\text{CeCu}_2(\text{Si}_{1-x}\text{Ge}_x)_2$  [13, 42, 43], as well as in  $\text{CePd}_2\text{Si}_2$  and  $\text{CeRh}_2\text{Si}_2$  [44, 45]. Here the tuning towards the antiferromagnetic QCP takes place via pressure, pushing forward the idea of an unconventional magnetically-mediated pairing mechanism.

After all, the Doniach phase diagram is quite reminiscent of the rich phase diagram of cuprates, as both feature several competing ground states, one of which being superconducting – with the difference that the delocalization of the  $f$  electrons happens due to their coupling to the conduction band and not because of addition or removal of charge carriers.

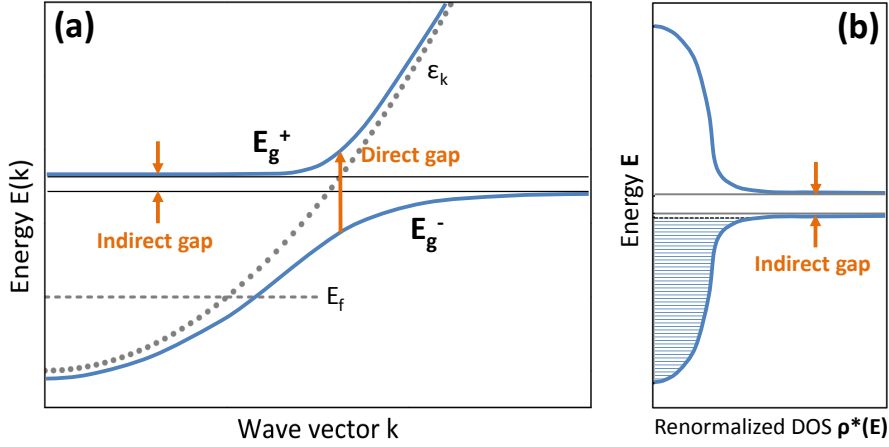


Figure 1.2: (Redrawn following Fig. 17 in Ref. [3]) (a) Schematic band picture of the hybridized bands in a Kondo lattice system. The dashed and dotted gray lines ( $E_f$  and  $\epsilon_k$ ) represent the unhybridized  $4f$  and conduction bands, respectively. The  $c$ - $f$  hybridization leads to the formation of an upper ( $E_g^+$ ) and a lower ( $E_g^-$ ) Fermi band (blue lines), which feature a direct and an indirect gap. (b) Corresponding renormalized density of states where the indirect hybridization gap can be seen close to the Fermi level.

**Kondo insulators** The call for a universal formalism for the treatment of strongly correlated electron systems meets the problem of how to essentially consider the large interactions involved in this material class. Gauge theories, the so-called large  $N$  expansion and mean-field theory come into play, and for a deeper insight the interested reader may be referred to the diverse reviews on this topics and the references therein [2, 3, 46, 47]. An important consequence in the mean-field approach of the Kondo lattice is that the hybridization between the conduction and the  $f$  electrons ( $c$ - $f$  hybridization), which in the most simple approximation is assumed to be  $k$ -independent, leads to a renormalized hybridized-band model with an upper ( $E_g^+$ ) and a lower ( $E_g^-$ ) Fermi band, which have both  $f$  and conduction band character. Apart from the direct gap between them of size  $2V$ , they exhibit an indirect hybridization gap of width  $\Delta_g \sim T_K$  (see Fig. 1.2a) close to the Fermi level. The DOS of the heavy quasiparticles is zero inside the gap but in the immediate vicinity of the gap two extremely sharp features arise (Fig. 1.2b). The direct hybridization gap has been observed in optical conductivity measurements as a thin Drude peak at low frequencies being separated from a broad high-frequency interband component associated with the conduction electrons [48]. The indirect and direct gap sizes and the effective mass of the heavy electrons are theoretically found to be related via:

$$\frac{m^*}{m_e} \propto \left( \frac{2V}{T_K} \right)^2 \quad (1.3)$$

Optical conductivity measurements on numerous HF compounds [4, 48] confirm this quadratic scaling law of the effective mass and electron spectroscopy [49, 50] indeed observes the extremely temperature-dependent narrow  $f$  peaks in the DOS, thereby strengthening the validity of the Kondo lattice concept [3].

We have seen that the hybridization of a flat  $f$  band with a broad conduction band leads to the formation of a band of heavy quasiparticles and a narrow hybridization gap close to the Fermi level. The most extraordinary consequence of this is that, depending on the detailed gap structure and the chemical potential in these systems, a *Kondo insulator* or narrow-gap semiconductor can evolve [5]. Kondo insulators are regarded as highly renormalized band insulators [3] since band structure calculations – not taking into account the interactions relevant for the gap formation – yield significantly larger gap sizes than observed in optical, magnetic or transport measurements.

Kondo insulators are HF metals which experience a transition to an insulating state when the heavy-electron band forms and the chemical potential of the system lies in the middle of the resulting hybridization gap.<sup>1</sup> At high temperatures they can be regarded as metals with well localized  $f$  moments producing a Curie-Weiss-like magnetic susceptibility, and ‘light’ non-interacting conduction electrons. At low temperatures the susceptibility and conductivity nearly vanish on the same temperature scale as the  $c$ - $f$  hybridization leads to the formation of the heavily dressed quasiparticles. (Actually, the presence of non-avoidable impurities in combination with the narrow gap sizes often hampers the realization of a perfectly insulating state.) If we consider two electrons per unit cell and doubly degenerate hybridized bands, at  $T = 0$  the low-lying hybridized band is occupied by these electrons and the upper one is empty, i.e. the occupation is exactly at half-filling and the chemical potential lies within the gap. This is the non-interacting limit, in which the Coulomb repulsion between a pair of  $f$  electrons at one site is ‘off’ ( $U \rightarrow 0$ ). Going to an interacting system by adiabatically ‘turning on’  $U$  maintains the insulating ground state according to Luttinger’s theorem [5]. This insulating situation is destroyed when  $T$  increases across  $T_K$  because the  $f$  electrons become localized and the bands become filled with a fractional number of electrons per  $f$  ion – the hybridization gap vanishes above the coherence Kondo temperature. To put it differently, when coming from the high- $T$  side and cooling down below  $T_K$  one observes a loss of charge carriers caused by the Kondo effect at low energies. This is why these materials are also called *low-carrier Kondo systems*.

This theoretical understanding of Kondo insulators is supported from the experimental side and for an extensive review and interpretation of their properties the reader may be referred to Ref. [5]. For instance, investigations on  $\text{Ce}_3\text{Bi}_4\text{Pt}_3$  show that the gap formation is well visible in temperature-dependent optical conductivity [4, 51] and inelastic neutron scattering measurements [52], and in a sudden increase of the resistivity at low  $T$  [53]. Moreover, the indirect hybridization gap can be closed by applying an external magnetic field of  $\sim 30$  T in the case of  $\text{Ce}_3\text{Bi}_4\text{Pt}_3$  [54, 55]. And interestingly, when the magnetic ions in Kondo insulating materials are substituted by an isoelectronic nonmagnetic equivalent (e.g. La can be used to replace Ce), the system is effectively doped and the gap size decreases [56].

**HF superconductivity and quantum criticality** The list of heavy-fermion superconductors (HFSCs) has increased to contain close to 40 examples since its premiere in  $\text{CeCu}_2\text{Si}_2$  [2, 15, 57, 58]. The unconventional character and the involvement of the ‘heavy’  $f$  electrons in the pairing mechanism was indicated by comparable specific heat entropies for the normal and

---

<sup>1</sup>Note that the term ‘Kondo insulator’ refers to the presence of the Kondo-insulating state and is used as a generic term, including also Kondo semiconductors and Kondo semimetals.

SC state, and by the measured sizes of the London penetration depth and the superconducting coherence length reflecting the large mass renormalization [3]. In contrast to classical BCS superconductors, *electronic* interactions are assumed to drive the formation of Cooper pairs and the proximity to an AFM phase (as e.g. in UPt<sub>3</sub> [59], CeCu<sub>2</sub>Ge<sub>2</sub> [60] or CeRh<sub>2</sub>Si<sub>2</sub> [45]) suggests that the SC originates from antiferromagnetic spin fluctuations.

Many HFSCs exhibit non-Fermi liquid behavior close to the SC dome, which marks the vicinity of a QCP [61–65]. Tuning the exchange interaction towards the critical value  $J_{\text{ex}}^c$  (see Doniach phase diagram, Fig. 1.1) continuously reduces the AFM order and its complete suppression represents the quantum critical singularity in the phase diagram, which often happens at high pressure or large magnetic fields. The interdependencies between NFL behavior, AFM fluctuations and SC are of uttermost interest for the search for the microscopic origins of HFSC. In the characterization of a QCP one basically distinguishes between the *spin-density wave* (SDW) model and the *Kondo breakdown* scenario [61, 64]. The former is the itinerant case in which the heavy charge carriers exist on either side of the QCP, i.e. the AFM order arises from a spontaneous spatial modulation of the spins of the charge carriers (SDW instability). In the latter ‘local’ scenario the heavy charge carriers exist only in the paramagnetic phase and the Kondo singlets break up when entering the AFM region.

At the example of CeCu<sub>2</sub>Si<sub>2</sub> the importance of hybridization and the anisotropy of the ground-state orbital in the context of quantum criticality becomes evident. The SC phase in the  $P$ - $T$  phase diagram exhibits a double-dome structure, with maximal critical temperatures of  $T_c = 0.6$  K at low pressure ( $P_c = 0.45$  GPa) and  $T_c = 2$  K at a ten times higher pressure [66, 67]. The two domes were found to become disconnected in partially Ge-substituted CeCu<sub>2</sub>Si<sub>2</sub>, thus indicating that the two QCPs and therefore the SC are of different origin [42]. More precisely, the low- $P$  dome is associated with an AFM QCP, whereas the mechanism behind the high- $P$  QCP is still a matter of debate. Here, critical valence fluctuations were proposed to trigger the formation of Cooper pairs [68, 69] but corresponding fluctuations in the occupation of the  $4f$  states were not observed by x-ray absorption spectroscopy [70]. As an alternative, an orbital transition between two crystal-field states with different hybridizations has been suggested on the basis of LDA+DMFT calculations [71, 72]. The coupling between the resulting critical orbital fluctuations and charge fluctuations may provide a possible glue for superconductivity.

## 1.2 Non-integer $4f$ occupation

Depending on the position of the  $f$  (impurity) level  $E_f$  with respect to the Fermi level  $E_F$ , the hybridization in HF systems gives rise to a non-integer occupation of the  $f$  shell. The case that the occupation deviates significantly from integer is referred to as *intermediate valence* behavior [24, 73, 74]. In order to illustrate how the intermediate valence emerges, we follow the line of thought presented in Chapter 13 of Ref. [24].

If the Coulomb interaction is large ( $U \rightarrow \infty$ ), the exchange coupling  $J_{\text{ex}}$  in the Kondo lattice model (Eq. 1.2) will depend only on the hybridization  $V$  and the energy difference between the  $f$  and the Fermi level [24]:

$$J_{\text{ex}} = \frac{2V^2}{E_F - E_f} \quad (1.4)$$

The closer the  $f$  level is to the Fermi level, the stronger is the exchange interaction  $J_{\text{ex}}$ . In Fig. 1.3 the Doniach phase diagram is reconsidered – but now with  $E_f$  on the  $x$  axis – to illustrate what happens when the impurity level moves closer towards the Fermi level. For  $E_f \ll E_F$  (regime I in Fig. 1.3) the deep  $f$  level is occupied by one electron ( $n_f = 1$ ), and the RKKY interaction wins over the Kondo interaction since  $J_{\text{ex}}$  is small (as described above in the context of the Kondo lattice model), meaning that a magnetically ordered ground state with localized magnetic moments forms. The coherent peak of the  $f$  level (see energy level structure of regime I in Fig. 1.3b) has a width of  $\Gamma = \pi N(0)V^2$ , with  $N(0)$  being the density of conduction electron states. In the heavy fermion phase (regime II in Fig. 1.3) the  $f$  level is located still below but closer to  $E_F$ , so that still  $n_f \approx 1$ . Due to the closeness to the Fermi level, the Kondo resonance peak develops close-by – the width of which is proportional to  $T_K$ . The increasing influence of the Kondo screening reduces the magnetic moments and thereby the magnetic ordering temperature. This can lead either to a ground state which is characterized by a coexistence of Kondo-behavior and magnetic order (IIa) or a nonmagnetic heavy Fermi liquid state when the Kondo interaction is dominant (IIb).

The occupation of the  $f$  state deviates significantly from integer ( $n_f \neq 1$ ) when the  $f$  level moves further up and reaches  $E_F$  (regime III in Fig. 1.3). We enter the region of intermediate valence and its ground state is also described by a Fermi liquid behavior, with the temperature dependence of the magnetic susceptibility deviating from Curie-Weiss-like behavior and showing enhanced Pauli paramagnetism for  $T \rightarrow 0$ . However, in comparison with the heavy fermion phase the Kondo scale is considerably larger<sup>2</sup> since  $E_F - E_f$  is very small, and the Kondo peak may not be even distinguished from the coherent  $f$  peak any more (see Fig. 1.3b). Finally, when going beyond the Fermi level ( $E_f > E_F$ ) a normal, nonmagnetic metallic state arises (regime IV in Fig. 1.3) with no electrons occupying the  $f$  shell any more. The importance of  $E_f$  for classifying HF materials in the context of the Doniach phase diagram is evident from these considerations.

Prominent examples featuring intermediate valence behavior are for instance CePd<sub>3</sub>, CeSn<sub>3</sub>, CeIn<sub>3</sub> or YbAl<sub>2</sub> (see e.g. Refs. [73, 75, 76]). A fractional  $f$  occupation  $n_f$  is thought of as quantum fluctuations between different valence configurations. Quantum-mechanically this is described by means of a hybrid wave function, meaning a superposition of states accounting for the different  $f$  electron distributions. In the case of cerium and no hybridization, one electron occupies the  $f$  shell ( $f^1$ ), but when hybridization is present the hybrid wave function reads

$$|\phi_{\text{GS}}\rangle = c_0|f^0\rangle + c_1|f^1\underline{L}\rangle + c_2|f^2\underline{L}\rangle \quad (1.5)$$

with additional contributions coming from the divalent ( $f^2$ ) and tetravalent ( $f^0$ ) states.  $\underline{L}$  and  $\underline{L}$  denote the number of ligand holes here. The determination of the  $f^n$  weights  $c_n$ , which in turn determine the  $f$  occupation  $n_f$ , is of great interest since it gives a first approximation for the degree of hybridization in the system and in principle allows to deduce the decisive interaction parameters like  $E_f$  or  $T_K$  from it. In Chapter 2.2.3 a model for the analysis of photoelectron spectroscopy data will be presented (and later applied in Chapter 5), which enables the access

<sup>2</sup>Note that if the Kondo scale, i.e.  $T_K$ , is large, then the mass renormalization will not be so large any more – the system is no longer ‘heavy’. However, it is still correlated with some *moderate* mass enhancement with respect to band structure by a factor of 2–5 (instead of 100–1000).

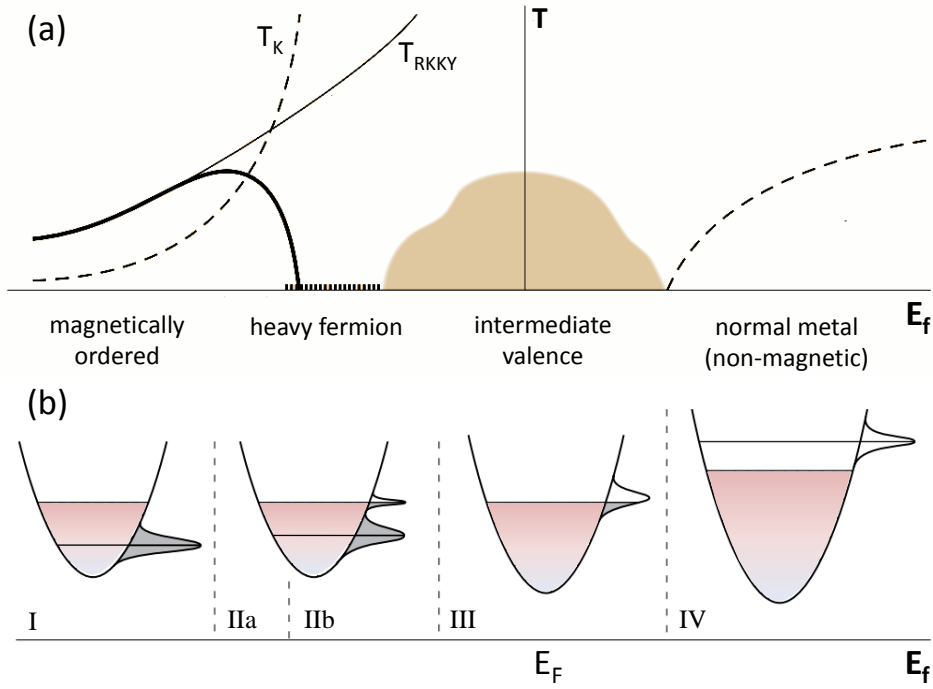


Figure 1.3: (Redrawn following Fig. 13.10 and 13.11 in Ref. [24]) (a) ‘Extended’ Doniach phase diagram (cf. Fig. 1.1), illustrating which phases develop in heavy fermion systems depending on the energy  $E_f$  of the impurity level. The scales of the RKKY and Kondo interaction are denoted by  $T_{\text{RKKY}}$  and  $T_K$ , respectively. (b) Corresponding evolution of the energy structure with increasing  $E_f$ . In the intermediate-valence region III the  $f$  level is close to the Fermi level  $E_F$ .

to the intermediate valence ground state and allows to disentangle Eq. 1.5 with regard to the configuration interaction parameters.

### 1.3 Crystalline electric field

The origin of the fascinating and diverse phenomena in Kondo insulators, and Kondo lattice materials in general, is the strongly interacting ground state of the  $4f$  electrons. Therefore, the ground-state wave function and its symmetry, which depend vigorously on the crystalline environment within the material, are of great interest for a full understanding of the underlying physics. This crystalline environment, in which the highly localized  $4f$  electrons are located in, reflects the local point symmetry and induces a splitting of the Hund’s rule ground state. The resulting crystal-field-split states (for Ce given by Kramers’ doublets or quartets) are no longer isotropic but rather feature a pronounced anisotropy in the spatial distribution of the  $4f$  electrons, and consequently in most physical properties. The crystal-field-split states can be described by a crystalline electric field (CEF) model. Yet, this is to be understood as an

effective model: effective in the sense that the parameters and energies are given mostly by the anisotropic hybridization of the  $4f$  with its ligands and not so much by a real electrostatic potential from the ligands.

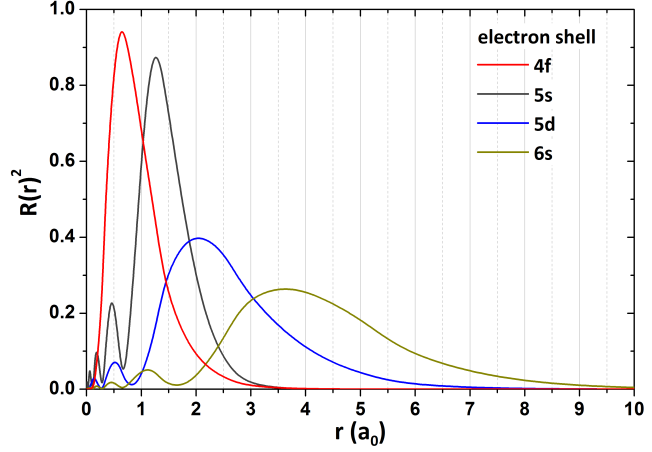
Both in past and recent literature a plethora of examples can be found which emphasize the significance of the crystal-field anisotropy for Kondo systems. Levy and Zhang relate the CEF splittings to the anisotropy of the  $c$ - $f$  hybridization [77] and find essential differences in the resistivity and susceptibility when anisotropic effects are considered [78]. Around the same time, Gunnarsson and Christensen also calculated how the hybridization varies for the different CEF-split  $4f$  states in  $\text{CeCu}_2\text{Si}_2$  and how the magnetic susceptibility is influenced by that [79]. The anisotropies arising from the crystal lattice structure turned out to be important for the quantitative description of the quasiparticle properties in  $\text{CeRu}_2\text{Si}_2$  [46]. The issue was further addressed in the archetype Kondo insulators  $\text{CeNiSn}$  [80–82] and  $\text{CeRhAs}$  [83]. Although standard *ab initio* band structure approaches were shown to be inadequate to realistically model the quasiparticle bands of strongly correlated electron systems, the properties of the Fermi surface and the large effective masses can be understood within *renormalized* band structure calculations, and these need the proper CEF states as an input to correctly reproduce the energy dispersion of the quasiparticle states [46]. Also, a good description of HF superconductivity has early been found to require the inclusion of the anisotropy due to the CEF [46]. Recently, the concept of a topological Kondo insulator (TKI) came up and gave the knowledge of the CEF symmetry further importance [6]. The non-trivial topological structure in TKIs, giving rise to conducting surface states, is strongly connected to the spatial symmetry of the hybridization interaction which in turn depends on the symmetry of the CEF ground state.

### Crystal-field model

CEF effects in rare earth materials can be well interpreted in the ionic picture provided by crystal-field theory. Let us start with a free atom in vacuum, where the only interaction the electrons are exposed to originates from the core's Coulomb potential. This potential is characterized by spherical symmetry, meaning that the eigenfunctions to the corresponding Hamiltonian are degenerate and the resulting spatial distribution of the electrons is isotropic. Inside a crystal structure the free ions are 'kept together' by metallic- or covalent-type bonding mechanisms. Here a particular characteristic of the lanthanide series (from La to Lu) with the electronic configuration  $4f^n 5d^1 6s^2$  ( $n = 0 - 14$ ) comes into play: The  $4f$  shell in rare earths is well localized (see Fig. 1.4) and only weakly overlaps with orbitals from neighboring ligands, which is disadvantageous for covalent bonding. The  $4f$  electrons therefore have atomic-like character and can be treated in an ionic model. Here cerium- and ytterbium-based systems are particularly simple because of the single electron/hole in the  $\text{Ce}^{3+}/\text{Yb}^{3+}$  configuration.

Putting a free magnetic ion into a crystalline environment, it will experience the static electric field produced by the neighboring atoms. This destroys the spherical symmetry and introduces anisotropy to the system. Effectively, the crystal field is regarded as a perturbation to the atomic scenario [84] and is modeled by the CEF or Madelung potential  $V_{\text{CEF}}(\mathbf{r})$  stemming from the surrounding point charges that act on the central ion. Mathematically, a crystal-field Hamiltonian  $H_{\text{CEF}} = -e \cdot V_{\text{CEF}}(\mathbf{r})$  is added to the atomic one and all information about the local environment of the rare earth ion is included into the CEF potential.

Figure 1.4: Square of the atomic radial wave functions for the 4*f*, 5*s*, 5*d* and 6*s* electron shells, as calculated with the Hartree-Fock method for Ce<sup>3+</sup>. On the *x* axis the distance *r* from the nucleus is given in units of the Bohr radius *a*<sub>0</sub>.



For the parametrization of the crystal field we separate the wave function into an angular and a radial part as  $\phi(r, \theta, \varphi) = R_n^l(r) \cdot Y_l^m(\theta, \varphi)$  (the quantum numbers *n*, *l* and *m* follow the usual notation, see also Sec. 2.1.2). This separation can be analogously applied to the CEF potential by expanding it in spherical harmonics  $Y_l^m(\theta, \varphi)$ , which are the orthonormal eigenfunctions of the square of the orbital angular momentum operator [85]:

$$V_{\text{CEF}}(r, \theta, \varphi) = \sum_{k=0}^{\infty} \sum_{m=-k}^k A_k^m \cdot r^k \sqrt{\frac{4\pi}{2k+1}} \cdot Y_k^m(\theta, \varphi) \quad (1.6)$$

with

$$Y_k^m(\theta, \varphi) = \sqrt{\frac{2k+1}{4\pi} \frac{(k-m)!}{(k+m)!}} \cdot P_k(\cos \theta) \cdot e^{im\varphi} \quad (1.7)$$

The functions  $P_k(\cos \theta)$  are the Legendre polynomials. With Eq. 1.6 and 1.7 the matrix elements  $\langle \phi_i | V_{\text{CEF}} | \phi_j \rangle$  of the crystal-field Hamiltonian are given by:

$$H_{i,j}^{\text{CEF}} = -e \sum_{k=0}^{\infty} \sum_{m=-k}^k A_k^m \left\langle R_{n_i}^{l_i}(r) \left| r^k \right| R_{n_j}^{l_j}(r) \right\rangle \cdot \sqrt{\frac{4\pi}{2k+1}} \left\langle Y_{l_i}^{m_i}(\theta, \varphi) \left| Y_k^m(\theta, \varphi) \right| Y_{l_j}^{m_j}(\theta, \varphi) \right\rangle \quad (1.8)$$

The integrals over spherical harmonics in the angular part can be solved analytically, and the integrals over the radial part  $\left\langle R_{n_i}^{l_i}(r) \left| r^k \right| R_{n_j}^{l_j}(r) \right\rangle$  follow from atomic Hartree-Fock calculations. This leaves us with the parameters  $A_k^m$  which have to be determined experimentally. To avoid the problem that the atomic radial wave functions do not correspond to the radial wave functions of an ion within a solid, the expectation value and the  $A_k^m$  are merged:

$$\check{A}_k^m \equiv A_k^m \left\langle R_{n_i}^{l_i}(r) \left| r^k \right| R_{n_j}^{l_j}(r) \right\rangle \quad (1.9)$$

The  $\check{A}_k^m$  are the experimentally observable crystal-field parameters. Mathematical and symmetry aspects limit the number of allowed parameters, so that a full determination of the crystal-field potential becomes feasible.

### Crystal-field parameters

From the mathematical point of view the so-called *3j symbols* [86] describe the integrals over the angular part. In this framework the triangle inequality holds, meaning that the integral does not vanish only if  $k \leq l_i + l_j$ . Furthermore,  $k + l_i + l_j$  has to be even because otherwise the integration is performed over an odd function and the expectation value vanishes as well. The Hamiltonian also has to be a Hermitian matrix, i.e.  $\check{A}_k^m = (-1)^m (\check{A}_k^{-m})^*$ , and from quantum mechanics  $m$  is restricted to the values  $m = -k, \dots, k$ .

The next significant reduction of allowed  $\check{A}_k^m$  is procured by the point symmetry of the rare earth ion. The arrangement of the ligands around the ion under consideration, given by the crystalline point group, has to be included in the CEF potential. Assuming that the highest rotational symmetry is given by a  $p$ -fold rotational axis (usually the quantization axis), then  $V_{\text{CEF}}$  has to fulfill the condition  $V_{\text{CEF}}(r, \theta, \varphi) = V_{\text{CEF}}(r, \theta, \varphi + \frac{2\pi}{p})$ . This is the case if  $m = n \cdot p$  (with  $n \in \mathbb{Z}$ ) since the spherical harmonics – which compose the angular part of  $V_{\text{CEF}}$  – are proportional to  $e^{im\varphi}$ . Effectively, the order of rotational symmetry yields a selection rule for the  $J_z$  quantum number, namely  $\Delta J_z = p$ .<sup>3</sup>

After considering all possible constraints, the remaining  $\check{A}_k^m$  are obtained from fitting the experimental data (see Sec. 2.1.3). In principle, an *ab initio* calculation of the CEF potential can be performed via an Ewald summation over the ligand point charges (a program for such a calculation can be found for instance in Appendix B of Ref. [87]), but this often yields only a crude approximation. Within the phenomenological method no assumptions about the point-charge distribution have to be made so that it generally gives better results.

The description can be simplified even more. Both in transition metal and in rare earth compounds the Coulomb interaction is the strongest. However, unlike in transition metals, the spin-orbit coupling  $\zeta$  ( $\sim 10^{-1}$  eV) in rare earths is about one order of magnitude larger than the crystal-field interaction ( $\sim 10^{-2}$  eV), ergo  $V_{\text{CEF}} < \zeta(r_j) \mathbf{l}_j \cdot \mathbf{s}_j < \frac{e^2}{r_{ij}}$  (see Fig. 1.5). The operators  $\mathbf{L}$  and  $\mathbf{S}$  (total orbital and spin angular momentum, respectively) commute with the Coulomb operator, thus the multiplets due to Coulomb repulsion can be described by the quantum numbers  $L$  and  $S$ . With the spin-orbit coupling being much smaller than the Coulomb interaction the *LS*-coupling scheme can be applied. A splitting due to different total angular momentum  $J = L \pm S$  is the consequence. By now  $L$ ,  $S$  and  $J$  are good quantum numbers but ‘switching on’ the crystal field breaks the spherical symmetry and states with different  $J$  can mix, so that  $J$  is no longer a good quantum number. In  $H_{\text{CEF}}$  this is expressed by the resulting off-diagonal elements.

This thesis focuses on HF cerium compounds, so at the end of this section let us consider a  $\text{Ce}^{3+}$  ( $4f^1$ ) system and apply the crystal-field description to it. The quantum numbers are  $L = 3$ ,  $S = 1/2$  and  $J = 5/2, 7/2$ . The  $J = 5/2$  and  $J = 7/2$  multiplets are split by spin-orbit interaction and according to Hund’s rules the  $J = 5/2$  is the ground state multiplet. The remaining  $(2J + 1)$ -degeneracy of each multiplet is lifted by the presence of a crystal field; the  $J = 5/2$  multiplet splits into three and the  $J = 7/2$  into four Kramers’ doublets. According to the constraints mentioned above, an orbital momentum of 3 only allows  $\check{A}_k^m$  with  $k = 0, 2, 4, 6$ . The local symmetry of the rare earth ion reduces the number of allowed  $m$  values: For tetragonal

<sup>3</sup>Writing up the CEF Hamiltonian shows that the existence or non-existence of a certain  $\check{A}_k^m$  decides which  $J_z$  admixtures can occur in the respective states [85].

symmetry (e.g. point groups  $C_{4v}$  or  $D_{4h}$ ) with a fourfold rotational axis we have  $m = 0, 4$ , for an orthorhombic crystal field  $m = 0, 2, 4, 6$  since the rotational symmetry is twofold, and for the case of a sixfold rotational axis in hexagonal symmetry  $m$  can be 0 or 6. More precisely, for the tetragonal case this means that only  $J_z = \pm 3/2$  and  $J_z = \mp 5/2$  can mix and  $J_z = \pm 1/2$  forms a pure  $J_z$  state. In a hexagonal CEF only pure  $J_z$  states are allowed. Figure 1.5 summarizes the energy level scheme of a  $Ce^{3+}$  ion in a tetragonal CEF environment. For a more comprehensive introduction to the CEF description, including an overview of the possible local symmetries and the corresponding non-vanishing crystal-field parameters, see Ref. [85]. A good review on CEF effects in metallic  $4f$  systems is given in Ref. [88].

What is now the goal when performing an experiment on the search for the  $4f$  ground-state wave function? To illustrate the experimental concept we assume a tetragonal crystal field ( $D_{4h}$  point symmetry). As explained, the CEF Hamiltonian in Eq. 1.8 is simplified considerably and the three independent parameters  $\check{A}_2^0, \check{A}_4^0$  and  $\check{A}_4^4$  fully describe the CEF potential. For the Hund's rule ground state with  $J = 5/2$  the  $\check{A}_k^m$  with  $k = 6$  can be neglected if the intermixing with the higher  $J = 7/2$  multiplet is small. The sixfold (eightfold) degeneracy of the  $J = 5/2$  ( $J = 7/2$ ) multiplet is lifted by the tetragonal CEF and three (four) Kramers' doublets are formed. Within the low-lying  $J = 5/2$  multiplet a  $J_z$ -representation is chosen for the CEF wave functions, i.e. the CEF-split states are written as linear combinations of the  $|J = 5/2, J_z\rangle \equiv |J_z\rangle$  states:

$$\begin{aligned}\Gamma_7^1 &= \alpha | \pm 5/2 \rangle + \beta | \mp 3/2 \rangle \\ \Gamma_6 &= | \pm 1/2 \rangle \\ \Gamma_7^2 &= \beta | \pm 5/2 \rangle - \alpha | \mp 3/2 \rangle\end{aligned}\tag{1.10}$$

with  $\alpha^2 + \beta^2 = 1$ . The mixing parameter  $\alpha$  defines the anisotropy of the  $\Gamma_7$  states, or in other words the spatial distribution of the  $4f$  electrons (also referred to as  $4f$  orbital). Together with the crystal-field transition energies  $\Delta E_1$  and  $\Delta E_2$  from the ground state to the first and second excited CEF level, respectively, these parameters represent a set equivalent to the three  $\check{A}_k^m$ . Following simple algebraic considerations, the  $\check{A}_k^m$  can be expressed by  $\alpha, \Delta E_1$  and  $\Delta E_2$ , and vice versa (cf. Appendix A.4 in Ref. [89]).

This crystal-field description works reasonably well for the case of rare earths and provides a concrete way to access the  $4f$  ground state, the knowledge of which is the basis for the characterization of the  $f$  electron physics in Kondo lattice materials. Depending on the detailed crystal structure, in Ce and Yb compounds the problem reduces to determining a handful of parameters (or even less) which is possible via different experimental approaches. In Chapter 2 the high suitability of polarization-dependent x-ray absorption spectroscopy for this purpose will be shown.

For completeness it should be noted that in the present thesis all multiplets are taken into account, but in the case of  $4f$  states the crystal-field splitting is small with respect to the spin-orbit splitting. Therefore, often the intermixing between different  $J$  multiplets is very small and the off-diagonal elements in the Hamiltonian are neglected ( $J$  is a good quantum number again). As the main interest lies in the ground-state properties, the calculation is then limited to the energetically lowest  $J$  multiplet. This concept to focus on the lowest  $J$  multiplet and minimize the dimension of the Hamiltonian matrix is called *Stevens approximation* after K. W. H. Stevens [90]. The mathematical formalism is different from the description above. In

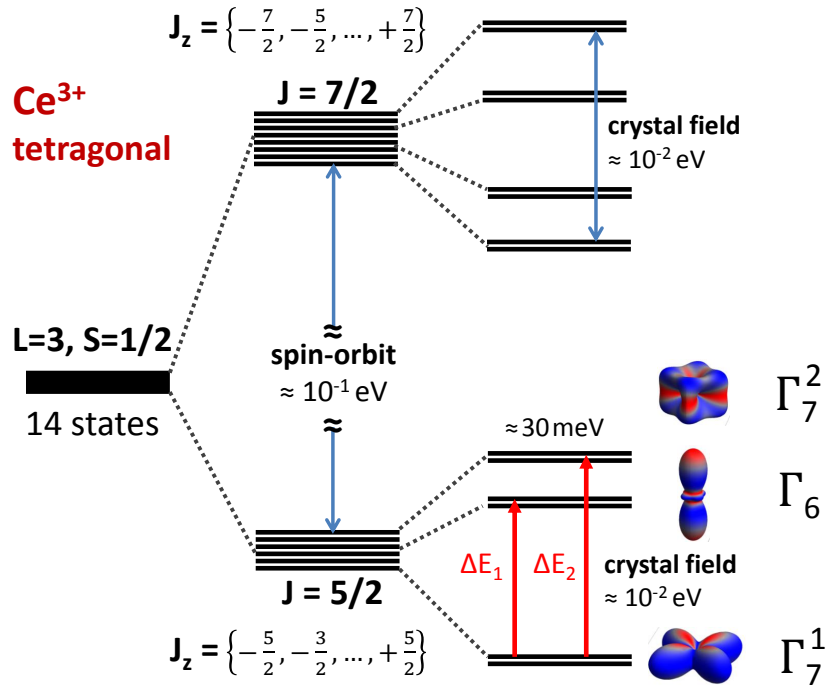


Figure 1.5: Schematic illustration of the energy level scheme for the case of a  $\text{Ce}^{3+}$  ion in a tetragonal crystal-field. The spin-orbit interaction is of the order of  $10^{-1}$  eV and splits the  $J = 5/2$  and  $J = 7/2$  into a sixfold and an eightfold degenerate multiplet, respectively. The crystal-field is of the order of  $10^{-2}$  eV and lifts the degeneracy within each multiplet, inducing anisotropy in the resulting Kramers' doublets.

the Stevens approximation so-called operator equivalents are created from the operators  $\mathbf{J}_x, \mathbf{J}_y$  and  $\mathbf{J}_z$ , thereby defining the *Stevens operators*  $\hat{O}_k^m$ , for example  $\hat{O}_2^0 = 3J_z^2 - J^2$ . The use of such operator equivalents is only valid within one  $J$  multiplet. The CEF Hamiltonian is then written as

$$H^{\text{CEF}} = \sum_{k=0}^{\infty} \sum_{m=-k}^k B_k^m \hat{O}_k^m \quad (1.11)$$

with the *Stevens parameters*  $B_k^m$ . These  $B_k^m$  are commonly used in literature. To compare the full theory parameters with the Stevens parameters, it is necessary to convert the  $B_k^m$  into  $\check{A}_k^m$ , or vice versa. The conversion factors and their derivation can be found in Ref. [89].

## 1.4 Scope of the thesis

The high relevance of an accurate description of the ground state in strongly correlated Kondo lattice systems and Kondo insulators becomes evident from the manifold of exotic phases present in these materials. The detailed symmetry of the Ce  $4f$  wave function and the degree of hybridization are significant parameters for the ground state formation, i.e. whether a magnetically ordered or an (unconventional) superconducting state forms, or whether a Kondo-insulating state develops.

When it comes to the determination of the CEF ground state in ‘high-symmetry’ (tetragonal and cubic) rare earth compounds, polarization-dependent soft x-ray absorption spectroscopy (XAS) has recently been shown to be extremely valuable [91–95] and provide a complementary method to inelastic neutron scattering, which often reaches its limits in HF materials due to the presence of hybridization. Core-level spectroscopy is also known to be one of the most powerful techniques for investigations of the  $4f$  occupation, and as very accurate models for the description of core-level spectra are available (and continuously improved), the accessible information about configuration interaction parameters and the hybridization is comprehensive. Here our method of choice is hard x-ray photoelectron spectroscopy (HAXPES) which offers a bulk-sensitive probe of the electronic structure, thereby avoiding that surface effects distort the obtained results.

In this thesis cerium-based Kondo insulators with low symmetries are analyzed by means of core-level spectroscopy. The first materials of interest are the orthorhombic Kondo semiconductors  $\text{CeM}_2\text{Al}_{10}$ , where the appearance of antiferromagnetic order for  $M = \text{Ru}$  and  $\text{Os}$  with very unusual characteristics and the lack of magnetic order for  $M = \text{Fe}$  is suggested to be substantially connected to the varying hybridization strength within the series and to its strong anisotropic character. However, a reliable picture of the CEF is still missing since the information from inelastic neutron scattering data is limited due to the strongly broadened CEF excitations and the presence of spin gaps. Chapters 3 and 4 deal with the determination of the  $4f$  CEF ground-state wave function of the three  $\text{CeM}_2\text{Al}_{10}$  compounds via linearly polarized XAS. The technique will be applied to *Kondo-insulating* systems of *orthorhombic* symmetry for the first time and the  $4f$  CEF ground state will be unambiguously determined, showing the high potential of polarization-dependent XAS for this material class. In Chapter 5 the hybridization interaction within the same compound family is examined in a detailed HAXPES study. A configuration interaction model will be combined with full multiplet calculations to describe the Ce  $3d$  core level spectra and extract *quantitative* numbers for hybridization interaction and the effective binding energy of the  $f$  impurity level in the  $\text{CeM}_2\text{Al}_{10}$  compounds. As an archetype representative of the class of Kondo insulators,  $\text{CeNiSn}$  is investigated in Chapter 6. Although  $\text{CeNiSn}$  is one of the most intensively studied Kondo insulators, the  $4f$  ground state is still unknown, but of crucial importance for understanding how the hybridization gap forms, which gives rise to the anomalous low-temperature properties. Again, linearly polarized XAS will be used to access the CEF ground-state wave function and thereby help to revisit the open question about the mechanism behind the gap formation. In Chapter 7 we temporarily leave the circle of Kondo insulators and consider the metallic  $\text{CeMIn}_5$  heavy-fermion compounds. In a systematic study on the substitution series  $\text{CeRh}_{1-x}\text{Ir}_x\text{In}_5$ , the  $4f$  orbital anisotropy will be shown to correlate with different ground-state properties (from AFM to SC) developing for different  $x$ .

The results stress the importance of the CEF anisotropy further, and suggest to perform similar studies on Kondo insulators, where substitution also often goes along with drastic changes of ground-state properties. Here the  $\text{Ce}M_2\text{Al}_{10}$  materials might offer an ideal playground since the transition temperature of the magnetic order and the direction of the ordered moment are strongly influenced by small amounts of electron- or hole-doping. Finally, Chapter 8 concludes the thesis by summarizing and discussing all findings, and giving an outlook for the direction of further research in this field.

Altogether, the present thesis investigates the rising importance of  $c$ - $f$  hybridization, CEF effects, orbital anisotropy and possible correlations in the field of  $4f$ -electron physics on a highly *quantitative* level, with the goal to obtain reliable input for the research area and provide the basis for a better understanding of the rich phase diagrams of strongly correlated electron systems.

Before presenting the above-mentioned studies, the investigated materials are briefly characterized below. In Chapter 2 the spectroscopic techniques used in the experiments of this thesis, i.e. XAS and HAXPES, are presented and the theoretical foundations for the analysis of the core-level spectra are provided.

- **$\text{Ce}M_2\text{Al}_{10}$**  A prominent example showing the impact of the CEF ground state in Kondo (insulator) compounds is the orthorhombic  $\text{Ce}M_2\text{Al}_{10}$  ( $M = \text{Ru}, \text{Os}$  and  $\text{Fe}$ ) family, which gained a great amount of interest at the time when the work on this thesis started.  $\text{CeFe}_2\text{Al}_{10}$  features a Kondo semiconducting non-magnetic ground state which strongly resembles the situation in  $\text{CeNiSn}$ , while in  $\text{CeRu}_2\text{Al}_{10}$  and  $\text{CeOs}_2\text{Al}_{10}$  semimetallic behavior and an AFM ground state with unusually high ordering temperatures of  $T_N = 27 \text{ K}$  ( $M = \text{Ru}$ ) and  $28.5 \text{ K}$  ( $M = \text{Os}$ ) are found. Apart from the surprisingly high values for  $T_N$ , the magnetic order brings up more questions since the ordered magnetic moment is highly reduced (to about  $0.3 - 0.4 \mu_B$  per Ce) and not aligned along the easy axis. (A nice summary of all physical properties of the  $\text{Ce}M_2\text{Al}_{10}$  compounds and the corresponding references can be found in Ref. [96].) At an early stage, static magnetic susceptibility measurements [97] revealed a strong magnetic anisotropy (presumably due to CEF effects) and in analogy to  $\text{CeNiSn}$  the CEF ground-state symmetry was expected to have important consequences for the (anisotropic) hybridization, and thus for the (non-)emergence of magnetic order and its puzzling properties [98, 99].
- **$\text{CeNiSn}$**  As one of the first cerium-based heavy-fermion compounds,  $\text{CeNiSn}$  was identified to belong to the class of narrow-gap Kondo insulators [100]. Soon  $\text{CeNiSn}$  turned into the focus of many studies since compared to other Kondo insulators (like e.g.  $\text{SmB}_6$  or  $\text{YbB}_{12}$ ) its energy gap – later classified as ‘pseudogap’ – was found to be particularly small and, together with the isostructural  $\text{CeRhSb}$  and  $\text{CeRhAs}$ , it has a non-cubic crystal structure [101]. By and by cleaner samples were obtained and  $\text{CeNiSn}$  was found to be effectively a semimetal [102] and from NMR experiments a peculiar ‘V’-shaped density of states with a finite value at  $\omega = 0$  was found [103, 104]. Despite extensive experimental and theoretical investigations of the pseudogap [5], the mechanism behind the gap formation is still not fully understood. However, the *symmetry* of the  $f$  electron’s ground state seems to be an important ingredient for the gap formation. In their

description for the formation of the Kondo insulating state, Ikeda and Miyake proposed that the hybridization gap in CeNiSn and CeRhSb has a nodal character [80], i.e. the hybridization vanishes along a single symmetry axis of the crystal, and that this goes along with the selection of a specific CEF ground-state symmetry. In the monoclinic point groups of CeNiSn and CeRhSb, where the low symmetry imposes only weak constraints to the composition of the low-lying Kramers' doublet, this selection of the nodal configuration seems somehow curious. Moreno and Coleman suggested an alternative many-body mechanism driven by Hund's interactions, which finds an axial and a quasi-octahedral state as possible solutions – of which the former corresponds to the CEF found by Ikeda and Miyake, and the latter appears most promising for the explanation of the 'V'-shaped DOS and the low-temperature properties of the Kondo insulating materials [105].

- **CeMIn<sub>5</sub>** In the CeMIn<sub>5</sub> (Ce115) series ( $M = \text{Rh, Ir and Co}$ ) the idea came up that some crystal structures, and thus certain ground-state wave functions, may work in favor of superconductivity [106], while others are detrimental to it. Models were proposed in which the different ground states realized by the isostructural CeMIn<sub>5</sub> compounds (paramagnetic, antiferromagnetic, superconducting and a coexistence of AFM and SC) are controlled by the CEF splitting energies or the orbital symmetry of the ground-state wave function [107, 108]. This was confirmed by band-structure calculations [109] showing that the effects of the CEF are the key to understand the difference in the electronic properties of the Ce115 compounds. HFSCs have in common that their gap function vanishes along lines on the Fermi surface, which classifies them as 'anisotropic SC' [3]. Detailed theoretical studies discuss how momentum( $k$ )-dependent hybridization in combination with the CEF anisotropy plays a role in the selection of the ground state. For instance, Burch *et al.* [110] concretely state that the hybridization gap values vary due to the  $k$ -dependence of the  $c$ - $f$  hybridization, leading to nodes in the hybridization gap which allow for the formation of antiferromagnetic fluctuations which in turn can couple to the mobile charges and provide a possible pairing mechanism for superconductivity. Very specific predictions for CeIrIn<sub>5</sub> on the basis of DMFT calculations were made by Shim *et al.* [111]. They show that the hybridization is stronger in the direction out of the tetragonal basal plane, thereby making the system more itinerant, which is rigorously connected with the spatial distribution of the  $4f$  electrons.

## 2 Spectroscopic techniques: Theoretical and experimental background

The main tasks of the studies in this thesis are (a) to gain access to the crystalline electric field and (b) to quantify the non-integer  $4f$  occupation of heavy-fermion materials, in particular of Kondo-insulating systems. For this purposes we realize and establish new experimental approaches by exploiting the potential of two of the most prominent techniques in the field of core level spectroscopy, namely **soft x-ray absorption spectroscopy** and **hard x-ray photoelectron spectroscopy**. Severe drawbacks, which occur in this context when other (common) techniques are used, are avoided – thereby giving a most reliable and quantitative insight into the electronic structure of the materials under consideration.

**Conventional methods** Depending on the studied material class, different techniques have been established for the experimental determination of the crystal-field ground state. These include optical (Raman) methods, electron spin resonance (ESR), nuclear magnetic resonance (NMR), Mößbauer spectroscopy, specific heat, inelastic neutron scattering (INS) and static magnetic susceptibility measurements [88]. The latter two are the standard methods in the field of rare earths. The non-spherical symmetry of the ground state is reflected in the anisotropy of the magnetic moments, which can be imaged by these techniques.

In temperature-dependent magnetic susceptibility the anisotropy observed when applying an external field along different crystallographic directions (e.g.  $B \parallel [100]$  and  $B \parallel [001]$  for tetragonal symmetry) is investigated. It can be modeled by adding the magnetic field operator  $H^{\text{mag}} = \mathbf{B}_{\text{ext}} \cdot (\mathbf{L} + 2\mathbf{S})$  to the system's Hamiltonian [85, 112]. The susceptibility  $\chi(T)$  is then obtained from the Boltzmann-weighted expectation value of the magnetization operators  $\mathbf{M}_x$ ,  $\mathbf{M}_y$  and  $\mathbf{M}_z$ . Different crystal-field symmetries yield rather different anisotropies at high temperatures and furthermore conclusions about the excited states can be drawn from the evolution of  $\chi(T)$  with increasing temperature. Neutrons can directly 'see' the magnetic moments in matter, which makes INS a straightforward tool to reveal the CEF scheme. Information about the ground state's spatial distribution is contained in the intensity ratios of the quasielastic and inelastic excitation lines and the energy positions of the inelastic excitations yield the crystal-field transition energies [85].

However, both techniques come with several drawbacks which often prevent an unambiguous result: If the sample is not sufficiently large, the count rates in an INS experiment will become rather small and the measurement unfeasible. In this context also the material's constituents matter because many elements (e.g. Rh, In or Sm) are strongly absorbing for neutrons. The magnetic scattering is often superimposed by phonon contributions which are difficult to correct for. But the most severe problem arises for strongly correlated electron systems, where electron-electron interactions are large, because this results in very broad line widths obscuring the information hidden in the spectrum. The situation can get even worse in Kondo insulators when

information about the quasielastic line is lost due to gaps in the spin excitation spectrum (spin gaps). The interpretation of magnetic susceptibility data also bears certain insecurities because (1) the excited states have to be taken into account via thermal averaging – meaning that the crystal-field energies become additional unknown fitting parameters, if they are not known from INS – and (2) the crystal field is not the only interaction inducing an anisotropy in  $\chi(T)$ . Both RKKY and Kondo interactions can significantly contribute to the magnetic anisotropy and it is not possible to separate the particular contributions without further ado [112].

When it comes to the investigation of the  $4f$  electronic structure of (cerium) rare earth systems, tools like valence band and core-level ( $3d$ ) x-ray photoelectron spectroscopy, as well as x-ray absorption, play a central role [113]. The obtained spectral structures are strongly related to the  $4f$  states, and by analyzing their energy positions, relative intensities and line shapes, a great amount of information can be extracted. Here the Anderson model has proven to provide a useful theoretical framework to deduce parameters like the position of the  $f$  level, the hybridization strength, or the  $f$  occupation. However, usually these experiments are performed in the range of soft x-rays, so that the probing depth is limited (see Sec. 2.2.4) and contributions from the surface are substantial. It is obvious to assume the electronic structure and the electron correlations to be different close to the surface (e.g. the hybridization is known to be reduced relative to the bulk), meaning that the corresponding spectra do not reflect the actual bulk properties.

In order to avoid all these drawbacks we use (a) the relatively new method of *polarization-dependent* x-ray absorption for the determination of the  $4f$  CEF ground state, in which the sensitivity to the ground-state symmetry is ensured by the selection rules of linear polarized light, and (b) core-level photoelectron spectroscopy with *hard x-rays* to determine the non-integer  $4f$  occupation. In the range of hard x-rays the electron inelastic mean free path is considerably enhanced, ensuring a sufficiently high probing depth to image the true bulk electronic structure.

In the following, the general principles and fundamental theoretical aspects of soft x-ray absorption and photoelectron spectroscopy will be introduced. The models for the determination of the CEF ground state and  $4f$  occupation will be elaborated and the respective experimental environments will be described. For further reading on core level spectroscopy, the comprehensive books by **de Groot and Kotani** [84] and **Hüfner** [114] shall be mentioned, on which the information in this chapter is based on. All experiments presented in this thesis were carried out at synchrotron light sources, which will be briefly treated at the end of this chapter, following the introduction in Ref. [115].

## 2.1 Soft x-ray absorption spectroscopy

When a solid is irradiated, the incoming x-rays can be scattered or annihilated via the photoelectric effect. Comparing the intensity of the radiation before and after the interaction with the sample can reveal plenty of information about its electronic structure. In x-ray absorption spectroscopy (XAS) a deeply-bound core electron is excited into an unoccupied valence state by the absorption of a photon. If the energy of the incident photons is tuned to an absorption edge,

i.e. corresponds to the binding energy of a core level, a sharp rise of the absorption will occur which marks the transition from the ground state to the lowest empty state. The absorption threshold energy for this process varies from element to element since the number of protons in the nucleus determines how strongly the electrons are bound to the ion – making XAS an element-selective technique. The XAS process is dominated by dipole transitions, which have very large absorption cross-sections, so that – in combination with the high flux of synchrotron radiation – very high spectral intensities are achieved.

Instead of the standard atomic notation, a special nomenclature is used to label the absorption peaks in XAS. The principal quantum numbers are replaced by the letters  $K$ ,  $L$ ,  $M$ , ..., and starting from the energetically lowest core-hole sub shell the orbital quantum numbers are expressed by the numbers 1, 2, 3, etc. For instance, in x-ray notation the excitations from the spin-orbit-split  $2p$  into the  $3d$  shell are denoted by  $L_{2,3}$ . The  $L$  edges of  $3d$  transition metals lie in the energy region from 350 to 1000 eV and are intensively investigated. Other absorption edges of interest in the soft x-ray regime are the  $M$  edges ( $3d$ -to- $4f$  excitations) in the case of rare earth systems, located between 800 and 1700 eV, or the oxygen  $K$  edge of transition metal oxides around 530 eV.

A typical  $2p$  XAS spectrum is shown in Fig. 2.1 by the example of the  $L_{2,3}$  edge of NiO [87]. Due to the  $2p$  spin-orbit coupling, the  $L$  edges of NiO split into the  $L_3$  edge around 851 eV and the  $L_2$  edge at about 868 eV. As marked by black arrows, after the respective absorption edges broad edge jumps occur, which arise from excitations into a continuum of delocalized states.

The most simple, yet also most unrealistic approach to understand the spectral line shapes and intensities in core level spectroscopy is given by the one-electron picture. In this model, electron-electron correlations are not considered, meaning that the ground-state density of states (DOS) is used (for example as calculated by density functional theory or Hartree-Fock methods) and the effects of extra valence electrons and the core hole creation are neglected. From this point of view the line shapes of the  $L_3$  and  $L_2$  edges are expected to be the same and their relative intensities defined by the degeneracy of the related states, i.e. a peak ratio of 2:1 is expected for the fourfold degenerate  $2p_{3/2}$  versus the twofold degenerate  $2p_{1/2}$ . Obviously, the  $L_{2,3}$  spectrum for NiO (Fig. 2.1) does not obey these rules. This is because NiO is a so-called correlated material where the interactions among electrons and between core hole and valence states are important. They lead to a multiplet structure which cannot be accounted for by the one-electron picture.

The strong attraction of the excited electron by the generated core hole yields a so-called excitonic state, which is the strongly interacting final-state electron-hole pair. The simple single-electron approach on the basis of the ground-state DOS usually works well for the  $K$  edge ( $1s$  to  $2p$ ), but for direct transitions into a partly filled  $d$  or  $f$  shell (e.g. transition metal  $L_{2,3}$  and rare earth  $M_{4,5}$  edges) XAS does not reflect the corresponding partial DOS because of the significant overlap of the core and valence wave functions in the excitonic final state. The description of the latter requires a many-body wave function. Excitons are highly localized and have large binding energies. This allows to treat them in an atomic picture yielding a good description of the spectral features. The average lifetime of a core hole is of the order of  $10^{-15}$  s, which corresponds to an uncertainty in energy of about 100 meV, giving rise to sharp and distinct spectral lines. Note, the above-mentioned continuum edge jump (or background)

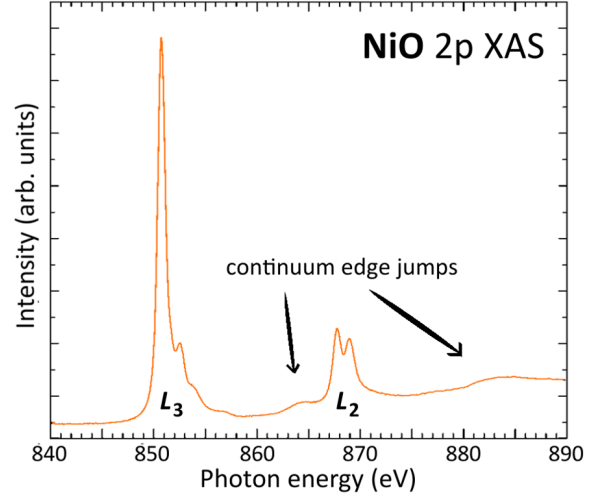


Figure 2.1: An exemplary x-ray absorption spectrum: the  $L_{2,3}$  edges ( $2p$ -to- $3d$  transitions) of NiO (redrawn from Ref. [87], Fig. 2.2).

reflects spectral weight due to non-bound final states and shall remain unconsidered in the following since its contribution is only minor.

The multiplet structure in XAS – together with the dipole selection rules (see below) – can give very detailed information about the valence state, orbital occupation, spin state and crystalline electric field of the ground and excited states. The creation of a core hole effectively probes the valence state. Even very small changes in the valence have an impact on the core hole potential and modify the multiplet structure, and thereby the spectral line shape, significantly. Sensitivity towards the orbital occupation or different spin occupations is achieved in linear/circular dichroism experiments by exploiting the polarization dependence of the absorption, using either linearly or circularly polarized light.

### 2.1.1 Theoretical description

Following the presentation in Ref. [84], the basic theoretical framework to describe the XAS process is outlined in this section. The complete interaction Hamiltonian for the description of x-rays interacting with atomic electrons in matter is given by

$$H = H_{\text{rad}} + H_{\text{atom}} + H_{\text{int}} \quad (2.1)$$

consisting of the radiation field Hamiltonian, the Hamiltonian of the atomic electrons and the interaction Hamiltonian. The former two can be written as:

$$H_{\text{rad}} = \sum_{\mathbf{k}\lambda} \hbar\omega_{\mathbf{k}} \left( n_{\mathbf{k}\lambda} + \frac{1}{2} \right) \quad \text{and} \quad H_{\text{atom}} = \sum_i \left( \frac{\mathbf{p}_i^2}{2m} + V_{\text{pot}}(\mathbf{r}_i) \right) \quad (2.2)$$

The summation in  $H_{\text{rad}}$  goes over the wave vectors  $\mathbf{k}$  and polarizations  $\lambda$ , and  $\frac{1}{2}\hbar\omega_{\mathbf{k}}$  is the zero point energy. The two terms in the Hamiltonian of the atomic electrons  $i$  account for their kinetic and potential energy, respectively. In  $H_{\text{atom}}$  the Coulomb interaction with the nucleus, the electron-electron Coulomb repulsion and the spin-orbit coupling can be included. The

interaction itself is treated as small perturbation and the first- and second-order terms read:

$$H_{\text{int}}^{(1)} = \frac{e}{mc} \sum_i \mathbf{p}_i \cdot \mathbf{A}(\mathbf{r}_i) + \frac{e}{2mc} \sum_i \sigma_i \cdot \nabla \times \mathbf{A}(\mathbf{r}_i) \quad (2.3)$$

$$H_{\text{int}}^{(2)} = \frac{e^2}{2mc^2} \sum_i \mathbf{p}_i \cdot \mathbf{A}(\mathbf{r}_i)^2 \quad (2.4)$$

Here,  $\mathbf{A}$  is the vector potential of the electromagnetic field,  $\mathbf{p}$  the electron momentum operator and  $\sigma$  the spin operator. The two expressions in  $H_{\text{int}}^{(1)}$  describe the interaction between the electric field  $\mathbf{E}$  and the electron momentum, and between the magnetic field  $\mathbf{B} = \nabla \times \mathbf{A}$  and the electron spin.

An expression for the probability  $W_{0 \rightarrow f}$  of a transition between two states via the absorption of a photon with the energy  $\hbar\omega$  is provided by Fermi's golden rule:

$$W_{0 \rightarrow f} = \frac{2\pi}{\hbar} |\langle \phi_f | T | \phi_0 \rangle|^2 \delta(E_f - E_0 - \hbar\omega) \quad (2.5)$$

The initial and final state wave functions are denoted by  $\phi_0$  and  $\phi_f$ , and  $T$  is the transition operator. The  $\delta$ -function makes sure that the energy conservation is not violated.<sup>1</sup> An expression for  $T$  can be found by solving the Lippmann-Schwinger equation [116]. In first order one obtains  $T_1 = H_{\text{int}}^{(1)}$  and this solution adequately describes one-photon transitions like XAS or photoemission. After introducing the vector potential  $\mathbf{A}(\mathbf{r})$  in second quantization, neglecting the spin interaction term in Eq. 2.3 and doing a Taylor expansion of the exponential function up to second order (for the full derivation see Chapter 2 in Ref. [84]), one ends up with

$$T_1 = \sum_{\mathbf{k}, \lambda} b_{\mathbf{k}\lambda} \frac{e}{mc} A_0 [(\mathbf{e}_{\mathbf{k}\lambda} \cdot \mathbf{p}) + i(\mathbf{e}_{\mathbf{k}\lambda} \cdot \mathbf{p})(\mathbf{k}\mathbf{r})] \quad (2.6)$$

where  $b_{\mathbf{k}\lambda}$  is the annihilation operator and  $\mathbf{e}_{\mathbf{k}\lambda}$  gives the vectors describing the polarization. Since XAS is a dipole technique, it is sufficient to look at the first term in Eq. 2.6. The second term represents the electric quadrupole transition and does not contribute in first approximation for  $\hbar\omega \ll 10$  keV. Consequently, in dipole approximation the transition operator  $T$  becomes

$$T = \sum_{\mathbf{k}, \lambda} b_{\mathbf{k}\lambda} \frac{e}{mc} A_0 (\mathbf{e}_{\mathbf{k}\lambda} \cdot \mathbf{p}) \quad (2.7)$$

which means that  $T \propto \mathbf{e}_{\mathbf{k}\lambda} \cdot \mathbf{p}$ . In combination with Fermi's golden rule (Eq. 2.5) we now have an expression for the spectral intensity  $I$  to be expected in an XAS experiment for a dipole excitation from the initial state with the wave function  $\phi_0$  to one of the final states with the wave function  $\phi_f$ :

$$I \propto |\langle \phi_f | \mathbf{p} \cdot \mathbf{e}_{\mathbf{k}\lambda} | \phi_0 \rangle|^2 \delta(E_f - E_0 - \hbar\omega) \quad (2.8)$$

The dipole selection rules are an important ingredient to exploit the full power of XAS and be able to explain the multiplet structure of a spectrum. They define whether a transition

<sup>1</sup>Here  $E_f$  is the final state energy and not to be confused with the energy of the impurity  $f$  level in the Anderson model (Chapter 1).

is quantum-mechanically allowed or not in the dipole approximation. The transition rate  $|\langle \phi_f | T | \phi_0 \rangle|$  in Fermi's golden rule corresponds to an integral over the whole space, which is non-zero only for an even integrand. The wave functions of  $s$  and  $d$  orbitals are even, whereas  $p$  and  $f$  wave functions are odd [87]. Since the dipole operator  $T$  is odd, transitions are only allowed if the final state has a different parity compared to the initial state. The dipole selection rules follow from these symmetry considerations and the conservation<sup>2</sup> of angular momentum and spin:

$$\Delta l = \pm 1; \quad \Delta j = 0, \pm 1; \quad \Delta m_l = 0, \pm 1; \quad \Delta m_s = 0; \quad \Delta L = 0, \pm 1; \quad \Delta S = 0; \quad \Delta J = 0, \pm 1 \quad (2.9)$$

where  $l$  is the orbital,  $m_l$  the magnetic,  $m_s$  the spin and  $j$  the total angular momentum quantum number.

### 2.1.2 Atomic full multiplet theory

In Sec. 2.1 it was already pointed out that for strongly correlated electron systems the one-electron picture is not sufficient. Many-body effects have to be considered to model the fine structure of the core level spectra and are particularly important for XAS (e.g. on rare earth compounds) due to the strongly interacting excitonic final state. Contrary to expectations, the electron-electron interactions leading to the multiplet splitting are hardly screened within a solid [87]. The experimentally determined Slater integrals of some metals were found to be comparable with Hartree-Fock values calculated for a free ion [117], showing that the order of magnitude of multiplet effects in atoms and solids is similar. Yet, a slight reduction of the atomic values still might be necessary to account for configuration interaction effects which are not covered by the Hartree-Fock calculations.

The simulation of an XAS spectrum requires the calculation of the final and also of the initial state (see Eq. 2.8). This is why ground-state properties can be deduced from it. In this thesis the program XTLS (v8.3 and v9.0) of A. Tanaka [118] was used for simulations. It provides the possibility to analyze high-energy core-level spectra in an atomic full multiplet model based on ligand-field theory. For further calculations of orbital shapes, susceptibilities or magnetic moments, the *Mathematica* package Solid State Physics [119] created by M. W. Haverkort was used. In both codes the Hamiltonian is built on a many-electron basis, or configuration interaction basis, based on spherical harmonics (see below and Sec. 1.3). It is due to the very localized character of excitons that atomic full multiplet theory can adequately describe the XAS data.

The general idea behind the model is to focus on a central single atom and disregard the translational symmetry. A mean-field ansatz is used for the surrounding ligands and the local symmetry [112]. Here we distinguish between the crystal-field and the ligand-field approach. In the former – a purely ionic model proposed by H. Bethe in 1929 [120] – the surrounding ions are approximated as simple point charges and their influence on the valence electrons of the central (metal) ion is given by the resulting static electric field. Ligand-field theory, which is based on molecular orbital theory, goes one step further and also considers covalency or, in other words, the overlap of the valence orbital of the central ion with the ligand's valence

<sup>2</sup>An x-ray photon has an angular momentum of 1 and does not carry any spin.

orbital [121]. For further and more detailed reading on ligand-field theory and full multiplet calculations the Refs. [121–124] are recommended. In rare earth compounds the simple ionic crystal-field model can already give a good description [89, 112] because the physics in these systems is driven by the  $4f$  electrons, which are known to be well localized. In other cases, e.g. for transition metal oxides, it might be necessary to include charge-transfer effects by explicitly considering a small cluster of ligands surrounding the central atom [84, 87].

Now the construction of the many-electron basis for the full-multiplet Hamiltonian based on single-electron wave functions  $\phi(r, \theta, \varphi)$  shall be explained, following the considerations in Refs. [87, 112]. It is possible to separate the angular and radial part and write  $\phi(r, \theta, \varphi) = R_n^l(r) \cdot Y_l^m(\theta, \varphi)$  if they behave atomic-like. The quantum numbers follow the usual notation, meaning that  $n$  is the principal quantum number of the electron shell,  $l$  the orbital angular momentum quantum number (subshell) and  $m$  the magnetic quantum number.  $Y_l^m(\theta, \varphi)$  are the orthonormal spherical harmonics, which depend only on the angular degrees of freedom, and  $R_n^l(r)$  represents the radial part, which is determined by the element and the electronic (shell and subshell) configuration. The full anti-symmetrized many-electron wave function  $\phi(r_1, \dots, r_N)$  is then given by the Slater determinant of the single-electron wave functions. The antisymmetry ensures that the Pauli exclusion principle is not violated.

$$\phi(r_1, \dots, r_N) = \begin{vmatrix} \phi_1(r_1) & \cdots & \phi_1(r_n) \\ \vdots & \ddots & \vdots \\ \phi_N(r_1) & \cdots & \phi_N(r_n) \end{vmatrix} \quad (2.10)$$

Which interactions have now to be included into the Hamiltonian to solve the eigensystem and find the initial and final state wave function? Apart from the crystal-field – its implementation is comprehensively explained in Sec. 1.3 – the essential contributions come from the Coulomb and spin-orbit interactions. For the description of magnetic properties, an external magnetic field  $\mathbf{B}_{\text{ext}}$  and an internal exchange field  $\mathbf{H}_{\text{int}}$  can be added via the operators  $H^{\text{mag}} = \mathbf{B}_{\text{ext}} \cdot (\mathbf{L} + 2\mathbf{S})$  and  $H^{\text{ex}} = \mathbf{H}_{\text{int}} \cdot \mathbf{S}$ , respectively.

The general spin-orbit operator in first quantization reads

$$H^{\text{so}} = \sum_{j=1}^{N_e} \zeta(r_j) \mathbf{l}_j \cdot \mathbf{s}_j \quad (2.11)$$

where  $N_e$  is the number of electrons in the shell under consideration and the parameter  $\zeta(r_j)$  gives the spin-orbit coupling strength. Due to the spin-orbit interaction the spin and orbital angular momenta couple to a total angular momentum  $\mathbf{J} = \mathbf{L} + \mathbf{S}$ . In the case of the Ce  $M_{4,5}$  absorption edges the spin-orbit interaction of the  $3d$  core hole and the spin-orbit interaction of the  $4f$  electrons are considered.

Unlike  $H^{\text{so}}$ , which is a one-particle operator, the Coulomb interaction involves pairs of electrons and consequently requires a two-particle operator. More precisely, the Coulomb interaction between the  $3d$  hole and the  $4f$  electron plus the Coulomb interaction between the  $4f$  electrons is taken into account for the calculation of the cerium  $M$  edge XAS spectra. The Coulomb terms capture the electron-electron interaction and are the key ingredients for the reproduction of the fine multiplet structure observed in core level spectroscopy. They

are described by a scattering event from the two-electron state  $|ij\rangle$  into the state  $|i'j'\rangle$ . The scattering potential is given by the Coulomb potential

$$A^{\text{Coul}}(\mathbf{r}_i, \mathbf{r}_j) = \frac{e^2}{|\mathbf{r}_i - \mathbf{r}_j|} = \frac{e^2}{r_{ij}}. \quad (2.12)$$

After introducing Legendre polynomials and expanding the potential in spherical harmonics, the wave function can be factorized into an angular and a radial part (as it is done for the crystal field potential, see Sec. 1.3). The angular dependence is given basically by integrals over the spherical harmonics and usually can be simplified by applying several selection rules. It can be solved analytically. The radial dependence consists of the so-called Slater integrals over the radial part of the wave function

$$R^k(ij i' j') = e^2 \int_0^\infty \int_0^\infty \frac{r_{<}^k}{r_{>}^{k+1}} R_i(r_i) R_j(r_j) R_j(r_i) R_i(r_j) r_i^2 r_j^2 dr_i dr_j \quad (2.13)$$

which cannot be calculated analytically.  $k$  denotes the different multipole parts of the interaction (e.g.  $k = 0$  the monopole,  $k = 2$  the dipole and  $k = 4$  the quadrupole integral) and  $r_{<} = \min(r_i, r_j)$  and  $r_{>} = \max(r_i, r_j)$ . The values for the Slater integrals and the spin-orbit parameters are determined for a free ion with the atomic structure code RCN36K by R. D. Cowan [86] based on the Hartree-Fock approximation.

Once more the importance of the correct and full implementation of the electron-electron repulsion shall be emphasized. In Ref. [87] the consequences of simplifications in the electron-electron Hamiltonian are discussed in great detail. For instance, in the simplest approximation two parameters are used to describe the repulsion between a pair of electrons:  $U_0$  for the repulsive Coulomb energy, and the Hund's rule exchange  $J_H$  for the attractive interaction between two electrons with parallel spin. The resulting approximated Hamiltonian is remarkably simple but it turns out that, as soon as other states than the Hund's rule ground state are involved, it gives a completely different – and therefore wrong – picture of the multiplet splitting compared to the full multiplet theory. The differences matter especially when high-energy excitations have to be simulated, but also ground-state properties are not captured correctly in the simple scheme because it yields wrong multiplicities. These kinds of problems persist also for other less simple approximations, so that the full multiplet theory, i.e. the complete and correct inclusion of the electron-electron interaction, remains the method of choice to understand the underlying fine structure in soft XAS as well as ground-state properties.

### 2.1.3 Determination of crystal fields

In 2008, Hansmann *et al.* [91] illustrated at the example of CePd<sub>2</sub>Si<sub>2</sub> how polarization-dependent soft XAS at the Ce  $M_{4,5}$  edge can be used as a complementary technique to neutron scattering for the determination of the CEF ground state in rare earth heavy-fermion compounds. Since then the method has proven to be very successful, as many publications [92–95, 112] and the results in the present thesis show.

In an XAS experiment the sensitivity to the ground-state symmetry is achieved by exploiting the dichroism effect of linearly polarized light. The transition probability depends on the orbital

contribution parallel to the electric field vector of the incoming light. The Ce  $M_{4,5}$  absorption edge originates from an excitation of a  $3d$  electron into the  $4f$  shell. Starting from  $3d^{10}4f^1$ , the final-state configuration is  $3d^94f^2$ . As repeatedly stressed in this chapter, this excitonic final state can be described by atomic full multiplet theory. Without selection rules there are  $10 \cdot \frac{14 \cdot 13}{2} = 910$  possible final states, but since we are dealing with a dipole transition, far less multiplet lines contribute to the experimental spectra (see Eqs. 2.9). Additional selection rules due to the use of linearly polarized light reduce the number of possible final-state multiplets even more and introduce the aforementioned orbital sensitivity.

In the top left panel of Fig. 2.2 the calculated Ce<sup>3+</sup>  $M_{4,5}$  XAS spectra for the pure  $|J_z\rangle$  states of the  $J = 5/2$  multiplet (cf. Sec. 1.3) and the shape of the corresponding  $4f$  orbitals are shown. For tetragonal symmetry the simulation is performed for light polarized with  $E \parallel c$  (red) and  $E \perp c$  (blue). The quantization axis  $c$  is chosen to be the ‘long’ tetragonal axis with fourfold rotational symmetry. The difference between the two polarizations – the linear dichroism (LD) – is shown in the bottom panel. In the isotropic case (without crystal field) the spatial distribution of the  $4f$  electrons would be spherical and the LD zero (see top black curve in the left panel). Each of the pure  $|J_z\rangle$  states has its own very characteristic polarization dependence. The right panels of Fig. 2.2 shows the same kind of calculations but now for various  $\alpha$ -admixture of the  $\Gamma_7$ -type state (see Eqs. 1.10). One can clearly see that the LD strongly depends on whether the ground state is more  $|5/2\rangle$ - or  $|3/2\rangle$ -like (large or small  $\alpha$ , respectively), thereby yielding a spectroscopic fingerprint for a certain crystal-field anisotropy and allowing an unambiguous determination of the ground-state wave function.

For the experimental procedure it is important that the sample temperature  $T_{\text{sample}}$  is chosen low enough, in a way that only the lowest CEF doublet is populated. Only then all information obtained from the XAS spectra is directly related to the ground-state composition. In practice this means  $k_B T_{\text{sample}} \ll \Delta E_{\text{CEF}}$ . Note that the experimental resolution ( $\sim 150 - 400$  meV) in this approach is not limiting the access to the CEF information, although the  $4f$  CEF splittings are small ( $\sim$  meV), because the CEF symmetry is concealed in the polarization dependence which can be rather large. Linear polarized XAS is an element-specific method so that other constituents in the sample do not hamper the analysis. Absorption effects as in INS do not occur and thanks to the high level of technical advancement in third-generation synchrotrons very intense and well focused x-ray beams allow the use of small samples of a size less than  $1 \text{ mm}^3$ . In combination with the large absorption cross-sections for dipole transitions, nearly noise-free spectra with very intense peaks on a relatively low background are obtained.

After its debut in Ref. [91], where the debate about the CEF ground state of CePd<sub>2</sub>Si<sub>2</sub> was settled, linear polarized XAS has been applied to several tetragonal cerium systems [92–94], cubic YbInNi<sub>4</sub> [95], hexagonal CeRh<sub>3</sub>B<sub>2</sub> [112] and also other rare earth compounds like TmB<sub>4</sub> and HoB<sub>4</sub> [125]. The studies presented in this thesis extend the method to systems with lower symmetries, emphasizing its high relevance for the investigation of the crystal-field anisotropy in rare earths.

Before closing this section, a last point shall be briefly addressed. Linear polarized XAS – as well as INS or magnetic susceptibility – is governed by dipole excitations, meaning that higher than twofold symmetries cannot be distinguished in the measurement. Yet, the knowledge about the actual rotation of the ground-state orbital might be of relevant importance e.g. for hybridization effects with the neighboring ligand atoms. Considering an orbital with tetragonal

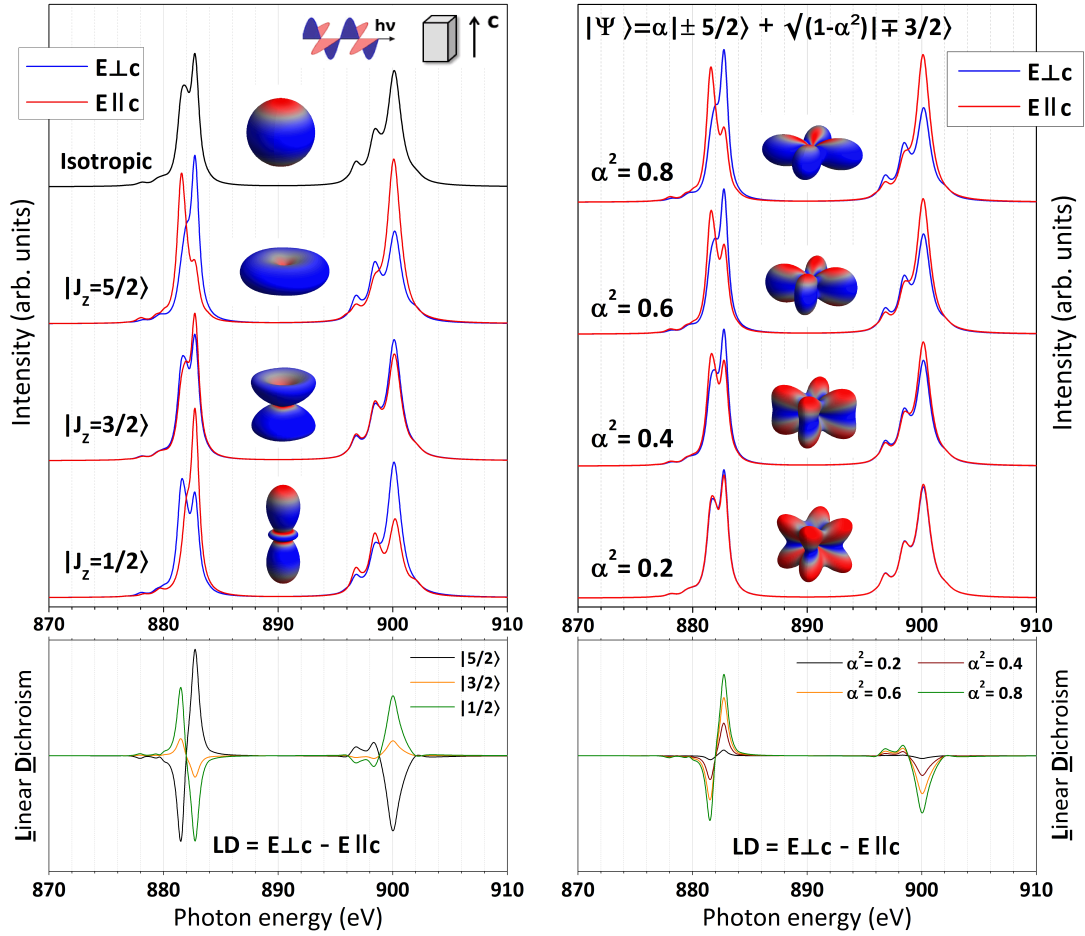


Figure 2.2: Left: Calculation of the polarization-dependent Ce  $M_{4,5}$  XAS spectra for the pure  $|J = 5/2, J_z\rangle$  states of  $Ce^{3+}$ . The simulations are shown for incoming light polarized with  $E \parallel c$  (red) and  $E \perp c$  (blue), with  $c$  being the fourfold rotational axis in tetragonal symmetry. The isotropic spectrum is shown as top curve (black). Right: Simulations for different tetragonal anisotropies, i.e. different  $\alpha^2$  values, of the  $\Gamma_7$ -type ground-state wave function  $\alpha|\pm 5/2\rangle + \sqrt{1-\alpha^2}|\mp 3/2\rangle$ . In both panels the insets show the respective angular distribution of the 4f electrons. Moreover, in the two bottom panels the linear dichroism (LD), i.e. the difference spectra  $E \perp c - E \parallel c$ , for the pure (bottom left) and the different mixed states (bottom right) are included.

symmetry of  $\Gamma_7$ -type (see right panel of Fig. 2.2), the dipole limitations of XAS do not allow to determine whether the lobes of the orbital point along [100] or along [110] (rotated by  $45^\circ$  within the tetragonal plane). Mathematically this means that the technique is not sensitive to  $\alpha$ , but only to  $\alpha^2$  (or  $|\alpha|$ ). This issue can be solved by going beyond the dipole limit with non-resonant inelastic x-ray scattering (NIXS). In a NIXS experiment with hard x-rays and at large momentum transfers  $|\mathbf{q}|$  the sign of  $\alpha$  can be determined by exploiting vector- $\mathbf{q}$  dependence of the dynamical structure factor [126], thereby gaining access to the orbital rotation within the plane. Another very recent work by Mori *et al.* shows that the  $4f$  ground state of Yb compounds can also be detected by core-level photoelectron spectroscopy [127]. Similarly to the XAS approach, the polarization dependence gives the sensitivity to the ground-state symmetry, and in addition to that the angular dependence (defined by the angle of the photoelectron detection direction) can be exploited to obtain information about the in-plane rotation of the  $4f$  orbital.

## 2.1.4 Experimental aspects

### Detection modes

Aside from measuring the absorption in a *transmission* experiment through comparison of the intensity of the incident x-rays with the intensity after the sample, several other detection techniques are possible [84], with different advantages and disadvantages. These techniques rely on core hole decay processes and are called *yield modes*; namely we distinguish between *fluorescence yield* and *electron yield*. It is even possible to measure ionized atoms escaping from the sample in the *ion yield* technique.

In general, when working in transmission the linear absorption coefficient  $\mu(\hbar\omega)$  describes the absorption of an x-ray beam interacting with a sample (via photoelectric and scattering processes):

$$I(\hbar\omega) = I_0(\hbar\omega) \cdot e^{-\mu(\hbar\omega) \cdot x} \quad (2.14)$$

where  $I_0$  and  $I$  are the initial and transmitted intensities, respectively, and  $x$  the sample thickness. For hard x-rays and homogeneous (preferably thin) samples the transmission mode works well but becomes problematic for soft x-rays below 1 keV because of the short x-ray attenuation length [84].

At this point the aforementioned yield modes come into play, which provide an indirect measurement of the absorption cross-section. After the core hole excitation the system is in an excited state and subsequently relaxes by the decay of the core hole. Basically, this happens through emission of photons (fluorescence) or secondary electrons of lower binding energies. The general assumption behind the yield modes is that the x-ray absorption cross-section is proportional to the number of core holes and that the decay processes can be directly related to the number of core holes [84]. A necessary requirement for the yield detection is that the escape depth of the electrons/photons is short compared to the mean absorption length [128].

The filling of the core hole by the decay of an excited electron gives rise to the emission of photons. In the total fluorescence yield (TFY) mode all the fluorescent decay products in a wide energy range are measured, e.g. by a photodiode or a channel electron multipliers [129]. In the past, the partial fluorescence yield (PFY) technique became prominent, in which the detector is tuned to a specific fluorescence energy [130–134]. This selective measurement in principle

allows to choose a particular valence, spin orientation or chemical nature of the neighboring atoms, and measure only the absorption signal related to the selected state. Moreover, the spectral resolution in PFY-XAS spectra is increased by taking advantage of the longer lifetime of a less-excited final state.

The most frequently used detection method – also employed in the XAS studies presented in this thesis – is the total electron yield (TEY) mode. As the name suggests, all electrons emitted from the sample are detected in this case. Usually this is done by recording the drain current  $I_{\text{drain}} \approx \mathcal{O}(1 \text{ pA} - 1 \text{ nA})$  of the sample with an amperemeter. The contributions to the TEY signal come from the primary Auger electrons and additionally from electrons with lower energies [128], since the primary electrons inelastically scatter on their way to the surface producing an avalanche of secondary electrons. Similarly to PFY, it is possible to work in the partial electron yield (PEY) mode, in which a lower threshold is set for the kinetic energy or a particular energy window is considered, so that only primary (unscattered) Auger electrons from the surface-near region or specific (secondary) Auger decay channels can be selected [84].

The probing depth of XAS varies depending on the detection mode and defines whether the obtained information is more surface- or bulk-related. Because photons travel more freely in matter compared to electrons, the average probing depth in fluorescence yield measurements is much higher than for electron yield. To be precise, the mean free path of the incident soft x-rays reaches  $\sim 1000 \text{ \AA}$  which also corresponds to the mean free path of the outgoing fluorescent light, assuring a high bulk-sensitivity in TFY. The probing depth of TEY is one or two magnitudes smaller ( $\sim 30 - 100 \text{ \AA}$ ) and depends on the material under investigation. It further depends on the exact nature of the inelastic processes taking place in the Auger decay cascade [128], nevertheless, in most cases the TEY signal is assumed to be proportional to the number of created core holes and yield mostly bulk-related information.

A severe drawback in fluorescence yield measurements is the self-absorption effect [84]. Due to the long mean free path, the emitted x-rays will not reach the sample surface undisturbed but are partly re-absorbed on their way, which results in significant distortions of the spectral shape. Intense peaks become compressed with respect to the less intense features and the background. This effect is negligible in dilute materials with light elements but matters for concentrated or heavier elements. Thus, most suitable for studies of the transition metal  $L_{2,3}$  or rare earth  $M_{4,5}$  edges is the electron yield mode, in which the problem of self-absorption does not arise because the x-ray penetration depth is much larger than the escape depth of the electrons [135].

### Technical conditions

Soft XAS measurements have to be carried out at very low pressure ( $\sim 10^{-10} - 10^{-9}$  mbar) in ultra-high vacuum (UHV) for several reasons. First of all, soft x-rays are strongly absorbed when passing through air. Second, due to the limited probing depth, a clean sample surface is required over an extended period of time. Initially, a clean surface is obtained by cleaving the sample *in situ*, either by breaking or cutting it with a sharp blade. This yields a fresh surface, which has not been exposed to air before. The time for the formation of one monolayer of contaminations depends on the pressure conditions – it is of the order of seconds in the  $10^{-6}$  mbar range and of the order of a few hours for pressures around  $10^{-9}$  mbar. Consequently, pressures  $\leq 10^{-9}$  mbar are needed in order to ensure a constant sample quality throughout the measurements. These

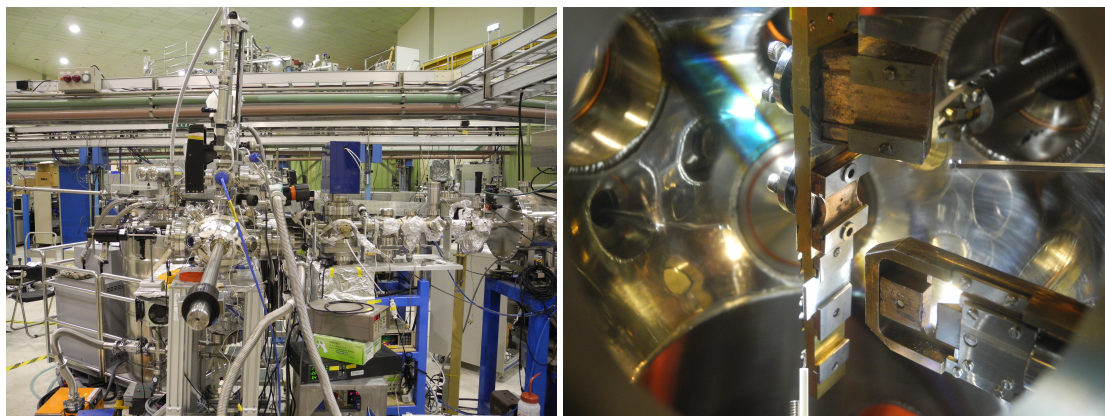


Figure 2.3: Left: Photograph of the XAS endstation of beamline BL08A at the NSRRC in Hsinchu, Taiwan. Right: View inside the main UHV measurement chamber. The vertical arm with several slots for the sample plates and different tools can be seen (e.g. the cleaver at the bottom right corner).

are of course rough estimates only, as the actual surface degradation time varies from material to material and also the composition of the residual gases in the UHV chamber might have an impact.

### 2.1.5 Light sources and beamlines

The XAS experiments presented in this work were carried out at three different synchrotron facilities: The National Synchrotron Radiation Research Center (NSRRC) in Hsinchu, Taiwan, the storage ring BESSY II of the Helmholtz Zentrum in Berlin, Germany, and the European Synchrotron Radiation Facility (ESRF) in Grenoble, France. In the former ones the operating energy of the electron beam is 1.5 and 1.7 GeV, in the latter one 6 GeV. At the NSRRC the bending magnet beamlines BL11A1 and BL08A were used, which have the so-called 'Dragon design' by C. T. Chen [136]. Characteristic of this construction is the use of separate horizontal and vertical focusing mirrors, a movable exit slit and only one spherical grating mirror, which works as monochromator. At BESSY II the measurements were performed at the undulator beamline UE46-PGM1 and at the ESRF the XAS endstation of the undulator beamline ID08 was used.

All XAS endstations feature a similar UHV environment with a base pressure of the order of  $10^{-10}$ – $10^{-9}$  mbar. As an example, Fig. 2.3 shows a photograph of the XAS endstation used at the NSRRC light source in Taiwan and a look inside the measurement chamber. To obtain a clean sample surface the single crystalline samples were cleaved *in situ* just before commencing the measurements. The data collection took place at normal incidence in the TEY mode and for normalization of the absorption signal the incoming photon flux  $I_0$  was recorded before the experimental chamber. The energy resolution in the region of the Ce  $M_{4,5}$  edge ( $h\nu \approx 870$ – $910$  eV) varies between 0.15 and 0.4 eV, depending on the beamline and measurement conditions. At the undulator beamlines of BESSY II and the ESRF the polarization of the incoming light can be selected so that the same sample spot can be probed with horizontally and vertically

polarized light. This is not possible at the bending magnet beamlines of the NSRRC. Here the incoming radiation is horizontally polarized and in order to perform polarization-dependent measurements the sample has to be rotated around the Poynting vector of the light. By rotating the sample in steps of  $90^\circ$  two equivalent polarizations at two sample positions are measured. The full experimental details for the different studies are given in the respective chapters.

## 2.2 Hard x-ray photoelectron spectroscopy

Photoelectron spectroscopy (PES) is a well established method to determine the electronic structure or the chemical composition of a sample. It is based on the photoelectric effect, which was first observed in 1887 by Hertz [137]. Theoretically the effect was not understood until 1905 when Einstein postulated the quantum nature of light [138]. Today we know that if photons impinge on a sample with sufficient high energy, electrons from occupied energy states will be excited via the photoelectric effect and leave the material with a certain kinetic energy. This corresponds to a transition from an  $N$ -particle initial state to a final state with  $N - 1$  particles.

For the energy of the incoming photons we distinguish between the ultraviolet regime (UPS,  $\approx 5 - 100$  eV), the soft x-ray domain (XPS,  $\approx 100 - 2000$  eV) and the hard x-ray region above 2000 eV (HAXPES). In UPS mainly valence band states can be studied with high resolution and high surface sensitivity. Access to core-level states is possible with XPS and HAXPES, the latter one having a much higher bulk sensitivity.

In the following, the general theoretical and experimental background of (hard x-ray) photoelectron spectroscopy is outlined. For more information about technical details and further reading on the theoretical description of PES, the reader is referred to Refs. [84, 114], as well as to Refs. [115, 139], on which the presentation in this section is based on.

### 2.2.1 General principle

In a standard PES setup a gas-discharge lamp, an x-ray tube or a synchrotron storage ring provide the radiation for the experiment. The sample is illuminated by monochromatic light coming from these sources, so that the electrons excited by the photoelectric effect – the photoelectrons – leave the sample and can be detected and counted by an electrostatic analyzer.

In order to make the electrons leave the sample, the energy of the photons  $h\nu$  has to be higher than the binding energy  $E_B$  of the electrons in the sample. The analysis of the excited photoelectrons takes place with respect to their kinetic energy  $E_{\text{kin}}$  and their momentum  $p$ . For angle-resolved experiments one is also interested in the angle between photoelectrons and the impinging light and the polar and azimuthal angle under which the electrons leave the surface. The kinetic energy of a photo-excited electron in vacuum is given by Einstein's famous equation  $E_{\text{kin}} = h\nu - |E_B| - \phi_{\text{sam}}$ , expressing the energy conservation during the photoemission process.  $\phi_{\text{sam}}$  is the work function of the sample and is a measure of the potential barrier at the surface which has to be overcome by the photoelectrons to escape into the vacuum. Since the analyzer also has a characteristic work function  $\phi_a$ , the kinetic energy it measures is effectively reduced by the difference  $\phi_a - \phi_{\text{sam}}$  [140, 141] so that

$$E_{\text{kin}} = h\nu - |E_B| - \phi_a. \quad (2.15)$$

Knowing  $\phi_a$ , a direct relation between  $E_{\text{kin}}$  and  $E_B$  is obtained. The work function of the analyzer  $\phi_a$  ( $\approx 4 - 5$  eV) is usually determined by reference measurements on the Fermi edge of gold or silver samples. The momentum  $p$  can be immediately derived from the respective kinetic energy using  $E_{\text{kin}} = p^2/2m$ .

In a PES spectrum several sharp peaks occur due to electrons that leave the surface with a negligible energy loss. But because of inelastic scattering processes, some electrons lose energy on their way out of the sample and a background of secondary electrons is created. Another secondary effect is the Auger decay of an outer electron into the core hole created in the photoemission process, which also gives rise to spectral features. Since this process is independent from the incident photon energy, Auger lines always appear at the same kinetic energy.

The information that can be obtained from a PES spectrum is manifold. In principle – but not straightforward in general – the chemical composition (i.e. the relative concentrations of the elements in the sample) can be extracted from the core level peak intensities because each element has a unique set of binding energies and photoionization cross-sections. From binding energy shifts information about the chemical state (or valence) can be deduced, and from the energy and momentum distributions of the electrons, as measured in angle-resolved PES (ARPES), the dispersion  $E(\mathbf{k})$  can be derived. Many more aspects of the electronic structure can be found and understood e.g. by analyzing charge-transfer and multiplet effects [84].

### 2.2.2 Theoretical description

For the basic description of x-ray photoemission spectroscopy (cf. Chapter 3 of Ref. [84]) the complex of core-electron system, photoelectron system and valence-electron system (VES) is considered. The former two are independently described by a single-electron wave function  $|\phi_c\rangle$  and a Bloch state  $|\phi_{n\mathbf{k}}\rangle$ , respectively. The interaction between the core hole in the final state and the VES is called  $U$  and the interaction between the VES and the photoelectron is neglected. This is known as the *sudden approximation* and holds for a sufficiently high kinetic energy of the photoelectron, i.e. if the core-hole potential is suddenly applied to the VES.

The Hamiltonian of the initial state may be denoted by  $H_0$  and the one of the final states by  $H = H_0 + U$  (where  $U$  is the interaction between the final-state core hole and the valence electrons, as mentioned above). Then we can write:

$$\begin{aligned} H_0|0\rangle &= E_0|0\rangle \\ H|f\rangle &= E_f|f\rangle \end{aligned}$$

Using Fermi's golden rule (Eq. 2.5) and the dipole transition operator  $\mathbf{p} \cdot \mathbf{e}$  (cf. Sec. 2.1.1), the photoemission spectrum can be shown to be given by:

$$F(\epsilon, \omega) = \sum_{n, \mathbf{k}, f} |\langle \phi_{n\mathbf{k}} | \mathbf{p} \cdot \mathbf{e} | \phi_c \rangle|^2 |\langle f | 0 \rangle|^2 \delta(\epsilon_{n\mathbf{k}} - \epsilon_c + E_f - E_0 - \hbar\omega) \delta(\epsilon - \epsilon_{n\mathbf{k}}) \quad (2.16)$$

The ansatz behind Eq. 2.16 is that the products  $|\phi_c\rangle|0\rangle$  and  $|\phi_{n\mathbf{k}}\rangle|f\rangle$  with the energies  $\epsilon_c + E_0$  and  $\epsilon_{n\mathbf{k}} + E_f$  represent the initial and final states, respectively.  $\epsilon$  is the kinetic energy of the

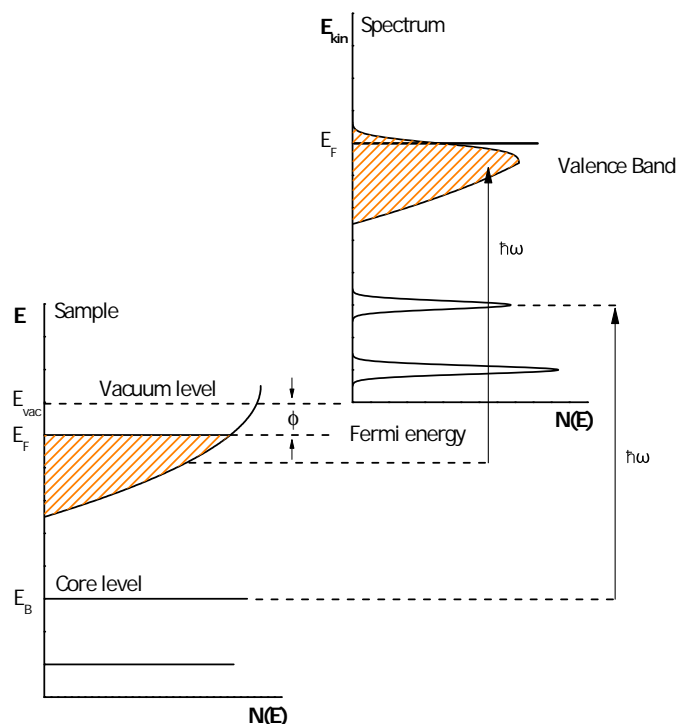


Figure 2.4: One-electron interpretation of the relation between a photoelectron spectrum and the density of states of the sample (redrawn from Ref. [114], Fig. 1.5). The energy of the impinging photons is denoted by  $\hbar\omega$ , the Fermi level by  $E_F$ , the electron binding energy by  $E_B$ , and the work function by  $\phi$ .

photoelectron. Further simplifications lead to

$$F(E_B) = \sum_f |\langle f|0\rangle|^2 \cdot \delta(E_B - E_f + E_0) \quad (2.17)$$

with  $E_B = \hbar\omega - \epsilon + \epsilon_c$ . For a full derivation of Eq. 2.17 see Ref. [84] (Chapter 3 and Appendix A). Note that the sudden approximation is only valid in the limit of an infinitely large mean free path of the photoelectron, i.e. for high kinetic energies of several keV or energies below 10 eV (see Sec. 2.2.4). Here the so-called *one-step model* is used to picture the whole photoemission process and a basic formula for the description of a PES spectrum is obtained. The complexity of the one-step process can be avoided by separating it into three single steps: (1) the optical excitation of the photoelectron in the solid via absorption of the x-ray; (2) the travel of the photoelectron to the sample's surface; (3) the escape from the surface into the vacuum. Each step contains certain aspects of the photoemission process, for instance the information about the intrinsic electronic structure is comprised in step (1), however, this division into several independent events has its flaws since it completely neglects many-body effects, which are most important for the understanding of PES spectra of highly correlated materials.

A popular illustration of PES is the one-electron picture shown in Fig. 2.4, where the electron energy distribution is directly related to the density of states (DOS) in the material. The work function  $\phi$  separates the Fermi level  $E_F$  from the vacuum level  $E_{\text{vac}}$ . The photoabsorption process excites electrons with the binding energy  $E_B$  from the solid into the vacuum, where they will be detected with the kinetic energy  $E_{\text{kin}}$  according to Eq. 2.15. In this one-electron interpretation the PES spectrum reflects the occupied DOS. However, in reality a many-body approach has to be applied to capture the charge-transfer and multiplet effects in PES, i.e. the correct description should take place in terms of an optical transition between initial and final states consisting of many-body wave functions that obey appropriate boundary conditions at the surface of the solid [139]. Otherwise, conclusions about ground-state properties are usually not self-evident. The importance of many-body effects for instance becomes clear when investigating magnetic materials with incompletely filled  $d$  or  $f$  shells, where the strong coupling between the electrons in these shells and the core hole leads to characteristic line splittings in the spectra. Another intriguing many-body effect is the intermediate-valence behavior occurring e.g. in intermetallic cerium compounds, which is investigated in this thesis (see Sec. 1.2 and Chapter 5).

### 2.2.3 Full multiplet configuration interaction model

When performing a PES experiment on intermetallic Ce compounds, the main emission lines in the  $3d$  core-level spectrum are accompanied by satellites on the low and high binding energy side. This was shown to be well interpreted by the Anderson impurity model (AIM) in the formalism of Gunnarsson and Schönhammer by considering the hybridization between the conduction electrons and the  $4f$  level ( $c$ - $f$  hybridization) [10, 75, 142, 143].

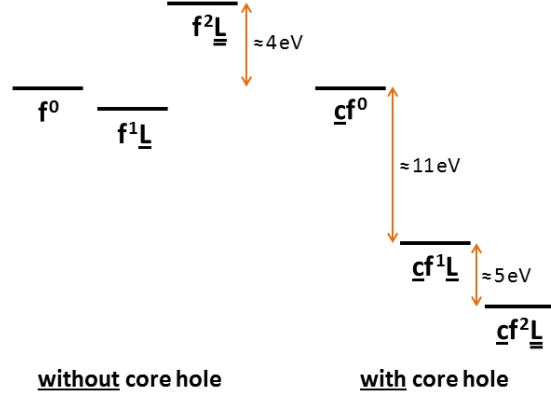
Non-hybridized  $\text{Ce}^{3+}$  systems have  $4f^1$  occupancy. Because of hybridization effects the  $f$  electrons become partially delocalized and the ground state can be written as a quantum-mechanical mixture of  $4f^0$ ,  $4f^1$  and  $4f^2$ , which corresponds to a non-integer  $4f$  occupation (intermediate valence ground state, see Sec. 1.2). This was expressed by Eq. 1.5:

$$|\phi_{\text{GS}}\rangle = c_0|f^0\rangle + c_1|f^1\underline{\underline{L}}\rangle + c_2|f^2\underline{\underline{L}}\rangle$$

$\underline{\underline{L}}$  and  $\underline{\underline{L}}$  denote the number of ligand holes here. The  $|f^2\underline{\underline{L}}\rangle$  contribution  $c_2$  in the initial state is small because the energy difference between  $|f^1\underline{\underline{L}}\rangle$  and  $|f^2\underline{\underline{L}}\rangle$  is relatively large compared to the coupling between the states, but it is not negligible. In the presence of a core hole the resulting attractive potential  $U_{f_c}$  pulls down the  $4f$  levels, having no impact on  $|f^0\rangle$  and acting “once” and “twice” on  $|f^1\underline{\underline{L}}\rangle$  and  $|f^2\underline{\underline{L}}\rangle$ , respectively. This reordering of the different  $c f^n$  configurations is schematically depicted in Fig. 2.5. Here the  $c$  denotes the core hole. It is due the strong Coulomb interaction  $U_{f_c}$  between core hole and  $f$  electrons that core level spectroscopy gains access to the different  $4f$  ground-state contributions. In a PES spectrum the satellite on the high binding energy side of the main  $|c f^1\underline{\underline{L}}\rangle$  feature reflects the  $|c f^2\underline{\underline{L}}\rangle$  and the one at lower binding energy the  $|c f^0\rangle$  final state.

At this point the question arises how the three spectral contributions in the final-state PES spectra are connected to the actual ground-state admixtures  $c_0$ ,  $c_1$  and  $c_2$ . Actually, the measured spectral weights  $w(c f^n)$  cannot be translated into initial-state contributions one-to-one because,

Figure 2.5: Schematic illustration of the energy levels of the  $f^n$  configurations in intermediate valence Ce compounds when a core hole ( $\underline{c}$ ) is present and without a core hole (redrawn from Ref. [143], Fig. 1). The number of ligand holes is indicated by  $\underline{L}$  and  $\underline{\underline{L}}$ . Typical energy differences are also given within the picture.



in addition to the initial-state hybridization, a mixing of the  $f^n$  configurations in the final state exists [75, 144, 145]. The energy separation between  $|\underline{c}f^0\rangle$  and  $|\underline{c}f^1_{\underline{L}}\rangle$  is about 11 eV (see Fig. 2.5), and the  $f^1$ - $f^0$  mixing in the final state happens only through hybridization with the conduction states [75], leading to a small deviation from a proportional dependence  $w(\underline{c}f^0) = \text{const} \cdot c_0$ . The observed spectral weight  $w(\underline{c}f^0)$  underestimates the actual  $c_0$ . On the other hand,  $w(\underline{c}f^2_{\underline{\underline{L}}})$  appears larger than suggested by  $c_2$  because of the impact of the  $f^1$ - $f^2$  final-state mixing (which also matters more the stronger the hybridization is). See Section 2.2.6 for an illustration of the final-state effects at the example of a simplified ground state consisting of only two different  $f^n$  configurations.

Thus, it is not straightforward to draw reliable and quantitative conclusions about the real initial state configuration by simply reading out the spectral weights. A solution is provided by the AIM which considers initial and final state effects so that the initial  $f^n$  contributions can be deduced from the measured  $w(\underline{c}f^n)$ . The basic concept of the AIM has already been introduced in Chapter 1. We now have a closer look at the Hamiltonian of the AIM (Eq. 1.1) and apply it to the case of a Ce  $4f$  system to introduce the parameters needed for the theoretical simulation of a  $3d$  PES spectrum. The first term  $H_{0f}$  describes the unperturbed energy of the  $f$  impurity states and contains the  $f$  electron binding energy  $\Delta_f$  and the spin-orbit interaction  $\zeta_f$ :

$$H_{0f} = [\Delta_f + (\mathbf{L} \cdot \mathbf{S}) \zeta_f] n_f \quad (2.18)$$

Note that  $n_f$  represents the number operator here. The spin-orbit term accounts for the splitting between the  $(2J + 1)$ -degenerate  $J = 5/2$  and  $J = 7/2$  states. The Coulomb interactions between  $f$  states is captured by the second term  $H_{ff}$ . The repulsive interaction  $U$  therein is expressed by

$$U = \int e^2 |\varphi_f(\mathbf{r}_1)|^2 |\varphi_f(\mathbf{r}_2)|^2 |\mathbf{r}_1 - \mathbf{r}_2|^{-1} d^3\mathbf{r} \quad (2.19)$$

where the functions  $\varphi_f(\mathbf{r})$  represent the spatial distributions of the  $4f$  orbitals. Effectively,  $U$  can be related to the Slater integrals  $F^k$  and the Coulomb-exchange interaction  $U_{ff}$  (see e.g. Ref. [87] or also [146]). The biggest computational challenge comes with the treatment of the conduction band since a full inclusion requires an enormous amount of states. Here a simple description is provided by using the zero-bandwidth approximation [147], i.e. one effective state

is used to model the band of extended valence states. In this simplified version of the AIM the interactions between conduction electrons are neglected and no momentum-dependent energy dispersion exists any more. The energy of the effective state can be arbitrarily chosen to be zero [146] so that  $H_{0v} = 0$  in Eq. 1.1. The heart of the AIM is  $H_{fv}$ , the hybridization term,<sup>3</sup> in which the coupling between  $4f$  and conduction electrons is included via  $V(\mathbf{k})$ . In the simple zero-bandwidth limit this is reduced to an effective  $V_{\text{eff}}$  between one  $f$  electron and the single band state. The influence of the core hole also has to be considered by setting up a Hamiltonian  $H_{\text{core}}$ . Exciting a  $3d$  core electron gives rise to a partially filled  $3d$  shell, meaning that  $H_{\text{core}}$  has to contain the  $3d$  spin-orbit splitting  $\zeta_d$ . The Coulomb interactions between  $f$  states and the core hole – given by the Slater integrals  $F^k$  and the Coulomb-exchange  $U_{fc}$  – are included analogously to  $H_{ff}$ .

In the following this simplified form of the AIM is called **configuration interaction (CI) model** with an infinitely narrow band (given by one ligand state) representing the conduction band. As discussed by Imer and Wuilloud [147], the model has its drawbacks when compared to the original approach by Gunnarsson and Schönhammer [143], especially regarding the low-energy excitations reflected by the Kondo peak in valence band PES. It is no longer possible to extract reliable values for the Kondo temperature. However, the CI calculations provide the simplest way to consider the important hybridization effects and qualitatively reproduce the main features in Ce core-level spectra.

Another great advantage is the significantly reduced computational time of the CI approach, allowing to combine it with full multiplet calculations. In some cases the multiplet coupling effect (Sec. 2.1.2) also is of crucial importance in photoelectron spectroscopy. Especially when it comes to an accurate description of spectral line shapes, the inclusion of the full multiplet structure is indispensable. For instance, in core hole PES of cerium systems the multiplet effect is responsible for the different shapes of the spin-orbit-split  $3d_{5/2}$  and  $3d_{3/2}$  emission features, which both contain the different contributions from the  $f^n$  configurations. Within the spin-orbit-split multiplets the shapes of the  $f^1$  and  $f^2$  spectral weights also differ due to different underlying multiplet structures, whereas the  $f^0$  is given by a single emission line and therefore gives rise to a distinct spectral feature. In our analysis of the Ce  $3d$  spectra (Chapter 5) the program XTLS v9.0 [118] has been used to realize a **full multiplet configuration interaction (fm-CI) model**. This approach accounts for the important final-state effects and at the same time ensures that the shapes of the  $3d$  multiplets are captured correctly.

The values for the Slater integrals and the spin-orbit parameters are determined with the atomic structure code RCN36K by R. D. Cowan [86] based on the Hartree-Fock approximation. Consequently, the theoretical description of a Ce  $3d$  spectrum within the fm-CI model is left with four essential parameters: the Coulomb-exchange interactions  $U_{ff}$  among  $f$  electrons and  $U_{fc}$  between an  $f$  electron and a core hole in the  $d$  shell, the hybridization strength  $V_{\text{eff}}$  and the effective  $f$  binding energy  $\Delta_f$ , which is the energy difference between the initial states  $|f^0\rangle$  and  $|f^1\bar{L}\rangle$ .

---

<sup>3</sup>This is called *s-d interaction term* in Anderson's original work.

### 2.2.4 Experimental aspects

The transmission through 10 cm of air for 1 keV x-rays is about 10–15 % [148]. In contrast, for hard x-rays the absorption in air becomes weak – at 6 keV the transmission already amounts to 99 %. This allows to leave small air gaps between the vacuum sections of the different beamline components (monochromators, focusing mirrors, etc.) and use low absorbing windows at their entrance and exit. Due to the smaller wavelengths ( $\lambda \sim 100\text{--}400$  pm) of hard x-rays, it is furthermore necessary to use single crystals to monochromatize the x-ray beam. However, the experiment still has to be carried out in UHV to ensure that the mean free path of the outgoing electrons is long enough to reach the analyzer. High vacuum conditions also minimize possible surface degradation effects over time.

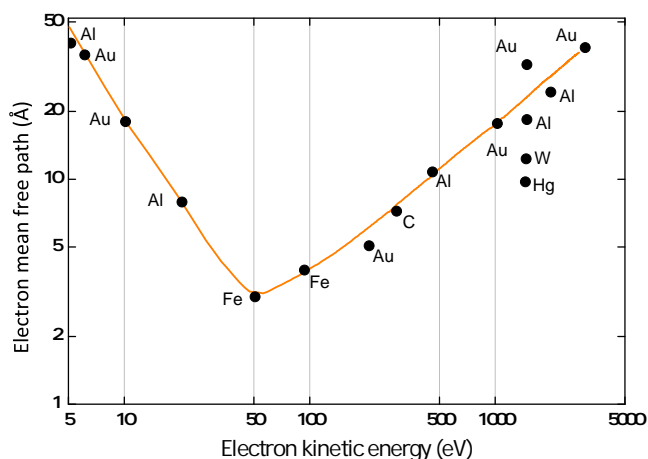
The photoelectrons are detected and analyzed by an electron energy analyzer which consists of the following main components: Two concentric hemispheres represent the hemispherical deflection analyzer. In between the two spheres a deflecting electrostatic field is built up, which determines the so-called pass energy, i.e. the center of a narrow energy window in which the electrons can pass through the hemispheres. An electron-lens system focuses the photoelectrons onto the analyzer's entrance slit and de- or accelerates them from the desired kinetic energy (swept through the selected energy scanning range) to the pass energy of the analyzer. Finally, in micro-channel plates (MCPs) the signal is enhanced via secondary electron emission. In a non-angular-resolved photoemission experiment the so-called transmission mode is used, in which the momentum information is averaged over all photoelectrons within a given acceptance angle.

#### Probing depth

The finite escape depth of electrons emerging from a surface has to be taken into account. It is mainly due to electron-electron and electron-phonon collisions and can be expressed by the electron inelastic mean free path (IMFP). Fig. 2.6 shows the IMFP as a function of the kinetic energy for different metals. The typical energy region for standard PES is between 10 and 2000 eV, which corresponds to a mean free path of about 2–20 Å. Because of the limited probing depth, effectively only a thin surface region is probed by electron spectroscopy and the resulting data are not representative for the bulk. This calls for high quality samples and clean surfaces, meaning that – as in XAS – the experiments have to be carried out under UHV conditions (cf. Sec. 2.1.4). As suggested by Fig. 2.6, the probing depth can be significantly increased by the use of hard x-rays. In HAXPES, with the kinetic energy of the photoelectrons being 5–10 keV, the probing depth can reach 50 Å and more, so that the bulk contribution dominates the experimental spectra (see for instance Refs.[149–151] and references therein).

It is important to note that this empirical 'universal' curve gives only a rough estimate of the mean free path of the escaping electrons and does not provide a general description since the mechanisms for the losses are different in insulators or semiconductors. Also, the probing depth does not only depend on the kinetic energy of the excited electrons, but can also be tuned via the experimental emission angle. In a grazing emission geometry only the surface layer is probed, whereas in normal emission the bulk sensitivity is significantly enhanced.

Figure 2.6: Electron inelastic mean free path versus kinetic energy for different metals. The orange line indicates the empirical ‘universal’ curve, which gives an estimate of the bulk sensitivity of PES experiments. (Figure redrawn from Ref. [114], Fig. 1.11.)



### Photoionization cross-section

The emission of an electron from a certain electronic (sub-)shell by absorption of a photon has a certain probability, which is called the photoionization cross-section (tabulated in Refs. [152, 153]). It strongly depends on the element under consideration and which (sub-)shell is considered, as well as on the photon energy because the dipole transition matrix element depends strongly on the photon energy. This can be used in an experiment to pronounce or suppress specific features in a photoemission spectrum. Complicated spectra can become comprehensible by choosing the right photon energy [154].

### Line shape, background and plasmons

The spectral lines in PES spectra become broadened due to the finite instrumental resolution (Gaussian broadening) and the limited lifetime of the excited states (Lorentzian broadening). For the description of the asymmetric shape of a core-level emission line in metallic samples the Doniach-Sunjić [155] or the Mahan [156] line shape can be used: The asymmetric tail develops because a photoelectron excites electron-hole pairs on its way through the sample (arising from the interaction between the core hole and the conduction electrons) and thereby experiences small energy losses. The density of states close to the Fermi level determines the asymmetry [157], meaning that this line shape effect is particularly important for metallic samples. Apart from these line shape effects, two other features have to be treated in the quantitative analysis of a PES spectrum, namely the spectral background and plasmons.

Before a photoelectron leaves the sample surface it has a rather turbulent travel and experiences electron-electron and electron-ion collisions. The energy losses due to these inelastic scattering effects produce a smooth spectral background which has to be subtracted to isolate the primary PES spectrum and be able to analyze line shapes or energy positions. A common method to do so is the integral background as developed by Shirley [158]. It is recursively defined and given by

$$B_S(E) = A \int_{E' > E} dE' [P(E') - P_0] \quad (2.20)$$

where  $P(E)$  is the measured spectrum.  $P_0$  and  $A$  determine the background intensity before and behind the features of interest, respectively. The real background can be also determined experimentally by EELS (Electron Energy-Loss Spectroscopy), yet the Shirley procedure gives a decent approximation [114] and in general is sufficient when investigating and comparing the same core lines in a series of isostructural compounds.

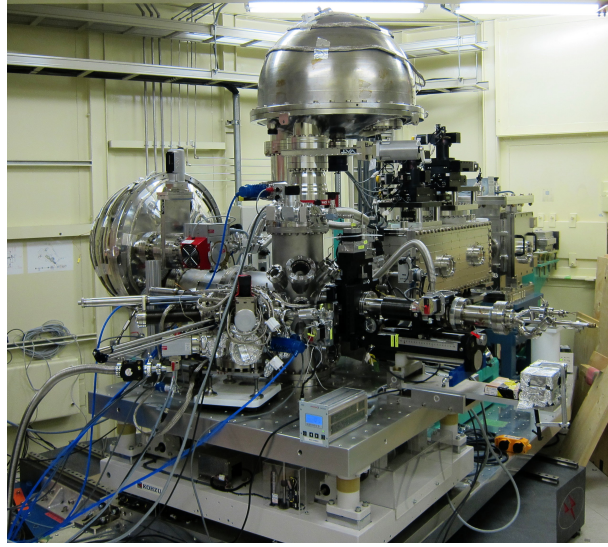
Another important secondary inelastic process, which has not been considered up to now and matters particularly for the analysis presented in Chapter 5, is the so-called plasmon scattering. One distinguishes between *extrinsic* and *intrinsic* plasmon effects [114]. Extrinsic plasmons are created during the photoelectron's journey to the surface by Coulomb interaction between the photoelectron and the conduction electrons. Intrinsic plasmons are quantized excitations originating from the screening of the (suddenly created) core hole. For both types the energy losses have the characteristic energy  $\Delta E_p = \hbar\omega_p$  leading to plasmon features in the PES spectrum at this energy distance  $\Delta E_p$  (or at an integer multiple of  $\Delta E_p$ ) towards higher binding energies. Furthermore, they are subject to an additional lifetime broadening. The plasmon intensity distribution depends on the kinetic energy of the excited core photoelectron. In core-level HAXPES a regime of considerably high kinetic energies is reached, in which the contributions from intrinsic plasmons and interference effects between intrinsic and extrinsic plasmons are small [159, 160]. The plasmon losses have mainly extrinsic character and the photoelectrons' mean free path basically determines the plasmon loss function [159], so that in the limit of large kinetic energies the losses become independent from the kinetic energy. Thus, in good approximation different core levels give rise to the same plasmon loss functions, i.e. within one sample the plasmon properties (intensity, broadening and energy loss) can be regarded to be the same in different energy regions. Extrinsic and intrinsic plasmon contributions occur simultaneously and are hard to distinguish. Hence, they are not separated in the analysis of the Ce 3d core level spectra presented in Chapter 5.

### 2.2.5 Light source and beamline

The HAXPES measurements were carried out at the Super Photon Ring 8 GeV (SPring-8) located in the prefecture of Hyōgo in Japan. The 8 GeV denotes the energy of the electron beam in the storage ring. The experiment took place at the Taiwan beamline BL12XU. At the main line of BL12XU inelastic x-ray scattering experiments can be performed, whereas the side line features a dedicated HAXPES end station (see Fig. 2.7). It was constructed in a joint project of the Max Planck Institute for Chemical Physics of Solids (MPI CPFS), the Taiwanese National Synchrotron Radiation Research Center (NSRRC) and the University of Cologne. What makes the end station unique is the use of two hemispherical A-1HE analyzers from MB Scientific (MBS), one of which is mounted in horizontal geometry, i.e. parallel to the electrical field vector of the beam, and the other one in vertical geometry, i.e. perpendicular to the electrical field vector. This allows to perform polarization-dependent measurements and exploit the different photoionization cross-sections for the identification of different orbital contributions [154]. However, in the measurements presented in this thesis only the horizontal layout was used.

In the undulator beamline first a single-bounce diamond monochromator is used to select photon energies from 6 to 12 keV, then the energy bandwidth is further reduced by a high-resolution silicon channel cut monochromator and focused via a K-B mirror system to a spot

Figure 2.7: HAXPES end station at the Taiwan beamline at SPring-8 in Japan (BL12XU), with the two hemispherical MBS analyzers, the preparation chamber and the manipulator for sample transfer. In the back also the high-resolution monochromator and the K-B focusing mirror can be seen. Photograph provided by J. Weinen.



size of approximately  $40 \times 40 \mu\text{m}^2$  at the sample position. From the monochromator side the energy resolution can go down to about 100 meV, depending on which channel-cut is used. The base pressure in the measurement chamber is of the order of  $10^{-9}$  mbar or lower and separated from the preparation chamber, where the samples can be stored after being introduced through a load lock chamber. In order to obtain a clean sample surface, the crystals can be fractured *in situ* in the preparation chamber at room temperature with the help of a commercially available crystal cleaver, or directly in the measurement chamber at low temperature via post-cleave.

### 2.2.6 Addendum: $4f$ spectral weights

The actual ground-state admixtures of the intermediate valence ground state cannot be directly read off from the relative spectral intensities of the different  $f^n$  peaks, because hybridization effects in the final state lead to deviations from a one-to-one correspondence between the spectral weights and the ground-state  $f^n$  contributions. For illustration purposes, two configurations (e.g.  $f^1$ - $f^2$ ) are considered in the Ce intermediate valence ground state:

$$|\phi_{\text{GS}}\rangle = c_1|f^1\underline{\text{L}}\rangle + c_2|f^2\underline{\text{L}}\rangle \quad (2.21)$$

where  $c_1$  is dominant and  $c_2$  is very small ( $c_1 \gg c_2$ ). The final states in the presence of a core hole are given by the anti-bonding and bonding state of the form:

$$|\phi_{\text{final},1}\rangle = \hat{c}_1|c\underline{f}^1\underline{\text{L}}\rangle - \hat{c}_2|c\underline{f}^2\underline{\text{L}}\rangle \quad (2.22)$$

$$|\phi_{\text{final},2}\rangle = \hat{c}_2|c\underline{f}^1\underline{\text{L}}\rangle + \hat{c}_1|c\underline{f}^2\underline{\text{L}}\rangle \quad (2.23)$$

The spectral weights  $w(c\underline{f}^n)$  follow as  $|\langle\phi_{\text{final}}|c\underline{f}^n|\phi_{\text{GS}}\rangle|^2$  and read:

$$w(c\underline{f}^1\underline{\text{L}}) = |\langle\phi_{\text{final},1}|c\underline{f}^1\underline{\text{L}}|\phi_{\text{GS}}\rangle|^2 = |\hat{c}_1c_1 - \hat{c}_2c_2|^2 \quad (2.24)$$

$$w(c\underline{f}^2\underline{\text{L}}) = |\langle\phi_{\text{final},2}|c\underline{f}^2\underline{\text{L}}|\phi_{\text{GS}}\rangle|^2 = |\hat{c}_2c_1 + \hat{c}_1c_2|^2 \quad (2.25)$$

## 2 Spectroscopic techniques: Theoretical and experimental background

If the Coulomb interaction between the core hole and the  $4f$  electron is sufficiently large, the energy separation between  $|\phi_{\text{final},1}\rangle$  and  $|\phi_{\text{final},2}\rangle$  will be large and final-state mixing will be negligible, i.e.  $\hat{c}_1 \approx 1$  and  $\hat{c}_2 \approx 0$ , and consequently  $w(\underline{c}f^1) \approx c_1^2$  and  $w(\underline{c}f^2) \approx c_2^2$ . However, in reality final-state effects are not negligible and  $\hat{c}_1 > \hat{c}_2 > 0$ . Then the  $f^1$  spectral weight in Eq. 2.24 is still approximately given by  $c_1^2$ , because the product  $\hat{c}_2 c_2$  is very small. However, the  $f^2$ -related spectral weight in Eq. 2.25 is larger than  $c_2^2$  because both  $\hat{c}_2 c_1$  and  $\hat{c}_1 c_2$  are greater than  $c_2^2$ . In other words, the relative spectral weight related to the  $f^2$  contribution in the initial state appears larger than the actual  $f^2$  ground-state admixture.

The same line of thought can be applied to an initial state composed of  $f^0$  and  $f^1$ :

$$|\phi_{\text{GS}}\rangle = c_0|f^0\rangle + c_1|f^1\underline{\text{L}}\rangle \quad (2.26)$$

where again  $c_1$  is dominant and  $c_0$  is small ( $c_1 \gg c_0$ ). The anti-bonding and bonding final states after core ionization are given by

$$|\phi_{\text{final},0}\rangle = \hat{c}_1|\underline{c}f^0\rangle - \hat{c}_0|\underline{c}f^1\underline{\text{L}}\rangle \quad (2.27)$$

$$|\phi_{\text{final},1}\rangle = \hat{c}_0|\underline{c}f^0\rangle + \hat{c}_1|\underline{c}f^1\underline{\text{L}}\rangle \quad (2.28)$$

and the corresponding spectral weights are:

$$w(\underline{c}f^1\underline{\text{L}}) = |\langle\phi_{\text{final},1}|\underline{c}|\phi_{\text{GS}}\rangle|^2 = |\hat{c}_0 c_0 + \hat{c}_1 c_1|^2 \quad (2.29)$$

$$w(\underline{c}f^0) = |\langle\phi_{\text{final},0}|\underline{c}|\phi_{\text{GS}}\rangle|^2 = |\hat{c}_1 c_0 - \hat{c}_0 c_1|^2 \quad (2.30)$$

where  $c_1 > c_0 > 0$  due to  $f^1$ - $f^0$  configuration mixing in the final state. Again, the  $f^1$  spectral weight is given by  $c_1^2$  in good approximation since the product  $\hat{c}_0 c_0$  is small. The energy separation between  $f^0$  and  $f^1$  increases in the presence of a core hole compared to the situation in the initial state (see Fig. 2.5), so that  $\hat{c}_0 < c_0$  and consequently  $w(\underline{c}f^0) = |\hat{c}_1 c_0 - \hat{c}_0 c_1|^2 < c_0^2$ . The actual  $f^0$  contribution in the ground state is underestimated in the core level spectra.

### 2.3 Synchrotron radiation

The term synchrotron radiation refers to the electromagnetic radiation emitted by charged particles (e.g. electrons or positrons) moving at relativistic speed on a circular orbit. It was first observed in 1947 as an (unwanted) side effect in an electron synchrotron at General Electric in the USA. Its plethora of useful properties, the wide range of applications and in particular its high potential for the investigation of condensed matter was not recognized until the late 1960s, when the first generation of synchrotron light sources started their ascent. For an extensive introduction to synchrotron radiation and its applications, the reader may be referred to Ref. [115].

In general, every charged particle moving on a non-linear trajectory emits light. At small velocities ( $\frac{v}{c} \ll 1$ ) the angular distribution of the emitted radiation resembles that of a classic dipole, whereas at relativistic speeds ( $\frac{v}{c} \approx 1$ ) a strong forward pattern develops, i.e. the light is emitted predominantly in a narrow cone tangentially to the electron orbit (as illustrated in Fig. 2.8). A broad continuous band of the electromagnetic spectrum becomes available, reaching from the infrared and visible light to the ultraviolet and up to the soft and hard x-ray regime.

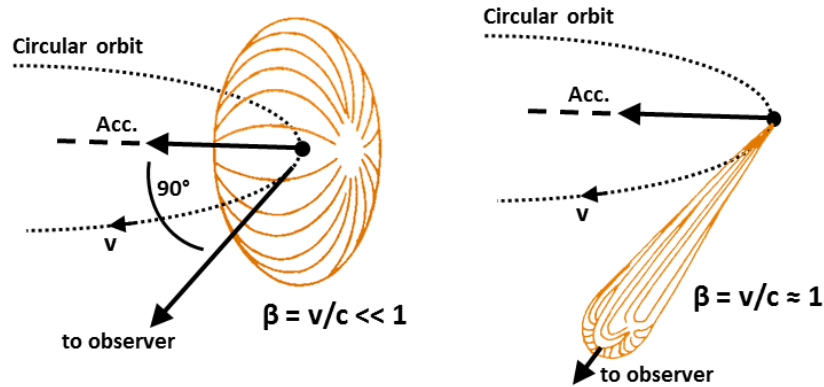


Figure 2.8: Qualitative emission characteristics of a charged particle moving at small speeds (left) and relativistic speeds (right) on a circular orbit (redrawn from Ref. [161], Fig. 1).

Compared to common laboratory x-ray tubes, which produce a maximum flux of  $10^{10}$  photons per second, synchrotron radiation is significantly more intense with up to  $10^{19}$  photons per second [84]. Furthermore, in the orbital plane the emitted light shows a high degree of linear polarization with the electric field vector  $E$  parallel to the plane. Above and below this plane right and left circular polarized light is obtained.

In order to use the full capability of synchrotron radiation, dedicated second generation light sources were built from the mid-1970s on. The general structure of a synchrotron facility is shown in Fig. 2.9. An electron gun generates electrons which are then injected into a linear accelerator (Linac), where they are brought to an energy of several MeV. In the so-called booster ring the electrons are further accelerated to the order of GeV before they are finally introduced to the storage ring. Bending magnets are used both in the booster ring and the storage ring to bring the electrons onto a circular orbit via the Lorentz force  $F_L \propto v \cdot B$ . Radio frequency cavities are placed within the storage ring to recover energy losses. Once in the storage ring, the electron beam is kept focused and stable at its designated energy by an array of magnets, and the wide spectrum of radiation – generated during the bending of the electron beam – is guided to the individual beamlines. Here the beam is optimized by monochromators, focusing mirrors, slits and other optical devices before finally entering the respective experimental endstation. A further increase of the radiation intensity and the spectral brightness is accomplished in the third generation of synchrotrons by the so-called insertion devices, which are periodic magnetic structures mounted in the straight (linear) sections of the storage ring. One distinguishes between wigglers and undulators. In a wiggler magnets with alternating polarity are arranged in an array forming a multipole magnet. The resulting alternating magnetic field forces the electrons on an oscillatory trajectory – with the oscillations perpendicular to the direction of motion – so that the additional bends intensify the synchrotron radiation. An undulator basically follows the same principle but smaller wiggling angles are realized, so that interference effects can be exploited to obtain a very intense and monochromatic beam. Advanced undulator setups also allow to switch between horizontal and vertical polarized light or even to produce circularly polarized radiation by the use of helical magnetic fields.

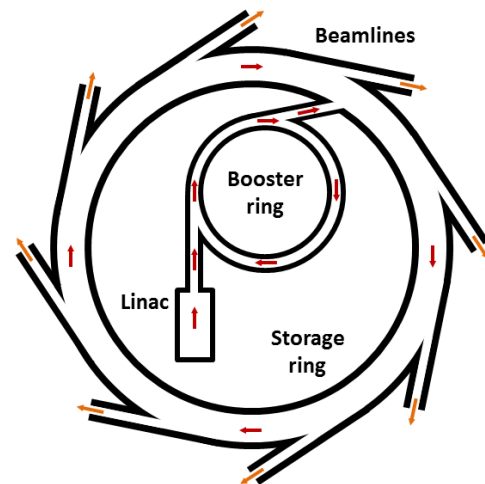


Figure 2.9: Schematic illustration of the basic structure of a synchrotron light source (re-drawn from Ref. [115], Fig. 1.2).

The very broad and continuous spectral range, the tunability of energy and polarization, a high degree of collimation and a pulsed time structure make synchrotron radiation extremely versatile. The good beam stability and high brilliance provided by state-of-the-art third generation light sources ensures a fast and reliable data acquisition.

## References of Chapter 1 and 2

- [1] G. R. Stewart. *Heavy-fermion systems*. Rev. Mod. Phys. **56** 755 (1984). DOI: 10.1103/RevModPhys.56.755.
- [2] P. Misra, ed. *Heavy-fermion systems*. Handbook of Metal Physics. Elsevier, 2008. DOI: 10.1016/S1570-002X(08)80003-1.
- [3] P. Coleman. *Heavy Fermions: Electrons at the Edge of Magnetism*. Handbook of Magnetism and Advanced Magnetic Materials **1** 95 (2007). DOI: 10.1002/9780470022184.
- [4] L. Degiorgi. *The electrodynamic response of heavy-electron compounds*. Rev. Mod. Phys. **71** 687 (1999). DOI: 10.1103/RevModPhys.71.687.
- [5] P. S. Riseborough. *Heavy fermion semiconductors*. Adv. Phys. **49** 257 (2000). DOI: 10.1080/000187300243345.
- [6] M. Dzero, K. Sun, V. Galitski, and P. Coleman. *Topological Kondo Insulators*. Phys. Rev. Lett. **104** 106408 (2010). DOI: 10.1103/PhysRevLett.104.106408.
- [7] W. de Haas, J. de Boer, and G. van den Berg. *The electrical resistance of gold, copper and lead at low temperatures*. Physica **1** 1115 (1934). DOI: 10.1016/S0031-8914(34)80310-2.
- [8] G. van den Berg. "Anomalies in Dilute Metallic Solutions of Transition Metals". In: *Low Temp. Phys. LT9*. Ed. by J. Daunt, D. Edwards, F. Milford, and M. Yaqub. Springer US, 1965, 955. DOI: 10.1007/978-1-4899-6443-4\_64.
- [9] J. Kondo. *Resistance Minimum in Dilute Magnetic Alloys*. Prog. of Theor. Phys. **32** 37 (1964). DOI: 10.1143/PTP.32.37.
- [10] P. W. Anderson. *Localized Magnetic States in Metals*. Phys. Rev. **124** 41 (1961). DOI: 10.1103/PhysRev.124.41.
- [11] K. Andres, J. E. Graebner, and H. R. Ott. *4f-Virtual-Bound-State Formation in CeAl<sub>3</sub> at Low Temperatures*. Phys. Rev. Lett. **35** 1779 (1975). DOI: 10.1103/PhysRevLett.35.1779.
- [12] S. Doniach. *The Kondo lattice and weak antiferromagnetism*. Physica B+C **91** 231 (1977). DOI: 10.1016/0378-4363(77)90190-5.
- [13] F. Steglich, J. Aarts, C. D. Bredl, W. Lieke, D. Meschede, W. Franz, and H. Schäfer. *Superconductivity in the Presence of Strong Pauli Paramagnetism: CeCu<sub>2</sub>Si<sub>2</sub>*. Phys. Rev. Lett. **43** 1892 (1979). DOI: 10.1103/PhysRevLett.43.1892.
- [14] Z. Fisk, H. R. Ott, T. M. Rice, and J. L. Smith. *Heavy-electron metals*. Nature **320** 124 (1986). DOI: 10.1038/320124a0.
- [15] M. Sigrist and K. Ueda. *Phenomenological theory of unconventional superconductivity*. Rev. Mod. Phys. **63** 239 (1991). DOI: 10.1103/RevModPhys.63.239.

## References of Chapter 1 and 2

- [16] G. R. Stewart. *Non-Fermi-liquid behavior in d- and f-electron metals*. Rev. Mod. Phys. **73** 797 (2001). DOI: 10.1103/RevModPhys.73.797.
- [17] H. v. Löhneysen, T. Pietrus, G. Portisch, H. G. Schlager, A. Schröder, M. Sieck, and T. Trappmann. *Non-Fermi-liquid behavior in a heavy-fermion alloy at a magnetic instability*. Phys. Rev. Lett. **72** 3262 (1994). DOI: 10.1103/PhysRevLett.72.3262.
- [18] L. D. Landau. *Theory of the Fermi liquid*. Soviet Phys. JETP **3** 920 (1957).
- [19] K. G. Wilson. *The renormalization group: Critical phenomena and the Kondo problem*. Rev. Mod. Phys. **47** 773 (1975). DOI: 10.1103/RevModPhys.47.773.
- [20] K. Kadowaki and S. Woods. *Universal relationship of the resistivity and specific heat in heavy-Fermion compounds*. Solid State Commun. **58** 507 (1986). DOI: 10.1016/0038-1098(86)90785-4.
- [21] L. Kouwenhoven and L. Glazman. *Revival of the Kondo effect*. Phys. World **14** 33 (2001).
- [22] A. A. Abrikosov. *Electron scattering on magnetic impurities in metals and anomalous resistivity effects*. Physics **2** 5 (1965).
- [23] H. Suhl. *Formation of Local Magnetic Moments in Metals*. Phys. Rev. Lett. **19** 442 (1967). DOI: 10.1103/PhysRevLett.19.442.
- [24] D. I. Khomskii. *Basic Aspects of the Quantum Theory of Solids: Order and Elementary Excitations*. Cambridge University Press, 2010. ISBN: 9781139491365.
- [25] J. W. Allen, S.-J. Oh, M. B. Maple, and M. S. Torikachvili. *Large Fermi-level resonance in the electron-addition spectrum of CeRu<sub>2</sub> and CeIr<sub>2</sub>*. Phys. Rev. B **28** 5347 (1983). DOI: 10.1103/PhysRevB.28.5347.
- [26] F. Patthey, W.-D. Schneider, Y. Baer, and B. Delley. *High-temperature collapse of the Kondo resonance in CeSi<sub>2</sub> observed by photoemission*. Phys. Rev. Lett. **58** 2810 (1987). DOI: 10.1103/PhysRevLett.58.2810.
- [27] F. Patthey, J.-M. Imer, W.-D. Schneider, H. Beck, Y. Baer, and B. Delley. *High-resolution photoemission study of the low-energy excitations in 4f-electron systems*. Phys. Rev. B **42** 8864 (1990). DOI: 10.1103/PhysRevB.42.8864.
- [28] D. Ehm, S. Hufner, F. Reinert, J. Kroha, P. Wölfle, O. Stockert, C. Geibel, and H. v. Löhneysen. *High-resolution photoemission study on low-T<sub>K</sub> Ce systems: Kondo resonance, crystal field structures, and their temperature dependence*. Phys. Rev. B **76** 045117 (2007). DOI: 10.1103/PhysRevB.76.045117.
- [29] V. Madhavan, W. Chen, T. Jamneala, M. F. Crommie, and N. S. Wingreen. *Tunneling into a Single Magnetic Atom: Spectroscopic Evidence of the Kondo Resonance*. Science **280** 567 (1998). DOI: 10.1126/science.280.5363.567.
- [30] W.-D. Schneider. *A local view of the Kondo effect: Scanning tunneling spectroscopy*. Pragma **52** 537 (1999). DOI: 10.1007/BF02829862.
- [31] M. Ternes, A. J. Heinrich, and W.-D. Schneider. *Spectroscopic manifestations of the Kondo effect on single adatoms*. J. Phys.: Condens. Matter **21** 053001 (2009). DOI: 10.1088/0953-8984/21/5/053001.

- [32] M. A. Ruderman and C. Kittel. *Indirect Exchange Coupling of Nuclear Magnetic Moments by Conduction Electrons*. Phys. Rev. **96** 99 (1954). DOI: 10.1103/PhysRev.96.99.
- [33] T. Kasuya. *A Theory of Metallic Ferro- and Antiferromagnetism on Zener's Model*. Progress of Theoretical Physics **16** 45 (1956). DOI: 10.1143/PTP.16.45.
- [34] K. Yosida. *Magnetic Properties of Cu-Mn Alloys*. Phys. Rev. **106** 893 (1957). DOI: 10.1103/PhysRev.106.893.
- [35] J. Custers, P. Gegenwart, H. Wilhelm, K. Neumaier, Y. Tokiwa, O. Trovarelli, C. Geibel, F. Steglich, C. Pépin, and P. Coleman. *The break-up of heavy electrons at a quantum critical point*. Nature **424** 524 (2003). DOI: 10.1038/nature01774.
- [36] J. Paglione, M. A. Tanatar, D. G. Hawthorn, E. Boaknin, R. W. Hill, F. Ronning, M. Sutherland, L. Taillefer, C. Petrovic, and P. C. Canfield. *Field-Induced Quantum Critical Point in CeCoIn<sub>5</sub>*. Phys. Rev. Lett. **91** 246405 (2003). DOI: 10.1103/PhysRevLett.91.246405.
- [37] A. Bianchi, R. Movshovich, I. Vekhter, P. G. Pagliuso, and J. L. Sarrao. *Avoided Antiferromagnetic Order and Quantum Critical Point in CeCoIn<sub>5</sub>*. Phys. Rev. Lett. **91** 257001 (2003). DOI: 10.1103/PhysRevLett.91.257001.
- [38] H. v. Löhneysen, A. Neubert, T. Pietrus, A. Schröder, O. Stockert, U. Tutsch, M. Loewenhaupt, A. Rosch, and P. Wölfle. *Magnetic order and transport in the heavy-fermion system CeCu<sub>6-x</sub>Au<sub>x</sub>*. Eur. Phys. J. B **5** 447 (1998). DOI: 10.1007/s100510050465.
- [39] A. Schröder, G. Aeppli, R. Coldea, M. Adams, O. Stockert, H. v. Löhneysen, E. Bucher, R. Ramazashvili, and P. Coleman. *Onset of antiferromagnetism in heavy-fermion metals*. Nature **407** 351 (2000). DOI: 10.1038/35030039.
- [40] N. D. Matur, F. M. Grosche, S. R. Julian, I. R. Walker, D. M. Freye, R. K. W. Haselwimmer, and G. G. Lonzarich. *Magnetically mediated superconductivity in heavy fermion compounds*. Nature **394** 39 (1998). DOI: 10.1038/27838.
- [41] C. Petrovic, P. G. Pagliuso, M. F. Hundley, R. Movshovich, J. L. Sarrao, J. D. Thompson, Z. Fisk, and P. Monthoux. *Heavy-fermion superconductivity in CeCoIn<sub>5</sub> at 2.3 K*. J. Phys.: Condens. Matter **13** L337 (2001). DOI: 10.1088/0953-8984/13/17/103.
- [42] H. Q. Yuan, F. M. Grosche, M. Deppe, C. Geibel, G. Sparn, and F. Steglich. *Observation of Two Distinct Superconducting Phases in CeCu<sub>2</sub>Si<sub>2</sub>*. Science **302** 2104 (2003). DOI: 10.1126/science.1091648.
- [43] H. Q. Yuan, F. M. Grosche, M. Deppe, G. Sparn, C. Geibel, and F. Steglich. *Non-Fermi Liquid States in the Pressurized CeCu<sub>2</sub>(Si<sub>1-x</sub>Ge<sub>x</sub>)<sub>2</sub> System: Two Critical Points*. Phys. Rev. Lett. **96** 047008 (2006). DOI: 10.1103/PhysRevLett.96.047008.
- [44] F. Grosche, S. Julian, N. Mathur, and G. Lonzarich. *Magnetic and superconducting phases of CePd<sub>2</sub>Si<sub>2</sub>*. Physica B: Condens. Matter **223 – 224** 50 (1996). Proceedings of the International Conference on Strongly Correlated Electron Systems. DOI: 10.1016/0921-4526(96)00036-1.

## References of Chapter 1 and 2

- [45] R. Movshovich, T. Graf, D. Mandrus, J. D. Thompson, J. L. Smith, and Z. Fisk. *Superconductivity in heavy-fermion  $CeRh_2Si_2$* . Phys. Rev. B **53** 8241 (1996). DOI: 10.1103/PhysRevB.53.8241.
- [46] G. Zwicknagl. *Quasi-particles in heavy fermion systems*. Adv. Phys. **41** 203 (1992). DOI: 10.1080/00018739200101503.
- [47] H. v. Löhneysen, A. Rosch, M. Vojta, and P. Wölfle. *Fermi-liquid instabilities at magnetic quantum phase transitions*. Rev. Mod. Phys. **79** 1015 (2007). DOI: 10.1103/RevModPhys.79.1015.
- [48] S. V. Dordevic, D. N. Basov, N. R. Dilley, E. D. Bauer, and M. B. Maple. *Hybridization Gap in Heavy Fermion Compounds*. Phys. Rev. Lett. **86** 684 (2001). DOI: 10.1103/PhysRevLett.86.684.
- [49] J. Allen. *Electron spectroscopy of strongly correlated systems*. Physica B: Condens. Matter **171** 175 (1991). DOI: 10.1016/0921-4526(91)90513-E.
- [50] D. Malterre, M. Grioni, P. Weibel, B. Dardel, and Y. Baer. *Electron spectroscopy studies of scaling behaviours in heavy fermions*. Physica B: Condens. Matter **199 – 200** 76 (1994). DOI: 10.1016/0921-4526(94)91741-8.
- [51] B. Bucher, Z. Schlesinger, P. C. Canfield, and Z. Fisk. *Kondo coupling induced charge gap in  $Ce_3Bi_4Pt_3$* . Phys. Rev. Lett. **72** 522 (1994). DOI: 10.1103/PhysRevLett.72.522.
- [52] A. Severing, J. D. Thompson, P. C. Canfield, Z. Fisk, and P. Riseborough. *Gap in the magnetic excitation spectrum of  $Ce_3Bi_4Pt_3$* . Phys. Rev. B **44** 6832 (1991). DOI: 10.1103/PhysRevB.44.6832.
- [53] M. F. Hundley, P. C. Canfield, J. D. Thompson, Z. Fisk, and J. M. Lawrence. *Hybridization gap in  $Ce_3Bi_4Pt_3$* . Phys. Rev. B **42** 6842 (1990). DOI: 10.1103/PhysRevB.42.6842.
- [54] G. Boebinger, A. Passner, P. Canfield, and Z. Fisk. *Studies of the Kondo insulator  $Ce_3Bi_4Pt_3$  in 61 T pulsed magnetic fields*. Physica B: Condens. Matter **211** 227 (1995). Research in High Magnetic Fields. DOI: 10.1016/0921-4526(94)00992-5.
- [55] M. Jaime, R. Movshovich, G. R. Stewart, W. P. Beyermann, M. G. Berisso, M. F. Hundley, P. C. Canfield, and J. L. Sarrao. *Closing the spin gap in the Kondo insulator  $Ce_3Bi_4Pt_3$  at high magnetic fields*. Nature **405** 160 (2000). DOI: 10.1038/35012027.
- [56] M. F. Hundley, P. C. Canfield, J. D. Thompson, and Z. Fisk. *Substitutional effects on the electronic transport of the Kondo semiconductor  $Ce_3Bi_4Pt_3$* . Phys. Rev. B **50** 18142 (1994). DOI: 10.1103/PhysRevB.50.18142.
- [57] C. Pfleiderer. *Superconducting phases of  $f$ -electron compounds*. Rev. Mod. Phys. **81** 1551 (2009). DOI: 10.1103/RevModPhys.81.1551.
- [58] F. Steglich, O. Stockert, S. Wirth, C. Geibel, H. Q. Yuan, S. Kirchner, and Q. Si. *Routes to heavy-fermion superconductivity*. J. Phys.: Conf. Ser. **449** 012028 (2013). DOI: 10.1088/1742-6596/449/1/012028.
- [59] G. R. Stewart, Z. Fisk, J. O. Willis, and J. L. Smith. *Possibility of Coexistence of Bulk Superconductivity and Spin Fluctuations in  $UPt_3$* . Phys. Rev. Lett. **52** 679 (1984). DOI: 10.1103/PhysRevLett.52.679.

- [60] D. Jaccard, K. Behnia, and J. Sierro. *Pressure induced heavy fermion superconductivity of  $CeCu_2Ge_2$* . Phys. Lett. A **163** 475 (1992). DOI: 10.1016/0375-9601(92)90860-O.
- [61] Q. Si, S. Rabello, K. Ingersent, and J. L. Smith. *Locally critical quantum phase transitions in strongly correlated metals*. Nature **413** 804 (2001). DOI: 10.1038/35101507.
- [62] P. Coleman and A. J. Schofield. *Quantum criticality*. Nature **433** 226 (2005). DOI: 10.1038/nature03279.
- [63] P. Gegenwart, Q. Si, and F. Steglich. *Quantum criticality in heavy-fermion metals*. Nature Physics **4** 186 (2008). DOI: 10.1038/nphys892.
- [64] F. Steglich, J. Arndt, S. Friedemann, C. Krellner, Y. Tokiwa, T. Westerkamp, M. Brando, P. Gegenwart, C. Geibel, S. Wirth, and O. Stockert. *Superconductivity versus quantum criticality: what can we learn from heavy fermions?* J. Phys.: Condens. Matter **22** 164202 (2010). DOI: 10.1088/0953-8984/22/16/164202.
- [65] S. Sachdev and B. Keimer. *Quantum criticality*. Physics Today **64** 29 (2011). DOI: 10.1063/1.3554314.
- [66] B. Bellarbi, A. Benoit, D. Jaccard, J. M. Mignot, and H. F. Braun. *High-pressure valence instability and  $T_c$  maximum in superconducting  $CeCu_2Si_2$* . Phys. Rev. B **30** 1182 (1984). DOI: 10.1103/PhysRevB.30.1182.
- [67] F. Thomas, J. Thomasson, C. Ayache, C. Geibel, and F. Steglich. *Precise determination of the pressure dependence of  $T_c$  in the heavy-fermion superconductor  $CeCu_2Si_2$* . Physica B: Condens. Matter **186–188** 303 (1993). DOI: 10.1016/0921-4526(93)90561-J.
- [68] A. T. Holmes, D. Jaccard, and K. Miyake. *Valence Instability and Superconductivity in Heavy Fermion Systems*. J. Phys. Soc. Jpn. **76** 051002 (2007). DOI: 10.1143/JPSJ.76.051002.
- [69] K. Miyake. *New trend of superconductivity in strongly correlated electron systems*. J. Phys.: Condens. Matter **19** 125201 (2007). DOI: 10.1088/0953-8984/19/12/125201.
- [70] J.-P. Rueff, S. Raymond, M. Taguchi, M. Sikora, J.-P. Itié, F. Baudalet, D. Braithwaite, G. Knebel, and D. Jaccard. *Pressure-Induced Valence Crossover in Superconducting  $CeCu_2Si_2$* . Phys. Rev. Lett. **106** 186405 (2011). DOI: 10.1103/PhysRevLett.106.186405.
- [71] K. Hattori. *Meta-Orbital Transition in Heavy-Fermion Systems: Analysis by Dynamical Mean Field Theory and Self-Consistent Renormalization Theory of Orbital Fluctuations*. J. Phys. Soc. Jpn. **79** 114717 (2010). DOI: 10.1143/JPSJ.79.114717.
- [72] L. V. Pourovskii, P. Hansmann, M. Ferrero, and A. Georges. *Theoretical Prediction and Spectroscopic Fingerprints of an Orbital Transition in  $CeCu_2Si_2$* . Phys. Rev. Lett. **112** 106407 (2014). DOI: 10.1103/PhysRevLett.112.106407.
- [73] C. M. Varma. *Mixed-valence compounds*. Rev. Mod. Phys. **48** 219 (1976). DOI: 10.1103/RevModPhys.48.219.
- [74] J. M. Lawrence, P. S. Riseborough, and R. D. Parks. *Valence fluctuation phenomena*. Rep. Prog. Phys. **44** 1 (1981). DOI: 10.1088/0034-4885/44/1/001.

## References of Chapter 1 and 2

- [75] J. C. Fuggle, F. U. Hillebrecht, Z. Zołnierrek, R. Lässer, C. Freiburg, O. Gunnarsson, and K. Schönhammer. *Electronic structure of Ce and its intermetallic compounds*. Phys. Rev. B **27** 7330 (1983). DOI: 10.1103/PhysRevB.27.7330.
- [76] E. Havinga, K. Buschow, and H. van Daal. *The ambivalence of Yb in YbAl<sub>2</sub> and YbAl<sub>3</sub>*. Solid State Commun. **13** 621 (1973). DOI: 10.1016/S0038-1098(73)80026-2.
- [77] P. M. Levy and S. Zhang. *Crystal-Field Splitting in Kondo Systems*. Phys. Rev. Lett. **62** 78 (1989). DOI: 10.1103/PhysRevLett.62.78.
- [78] S. Zhang and P. M. Levy. *Anisotropy of the resistivity and susceptibility of Kondo systems*. Phys. Rev. B **40** 7179 (1989). DOI: 10.1103/PhysRevB.40.7179.
- [79] O. Gunnarsson and N. E. Christensen. *Crystal-field and configuration dependence of hopping-matrix elements for CeCu<sub>2</sub>Si<sub>2</sub>*. Phys. Rev. B **42** 2363 (1990). DOI: 10.1103/PhysRevB.42.2363.
- [80] H. Ikeda and K. Miyake. *A Theory of Anisotropic Semiconductor of Heavy Fermions*. J. Phys. Soc. Jpn. **65** 1769 (1996). DOI: 10.1143/JPSJ.65.1769.
- [81] Y. Kagan, K. A. Kikoin, and A. S. Mishchenko. *Interplay between heavy fermions and crystal-field excitation in Kondo lattices: Low-temperature thermodynamics and inelastic neutron scattering spectra of CeNiSn*. Phys. Rev. B **55** 12348 (1997). DOI: 10.1103/PhysRevB.55.12348.
- [82] J.-Y. So, S.-J. Oh, J.-G. Park, D. T. Adroja, K. A. McEwen, and T. Takabatake. *Inelastic neutron scattering studies of doped CeNiSn and CeRhSb: Crystal-field excitations and origin of the pseudogap*. Phys. Rev. B **71** 214441 (2005). DOI: 10.1103/PhysRevB.71.214441.
- [83] F. Ishii and T. Oguchi. *Electronic Band Structure and Gap Formation in CeRhAs*. J. Phys. Soc. Jpn. **73** 145 (2004). DOI: 10.1143/JPSJ.73.145.
- [84] F. de Groot and A. Kotani. *Core Level Spectroscopy of Solids*. CRC Press, Boca Raton, 2008. DOI: 10.1201/9781420008425.fmatt.
- [85] E. Bauer and M. Rotter. "Magnetism of Complex Metallic Alloys: Crystalline Electric Field Effects". In: *Book Series on Complex Metallic Alloys – Vol. 2*. Ed. by E. Belin-Ferrero. World Scientific, 2009.
- [86] R. D. Cowan. *The Theory of Atomic Structure and Spectra*. University of California Press, Berkeley - Los Angeles - London, 1981.
- [87] M. W. Haverkort. *Spin and orbital degrees of freedom in transition metal oxides and oxide thin films studied by soft x-ray absorption spectroscopy*. PhD thesis, Cologne, 2005.
- [88] P. Fulde and M. Loewenhaupt. *Magnetic excitations in crystal-field split 4f systems*. Adv. Phys. **34** 589 (1985). DOI: 10.1080/00018738500101821.
- [89] P. Hansmann. *Crystal-Field ground states of rare earth materials determined by linear dichroism: A feasibility study and its experimental proof*. Diploma thesis, Cologne, 2007.
- [90] K. W. H. Stevens. *Matrix Elements and Operator Equivalents Connected with the Magnetic Properties of Rare Earth Ions*. Proc. Phys. Soc. Section A **65** 209 (1952). DOI: 10.1088/0370-1298/65/3/308.

- [91] P. Hansmann, A. Severing, Z. Hu, M. W. Haverkort, C. F. Chang, S. Klein, A. Tanaka, H. H. Hsieh, H.-J. Lin, C. T. Chen, B. Fåk, P. Lejay, and L. H. Tjeng. *Determining the Crystal-Field Ground State in Rare Earth Heavy Fermion Materials Using Soft-X-Ray Absorption Spectroscopy*. Phys. Rev. Lett. **100** 066405 (2008). DOI: 10.1103/PhysRevLett.100.066405.
- [92] T. Willers, B. Fåk, N. Hollmann, P. O. Körner, Z. Hu, A. Tanaka, D. Schmitz, M. Enderle, G. Lapertot, L. H. Tjeng, and A. Severing. *Crystal-field ground state of the noncentrosymmetric superconductor CePt<sub>3</sub>Si: A combined polarized soft x-ray absorption and polarized neutron study*. Phys. Rev. B **80** 115106 (2009). DOI: 10.1103/PhysRevB.80.115106.
- [93] T. Willers, Z. Hu, N. Hollmann, P. O. Körner, J. Gegner, T. Burnus, H. Fujiwara, A. Tanaka, D. Schmitz, H. H. Hsieh, H.-J. Lin, C. T. Chen, E. D. Bauer, J. L. Sarrao, E. Goremychkin, M. Koza, L. H. Tjeng, and A. Severing. *Crystal-field and Kondo-scale investigations of CeMIn<sub>5</sub> (M = Co, Ir, and Rh): A combined x-ray absorption and inelastic neutron scattering study*. Phys. Rev. B **81** 195114 (2010). DOI: 10.1103/PhysRevB.81.195114.
- [94] T. Willers, D. T. Adroja, B. D. Rainford, Z. Hu, N. Hollmann, P. O. Körner, Y.-Y. Chin, D. Schmitz, H. H. Hsieh, H.-J. Lin, C. T. Chen, E. D. Bauer, J. L. Sarrao, K. J. McClellan, D. Byler, C. Geibel, F. Steglich, H. Aoki, P. Lejay, A. Tanaka, L. H. Tjeng, and A. Severing. *Spectroscopic determination of crystal-field levels in CeRh<sub>2</sub>Si<sub>2</sub> and CeRu<sub>2</sub>Si<sub>2</sub> and of the 4f<sup>0</sup> contributions in CeM<sub>2</sub>Si<sub>2</sub> (M=Cu, Ru, Rh, Pd, and Au)*. Phys. Rev. B **85** 035117 (2012). DOI: 10.1103/PhysRevB.85.035117.
- [95] T. Willers, J. C. Cezar, N. B. Brookes, Z. Hu, F. Strigari, P. Körner, N. Hollmann, D. Schmitz, A. Bianchi, Z. Fisk, A. Tanaka, L. H. Tjeng, and A. Severing. *Magnetic Field Induced Orbital Polarization in Cubic YbInNi<sub>4</sub>: Determining the Quartet Ground State Using X-Ray Linear Dichroism*. Phys. Rev. Lett. **107** 236402 (2011). DOI: 10.1103/PhysRevLett.107.236402.
- [96] D. T. Adroja, A. D. Hillier, Y. Muro, T. Takabatake, A. M. Strydom, A. Bhattacharyya, A. Daoud-Aladin, and J. W. Taylor. *Muon-spin-relaxation and inelastic neutron scattering investigations of the caged-type Kondo semimetals*. Phys. Scr. **88** 068505 (2013). DOI: 10.1088/0031-8949/88/06/068505.
- [97] T. Nishioka, Y. Kawamura, T. Takesaka, R. Kobayashi, H. Kato, M. Matsumura, K. Kodama, K. Matsubayashi, and Y. Uwatoko. *Novel Phase Transition and the Pressure Effect in YbFe<sub>2</sub>Al<sub>10</sub>-type CeT<sub>2</sub>Al<sub>10</sub> (T = Fe, Ru, Os)*. J. Phys. Soc. Jpn. **78** 123705 (2009). DOI: 10.1143/JPSJ.78.123705.
- [98] K. Hanzawa. *Crystalline Electric Field Effects in CeT<sub>2</sub>Al<sub>10</sub> (T = Ru, Os)*. J. Phys. Soc. Jpn. **80** 023707 (2011). DOI: 10.1143/JPSJ.80.023707.
- [99] S.-I. Kimura, T. Iizuka, H. Miyazaki, T. Hajiri, M. Matsunami, T. Mori, A. Irizawa, Y. Muro, J. Kajino, and T. Takabatake. *Optical study of charge instability in CeRu<sub>2</sub>Al<sub>10</sub> in comparison with CeOs<sub>2</sub>Al<sub>10</sub> and CeFe<sub>2</sub>Al<sub>10</sub>*. Phys. Rev. B **84** 165125 (2011). DOI: 10.1103/PhysRevB.84.165125.
- [100] T. Takabatake, Y. Nakazawa, and M. Ishikawa. *Gap Formation in a Valence Fluctuation System of CeNiSn*. Jpn. J. Appl. Phys. **26** 547 (1987). DOI: 10.7567/JJAPS.26S3.547.

References of Chapter 1 and 2

- [101] T. Takabatake, T. Sasakawa, J. Kitagawa, T. Suemitsu, Y. Echizen, K. Umeo, M. Sera, and Y. Bando. *Thermoelectric properties of Ce-based Kondo semimetals and semiconductors*. Physica B: Condens. Matter **328** 53 (2003). DOI: 10.1016/S0921-4526(02)01808-2.
- [102] K. Izawa, T. Suzuki, T. Fujita, T. Takabatake, G. Nakamoto, H. Fujii, and K. Maezawa. *Metallic ground state of CeNiSn*. Phys. Rev. B **59** 2599 (1999). DOI: 10.1103/PhysRevB.59.2599.
- [103] M. Kyogaku, Y. Kitaoka, H. Nakamura, K. Asayama, T. Takabatake, F. Teshima, and H. Fujii. *NMR Investigation of Energy Gap Formation in the Valence Fluctuating Compound CeNiSn*. J. Phys. Soc. Jpn. **59** 1728 (1990). DOI: 10.1143/JPSJ.59.1728.
- [104] M. Kyogaku, Y. Kitaoka, H. Nakamura, K. Asayama, T. Takabatake, F. Teshima, and H. Fujii. *NMR study of quasiparticle gap in CeNiSn*. Physica B: Condens. Matter **171** 235 (1991). DOI: 10.1016/0921-4526(91)90521-F.
- [105] J. Moreno and P. Coleman. *Gap-Anisotropic Model for the Narrow-Gap Kondo Insulators*. Phys. Rev. Lett. **84** 342 (2000). DOI: 10.1103/PhysRevLett.84.342.
- [106] P. Pagliuso, N. Curro, N. Moreno, M. Hundley, J. Thompson, J. Sarrao, and Z. Fisk. *Structurally tuned superconductivity in heavy-fermion CeMIn5 (M = Co, Ir, Rh)*. Physica B: Condens. Matter **320** 370 (2002). DOI: 10.1016/S0921-4526(02)00751-2.
- [107] T. Takimoto, T. Hotta, and K. Ueda. *Superconductivity in the orbital degenerate model for heavy fermion systems*. J. Phys.: Condens. Matter **15** S2087 (2003). DOI: 10.1088/0953-8984/15/28/329.
- [108] K. Kubo and T. Hotta. *Orbital-Controlled Superconductivity in f-Electron Systems*. J. Phys. Soc. Jpn. **75** 083702 (2006). DOI: 10.1143/JPSJ.75.083702.
- [109] T. Maehira, T. Hotta, K. Ueda, and A. Hasegawa. *Relativistic Band-Structure Calculations for CeTIn5 (T = Ir and Co) and Analysis of the Energy Bands by Using Tight-Binding Method*. J. Phys. Soc. Jpn. **72** 854 (2003). DOI: 10.1143/JPSJ.72.854.
- [110] K. S. Burch, S. V. Dordevic, F. P. Mena, A. B. Kuzmenko, D. van der Marel, J. L. Sarrao, J. R. Jeffries, E. D. Bauer, M. B. Maple, and D. N. Basov. *Optical signatures of momentum-dependent hybridization of the local moments and conduction electrons in Kondo lattices*. Phys. Rev. B **75** 054523 (2007). DOI: 10.1103/PhysRevB.75.054523.
- [111] J. H. Shim, K. Haule, and G. Kotliar. *Modeling the Localized-to-Itinerant Electronic Transition in the Heavy Fermion System CeIrIn5*. Science **318** 1615 (2007). DOI: 10.1126/science.1149064.
- [112] T. Willers. *Spectroscopic Investigations of the Crystal Field and Kondo Effect in 4f Heavy-Fermion Systems*. PhD thesis, Cologne, 2011.
- [113] J. Allen, S. Oh, O. Gunnarsson, K. Schönhammer, M. Maple, M. Torikachvili, and I. Lindau. *Electronic structure of cerium and light rare-earth intermetallics*. Adv. Phys. **35** 275 (1986). DOI: 10.1080/00018738600101901.
- [114] S. Hüfner. *Photoelectron Spectroscopy: Principles and Applications*. Advanced Texts in Physics. Springer, Berlin - Heidelberg, 2003. DOI: 10.1007/978-3-662-09280-4.

- [115] S. Mobilio, F. Boscherini, and C. Meneghini. *Synchrotron Radiation: Basics, Methods and Applications*. Springer, Berlin - Heidelberg, 2015. DOI: 10.1007/978-3-642-55315-8.
- [116] B. A. Lippmann and J. Schwinger. *Variational Principles for Scattering Processes. I*. Phys. Rev. **79** 469 (1950). DOI: 10.1103/PhysRev.79.469.
- [117] E. Antonides, E. C. Janse, and G. A. Sawatzky. *LMM Auger spectra of Cu, Zn, Ga, and Ge. I. Transition probabilities, term splittings, and effective Coulomb interaction*. Phys. Rev. B **15** 1669 (1977). DOI: 10.1103/PhysRevB.15.1669.
- [118] A. Tanaka and T. Jo. *Resonant 3d, 3p and 3s PES in Transition Metal Oxides Predicted at 2p Threshold*. J. Phys. Soc. Jpn. **63** 2788 (1994). DOI: 10.1143/JPSJ.63.2788.
- [119] M. W. Haverkort. *Solid State Physics Mathematica package*. 2014. URL: <http://www.solstatphys.org/>.
- [120] H. Bethe. *Termaufspaltung in Kristallen*. Annalen der Physik **395** 133 (1929). DOI: 10.1002/andp.19293950202.
- [121] J. H. Van Vleck. *Quantum mechanics – The key to understanding magnetism*. Rev. Mod. Phys. **50** 181 (1978). DOI: 10.1103/RevModPhys.50.181.
- [122] C. J. Ballhausen. *Introduction to Ligand Field Theory*. Mac Graw-Hill, New York, 1962.
- [123] H. L. Schläfer and G. Gliemann. *Basic principles of ligand field theory*. Wiley-Interscience, London, 1969.
- [124] S. Sugano, Y. Tanabe, and H. Kamimura. *Multiplets of transition-metal ions in crystals*. Academic Press, New York, 1970.
- [125] T. Willers, K. Siemensmeyer, and E. Weschke. Unpublished (2011).
- [126] T. Willers, F. Strigari, N. Hiraoka, Y. Q. Cai, M. W. Haverkort, K.-D. Tsuei, Y. F. Liao, S. Seiro, C. Geibel, F. Steglich, L. H. Tjeng, and A. Severing. *Determining the In-Plane Orientation of the Ground-State Orbital of CeCu<sub>2</sub>Si<sub>2</sub>*. Phys. Rev. Lett. **109** 046401 (2012). DOI: 10.1103/PhysRevLett.109.046401.
- [127] T. Mori, S. Kitayama, Y. Kanai, S. Naimen, H. Fujiwara, A. Higashiya, K. Tamasaku, A. Tanaka, K. Terashima, S. Imada, A. Yasui, Y. Saitoh, K. Yamagami, K. Yano, T. Matsumoto, T. Kiss, M. Yabashi, T. Ishikawa, S. Suga, Y. Ōnuki, T. Ebihara, and A. Sekiyama. *Probing Strongly Correlated 4f-Orbital Symmetry of the Ground State in Yb Compounds by Linear Dichroism in Core-Level Photoemission*. J. Phys. Soc. Jpn. **83** 123702 (2014). DOI: 10.7566/JPSJ.83.123702.
- [128] M. Abbate, J. B. Goedkoop, F. M. F. de Groot, M. Grioni, J. C. Fuggle, S. Hofmann, H. Petersen, and M. Sacchi. *Probing depth of soft x-ray absorption spectroscopy measured in total-electron-yield mode*. Surf. Interface Anal. **18** 65 (1992). DOI: 10.1002/sia.740180111.
- [129] J. Weinen. *A New Detector for Bulk-Sensitive XAS on Highly Insulating Samples*. Diploma thesis, Cologne, 2009.
- [130] K. Hämäläinen, D. P. Siddons, J. B. Hastings, and L. E. Berman. *Elimination of the inner-shell lifetime broadening in x-ray-absorption spectroscopy*. Phys. Rev. Lett. **67** 2850 (1991). DOI: 10.1103/PhysRevLett.67.2850.

## References of Chapter 1 and 2

- [131] A. Kotani and S. Shin. *Resonant inelastic x-ray scattering spectra for electrons in solids*. Rev. Mod. Phys. **73** 203 (2001). DOI: 10.1103/RevModPhys.73.203.
- [132] C. Dallera, M. Grioni, A. Shukla, G. Vankó, J. L. Sarrao, J. P. Rueff, and D. L. Cox. *New Spectroscopy Solves an Old Puzzle: The Kondo Scale in Heavy Fermions*. Phys. Rev. Lett. **88** 196403 (2002). DOI: 10.1103/PhysRevLett.88.196403.
- [133] C. Dallera and M. Grioni. *Resonant Scattering of X Rays as a Probe of Valence and Hybridization in Solids*. Struct. Chem. **14** 57 (2003).
- [134] J.-P. Rueff and A. Shukla. *Inelastic x-ray scattering by electronic excitations under high pressure*. Rev. Mod. Phys. **82** 847 (2010). DOI: 10.1103/RevModPhys.82.847.
- [135] R. Nakajima, J. Stöhr, and Y. U. Idzerda. *Electron-yield saturation effects in L-edge x-ray magnetic circular dichroism spectra of Fe, Co, and Ni*. Phys. Rev. B **59** 6421 (1999). DOI: 10.1103/PhysRevB.59.6421.
- [136] C. Chen. *Concept and design procedure for cylindrical element monochromators for synchrotron radiation*. Nucl. Instr. Meth. Phys. Res. A **256** 595 (1987). DOI: 10.1016/0168-9002(87)90307-X.
- [137] H. Hertz. *Über den Einfluss des ultravioletten Lichts auf die elektrische Entladung*. Ann. der Physik **267** 983 (1887).
- [138] A. Einstein. *Über einen die Erzeugung und Verwandlung des Lichtes betreffenden heuristischen Gesichtspunkt*. Ann. der Physik **17** 132 (1905).
- [139] A. Damascelli. *Probing the Electronic Structure of Complex Systems by ARPES*. Physica Scripta **2004** 61 (2004). DOI: 10.1238/Physica.Topical.109a00061.
- [140] S. Hofmann. *Auger- and X-Ray Photoelectron Spectroscopy in Materials Science: A User-Oriented Guide*. Springer Series in Surface Sciences. Springer, 2012. ISBN: 9783642273803.
- [141] R. Schlaf. *Calibration of Photoemission Spectra and Work Function Determination*. 2013. URL: <http://rsl.eng.usf.edu/Documents/Tutorials/PEScalibration.pdf>.
- [142] A. Kotani and Y. Toyozawa. *Photoelectron Spectra of Core Electrons in Metals with an Incomplete Shell*. J. Phys. Soc. Jpn. **37** 912 (1974). DOI: 10.1143/JPSJ.37.912.
- [143] O. Gunnarsson and K. Schönhammer. *Electron spectroscopies for Ce compounds in the impurity model*. Phys. Rev. B **28** 4315 (1983). DOI: 10.1103/PhysRevB.28.4315.
- [144] R. Lässer, J. Fuggle, M. Beyss, M. Campagna, F. Steglich, and F. Hulliger. *X-ray photoemission from Ce core levels of CePd<sub>3</sub>, CeSe, CeAl<sub>2</sub> and CeCu<sub>2</sub>Si<sub>2</sub>*. Physica B+C **102** 360 (1980). DOI: 10.1016/0378-4363(80)90192-8.
- [145] F. U. Hillebrecht and J. C. Fuggle. *Invalidity of 4f count determination and possibilities for determination of 4f hybridization in intermetallics of the light rare earths by core-level spectroscopy*. Phys. Rev. B **25** 3550 (1982). DOI: 10.1103/PhysRevB.25.3550.
- [146] M. Sundermann. *Quantitative modeling of core level photoemission spectra for the determination of the Ce valency in Ce based heavy fermion compounds*. Master thesis, Cologne, 2014.

- [147] J.-M. Imer and E. Wuilloud. *A simple model calculation for XPS, BIS and EELS 4f-excitations in Ce and La compounds*. Zeitschrift für Physik B Cond. Mat. **66** 153 (1987). DOI: 10.1007/BF01311650.
- [148] B. Henke, E. Gullikson, and J. Davis. *X-Ray Interactions: Photoabsorption, Scattering, Transmission, and Reflection at  $E = 50 - 30000$  eV,  $Z = 1 - 92$* . Atomic Data and Nuclear Data Tables **54** 181 (1993). see also <http://henke.lbl.gov/>. DOI: 10.1006/adnd.1993.1013.
- [149] C. Dallera, L. Duò, L. Braicovich, G. Panaccione, G. Paolicelli, B. Cowie, and J. Zegenhagen. *Looking 100Å deep into spatially inhomogeneous dilute systems with hard x-ray photoemission*. Appl. Phys. Lett. **85** 4532 (2004). DOI: 10.1063/1.1814441.
- [150] A. X. Gray, C. Papp, S. Ueda, B. Balke, Y. Yamashita, L. Plucinski, J. Minár, J. Braun, E. R. Ylvisaker, C. M. Schneider, W. E. Pickett, H. Ebert, K. Kobayashi, and C. S. Fadley. *Probing bulk electronic structure with hard X-ray angle-resolved photoemission*. Nature Materials **10** 759 (2011). DOI: 1038/nmat3089.
- [151] S. Ouardi, G. H. Fecher, and C. Felser. *Bulk electronic structure studied by hard X-ray photoelectron spectroscopy of the valence band: The case of intermetallic compounds*. J. Electron Spectrosc. Relat. Phenom. **190B** 249 (2013). Recent advances in Hard X-ray Photoelectron Spectroscopy (HAXPES). DOI: 10.1016/j.eispec.2013.09.001.
- [152] M. B. Trzhaskovskaya, V. I. Nefedov, and V. G. Yarthemsky. *Photoelectron angular distribution parameters for elements  $Z=1$  to  $Z=54$  in the photoelectron energy range 100 - 5000 eV*. Atomic Data and Nuclear Data Tables **77** 97 (2001). DOI: 10.1006/adnd.2000.0849.
- [153] M. B. Trzhaskovskaya, V. K. Nikulin, V. I. Nefedov, and V. G. Yartzemsky. *Non-dipole second order parameters of the photoelectron angular distribution for elements  $Z=1-100$  in the photoelectron energy range 1-10 keV*. Atomic Data and Nuclear Data Tables **92** 245 (2006). DOI: 10.1016/j.adt.2005.12.002.
- [154] J. Weinen, T. Koethe, C. Chang, S. Agrestini, D. Kasinathan, Y. Liao, H. Fujiwara, C. Schüßler-Langeheine, F. Strigari, T. Haupricht, G. Panaccione, F. Offi, G. Monaco, S. Huotari, K.-D. Tsuei, and L. Tjeng. *Polarization dependent hard X-ray photoemission experiments for solids: Efficiency and limits for unraveling the orbital character of the valence band*. J. Electron Spectrosc. Relat. Phenom. **198** 6 (2015). DOI: 10.1016/j.eispec.2014.11.003.
- [155] S. Doniach and M. Sunjic. *Many-electron singularity in X-ray photoemission and X-ray line spectra from metals*. J. Physics C: Solid State Phys. **3** 285 (1970). DOI: 10.1088/0022-3719/3/2/010.
- [156] G. D. Mahan. *Collective excitations in x-ray spectra of metals*. Phys. Rev. B **11** 4814 (1975). DOI: 10.1103/PhysRevB.11.4814.
- [157] J. Folmer and D. de Boer. *XPS core level line shapes in metallic compounds: A probe for the nature of the electrons at the Fermi level*. Solid State Commun. **38** 1135 (1981). DOI: 10.1016/0038-1098(81)90973-X.
- [158] D. A. Shirley. *High-Resolution X-Ray Photoemission Spectrum of the Valence Bands of Gold*. Phys. Rev. B **5** 4709 (1972). DOI: 10.1103/PhysRevB.5.4709.

*References of Chapter 1 and 2*

- [159] J. Gadzuk. *Plasmon satellites in X-ray photoemission spectra*. J. Electron Spectrosc. Relat. Phenom. **11** 355 (1977). DOI: 10.1016/0368-2048(77)80012-1.
- [160] H. Shinotsuka, T. Uwatoko, T. Konishi, and T. Fujikawa. *Theoretical Study of Plasmon Loss Peaks in Core-level Photoemission Spectra: Energy and Angular Dependence*. J. Surf. Anal. **14** 332 (2008).
- [161] D. Tomboulia and P. Hartman. *Spectral and Angular Distribution of Ultraviolet Radiation from the 300-Mev Cornell Synchrotron*. Phys. Rev. **102** 1423 (1956). DOI: 10.1103/PhysRev.102.1423.

### 3 Crystal-field ground state of the orthorhombic Kondo insulator $\text{CeRu}_2\text{Al}_{10}$

Phys. Rev. B **86**, 081105(R) (2012)

*This chapter is published as Phys. Rev. B **86**, 081105(R) (2012). A. Severing supervised the project and guided the experiment, the scientific discussion and the publication process. The single-crystalline samples were synthesized and provided by Y. Muro, K. Yutani and T. Takabatake. The sample preparation and the experimental planning were carried out by T. Willers and myself. H.-J. Lin and C. T. Chen were the responsible beamline scientists at the NSRRC for the technical support during the experiment. T. Willers, Z. Hu, Y.-Y. Chin, S. Agrestini and myself constituted the experimental team and performed the experiment. The program code for the data simulation was provided by A. Tanaka. Further assistance for the calculations incl. the use of the ‘Mathematica Crystal Field Package’ was provided by M. W. Haverkort. Scientific discussion took place with L. H. Tjeng. The analysis/interpretation of the data and the writing of the manuscript were performed by myself.*

#### Abstract

We have succeeded in establishing the crystal-field ground state of  $\text{CeRu}_2\text{Al}_{10}$ , an orthorhombic intermetallic compound recently identified as a Kondo insulator. Using polarization-dependent soft x-ray absorption spectroscopy at the Ce  $M_{4,5}$  edges, together with input from inelastic neutron and magnetic susceptibility experiments, we were able to determine unambiguously the orbital occupation of the  $4f$  shell and to explain quantitatively both the measured magnetic moment along the easy  $a$  axis and the small ordered moment along the  $c$  axis. The results provide not only a platform for a realistic modeling of the spin and charge gap of  $\text{CeRu}_2\text{Al}_{10}$ , but demonstrate also the potential for soft x-ray absorption spectroscopy to obtain information not easily accessible by neutron techniques for the study of Kondo insulators in general.

#### 3.1 Introduction

$\text{CeRu}_2\text{Al}_{10}$  is a fairly new synthesized orthorhombic intermetallic compound [1, 2] and has initiated a flurry of experimental and theoretical research activities since the discovery of its Kondo insulating properties in 2009 [3–21]. The electrical resistivity shows a thermally activated behavior at elevated temperatures and has a more metallic-like form several degrees below  $T_0 = 27$  K where a phase transition occurs, as revealed by specific heat measurements [3, 4]. A large anisotropy is observed in the static susceptibility ( $\chi_a > \chi_c > \chi_b$ ) and along the easy axis the susceptibility is Curie-Weiss-like above  $T_0$  [4, 5, 15]. For some time it has been a matter of debate whether the phase transition is magnetic in origin [6–9, 11, 12]. In fact, in the structure of  $\text{CeRu}_2\text{Al}_{10}$  (space group  $Cmcm$ ) each Ce atom is situated in a polyhedral cage consisting of

16 Al and 4 Ru atoms, giving rise to very large Ce-Ce distances of more than 5 Å [2]. Thus, it is not obvious to explain the relative high ordering temperature using a standard model based on Ruderman-Kittel-Kasuya-Yosida (RKKY) exchange interactions.

Nevertheless, recent muon spin relaxation and neutron diffraction experiments confirmed the magnetic nature of the phase transition. The Ce moments order antiferromagnetically along the  $c$  direction with a small ordered moment of  $\mu_{\text{ord}} \approx 0.4 \mu_B$  [7–9, 11]. The latest NMR data agree with this scenario [12]. Below  $T_0$  inelastic neutron scattering (INS) experiments on a polycrystalline sample have found the existence of a spin gap of several meV, characterized by a magnetic mode with flat dispersion at about 8 meV [9]. Above  $T_0$  this excitation is drastically suppressed and therefore cannot be attributed to a crystal electric field (CEF) excitation. More recent INS results have found CEF splittings of 30 and 46 meV [22]. It has been suggested that the mixture of Kondo and CEF effects may be responsible for the small size of the ordered moment. A point charge model yields a moment of only  $0.62 \mu_B$  along  $c$  for the ground state (GS) [16], but the combination of large spin gap, small ordered moment and high ordering temperature remains quite puzzling. Recent optical studies have suggested an electronic structure with strong anisotropic hybridization between the  $4f$  and conduction electrons, which is weakest along the crystallographic  $b$  direction. It has been then speculated that a charge density wave can form along  $b$  which in turn may trigger the magnetic transition [13, 14].

The objective of the present Rapid Communication is to elucidate the local electronic structure of the  $4f$  electrons. The GS wave function of the  $4f$  electrons in this orthorhombic compound is expected to be highly anisotropic due to the presence of the CEF, with important consequences for the magnetic properties and the gap formation, as pointed out already by several groups in their study on other orthorhombic semiconductors like CeNiSn and CeRhSb [23–26].

Efforts to prove these theories experimentally turned out to be challenging because broadening of the CEF excitations due to hybridization and the existence of spin gaps prevented the determination of the ground states in these compounds by inelastic neutron scattering [27–31]. Hence there is need for an alternative approach. Our method of choice is x-ray absorption spectroscopy (XAS) at the Ce  $M_{4,5}$  edge, which has shown to be a complementary technique to neutron scattering to determine the GS wave function of CEF-split tetragonal cerium compounds [32–35]. The sensitivity to the initial state symmetry is achieved via the different absorption for light polarized  $E \parallel c$  (with  $c$  being the long tetragonal axis) and  $E \perp c$ . We now extend this method to an orthorhombic compound where the polarization dependence of the absorption, the linear dichroism (LD), has to be measured for all three directions, i.e. for  $E \parallel a$ ,  $E \parallel b$ , and  $E \parallel c$ , in order to determine the initial state symmetry.

## 3.2 Experimental and theoretical details

Single crystals of  $CeRu_2Al_{10}$  were grown by an Al self-flux method [36] and their quality and orientation were confirmed by Laue x-ray diffraction. All XAS measurements were carried out at the Dragon bending magnet beamline BL11A1 of the NSRRC in Taiwan. The energy resolution at the Ce  $M_{4,5}$  edge ( $h\nu \approx 870 - 910$  eV) was 0.4 eV. The single crystals were cleaved *in situ* in an ultra high vacuum of  $\sim 10^{-10}$  mbar to obtain clean sample surfaces. We measured the total electron yield (TEY) and normalized the signal to the incoming flux  $I_0$  as measured

on an Au mesh at the entrance of the experimental chamber. Two crystals were investigated: one mounted with the  $c$  and the other one with the  $a$  axis parallel to the Poynting vector of the incoming light. This way we were able to vary the electric field from  $E \parallel a$  to  $E \parallel b$  and from  $E \parallel b$  to  $E \parallel c$ , respectively, by rotating the crystals in steps of  $90^\circ$  around the Poynting vector. The spectra for  $E \parallel b$  were recorded on both samples so that the three polarizations could be normalized to each other. The data were reproduced by probing several positions on the samples and recleaving the crystals.

Ionic full multiplet calculations were performed with the XTLS 8.3 program [37] to simulate the XAS spectra. Initially, the experimental isotropic spectra  $I_{\text{isotropic}} = I_{E \parallel a} + I_{E \parallel b} + I_{E \parallel c}$  were fitted. The best agreement was achieved with a reduction of the atomic Hartree-Fock values of about 40 % for  $4f$ - $4f$  Coulomb interactions and of about 20 % for the  $3d$ - $4f$  interactions. The reduction factors account for configuration interaction effects not included in the Hartree-Fock scheme. Their size is in agreement with previous findings on tetragonal Ce systems [32–35]. We follow the coherent approach for our simulations, i.e. the XAS spectra are calculated directly from the CEF mixed GS wave functions, the latter being fabricated via CEF parameters since for orthorhombic symmetry the XAS spectra cannot be calculated as incoherent sums of the pure  $J_z$  spectra.

The CEF parameters are defined via the CEF Hamiltonian, which arises from the expansion of the Madelung potential in spherical harmonics:

$$V(r, \theta, \Phi) = \sum_{k=0}^{\infty} \sum_{m=-k}^k A_k^m r^k C_k^m(\theta, \Phi)$$

$C_k^m(\theta, \Phi) = \sqrt{\frac{4\pi}{2k+1}} Y_k^m(\theta, \Phi)$  are the semi-normalized spherical harmonics. The expectation value  $\langle r^k \rangle$  of the radial part of the wave function cannot be calculated analytically and is therefore included in the CEF parameters  $\check{A}_k^m = A_k^m \langle r^k \rangle$ , which are determined experimentally.

There are nine independent CEF parameters,  $\check{A}_2^0, \check{A}_2^2, \check{A}_4^0, \check{A}_4^2, \check{A}_4^4, \check{A}_6^0, \check{A}_6^2, \check{A}_6^4$ , and  $\check{A}_6^6$ , in the orthorhombic point group  $C_{2v}$  for the cerium ion in  $\text{CeRu}_2\text{Al}_{10}$  and the CEF splits the  $J=5/2$  and  $7/2$  multiplets of  $\text{Ce}^{3+}$  into seven Kramer's doublets. Each of these states can generally be represented in the basis of  $|J, J_z\rangle$  as

$$\sum_{J_z=-\frac{5}{2}, -\frac{3}{2}, \dots, \frac{5}{2}} \alpha_{J_z} |5/2, J_z\rangle + \sum_{J_z=-\frac{7}{2}, -\frac{5}{2}, \dots, \frac{7}{2}} \beta_{J_z} |7/2, J_z\rangle$$

for values of  $J_z$  which fulfill  $\sum_{J_z} (\alpha_{J_z}^2 + \beta_{J_z}^2) = 1$  and  $\Delta J_z = \pm 2$ . The full multiplet routine takes the higher  $J=7/2$  multiplet into account. However, for most Ce compounds the  $J=7/2$  does not mix with the lower  $J=5/2$  multiplet because the CEF splitting  $\Delta E_{\text{CEF}}$  is much smaller than the spin-orbit splitting  $\Delta E_{\text{SO}}$  of  $\sim 280$  meV. In such a case only the  $\check{A}_k^m$  parameters with  $k \leq 4$  affect the  $J_z$  mixing of the lower  $J=5/2$  multiplet and it is justified to set the higher order parameters to zero ( $\check{A}_6^m = 0$ ). For  $\Delta E_{\text{SO}} \gg \Delta E_{\text{CEF}}$  and  $\check{A}_6^m = 0$  the remaining  $\check{A}_k^m$  can be converted<sup>1</sup> to Stevens parameters  $B_k^m$ .

<sup>1</sup>In the case of  $f^1$  ( $J=5/2$ ) the relationship between the crystal-field parameters in spherical harmonics and Stevens approximation is:  $\check{A}_2^0 \leftrightarrow -35B_2^0, \check{A}_2^2 \leftrightarrow -\frac{7}{2}\sqrt{\frac{50}{3}}B_2^2, \check{A}_4^0 \leftrightarrow -\frac{7}{2}\sqrt{\frac{50}{3}}B_4^0, \check{A}_4^2 \leftrightarrow 1260B_4^2, \check{A}_4^4 \leftrightarrow 63\sqrt{10}B_4^4, \check{A}_4^6 \leftrightarrow 63\sqrt{10}B_4^6, \check{A}_4^4 \leftrightarrow 18\sqrt{70}B_4^4$  and  $\check{A}_4^6 \leftrightarrow 18\sqrt{70}B_4^6$

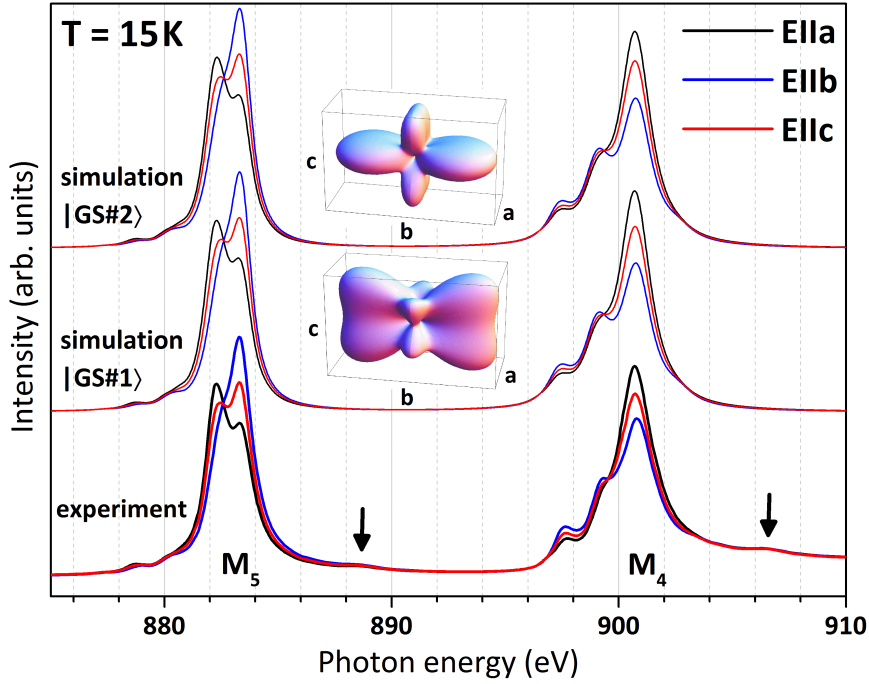


Figure 3.1: Measured and simulated linear polarized XAS spectra of  $\text{CeRu}_2\text{Al}_{10}$  at the  $M_{4,5}$  edge at  $T = 15$  K. The two simulations reproducing the experimental data are shown with the corresponding spatial distributions of the  $4f$  electrons as insets. The arrows indicate the spectral weight coming from the  $4f^0$  contribution in the initial state.

### 3.3 Results and discussion

The bottom curves in Fig. 3.1 are the measured low-temperature linear polarized XAS spectra of  $\text{CeRu}_2\text{Al}_{10}$ . The main absorption features are due to the absorption process  $3d^{10}4f^1 \rightarrow 3d^94f^2$  ( $M_4$  and  $M_5$  edges). The spectra show a clear polarization dependence in all three crystallographic directions as expected for an orthorhombic compound. From INS experiments the splitting between the CEF ground state and the first excited CEF state is known to be  $\sim 30$  meV [22], so that data taken at  $T = 15$  K are representative for the CEF ground state. There is some additional faint spectral weight at about 888 and 906 eV in the absorption spectra (indicated by the arrows in Fig. 3.1) due to the  $3d^{10}4f^0 \rightarrow 3d^94f^1$  absorption process, which is representative for the  $4f^0$  contribution in the initial state. However, we note that for  $\text{CeRu}_2\text{Al}_{10}$  this contribution is fairly small (compared with the  $f^0$  in 1:2:2 compounds) [35], which is in agreement with recent findings from  $3d$  photoemission spectroscopy [21]. The small  $4f^0$  contribution implies that the impact of the Kondo effect on the polarization of the  $4f^1$  absorption edges is minor.

The full multiplet routine yields two different wave functions (in the following referred to as  $|\text{GS}\#1\rangle$  and  $|\text{GS}\#2\rangle$ ) that describe the experiment very well (see Fig. 3.1). We use the  $c$  axis as the quantization axis and the corresponding  $J_z$  coefficients are listed in Table 3.1. Both solutions are mainly composed of the  $J = 5/2$  multiplet and have some small admixtures from the higher

	$ J, J_z\rangle$	$ \text{GS}\#1\rangle$	$ \text{GS}\#2\rangle$
Table 3.1: The $J_z$ coefficients $\alpha_{J_z}$ and $\beta_{J_z}$ of the two GS wave functions which describe the XAS data. The wave functions have been calculated with the full multiplet routine, using $c$ as the quantization axis. The corresponding $\check{A}_k^m$ are given in Table 3.2.	$ 5/2, \pm 5/2\rangle$	$\pm 0.47(2)$	$\pm 0.68(2)$
	$ 5/2, \pm 1/2\rangle$	$\pm 0.32(2)$	$\pm 0.73(2)$
	$ 5/2, \mp 3/2\rangle$	$\pm 0.82(2)$	$\mp 0.02(4)$
	$ 7/2, \pm 5/2\rangle$	$\mp 0.05(1)$	$\mp 0.02(1)$
	$ 7/2, \pm 1/2\rangle$	$\pm 0.01(1)$	$\mp 0.03(1)$
	$ 7/2, \mp 3/2\rangle$	$\mp 0.02(1)$	$\pm 0.02(1)$
	$ 7/2, \mp 7/2\rangle$	$\pm 0.03(1)$	$\pm 0.00(1)$

$J = 7/2$  multiplet. The effect of the  $J = 7/2$  contributions on the LD is negligible and cannot be seen in the spectra when changing into Stevens approximation. For solution  $|\text{GS}\#1\rangle$  the contribution  $|5/2, \mp 3/2\rangle$  is very strong in contrast to solution  $|\text{GS}\#2\rangle$ , which is dominated by  $|5/2, \pm 1/2\rangle$  and  $|5/2, \pm 5/2\rangle$ . The orbitals in the insets of Fig. 3.1 represent the spatial distributions of the  $4f$  electrons for the respective GS wave functions. It turns out that we can find CEF parameters for both wave functions which satisfy the results of INS, i.e. they yield the CEF transition energies  $\Delta E_1 = 30$  meV and  $\Delta E_2 = 46$  meV and the ratio of the inelastic neutron intensities  $I_1/I_2 = 1.35$  [22]. The respective CEF parameters are summarized in Table 3.2.

In Fig. 3.2 the experimental and the simulated temperature dependence of the XAS spectra are shown. Both CEF scenarios are based on the same energy splittings and at 300 K the population of the excited states at 30 and 46 meV amounts to only 20 % and 10 %. Consequently, both CEF models yield the same qualitative temperature dependence. We therefore omitted the simulations for  $|\text{GS}\#2\rangle$  in Fig. 3.2. As the isotropic spectrum  $I_{\text{isotropic}} = I_{E\parallel a} + I_{E\parallel b} + I_{E\parallel c}$  is temperature-independent, it is sufficient to consider the temperature dependence of two polarizations, and for reasons of clarity only the  $M_5$  absorption edges for  $E \parallel b$  and  $E \parallel c$  are included in the illustration. After the first cleave we measured at 15, 40, 100, 150, 200 and 300 K, then recleaved at 300 K, and measured in the reversed temperature order. Moreover, we cross-checked and reproduced the mutual polarization for the two available samples. There is also no change of polarization up to 100 K, which shows that no state gets populated, i.e. there is indeed no low-lying crystal-field excitation, which is in accordance with INS results [9, 22]. The change of polarization at 300 K with respect to 15 K is in agreement with excited CEF states at 30 meV and above (see right panel in Fig. 3.2).

	$\check{A}_2^0$	$\check{A}_2^2$	$\check{A}_4^0$	$\check{A}_4^2$	$\check{A}_4^4$
$ \text{GS}\#1\rangle$	4(5)	36(2)	110(5)	-30(10)	-69(5)
$ \text{GS}\#2\rangle$	-5(2)	38(5)	-40(10)	-112(5)	0 (5)

Table 3.2: Crystal-field parameters  $\check{A}_k^m$  in meV from full multiplet calculations with  $\check{A}_6^m = 0$  for  $m = 0, 2, 4, 6$ . For conversion to Stevens parameters  $B_k^m$  see footnote on page 59. Note that Stevens parameters will not yield the  $J=7/2$  contributions to the wave functions listed in Table 3.1.

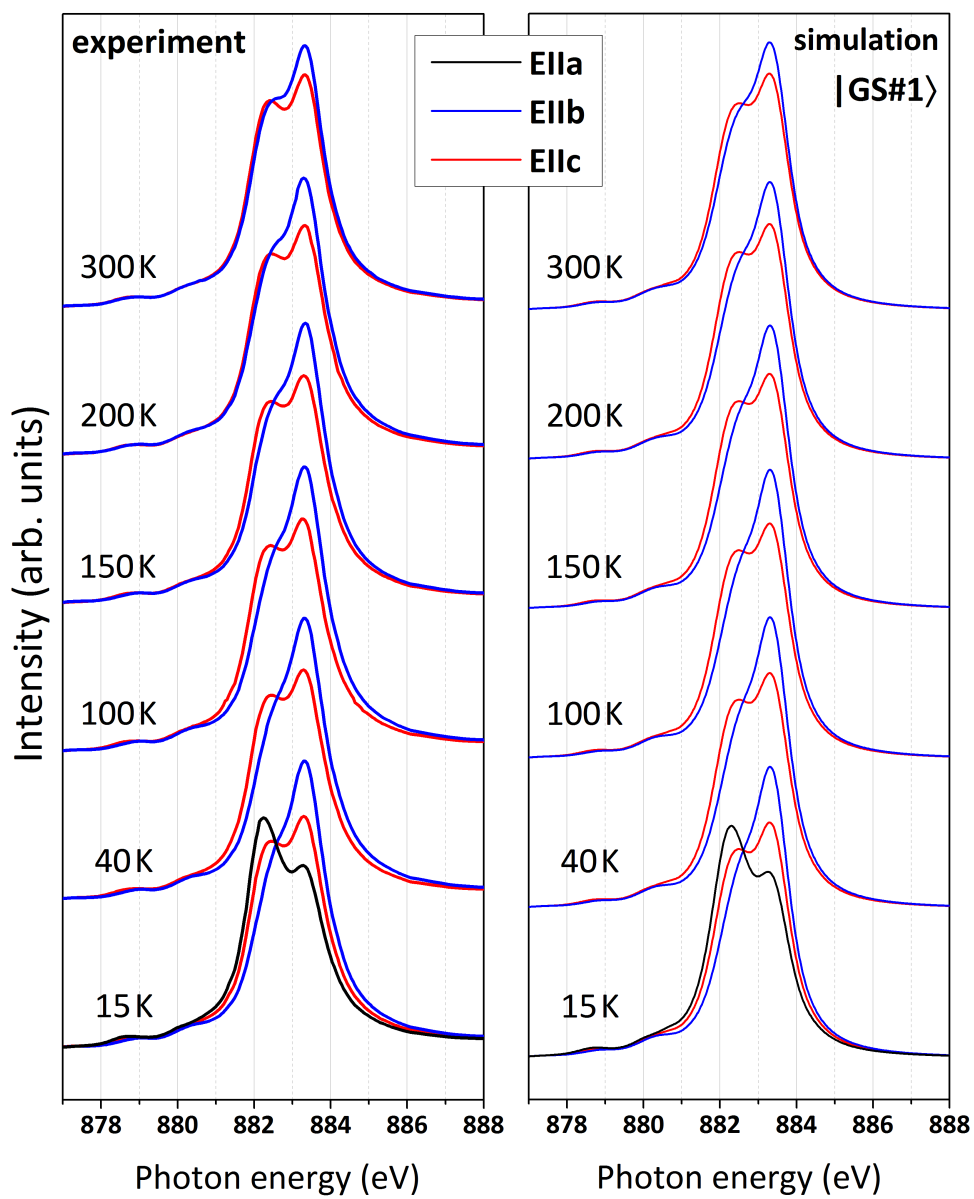


Figure 3.2: Left panel: Measured temperature-dependent XAS spectra of  $CeRu_2Al_{10}$  at the  $M_5$  edge. Right panel: Simulation of the  $M_5$  edge temperature dependence for  $|GS\#1\rangle$ . The spectra for  $|GS\#2\rangle$  show the same behavior and are omitted.

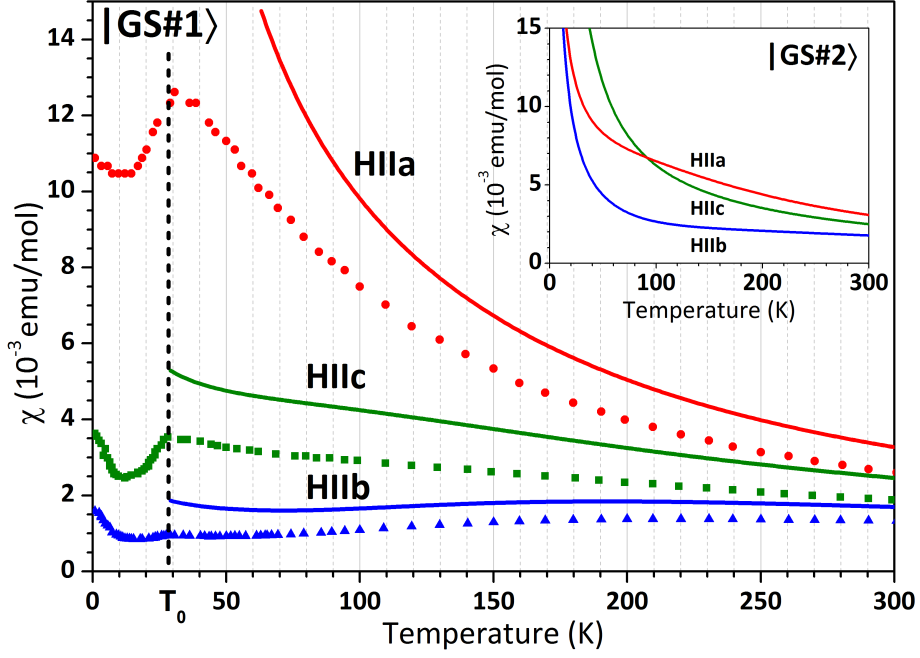


Figure 3.3: Comparison of the experimental magnetic susceptibility of  $\text{CeRu}_2\text{Al}_{10}$  as reported by Ref. [15] (symbols) and the simulated ones ( $T > T_0$ ) from the CEF parameter sets belonging to  $|\text{GS}\#1\rangle$  (lines in the main panel) and  $|\text{GS}\#2\rangle$  (inset).

The combined analysis of XAS and INS data still does not yield a unique solution for the ground-state wave function. We therefore calculate the temperature dependence of the static susceptibility at  $H = 1$  T in all three crystallographic directions and compare it to the experimental results found by Yutani *et al.* [15]. For this purpose the full Hamiltonian, including the crystal field, the magnetic field and the spin-orbit coupling, is diagonalized and the magnetization is calculated as the Boltzmann-weighted expectation value of the corresponding operator to obtain  $\chi_{\text{CEF}}^{\nu}$  ( $\nu = a, b, c$ ). The simulation for  $|\text{GS}\#1\rangle$  is plotted in the main panel of Fig. 3.3 (lines) together with the data points taken from Ref. [15]. The simulation for  $|\text{GS}\#2\rangle$  is included as an inset. For  $|\text{GS}\#1\rangle$  both the anisotropy and the qualitative temperature evolution are nicely reproduced for  $T > T_0$ . The  $|5/2, J_z\rangle$  contributions of solution  $|\text{GS}\#1\rangle$  agree quite well with the CEF analysis in Stevens approximation by Yutani *et al.* [15] and theoretical studies by Hanzawa who determined the  $4f$  level structure of  $\text{CeRu}_2\text{Al}_{10}$  in a point-charge model [16]. Note that Hanzawa uses the  $b$  axis as quantization axis. The change of coordinate system from  $abc \parallel yzx$  to  $abc \parallel xyz$  can be carried out according to Ref. [38]. In contrast, solution  $|\text{GS}\#2\rangle$  does not match the measured susceptibility well. It yields a crossover of  $\chi_{\text{CEF}}^a$  and  $\chi_{\text{CEF}}^c$  at about 100 K so that we exclude it as a possible ground-state wave function.

The CEF ground-state wave function  $|\text{GS}\#1\rangle$  yields the magnetic moments  $\mu_{\text{CEF}}^{a,b,c} = (1.44, 0.19, 0.38) \mu_{\text{B}}$ . Here an infinitesimal small temperature and magnetic field along the respective directions  $a$ ,  $b$ , or  $c$  have been taken into account. These moments agree very well with values from magnetization at 55 T and 1.3 K, which find 1.3 and  $0.3 \mu_{\text{B}}$  along the easy axis  $a$  and the

ordering axis  $c$ , respectively [20]. Also, the small moment of  $\mu_{\text{CEF}}^c = 0.38 \mu_{\text{B}}$  agrees well with the experimental findings for the ordered magnetic moment [7–9, 11], indicating that CEF effects are responsible for the small size of  $\mu_{\text{ord}}$ .

The remaining discrepancy between the measured and CEF-only susceptibility  $|\text{GS}\#1\rangle$  in Fig. 3.3 can be explained by considering corrections due to molecular and/or exchange fields and anisotropic hybridization between  $4f$  and conduction electrons. Such an anisotropic hybridization has been observed in optical conductivity measurements [13] and the resulting anisotropic Kondo interactions will affect the anisotropy of the static susceptibility.

## 3.4 Conclusion

In conclusion, the full multiplet simulation yields two GS wave functions which reproduce the low-temperature XAS data very well. By combining our XAS with susceptibility results [15] we unambiguously identify  $|\text{GS}\#1\rangle$  (see Table 3.1) as the GS wave function for  $\text{CeRu}_2\text{Al}_{10}$ , which is in good accordance with the theoretical findings by Hanzawa [16]. We can further give a set of CEF parameters that satisfies XAS, susceptibility, and INS data [22], and the resulting moments are in accordance with moments from magnetization measurements [20]. The fact that the CEF-only moment along  $c$  amounts to only  $\mu_{\text{CEF}}^c = 0.38 \mu_{\text{B}}$  implies that the small value of the ordered moment [7–9, 11] can be explained solely with CEF effects. The absence of any temperature dependence in the XAS data up to 100 K confirms that the excitation at 8 meV in the inelastic neutron spectra [9] is not a CEF transition. The above results show that the selection rules for linear polarized light make soft XAS a powerful tool to determine the CEF ground state wave function of orthorhombic Kondo insulators even in the presence of spin gaps.

This work was supported by DFG grant AOBJ 583872, Germany and KAKENHI No. 20102004 of MEXT, Japan.

## 4 Crystal-field ground state of the orthorhombic Kondo semiconductors $\text{CeOs}_2\text{Al}_{10}$ and $\text{CeFe}_2\text{Al}_{10}$

Phys. Rev. B **87**, 125119 (2013)

*This chapter is published as Phys. Rev. B **87**, 125119 (2013). A. Severing supervised the project and guided the experiments, the scientific discussion and the publication process. The single-crystalline samples were synthesized and provided by Y. Muro, K. Yutani and T. Takabatake. The sample preparation and the experimental planning were carried out by T. Willers and myself. The technical support during the experiments was provided by the beamline scientists Y.-Y. Chin, H.-J. Lin, T. W. Pi and C. T. Chen at the NSRRC, and E. Weschke and E. Schierle at BESSY II. T. Willers, Z. Hu, S. Agrestini, C.-Y. Kuo and myself constituted the experimental teams and performed the experiments. The program code for the data simulation was provided by A. Tanaka. Further assistance for the calculations incl. the use of the 'Mathematica Crystal Field Package' was provided by M. W. Haverkort. Scientific discussion took place with L. H. Tjeng. The analysis/interpretation of the data and the writing of the manuscript were performed by myself.*

### Abstract

Here we present linear-polarization-dependent soft x-ray absorption spectroscopy data at the Ce  $M_{4,5}$  edges of  $\text{CeOs}_2\text{Al}_{10}$  and  $\text{CeFe}_2\text{Al}_{10}$ . Despite the strong hybridization between  $4f$  and conduction electrons and the existence of spin gaps as seen in inelastic neutron scattering, we were able to determine the crystal-field ground-state wave functions by combining our spectroscopy data with magnetization measurements. The results quantitatively explain the small ordered moment along  $c$  and the measured magnetic moment along the easy  $a$  axis in  $\text{CeOs}_2\text{Al}_{10}$ .

### 4.1 Introduction

Among the strongly correlated electron systems, the Ce-based intermetallic compounds are known to possess many interesting and anomalous phenomena. The  $\text{Ce}M_2\text{Al}_{10}$  compounds with  $M = \text{Ru}, \text{Os},$  and  $\text{Fe}$  belong to a fairly new family of cerium Kondo semiconductors which gained considerable prominence for their unusual high magnetic ordering temperatures of  $T_0 = 27 \text{ K}$  ( $\text{CeRu}_2\text{Al}_{10}$ ) and  $29 \text{ K}$  ( $\text{CeOs}_2\text{Al}_{10}$ ) [3, 4]. This novel phase transition is, for example, observed in the electrical resistivity, the specific heat, and the magnetization, and several scenarios have been discussed to explain the origin of the magnetic order [3–16, 18–21, 36, 39–45]. Isostructural  $\text{CeFe}_2\text{Al}_{10}$  lacks any phase transition and shows the highest degree of hybridization between  $4f$  and conduction electrons ( $c$ - $f$  hybridization) within the family [4, 46–51].

The static magnetic susceptibility of these orthorhombic compounds (space group  $Cmcm$ ) is very anisotropic with  $\chi_a > \chi_c > \chi_b$  [4, 15, 36, 39, 51]. This is mainly due to crystalline electric field (CEF) effects. The susceptibility along the  $b$  and  $c$  axis is only weakly temperature-dependent in all three composites. The temperature dependence of the susceptibility along the easy  $a$  axis shows that the Kondo effect becomes more pronounced from  $M = Ru$  to  $Os$  to  $Fe$ : In  $CeRu_2Al_{10}$   $\chi_a$  is Curie-Weiss-like and drops sharply at the ordering transition at 27 K, whereas in  $CeOs_2Al_{10}$  and  $CeFe_2Al_{10}$  it undergoes a broad maximum at  $T_{max} \approx 45$  and 70 K, respectively, and shows enhanced Pauli paramagnetism at low temperatures. The absolute magnitude of  $\chi_a$  and  $\chi_c$  in  $CeFe_2Al_{10}$  is about half as much as in the  $Ru$  and  $Os$  compound.  $CeFe_2Al_{10}$  is therefore classified as an intermediate valence system [46].

Inelastic neutron scattering (INS) experiments have found spin gaps of 8 meV ( $Ru$ ) and 11 meV ( $Os$ ) in the ordered state [9, 40]. The long-range nature of the antiferromagnetic order in the  $Ru$  and  $Os$  compound has been confirmed by  $\mu SR$  and neutron diffraction experiments. However, the mechanism of the ordering remains puzzling [7–9, 11, 12, 40] because the  $Ce$ - $Ce$  distances of more than 5 Å in the cage-like crystal structure [1, 2] are very large and it is not easy to understand quantitatively the high ordering temperatures in the context of Ruderman-Kittel-Kasuya-Yosida exchange interactions. Further, the ordering temperatures are too high according to the de Gennes scaling from the  $Gd$  equivalents [4].

In  $CeM_2Al_{10}$  the  $J = 5/2$  and  $7/2$  multiplets of  $Ce^{3+}$  split into seven Kramer's doublets under the influence of an orthorhombic crystal field (point group  $C_{2v}$ ). In the basis of  $|J, J_z\rangle$  each of these states has the general form

$$\sum_{J_z = -\frac{5}{2}, -\frac{3}{2}, \dots, \frac{5}{2}} \alpha_{J_z} |5/2, J_z\rangle + \sum_{J_z = -\frac{7}{2}, -\frac{5}{2}, \dots, \frac{7}{2}} \beta_{J_z} |7/2, J_z\rangle \quad (4.1)$$

for values of  $J_z$  which fulfill  $\sum_{J_z} (\alpha_{J_z}^2 + \beta_{J_z}^2) = 1$  and  $\Delta J_z = \pm 2$ . The CEF ground-state (GS) wave function of the  $4f$  electrons in  $CeRu_2Al_{10}$  has been successfully determined in a previous study [52].<sup>1</sup> In the present work the investigation of the crystal-field GS is extended to the other two members of the compound family. The  $4f$  GS wave functions are expected to be highly anisotropic due to the presence of the CEF in the orthorhombic  $YbFe_2Al_{10}$ -type structure. The importance of CEF effects on ground state properties has been discussed in Ref. [52] (and references therein). As shown for the case of  $CeRu_2Al_{10}$ , linearly polarized x-ray absorption spectroscopy (XAS) at the  $Ce M_{4,5}$  edge is a powerful technique for determining CEF GS wave functions in orthorhombic Kondo semiconductors with spin gaps. The selection rules of linear polarized light yield the sensitivity to the initial state symmetry.

## 4.2 Experimental and theoretical details

Single crystals of  $CeOs_2Al_{10}$  and  $CeFe_2Al_{10}$  were grown by an Al self-flux method [36, 51] and their quality and orientation were confirmed by Laue x-ray diffraction. The XAS measurements were carried out at the synchrotron light sources BESSY II of the Helmholtz-Zentrum Berlin in Germany (undulator beamline UE46-PGM1) and the National Synchrotron Radiation Research

<sup>1</sup>Ref. [52] is included as Chapter 3 in this thesis.

Center (NSRRC) in Taiwan (Dragon bending magnet beamlines BL08A1 and BL11A1). The energy resolution at the Ce  $M_{4,5}$  edge ( $h\nu \approx 870 - 910$  eV) was about 0.15 eV (BESSY II) and 0.4 eV (NSRRC) and the crystals were cleaved *in situ* in a vacuum of  $\sim 10^{-10}$  mbar. Further details about the technical conditions and measurement procedure can be found in Ref. [52].

In cerium heavy fermion/Kondo compounds, where the well localized  $4f$  electrons hybridize with the conduction electrons, the ground (initial) state is a mixture of the configurations  $4f^0$ ,  $4f^1$ , and  $4f^2$  [53, 54]. However, typically the spectral weights in the XAS  $M$  edges due to the  $4f^0$  and  $4f^2$  initial configurations are minor with respect to  $4f^1$  (see below) and the  $3d \rightarrow 4f$  absorption is well characterized by atomic-like transitions into multiplet-split final states [53]. We therefore performed the same ionic full multiplet simulations for the data analysis as for CeRu<sub>2</sub>Al<sub>10</sub> [52] using the XTLS 8.3 program [37]. Reference [32] points out why for crystal-field purposes the ionic approach is preferable over the Anderson impurity model as long as the crystal-field splittings are large with respect to the Kondo temperature – something still valid for the two compounds under investigation in this work. Our ionic calculations comprise the intra-atomic  $4f$ - $4f$  and  $3d$ - $4f$  Coulomb interactions, the  $3d$  and  $4f$  spin-orbit coupling and the CEF parameters, which reflect the full symmetry of the ligand field surrounding the Ce ion. Hybridization or band effects are not included.

For the simulations the atomic parameters are adjusted at first, i.e. the Hartree-Fock values were reduced to reproduce the experimental isotropic spectra  $I_{\text{isotropic}} = I_{E\parallel a} + I_{E\parallel b} + I_{E\parallel c}$ . The reduction amounts to about 40 % for the  $4f$ - $4f$  and to about 20 % for the  $3d$ - $4f$  Coulomb interactions and accounts for the configuration interaction effects not included in the Hartree-Fock scheme. Subsequently, we used the coherent approach as described in Ref. [52] to simulate the low temperature XAS spectra, i.e. the relative size of the CEF parameters was varied to reproduce the anisotropy of the XAS data. It should be noted that for the CEF GS wave function only the *relative* size of the CEF parameters matters as long as the CEF energy splitting is small enough with respect to the spin-orbit splitting ( $\Delta E_{\text{SO}} = 280$  meV). The *absolute* size of the CEF parameters determines the size of the CEF splittings, which here only enter via thermal population when simulating the temperature evolution of the linear polarization (linear dichroism LD). For the simulation of the CEF-only static susceptibility for CeOs<sub>2</sub>Al<sub>10</sub> we assumed energy splittings of  $\Delta E_1 \approx 38$  meV and  $\Delta E_2 \approx 63$  meV between the GS and the first and second excited CEF doublet, respectively, and for CeFe<sub>2</sub>Al<sub>10</sub> a quasiquartet at about 51 meV. These numbers are based on INS data by Adroja *et al.* [55]

### 4.3 Results and discussion

In Fig. 4.1 the low-temperature linearly polarized XAS spectra of CeOs<sub>2</sub>Al<sub>10</sub> and CeFe<sub>2</sub>Al<sub>10</sub> are shown (bottom curves in the top and bottom panels). Due to the orthorhombic point symmetry of cerium in these compounds all three polarizations, i.e. for the incoming light polarized  $E \parallel a$ ,  $E \parallel b$ , and  $E \parallel c$ , were measured [52]. We know that at 15 and 20 K only the ground state is probed, because INS finds CEF excitations above 30 meV energy transfer [55]. Both compounds exhibit a strong polarization effect which can be simulated with the full multiplet routine. As for CeRu<sub>2</sub>Al<sub>10</sub> there are only two solutions describing the threefold anisotropy of the measured low-temperature linearly polarized XAS spectra [56], which in the following are referred to

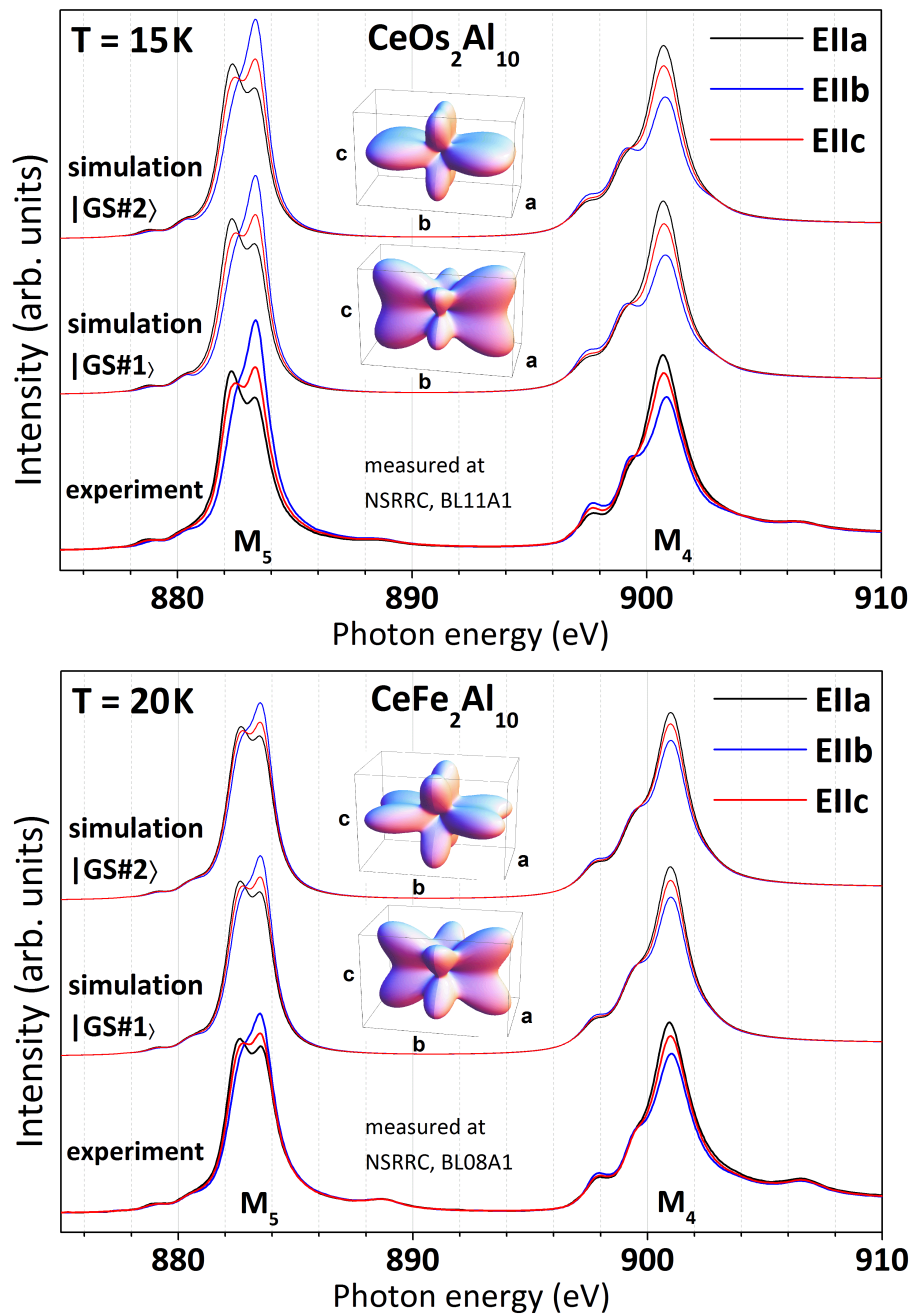


Figure 4.1: Experimental low-temperature linearly polarized soft x-ray absorption data of  $CeOs_2Al_{10}$  (bottom curves in the top panel) and  $CeFe_2Al_{10}$  (bottom curves in the bottom panel) at the  $M_{4,5}$  absorption edge. The middle and top set of spectra in each panel represent the two simulations which reproduce the experimental data. For both CEF ground states,  $|GS\#1\rangle$  and  $|GS\#2\rangle$ , the corresponding spatial distributions of the  $4f$  electrons are included as insets.

Table 4.1: The  $J_z$  coefficients  $\alpha_{J_z}$  and  $\beta_{J_z}$  describing the wave functions of the crystal-field GS Kramer's doublets for solution No.1. The wave functions have been calculated with the full multiplet routine, using  $c$  as the quantization axis.

$ J, J_z\rangle$	GS#1⟩	
	CeOs <sub>2</sub> Al <sub>10</sub>	CeFe <sub>2</sub> Al <sub>10</sub>
$ 5/2, \pm 5/2\rangle$	$\pm 0.48(2)$	$\pm 0.44(2)$
$ 5/2, \pm 1/2\rangle$	$\pm 0.27(2)$	$\pm 0.15(2)$
$ 5/2, \mp 3/2\rangle$	$\pm 0.83(2)$	$\pm 0.88(2)$
$ 7/2, \pm 5/2\rangle$	$\mp 0.06(1)$	$\mp 0.07(1)$
$ 7/2, \pm 1/2\rangle$	$\pm 0.00(1)$	$\pm 0.01(1)$
$ 7/2, \mp 3/2\rangle$	$\mp 0.04(1)$	$\mp 0.03(1)$
$ 7/2, \mp 7/2\rangle$	$\pm 0.02(1)$	$\pm 0.01(1)$

as |GS#1⟩ and |GS#2⟩. Both solutions are mainly composed of the  $J = 5/2$  multiplet. Some minor admixtures come from the higher  $J = 7/2$  multiplet, however, their effect on the LD is negligible and cannot be seen in the spectra when changing into Stevens approximation [52]. The respective  $4f$  orbitals for the solutions |GS#1⟩ and |GS#2⟩ are shown as insets. In the dipole limit the two  $4f$  distributions look the same so that a technique which is governed by dipole transitions – such as XAS – yields identical spectra for both orbitals.

We follow the same path as in CeRu<sub>2</sub>Al<sub>10</sub> and are able to discard one solution (|GS#2⟩) by calculating the temperature dependence of the static susceptibility at  $H = 1$  T in all three crystallographic directions and compare it to the experimental results found by Muro *et al.* [36, 51]. The simulations for the |GS#1⟩ scenario are plotted in the main panel of Fig. 4.2 (lines) together with the data points taken from Ref. [36] and [51]. The simulations for the |GS#2⟩ model are included as an inset. For CeOs<sub>2</sub>Al<sub>10</sub> the |GS#1⟩ scenario reproduces nicely the anisotropy and the qualitative temperature evolution for  $T > T_0$ . This is not the case for the CEF model based on |GS#2⟩. It yields a crossover of  $\chi_{\text{CEF}}^a$  and  $\chi_{\text{CEF}}^c$  at about 120 K and does not match the measured susceptibility. We therefore exclude it as a possible GS wave function. For CeFe<sub>2</sub>Al<sub>10</sub> the general anisotropy is also reproduced by the |GS#1⟩ scenario, whereas the |GS#2⟩ model produces intersections between  $\chi_{\text{CEF}}^a$  and the susceptibilities along the other two axes. The remaining discrepancy between the measured and CEF-only susceptibility |GS#1⟩ in Fig. 4.2 can be reduced by considering corrections due to molecular and/or exchange fields and anisotropic hybridization effects. Such an anisotropic  $c$ - $f$  hybridization has indeed been observed in optical conductivity measurements [13, 14, 50] and also the anisotropic spin dynamics as observed in INS on CeRu<sub>2</sub>Al<sub>10</sub> point in this direction [45]. These anisotropic Kondo interactions will affect the anisotropy of the static susceptibility more, the stronger the Kondo effect is. Hence it is not surprising that for CeFe<sub>2</sub>Al<sub>10</sub> the discrepancy between the calculated CEF-only susceptibility based on the |GS#1⟩ scenario is larger than in the Os and Ru [52] samples. This goes along with Hanzawa's findings for the Ru and Os compound that including  $4f$ - $5d$  mixing improves the agreement between calculated and measured susceptibility, and with his suggestion that in the Fe sample this intermixing is so large that the magnetic order is suppressed [16].

Using the  $c$  axis as the quantization axis, the corresponding  $J_z$  coefficients of solution |GS#1⟩ are as listed in Table 4.1. We find a very strong  $|5/2, \mp 3/2\rangle$  contribution for both compounds which is in agreement with susceptibility simulations by Yutani *et al.* [15] and theoretical studies

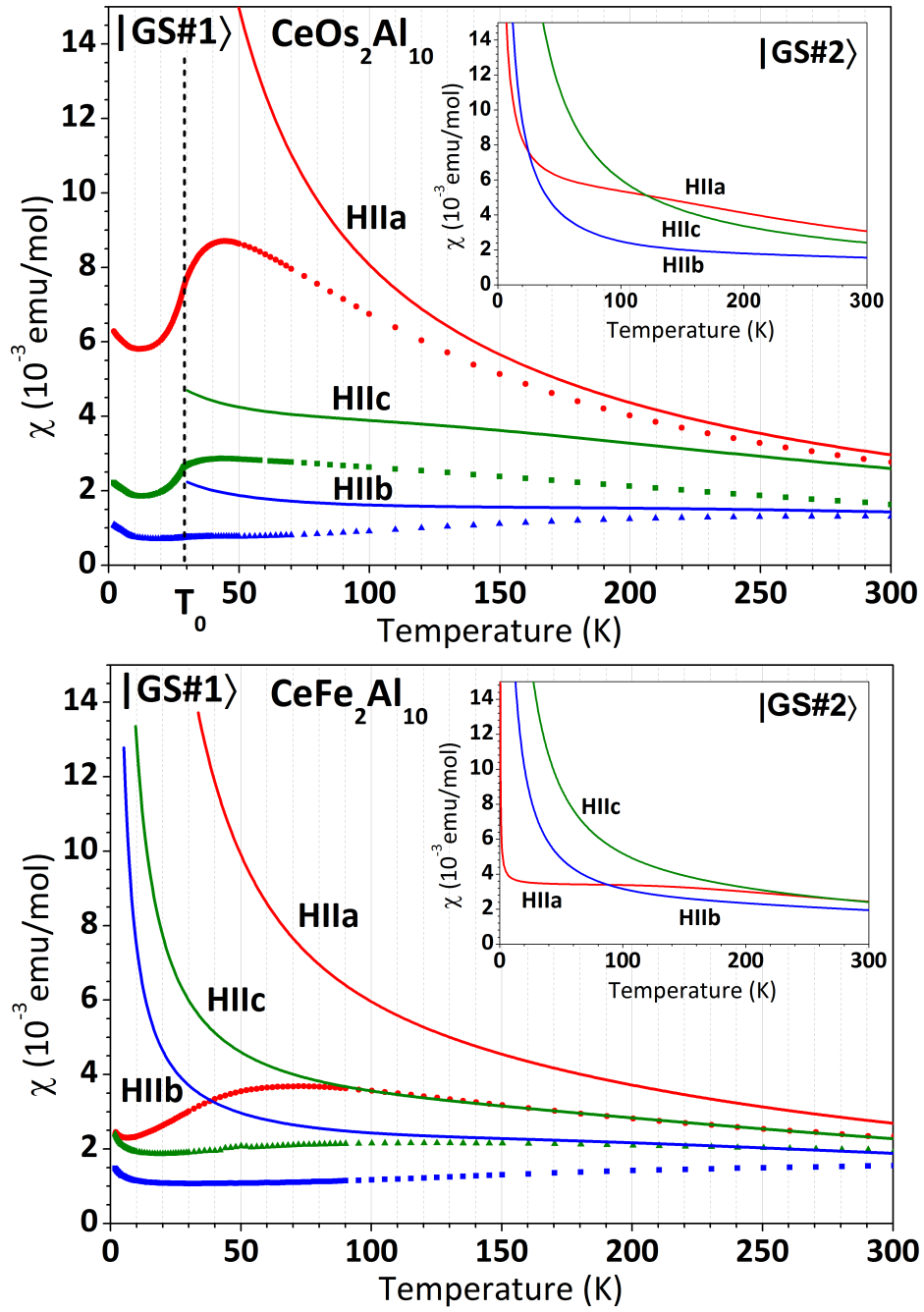


Figure 4.2: Temperature dependence of the static susceptibility adapted from Refs. [36] and [51] (symbols) and calculated from the two CEF models  $|GS\#1\rangle$  (lines in main panel) and  $|GS\#2\rangle$  (lines in insets).

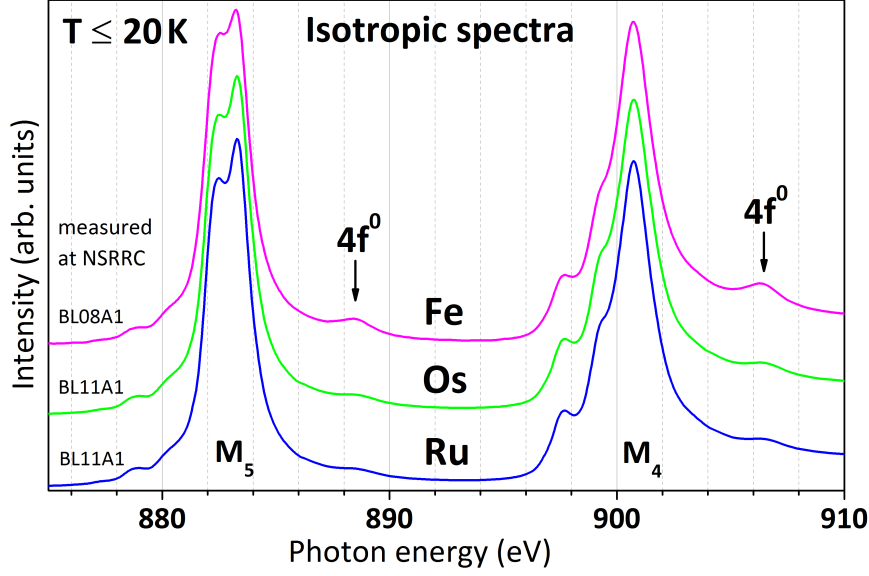


Figure 4.3: Experimental isotropic low-temperature XAS spectra  $I_{\text{isotropic}} = I_{E\parallel a} + I_{E\parallel b} + I_{E\parallel c}$  of  $\text{CeRu}_2\text{Al}_{10}$ ,  $\text{CeOs}_2\text{Al}_{10}$ , and  $\text{CeFe}_2\text{Al}_{10}$  at the  $M_{4,5}$  absorption edge. The arrows mark the absorption intensities due to the  $4f^0$  contribution in the ground state.

by Hanzawa [16], who determined the  $4f$  level structure of  $\text{CeOs}_2\text{Al}_{10}$  in a point-charge model.<sup>2</sup> Assuming the CEF splittings mentioned above, we obtain the CEF parameters as summarized in Table 4.2.

The CEF GS wave function  $|\text{GS}\#1\rangle$  yields the magnetic moments  $\mu_{\text{CEF}}^{a,b,c} = (1.35, 0.27, 0.30) \mu_{\text{B}}$  and  $(1.02, 0.39, 0.53) \mu_{\text{B}}$  for the Os and Fe samples, respectively. An infinitesimal small temperature and magnetic field along the respective crystallographic axes have been used to obtain these values within a single ion CEF calculation. For  $\text{CeOs}_2\text{Al}_{10}$  these CEF-only moments satisfactorily agree with the moment along the easy  $a$  axis as found in high field magnetization measurements,  $\mu_{H=55\text{T}}^a \approx 0.95 \mu_{\text{B}}$  [42], and the ordered magnetic moment along  $c$  determined

<sup>2</sup>Note: Hanzawa uses the  $b$  axis as the quantization axis.

$ \text{GS}\#1\rangle$	$\check{A}_2^0$	$\check{A}_2^2$	$\check{A}_4^0$	$\check{A}_4^2$	$\check{A}_4^4$
$\text{CeOs}_2\text{Al}_{10}$	42(5)	44(2)	160(8)	3(10)	-81(4)
$\text{CeFe}_2\text{Al}_{10}$	4(8)	19(2)	154(5)	7(10)	-103(5)

Table 4.2: Crystal-field parameters  $\check{A}_k^m$  in meV from full multiplet calculations. For definition and conversion to Stevens parameters  $B_k^m$  see footnote on page 59. Note that Stevens parameters by definition do not include the  $J = 7/2$  contributions to the wave functions listed in Table 4.1.

with neutron diffraction and  $\mu\text{SR}$ ,  $\mu_{\text{ord}}^c = 0.20 \mu_{\text{B}}$  [40]. For the Fe compound there are no values of the moments available from other techniques.

Figure 4.3 shows the experimental low-temperature isotropic spectra, constructed from  $I_{\text{isotropic}} = I_{E\parallel a} + I_{E\parallel b} + I_{E\parallel c}$ , of the three compounds  $\text{CeRu}_2\text{Al}_{10}$ ,  $\text{CeOs}_2\text{Al}_{10}$ , and  $\text{CeFe}_2\text{Al}_{10}$ . There are two strong absorption edges due to the transitions  $3d^{10}4f^1 \rightarrow 3d_{5/2}^9 4f^2$  ( $M_5$ ) and  $3d^{10}4f^1 \rightarrow 3d_{3/2}^9 4f^2$  ( $M_4$ ), and in addition some small humps at about 888 and 906 eV (see arrows) which are due to the  $4f^0$  contribution in the ground state. The  $4f^0$  amount is very small in  $\text{CeRu}_2\text{Al}_{10}$ , only slightly increased in the Os sample, but rather pronounced in the Fe compound. The  $4f^0$  contribution increases relatively as 1 to 1.4 to 3.8 from Ru to Os, and Fe. Here the  $f^0$  amounts have been determined by integration over the range of the  $4f^0$  humps after subtracting a linear background (see Ref. [35]). This trend agrees with findings from static susceptibility, i.e. that the  $c$ - $f$  hybridization increases from  $M = \text{Ru}$  to Os and is largest for Fe.

We have shown that the  $c$ - $f$  hybridization is reflected in the XAS data as small  $4f^0$  spectral weights. Hence, the question arises whether the presence of some  $4f^0$  contribution in the ground state has an impact on the validity of the CEF-only interpretation. Here the temperature dependence of the linear dichroism can give further insight. Figure 4.4 shows the  $M_5$  edge of the Os and Fe compound for several temperatures. For reasons of clarity only two polarizations are shown. The magnetic ordering and Kondo temperatures as estimated from the maximum in the static susceptibility [ $T_{\text{K}} \approx 3 T_{\text{max}}$  of  $\chi_a(T)$ ] are marked with red arrows. For the Os sample the polarization shows no temperature effect below 150 K, i.e. as in  $\text{CeRu}_2\text{Al}_{10}$  neither the magnetic ordering transition nor the spin gap has an impact on the polarization. Only for  $T \geq 150$  K the polarization decreases slightly. When cooling again below 150 K the polarization recovers.

The absence of a temperature effect across the magnetic ordering transition has been reported previously [35, 52]. It can be understood when considering that the Zeeman splitting of the Kramer's doublets due to the magnetic order is small with respect to the large CEF splittings. Consequently the two states of the Kramer's doublets remain unchanged. Moreover, the two states of a Kramer's doublet are identical so that they give rise to the same LD. The slight change of LD in the  $\text{CeOs}_2\text{Al}_{10}$  data when warming up from 100 to 150 K can be understood in two ways: At 150 K the population of the first excited CEF level at 38 meV amounts to  $\sim 5\%$ , i.e. the change in the LD could be purely explained by the population of an excited CEF state. However, if the variation of the LD was due to the Kondo effect or a mixture of Kondo and the population of a higher state, how large would be the mistake by applying a CEF-only analysis? At 150 K the system is in the single ion regime and through thermal population the first excited CEF state contributes  $\sim 5\%$  to the signal. Consequently the 150 K data contain 95% of the CEF ground-state anisotropy. This sets an upper limit for the mistake caused by ignoring the  $c$ - $f$  hybridization in the simulation of the low-temperature data. Also in the Fe compound the population of the excited CEF levels could account for the temperature dependence of the polarization. However, following the same line of thought as for Os we find that the 200 K data ( $T \geq T_{\text{K}}$ ) contain 90% of the ground-state polarization. We are still able to describe the low-temperature anisotropy in terms of a CEF-only model, although the potential error due to neglecting the hybridization is larger than for  $\text{CeOs}_2\text{Al}_{10}$ .

We note that for the present compounds linearly polarized soft XAS is able to describe the initial state symmetry in terms of a CEF model despite the presence of a strong Kondo effect.

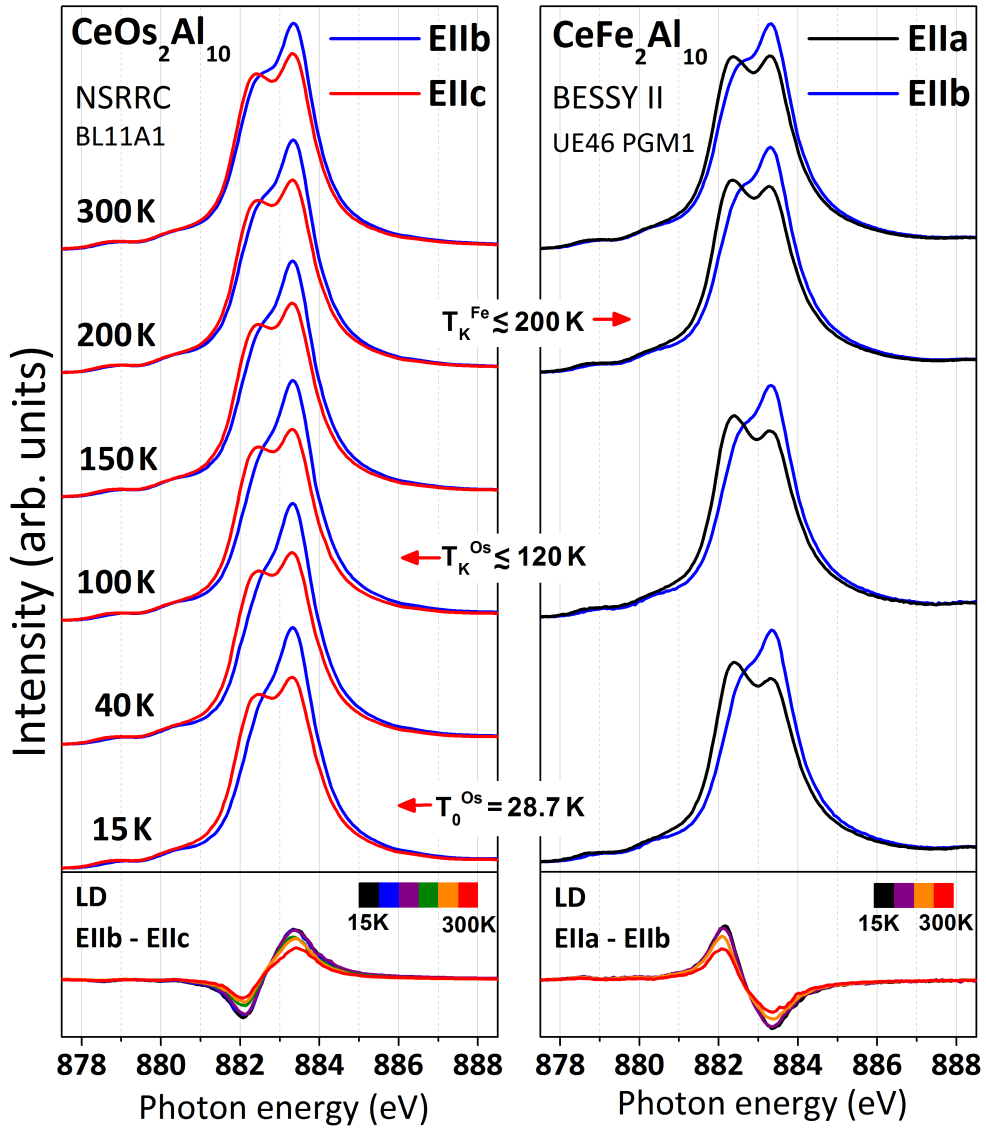


Figure 4.4: Measured temperature-dependent x-ray absorption spectra of  $\text{CeOs}_2\text{Al}_{10}$  (left) and  $\text{CeFe}_2\text{Al}_{10}$  (right) at the  $M_5$  edge. The bottom panels show the respective LD for each temperature. The magnetic ordering and Kondo temperatures as estimated from the maximum in the static susceptibility along the crystallographic  $a$  axis  $\chi_a(T)$  ( $T_K \lesssim 3T_{\text{max}}$ ) are marked with red arrows.

This is in contrast to INS, where the magnetic excitations suffer from strong intrinsic broadening due to strong  $c$ - $f$  hybridization such that it becomes hard to separate CEF excitations from the strong phonon background. For the present class of compounds the spin gap aggravates the problem to determine wave functions from the relative spectral weights of the magnetic quasi- and inelastic scattering in the INS data. Hence soft XAS is a very useful complementary method.

## 4.4 Conclusion

To summarize, we are able to give CEF GS wave functions for the two orthorhombic Kondo insulators CeOs<sub>2</sub>Al<sub>10</sub> and CeFe<sub>2</sub>Al<sub>10</sub> from a combined analysis of linearly polarized soft XAS and static susceptibility data [36, 51]. The analysis is not hampered by the spin gaps which have been found in INS and the CEF description can be applied despite the strong  $c$ - $f$  hybridization in these compounds. In CeOs<sub>2</sub>Al<sub>10</sub> the small ordered moment along the  $c$  direction can be explained with CEF effects only, something we also found for CeRu<sub>2</sub>Al<sub>10</sub> [52]. However, the difference between the CEF-only moment and the actual ordered moment might well be due to Kondo screening.

We thank D. T. Adroja for providing the unpublished CEF energies of CeOs<sub>2</sub>Al<sub>10</sub> and CeFe<sub>2</sub>Al<sub>10</sub>. This work was supported by Deutsche Forschungsgemeinschaft Grant No. 583872, Germany and KAKENHI No. 20102004 of MEXT, Japan.

## 5 Quantitative study of valence and configuration interaction parameters of the Kondo semiconductors $\text{CeM}_2\text{Al}_{10}$ ( $M = \text{Ru}, \text{Os}, \text{Fe}$ ) by means of bulk-sensitive hard x-ray photoelectron spectroscopy

J. Electron Spectrosc. Relat. Phenom. **199**, 56 (2015)

*This chapter is published as J. Electron Spectrosc. Relat. Phenom. 199, 56 (2015). A. Severing supervised the project and guided the experiment, the scientific discussion and the publication process. The single-crystalline samples were synthesized and provided by Y. Muro, K. Yutani and T. Takabatake. The sample preparation and the experimental planning were carried out by myself. K.-D. Tsuei and Y. F. Liao were the responsible beamline scientists at SPring-8 for the technical support during the experiment. A. Severing and L. H. Tjeng performed the experiment. The program code for the data simulation was provided by A. Tanaka and extended by M. Sundermann. Further assistance for the calculations came from M. W. Haverkort. Scientific discussion took place with P. Thalmeier and L. H. Tjeng. The analysis/interpretation of the data and the writing of the manuscript were performed by myself.*

### Abstract

The occupancy of the  $4f^n$  contributions in the Kondo semiconductors  $\text{CeM}_2\text{Al}_{10}$  ( $M = \text{Ru}, \text{Os}$  and  $\text{Fe}$ ) has been quantitatively determined by means of bulk-sensitive hard x-ray photoelectron spectroscopy (HAXPES) on the Ce  $3d$  core levels. Combining a configuration interaction scheme with full multiplet calculations allowed to accurately describe the HAXPES data despite the presence of strong plasmon excitations in the spectra. The configuration interaction parameters obtained from this analysis – in particular the hybridization strength  $V_{\text{eff}}$  and the effective  $f$  binding energy  $\Delta_f$  – indicate a slightly stronger exchange interaction in  $\text{CeOs}_2\text{Al}_{10}$  compared to  $\text{CeRu}_2\text{Al}_{10}$ , and a significant increase in  $\text{CeFe}_2\text{Al}_{10}$ . This shows the existence of a substantial amount of Kondo screening in these magnetically ordered systems and places the entire  $\text{CeM}_2\text{Al}_{10}$  family in the region of strong exchange interactions.

### 5.1 Introduction

In cerium compounds the localized  $f$  electrons of the  $4f$  shell interact with the surrounding conduction electrons which leads to a screening of the localized  $f$  spins (Kondo effect) as well as to an indirect Ruderman-Kittel-Kasuya-Yosida (RKKY) exchange interaction between the local spins. The latter leads to magnetic order with localized spins, the former to a non-magnetic

ground state with partially delocalized  $f$  electrons. The competition between these two effects governs the physics of Kondo lattice materials and is described in the Doniach phase diagram [57]. According to this phase diagram magnetically ordered ground states with localized  $4f$  moments are expected in materials with small exchange interaction  $J_{ex}$  and non-magnetic ones when  $J_{ex}$  is large. A consequence of the hybridization between  $f$  and conduction electrons is the opening of a hybridization gap close to the Fermi energy. In some of these compounds the Fermi energy falls into this gap so that the materials exhibit Kondo insulating, semiconducting or semimetallic behavior, depending on the gap structure (e.g. CeNiSn, CeBi<sub>4</sub>Pt<sub>3</sub>) [58]. The members of the  $CeM_2Al_{10}$  family are classified as Kondo semiconductors with narrow, anisotropic gaps of the order of a few meV [4, 10, 36, 46, 48, 49].

In  $CeFe_2Al_{10}$  Kondo screening appears large and the ground state is non-magnetic [4, 13, 46, 48, 49]. However, the members with  $M = Ru$  and  $Os$  exhibit antiferromagnetic order at fairly high temperatures of  $T_N = 27$  K ( $M = Ru$ ) and 29 K ( $M = Os$ ) although there are signs of a considerable amount of Kondo screening according to macroscopic and neutron measurements [3, 4, 8, 9, 40]. Keeping in mind the RKKY interaction gets weaker with increasing distance between the local moments, it is amazing that magnetic order forms at all in these compounds, in which the Ce atoms are more than 5 Å apart [1, 2], and then even at such high ordering temperatures. Following the de Gennes scaling from the Gd equivalents would imply much lower ordering temperatures [4]. The peculiarity of the magnetic order has led to a plethora of intensive studies and made the  $CeM_2Al_{10}$  compounds prominent examples for systems exhibiting unconventional order [5, 7, 11, 13, 14, 19, 21, 22, 36, 42–46, 48, 49, 51, 52, 59–74].

The Ce atoms are situated in a cage-like environment (space group  $Cmcm$ ) [1, 2] and the  $f$  electrons experience an orthorhombic crystal-electric field which is mainly responsible for the strong magnetic anisotropy  $\chi_a > \chi_c > \chi_b$  above  $T_N$  and to a large extent for the small ordered magnetic moments [4, 5, 36, 51, 52, 61]. The measured moments are only slightly reduced with respect to the crystal-field-only moments [52, 61]. Moreover, spin gaps have been found by inelastic neutron scattering for  $M = Ru$  and  $Os$  in the ordered state (8 and 11 meV) and for  $M = Fe$  in the paramagnetic state (12.5 meV) [9, 22, 40, 45]. The Kondo temperatures  $T_K$  are estimated to be 52 K and 92 K for  $M = Ru$  and  $Os$ , respectively, and beyond 300 K for  $M = Fe$  [22, 64], which in the case of the Fe compound is comparable to the expected crystal-field splitting [22].

The mechanism of the magnetic order, with its ordered moments aligned along the  $c$ -axis and not the easy axis  $a$ , is still an open question. There are some experimental and theoretical suggestions for the Kondo screening having an impact on the magnetic order [42, 60]. For example, it is meant to be strongest along the  $a$ -direction and thus responsible for the unexpected orientation of the ordered moments [42]. This seems to be consistent with the findings of the hybridization being anisotropic [14, 43, 62]. Interestingly, susceptibility measurements, muon spin relaxation and neutron diffraction show that only small amounts of electron doping with Rh or Ir – corresponding to one extra  $4d$  or  $5d$  electron in  $CeRu_2Al_{10}$  and  $CeOs_2Al_{10}$ , respectively – suppress the Kondo screening and flip the ordered moments parallel to the easy axis  $a$ , while the ordering temperatures remain almost unchanged [67–69]. On the contrary, for light hole doping in  $CeOs_2Al_{10}$  – by substituting Re for Os – the size of the ordered moments decreases significantly and their alignment along the hard axis  $c$  is maintained [70]. A Re substitution of only 5 % suppresses the magnetic order completely [71].

It is desirable to quantify the Kondo interaction because of its apparent connection with the

magnetic order. We recall that weakly hybridized Ce systems are well localized and have a valence of three ( $\text{Ce}^{3+}$ ) and a  $4f$  occupancy  $n_f = 1$  ( $f^1$ ). The presence of strong hybridization leads to a partial delocalization of the  $f$  electrons and the no longer integer-valent  $4f$  ground state can then be written as a mixed state  $|\Psi_{\text{GS}}\rangle = \alpha |f^0\rangle + \beta |f^1\underline{L}\rangle + \gamma |f^2\underline{\underline{L}}\rangle$  with additional contributions of the divalent and tetravalent states ( $f^2$  and  $f^0$ ). Here  $\underline{L}$  and  $\underline{\underline{L}}$  denote the number of ligand holes. The amount of  $f^0$  quantifies the degree of delocalization, which in the case of a moderately large  $\alpha^2$  is a synonym for the effectiveness of the Kondo screening. Core level spectroscopy techniques, like x-ray absorption or photoelectron spectroscopy (PES), are capable of seeing the different valence states because they involve the presence of a core-hole with an attractive potential which acts differently on the different  $f^n$  states. As a result the states are re-ordered energetically:  $|\underline{c}f^2\underline{\underline{L}}\rangle$  becomes the lowest configuration (with  $\underline{c}$  denoting the core hole), followed by  $|\underline{c}f^1\underline{L}\rangle$  (typically  $\Delta E_{f^1 f^2} \approx 5$  eV) and  $|\underline{c}f^0\rangle$  (typically  $\Delta E_{f^0 f^1} \approx 11$  eV), yielding three spectral features which correspond to the final states with mainly  $\underline{c}f^2\underline{\underline{L}}$ ,  $\underline{c}f^1\underline{L}$  and  $\underline{c}f^0$  character [75]. The corresponding spectral intensities  $I(\underline{c}f^0)$ ,  $I(\underline{c}f^1\underline{L})$  and  $I(\underline{c}f^2\underline{\underline{L}})$  contain information about  $\alpha^2$ ,  $\beta^2$  and  $\gamma^2$ , respectively, so that the  $f$  electron count  $n_f = \beta^2 + 2\gamma^2$  can be deduced. Note, because of hybridization effects in the final state, the spectral intensities are not directly proportional to  $\alpha^2$ ,  $\beta^2$  and  $\gamma^2$ . The translation of  $I(\underline{c}f^n)$  to the actual  $f^n$  contributions  $\alpha^2$ ,  $\beta^2$  and  $\gamma^2$  in the ground state is achieved using the full multiplet configuration interaction calculations as explained below. In the following we will use the short notation  $f^0$ ,  $f^1$  and  $f^2$  only, omitting the explicit notation of the core and ligand holes for simplicity.

We have carried out hard x-ray photoelectron spectroscopy (HAXPES) on the Ce  $3d$  core levels of  $\text{CeM}_2\text{Al}_{10}$  in order to determine the occupancy of the  $4f$  shell in  $\text{CeM}_2\text{Al}_{10}$ . Soft x-ray PES has proven to be a valuable technique for the investigation of the electronic states of rare earth compounds [76–78], but suffers from surface effects. Especially in correlated electron systems the degree of hybridization at the surface is known to be reduced with respect to the bulk [79–81]. The use of hard x-rays provides the bulk sensitivity needed to image the bulk electronic structure in these systems [81–83].

## 5.2 Experimental details

Polycrystals of  $\text{CeRu}_2\text{Al}_{10}$ ,  $\text{CeOs}_2\text{Al}_{10}$  and  $\text{CeFe}_2\text{Al}_{10}$  were synthesized by arc melting under an argon atmosphere and the sample quality and stoichiometry were confirmed by powder x-ray diffraction and electron-probe microanalysis [46]. The HAXPES measurements were performed at the Taiwan beamline BL12XU at SPring-8, Japan, with an incident photon energy of 6.47 keV and at an incidence angle of  $45^\circ$ . For the determination of  $E_{\text{F}}$  the valence band spectrum of a Au film was measured. The excited photoelectrons were collected and analyzed (MB Scientific A-1 HE) in the horizontal plane at an emission angle of  $45^\circ$  in ultrahigh vacuum with a base pressure of  $10^{-9}$  mbar. Clean sample surfaces were obtained by cleaving the polycrystals *in situ* at low temperature ( $T \leq 60$  K). Multiple single scans were recorded over a time period of several hours. Their reproducibility ensured that clean surfaces were maintained over time. The overall energy resolution was about 1 eV in the energy region of the Ce  $3d$  emission.

### 5.3 Experimental results

In Fig. 5.1 the Ce  $3d$  core level HAXPES spectra of  $CeM_2Al_{10}$  with  $M = Ru$  (red), Os (blue), and Fe (green) are shown. For simplicity the different compounds are referred to as *Ru*, *Os* and *Fe* in the following. The measurements were carried out at 40 K for Fe and Os and at 60 K for Ru which is low enough to be in the Kondo regime. In the panels (a)-(c) the raw data are shown. All spectra exhibit very low statistical noise and were highly reproducible. The dashed black lines display the standard integral background as developed by Shirley [84].

The main emission lines at about 883 and 901.5 eV binding energy represent the predominant spin-orbit split Ce  $3d_{5/2} f^1$  and  $3d_{3/2} f^1$  multiplets. The mixed ground state character is reflected in additional spectral weight at the shoulders of the  $f^1$  structures ( $f^2$  contributions,  $\sim 5.5$  eV on the lower binding energy side). The  $3d_{3/2} f^0$  feature comes up at  $\sim 914$  eV binding energy, whereas the  $3d_{5/2} f^0$  largely overlaps with the  $3d_{3/2} f^2$  features at about 895 eV. Strikingly, additional broad humps show up in all spectra at about 918 eV and in the Fe sample also around 860 eV (indicated by arrows in Fig. 5.1). These humps are identified as plasmon resonances [85].

As typical for cage-like structures, in the case of  $CeM_2Al_{10}$  the plasmon excitations originate from the polyhedral aluminum cage surrounding the Ce atom. Plasmon peaks of first and higher orders appear for each emission and multiplet line at a fixed energy distance. The main plasmonic contributions – which become notably visible at about 918 eV (see black arrows in Fig. 5.1) – belong to the Ce  $3d$  emission and have unfortunately a large overlap with the  $3d_{3/2} f^0$  feature, thereby preventing a direct extraction of its spectral weight. In  $CeFe_2Al_{10}$  the Fe  $2s$  emission at  $\sim 845$  eV gives rise to an additional plasmon satellite peaking at 860 eV. Its estimated contribution (up to third order) is shown in panel (a) of Fig. 5.1 as dashed orange line. Three Voigt profiles are used here and their intensity and line width is estimated on the basis of the Al  $1s$  analysis (see 5.7). Overcoming the drawbacks due to the appearance of plasmons in the Ce  $3d$  HAXPES spectra has been an important task for the data analysis.

In Fig. 5.1(d) the background-corrected and normalized Ce  $3d$  core level HAXPES spectra of  $CeM_2Al_{10}$  with  $M = Ru$  (red), Os (blue), and Fe (green) are shown. The integral backgrounds displayed in Fig. 5.1(a)-(c) have been subtracted from the data and the spectra have been normalized to the integrated intensity between 870 and 940 eV. In the case of Fe the estimated contribution from the plasmon satellites belonging to the Fe  $2s$  emission has also been subtracted. The energy positions of the different  $f$  contributions are indicated by the black ruler at the bottom of Fig. 5.1(d). Additionally, for a better visualization of the spectral differences between the three compounds, the  $CeFe_2Al_{10}$  spectrum is overlaid (gray curves) on the Ru and Os data. Comparing the three spectra with each other reveals already a qualitative trend for the  $f$  occupancy: While the  $f^1$  contributions to the spectrum decrease from Ru to Os to Fe, the  $f^0$  (tiny spikes on top of the plasmon intensities) and  $f^2$  spectral weights become more pronounced in the same direction. This points towards an increasing  $f$  delocalization in the same order, in agreement with previous experimental findings [4, 13, 21, 22, 36, 59, 61, 72]. However, a *quantitative* extraction of the different  $f^n$  contributions to the HAXPES spectrum requires an adequate modeling of the plasmon contributions arising from the Ce  $3d$  emission lines.

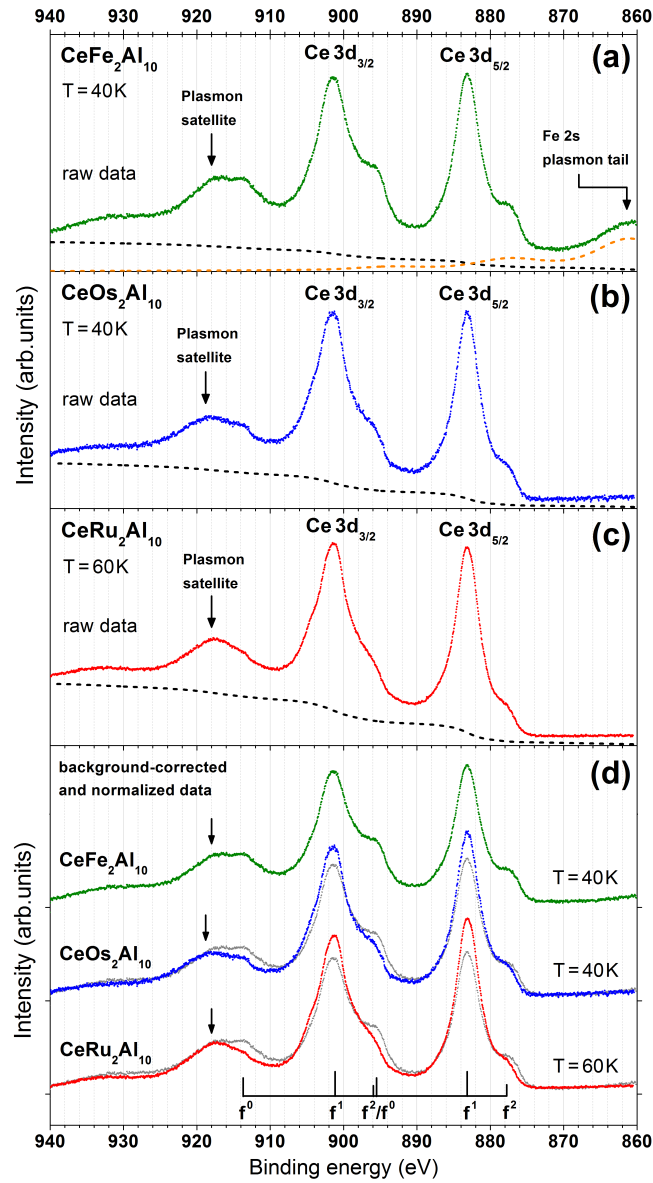


Figure 5.1: Low temperature Ce  $3d$  HAXPES spectra of  $CeM_2Al_{10}$  with  $M = Ru$  (red), Os (blue), and Fe (green). (a)-(c) Data as measured, i.e. before background subtraction and normalization. The black arrows at  $\sim 918$  eV indicate spectral weight due to plasmon contributions. In  $CeFe_2Al_{10}$  another plasmon, originating from the Fe  $2s$  emission, shows up. Its estimated contribution is plotted as orange dashed line in (a). The black dashed line in each panel shows the respective integral background. (d) Data after background subtraction and normalization. All data are normalized to the integrated intensity between 870 and 940 eV and the three spectra are displaced on the y-axis by an offset. For a better comparison, the  $CeFe_2Al_{10}$  spectrum is additionally overlaid on the Ru and Os data (in gray). The black ruler at the bottom indicates the energy positions of the  $f^n$  contributions and the black arrows indicate spectral weight due to plasmon contributions.

## 5.4 Quantitative analysis

### 5.4.1 Concept

Anderson proposed an impurity model to explain the moment of magnetic impurities in non-magnetic host metals [86]. The model was extended to the analysis of x-ray absorption and PES spectra of mixed valence Ce compounds by Gunnarsson and Schönhammer [87]. It considers a single  $f$  state in a bath of electrons, which are described in a band model, and the hybridization between them. Examples for its successful application to PES, core level spectroscopy and x-ray absorption data can be found in Refs. [76–79, 88]. A more recent example are the  $3d$  core level HAXPES data of  $CeRu_2Si_2$  and  $CeRu_2Ge_2$  by Yano *et al.* [89] However, these descriptions do not include a multiplet calculation, despite the complex underlying multiplet structure resulting from the  $f$ - $f$  Coulomb and exchange interactions, because computing times would become unreasonably long.

For our case here we do need to include a full multiplet calculation because the line shapes in the Ce  $3d$  emission spectra, which are primarily determined by the underlying multiplet structure, are complicated by the strong plasmons. Each emission line of the two spin-orbit split  $3d$  multiplets gives rise to first and higher order plasmons, thus preventing a simple phenomenological assignment of the respective  $f^n$  spectral weights with Gaussian and/or Lorentzian line profiles. In order to tackle this problem we had to combine a full multiplet calculation with a simpler form of the Anderson impurity model; simpler in order to keep computing times reasonable. This simplified form is a configuration interaction (CI) calculation in which the valence band is represented by a single ligand state. It captures the fundamental features of the core hole spectrum [90], i.e. it yields accurate  $f^n$  contributions and the resulting CI parameters give insight into the exchange interaction  $J_{ex}$ . The consequences of the simplification are discussed in 5.8.

Plasmons appear at well-defined energy distances at higher binding energies ( $\Delta E_n = nE_{\text{plasmon}}$ ) and the application of the full multiplet calculation allows the pinning of a plasmon and its multiples to each emission line with the same parameters for energy distance, line width and shape. The line shape parameters for the plasmon satellites can be determined from the Al  $1s$  single emission line in an independent measurement (see 5.7 and Fig. 5.3 therein), reducing the number of free fit parameters for the *reconstruction* of the spectra (Ce  $3d$  plus plasmons intensities). The combination of full multiplet and CI calculations (fm-CI), allows to extract the  $f^n$  contributions despite strong plasmons.

The fm-CI simulations were performed with the XTLS 9.0 program [37]. They account for the intra-atomic  $4f$ - $4f$  and  $3d$ - $4f$  Coulomb and exchange interactions and the  $3d$  and  $4f$  spin-orbit coupling, as calculated with Cowan's atomic structure code [91]. From earlier studies [52, 61], the reduction of the atomic Hartree-Fock values for the  $4f$ - $4f$  and  $3d$ - $4f$  Coulomb interactions are known to amount to  $\sim 40\%$  and  $\sim 20\%$ , respectively. The hybridization effects between the  $f$  and the conduction electrons are described by the  $f$ - $f$  Coulomb exchange ( $U_{ff}$ ), the Coulomb interaction between  $f$  electron and  $d$  core hole ( $U_{fc}$ ), the effective  $f$  binding energy  $\Delta_f$  (i.e. the energy difference between  $f^0$  and  $f^1L$  in the initial state) and the hybridization strength  $V_{\text{eff}}$ . Thus, in total there are four parameters plus line shape to be fitted (i.e. Lorentzian and Mahan broadening, see below). The energy distances between the  $f^n$  features and their respective

intensities uniquely determine the four CI parameters. The plasmon line shape and properties are fixed by the independent analysis of the Al 1s measurements.

### 5.4.2 Simulation of Ce 3d spectra

For each Ce 3d multiplet line, plasmonic contributions up to the order of  $n = 3$  are included using the line shape parameters and intensity ratios as determined in the analysis of the Al 1s spectra (see 5.7). Thus, each *line profile* consists of the main emission lines plus first, second and third order plasmon. The same line shape and intensity ratios were used for all 3d emission lines. Having fixed the line profiles, the spectra were calculated using the fm-CI routine.

This procedure is visualized in Fig. 5.2 (a), (b) and (c) for Fe, Os and Ru. In each panel the dots represent the low temperature Ce 3d HAXPES data (same color code as in Fig. 5.1). The multiplet simulation (orange curve) is broadened by a Gaussian function of 1 eV FWHM and a Lorentzian function of 1.3 eV FWHM to account for the instrumental resolution and lifetime broadening, respectively. In addition a Mahan function (cut-off parameter  $\xi = 1.8$  eV, asymmetry factor  $\alpha = 0.65$ ) is used to account for the asymmetric line shape of the 3d emission (see Eq. (1) in 5.7). The red curves in Fig. 5.2 are the resulting broadened Ce 3d multiplet spectra. The dashed lines represent the plasmons (first (black), second (dark gray) and third order (gray)) which are replica of the red curve using the intensity scaling factors, energy shifts and broadening as obtained from the fits to the Al 1s spectra (see 5.7, Table 5.2). The black lines are the total fit to the data, i.e. the sum of the red curve (3d emission) and all dashed lines (plasmons). Note that a change of the configuration interaction parameters in the theoretical model not only changes the multiplet structure but also leads to different plasmon intensity contributions.

In the top rows of Table 5.1 the resulting  $f$  weights and the  $f$  electron count  $n_f$  are given. The corresponding fit parameters for the  $f$ - $f$  Coulomb exchange ( $U_{ff}$ ), the Coulomb interaction between  $f$  electron and 3d core hole ( $U_{fc}$ ), the hybridization strength  $V_{\text{eff}}$  and the effective  $f$  binding energy  $\Delta_f$  (all given in eV) are listed in the bottom rows. These results describe the pure, background and plasmon corrected Ce 3d HAXPES spectra (red line curves in Fig. 5.2).

## 5.5 Discussion

There is an excellent agreement between the theoretical and the experimental spectra for all three compounds (see Fig. 5.2). All spectral features – including the different  $f^n$  contributions – and the plasmon humps are very well reproduced. The agreement is almost perfect for the Ce  $3d_{5/2}$  emission lines since the corresponding energy region is hardly influenced by plasmons and the background contribution can be assumed to be well determined. On the other hand, also above 892 eV binding energy the general Ce  $3d_{3/2}$  line shape and the  $f^0$  and  $f^2$  spectral features are nicely modeled by the fm-CI calculation. In particular, the  $f^0$  feature can be extracted reliably because it consists of only one single emission line and, therefore, appears very narrow compared to background and plasmons.

The overall size of the resulting configuration interaction parameters (see Table 5.1) is comparable with the results of e.g. the HAXPES analysis of CeRu<sub>2</sub>Si<sub>2</sub> by Yano *et al.* [89] in which the Anderson impurity model is used without considering multiplet effects. In recent resonant PES measurements on CeM<sub>2</sub>Al<sub>10</sub> the energy separation of the  $f^0$  feature is found to

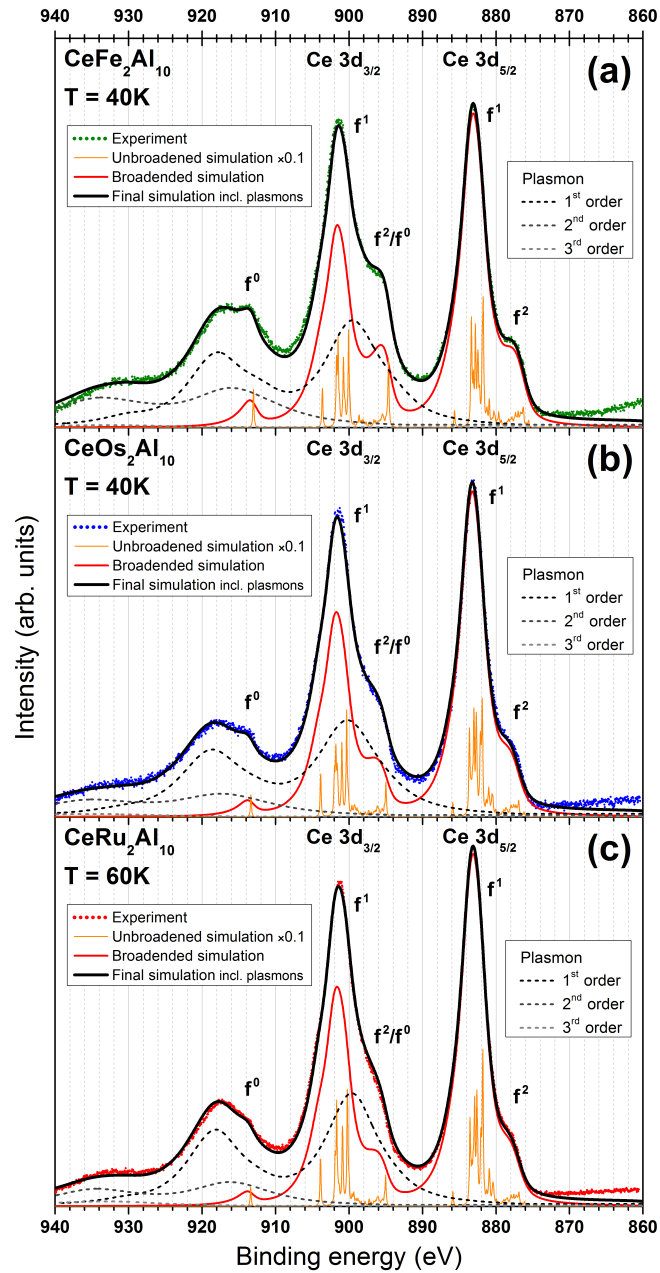


Figure 5.2: Transfer of the Al plasmon properties – as extracted from the Al 1s spectra – to the fm-CI simulation of the Ce 3d core emission for (a)  $CeRu_2Al_{10}$ , (b)  $CeOs_2Al_{10}$  and (c)  $CeFe_2Al_{10}$ . The experimental data is shown as green, blue and red dots, respectively (same as in Fig. 5.1). The simulated multiplet structure is shown as orange (unbrodened, scaled by  $\times 0.1$ ) and red (brodened) line curves. The calculated spectral weight due to plasmons (up to the third order) is represented by the dashed lines. The final simulations are represented by the black curves.

	CeRu <sub>2</sub> Al <sub>10</sub>	CeOs <sub>2</sub> Al <sub>10</sub>	CeFe <sub>2</sub> Al <sub>10</sub>
$f^0$	5.9(8) %	7.2(8) %	11.6(8) %
$f^1$	91.7(8) %	90.1(8) %	85.0(8) %
$f^2$	2.4(4) %	2.7(4) %	3.5(4) %
$n_f$	0.97(1)	0.96(1)	0.92(1)
$U_{ff}$	8.6(2)	8.5(2)	8.0(2)
$U_{fc}$	10.00(15)	10.00(15)	10.30(15)
$V_{\text{eff}}$	0.214(5)	0.230(5)	0.268(5)
$\Delta_f$	-2.4(1)	-2.3(1)	-1.9(1)

Table 5.1: Results from fitting the background- and plasmon-corrected Ce 3d HAXPES spectra of the CeM<sub>2</sub>Al<sub>10</sub> compounds within the fm-CI model (see Fig. 5.2 for the corresponding simulations). In the top rows the determined  $f^n$  contributions and  $f$  electron count  $n_f$  are given. The corresponding CI parameters are listed in the bottom rows: the  $f$ - $f$  Coulomb exchange  $U_{ff}$ , the Coulomb interaction between  $f$  electron and 3d core hole  $U_{fc}$ , the effective  $f$  binding energy  $\Delta_f$ , and the hybridization strength  $V_{\text{eff}}$  (all in eV). The margin of errors (given in parentheses) of all results in this table were estimated by variation of the parameter considered while keeping the others fixed.

be approximately 2 eV [74], which is consistent with our results for  $|\Delta_f|$ . The trend observed for the 4f valence in Ref. [74] as well as in earlier core level x-ray photoemission studies [13, 21, 59] is also generally in agreement with our findings, although the deviations from integer valence are smaller. It should be noted that these studies do not reach the same bulk sensitivity due to the use of soft x-rays [80–83]. The probing depth for Ce 3d core-level PES given by the photoelectrons’ inelastic mean free path at  $h\nu = 6.47$  keV is about 85 Å, whereas for soft x-rays ( $h\nu = 1000 - 1500$  eV) it amounts to 5 – 15 Å. Zekko *et al.* [72] investigated the substitution series Ce(Ru<sub>1-x</sub>Fe<sub>x</sub>)<sub>2</sub>Al<sub>10</sub> by means of bulk-sensitive partial fluorescence yield x-ray absorption (PFY-XAS) at the Ce  $L_3$  edge and also found a more pronounced difference between the Ce valence of CeRu<sub>2</sub>Al<sub>10</sub> ( $n_f = 0.95$ ) and CeFe<sub>2</sub>Al<sub>10</sub> ( $n_f = 0.89$ ).

The question arises to what extent the difference of surface sensitivity between HAXPES and PFY-XAS has an impact on the extraction of the  $f^n$  contributions. The latter is a photon-in-photon-out technique and thereby provides a probing depth of the order of 10 μm, making PFY-XAS truly bulk-sensitive. The bulk sensitivity of high-energy Ce 3d PES has been studied in detail by Braicovich *et al.* [82], showing that for  $h\nu = 3.85$  keV the bulk contribution to the spectra already dominates. Hence, in the present CeM<sub>2</sub>Al<sub>10</sub> spectra for  $h\nu = 6.47$  keV the remaining influence from the surface region is estimated to be non-relevant, especially because the samples were cleaved *in situ* under ultrahigh vacuum conditions and surface degradation with time was not observed.

While we believe that PFY-XAS is very powerful in determining small changes in the  $f^n$  contributions with temperature and especially with pressure, we also believe that there are

non-negligible ambiguities in the absolute assignment of the spectral weights. PFY at the Ce  $L$ -edge measures the empty  $5d$  density of states so that band structure determines the spectral distribution, giving rise to non-trivial line shapes. For example, most of the fits require a not further specified so-called satellite peak on the high energy side of the main  $f^1$  feature [72, 92, 93]. Moreover, different groups place the  $L_3$  edge jump at different energies (cf. Refs. [72, 92]) which may give rise to an absolute difference of a few percent in  $n_f$ . Band structure and lattice effects would have to be considered to describe the spectral shape and background, and be able to extract absolute values for the  $f^n$  contributions, in particular to quantify the  $f^0$  weight.

Back to the present HAXPES study, the analysis within the combined fm-CI model and the accurate treatment of the plasmon excitations gives a highly quantitative picture of the  $4f$  ground state in the  $CeM_2Al_{10}$  compounds. The results indicate a substantial delocalization of the  $f$  electrons in all three compounds of the  $CeM_2Al_{10}$  family – being slightly stronger in Os with respect to Ru and considerably larger in Fe.  $V_{\text{eff}}$  increases and  $|\Delta_f|$  decreases from Ru to Os to Fe, meaning that  $J_{\text{ex}}$  is a little bit larger for Os compared to Ru and significantly greater for Fe. Here we assume  $J_{\text{ex}}$  scales with the inverse of  $|\Delta_f|$  and quadratically with  $V_{\text{eff}}$ . The increasing exchange interaction is consistent with the simultaneous increase of  $f^0$  and  $T_K$  when going from Ru to Os to Fe. In total we conclude that  $J_{\text{ex}}$  is large. Consequently, due to the resulting moment screening the  $CeM_2Al_{10}$  family has to be considered as a *correlated* material and the de Gennes scaling law has lost its validity to predict ordering temperatures. Intuitively, in the magnetic region of the Doniach phase diagram a large  $J_{\text{ex}}$  should lead to high ordering temperatures when the  $1/R^3$  dependent RKKY interaction has a large amplitude. However, the distance between the local moments in these compounds are very large so that the ordering temperatures can only be high, when the RKKY interaction is very effective. This points to band structure effects which are not contained in the Doniach model. Furthermore, while the absence of magnetic order in the Fe compound can be understood within the Doniach model, it is not possible to explain its existence in the presence of a substantial amount of delocalized  $f$  electrons in the Ru and Os compounds. Both have as much  $f^0$  in the ground state ( $\approx 6\%$ ) as the non-magnetic compound  $CeRu_2Si_2$  [89].

Local-density approximation (LDA) band structure calculations for  $CeM_2Al_{10}$  find higher transition-metal  $d$  states in the vicinity of the Fermi level for  $M = Fe$ , relative to the Os  $5d$  and Ru  $4d$  density of states, thereby giving rise to a stronger hybridization between Fe  $3d$  and Ce  $4f$  states [13]. The total and partial density of states of Ru and Os show only minor differences. The LDA results qualitatively agree with the picture suggested by the interaction parameters in Table 5.1: The hybridization strength is only slightly higher in Os compared to Ru but clearly increases for the Fe compound.

The importance of the band structure is supported by the detailed macroscopic investigation of the  $CeOs_2Al_{10}$  substitution series where Os has been substituted with Re and Ir [71]. Here hole doping (Re) increases the hybridization while electron doping (Ir) leads to a stronger  $f$  electron localization. The important finding is that, as a function of substitution, the maximum in  $T_N$  coincides with the maximum in the hybridization gap, thus pointing towards a connection between the two [71]. Further studies are on their way.

The coexistence of magnetic order and  $f$  delocalization has been discussed in the context of the  $CeRh_{1-x}Co_xIn_5$  substitution series where the  $f$  electrons, with increasing Co content,

change from fairly localized to more itinerant well inside the antiferromagnetic phase [94]. The Doniach phase diagram cannot capture this. When it comes to a theoretical description, the original continuum Anderson single impurity model treats the Kondo aspect and a two-impurity model the RKKY interactions – but in reality we are dealing with Kondo lattices. There have been some models which go beyond the Anderson impurity ansatz and yield both on-site Kondo and inter-site RKKY correlations. For example Zerec *et al.* [95] use the Kondo lattice model (KLM) ansatz for Kondo clusters and their results show the importance of the electron density of states for the competition of Kondo screening and RKKY interactions. Another model treating the two-impurity model analytically points out the importance of the local moment separation [96]. Recently, Hoshino and Kuramoto suggested an extended phase diagram based on the KLM in a simplified approach [65]. Here the on-site Kondo screening is obtained in a dynamical mean-field theory (DMFT) and the RKKY interaction is added in a molecular field approximation to investigate how the mean-field magnetic states are influenced by the Kondo interaction. The model yields regions of coexisting RKKY interaction and Kondo screening for large exchange interactions and the authors point out that the Ru and Os compounds of the  $\text{CeM}_2\text{Al}_{10}$  family fall into this region of coexistence, while the Fe compound is located in a region where magnetic order is suppressed due to the strong Kondo effect. However, none of the above mentioned theories is able to make quantitative predictions and we conclude that it would be highly desirable to have theories which also include explicitly hybridization gaps as well as crystal-field effects to account for possible anisotropies in the hybridization.

## 5.6 Summary

We have presented bulk-sensitive Ce 3d HAXPES data of the Kondo semiconducting  $\text{CeM}_2\text{Al}_{10}$  family and shown that a quantitative analysis of the Ce 4f valence is possible despite strong plasmonic contributions in the spectra. The data were analyzed using a full multiplet configuration interaction model in which a single ligand state is used to mimic the valence band. The impact of this simplification is discussed in the Appendix. On the basis of the full multiplet structure the line shapes of the  $f^1$  and  $f^2$  final states could be well described and the spectral background and the broad plasmon satellites consistently modeled, so that also the narrow  $f^0$  feature was quantified, showing that strong  $f^0$  contributions are present in the spectra of all three compounds of the  $\text{CeM}_2\text{Al}_{10}$  family. The deduced configuration interaction parameters clearly indicate an increasing trend for  $J_{\text{ex}}$  from Ru to Os to Fe and in general  $J_{\text{ex}}$  is concluded to be large, showing the existence of  $f$  delocalization (Kondo screening) in the presence of magnetic order (RKKY interaction).

This work was supported by Deutsche Forschungsgemeinschaft, Germany (Grant No. 583872), and a Grant-in-Aid of MEXT, Japan (Grant No. 26400363).

## 5.7 Appendix A: Plasmon properties

Here the determination of the plasmon properties from the Al 1s HAXPES data shall be described. As mentioned in Sec. 5.3, the photoemission process often gives rise to plasmon satellites of first and higher order. The properties of these secondary excitations relative to the respective main

5 Valence and configuration interaction parameters of  $CeM_2Al_{10}$  ( $M = Ru, Os, Fe$ )

Order of plasmon n	CeRu <sub>2</sub> Al <sub>10</sub>			CeOs <sub>2</sub> Al <sub>10</sub>			CeFe <sub>2</sub> Al <sub>10</sub>		
	1	2	3	1	2	3	1	2	3
Scaling factor	0.65	0.35	0.12	0.63	0.33	0.10	0.68	0.40	0.12
Energy shift $\Delta E_n$ (eV)	16.6	33.2	49.8	17.2	34.4	51.6	16.5	33.0	49.5
Lorentzian FWHM (eV)	5	10	15	6	12	18	5	10	15

Table 5.2: Summary of the properties of the Al plasmons in  $CeM_2Al_{10}$  as obtained from fitting the Al 1s HAXPES spectra. The scaling factor gives the plasmon intensity with respect to the main 1s emission line,  $\Delta E_n$  is the energy distance relative to the position of the main line and in the last row the applied additional Lorentz broadening is noted.

emission line (i.e. intensity, energy distance and broadening) depend on the kinetic energy of the excited core electron. However, in the limit of large kinetic energies, as it is the case in this HAXPES experiment, this dependence becomes minor [97, 98]. We therefore can use the Al 1s spectrum for each compound to model quantitatively the plasmons contribution in the Ce 3d spectrum.

The Al 1s core level gives rise to a single well defined emission line without overlap with other core levels, thus is easy to model. Fig. 5.3 shows the background-corrected HAXPES Al 1s spectrum measured for CeOs<sub>2</sub>Al<sub>10</sub> (black dots) at 40 K. For the background correction the standard integral background was used [84]. Apart from the main emission at 1558.5 eV the spectrum shows at least two plasmon satellites (first and second order) on the higher binding energy side. At around 1610 eV a third order plasmon is faintly visible. The 1s feature exhibits a slight asymmetric line shape, characteristic for metals [85] – which is also observable in the first plasmon peak – with a tail extending to higher binding energies. To simulate the spectrum the discrete emission line is convoluted with a Gaussian and a Lorentzian function of 1 eV and 0.2 eV FWHM, respectively. The so-called Mahan broadening function

$$B_{\text{Mahan}}(\omega) = \frac{\Theta(\omega)}{\Gamma(\alpha) \cdot \omega} \left( \frac{\omega}{\xi} \right)^\alpha e^{-\omega/\xi} \quad (5.1)$$

describes the asymmetry. Here  $\Theta(\omega)$  is the Heaviside step function and  $\Gamma(\alpha)$  the Gamma function. The cut-off parameter is  $\xi = 1.8$  eV and the asymmetry factor is about  $\alpha = 0.5$  for all three compounds.

In a second step the plasmons are fitted: Each plasmon of the order n is generated by duplicating the main emission line, shifting it in energy ( $\Delta E_n = nE_{\text{plasmon}}$ ) and adding it to the theoretical spectrum. The plasmon features are additionally broadened by a Lorentzian and scaled in intensity to match the experimental data. The broadening applied to the first order is doubled for the second order and tripled for the third order plasmon. The red line in Fig. 5.3 represents the fitting result for CeOs<sub>2</sub>Al<sub>10</sub> containing the Al 1s emission and plasmon contributions up to the third order. The agreement between experiment and simulation is very good. The Al 1s spectra of CeRu<sub>2</sub>Al<sub>10</sub> and CeFe<sub>2</sub>Al<sub>10</sub> have been analyzed correspondingly (not shown here), yielding an independent and complete characterization of the plasmon features for each sample. All fitting results are summarized in Table 5.2. The plasmon attributes obtained

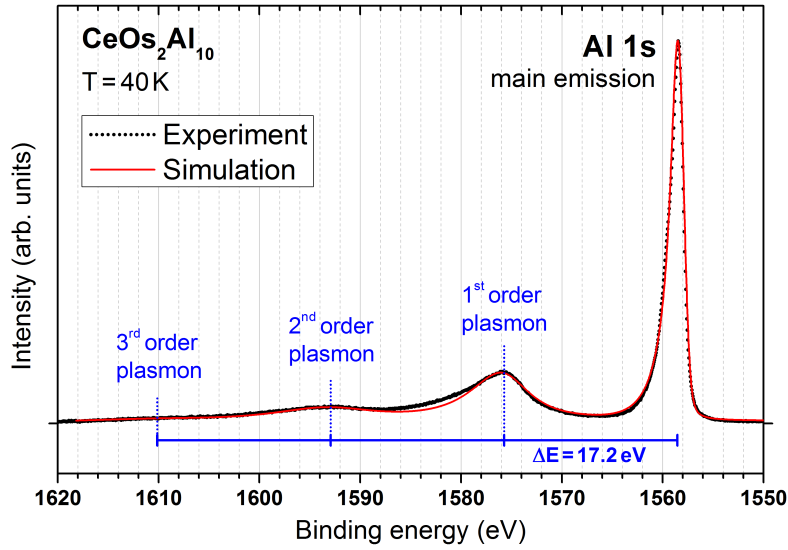


Figure 5.3: Low temperature HAXPES spectrum of the Al 1s core level and its plasmon satellites, measured on  $\text{CeOs}_2\text{Al}_{10}$ . The black dots show the experimental data and the red line represents the simulation of the 1s emission including the plasmon contributions up to the third order (see text). The blue ruler at the bottom marks the energy position of the plasmon peaks relative to the main line.

from the Al 1s spectra of the three compounds show a high resemblance, nevertheless there are faint but notable differences – especially regarding the energy positions (see Table 5.2).

## 5.8 Appendix B: Consequences of the fm-CI model

Here the consequences of using the fm-CI model, which has been applied for the analysis of the present HAXPES data, shall be discussed. The essential simplification is the representation of the valence states by one ligand state, i.e. by an infinitely narrow band. This model reproduces the main features of the core level spectra (see e.g. Ref. [90]) and has the great advantage that the computational aspect becomes easy to handle, so that it can be combined with a full multiplet calculation. However, it fails to account for the low-energy excitations, as e.g. in valence band PES [99], and does not give realistic values for the Kondo temperature and RKKY interaction, since for these the host band must be included explicitly. Yet, for the Ce 3d core level spectra in which the energy separation between the  $c f^0$ ,  $c f^1 L$ , and  $c f^2 \underline{L}$  configurations are large, the effect of the host band is to produce asymmetric line shapes, which can be taken into account by the use of the Mahan function.

Another artifact of the fm-CI is the overestimation of the contribution of the  $J = 7/2$  multiplet in the ground state. Here we recall that in cerium the spin-orbit splitting ( $\Delta_{\text{SO}} \approx 0.3 \text{ eV}$ ) is often of the order of the hybridization  $V_{\text{eff}}$  (see Table 5.1) so that the higher multiplet intermixes with the ground state, the more the stronger the hybridization [100]. Assuming a realistic bandwidth

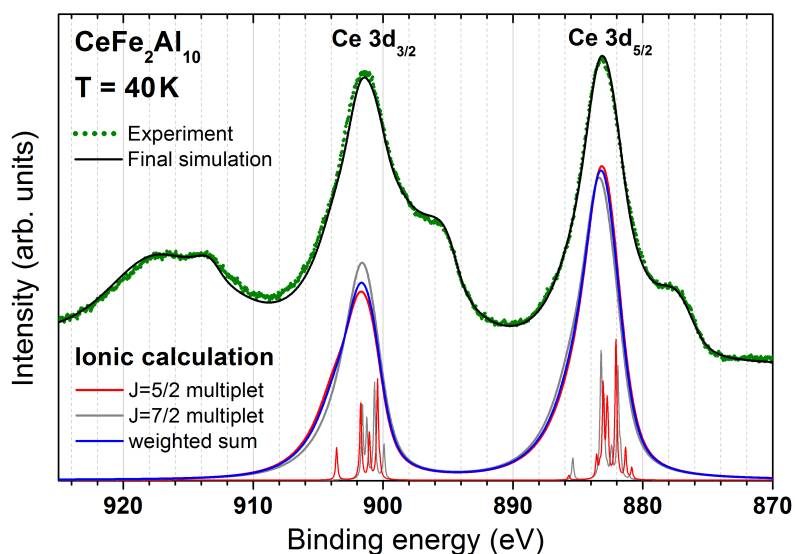


Figure 5.4: Ionic simulation of the Ce  $3d$  PES spectra of the pure  $J = 5/2$  (red) and  $J = 7/2$  (gray) states. The calculations are shown both before (underlying multiplet structure scaled by  $\times 0.1$ ) and after the broadening functions have been applied. Here the same Gaussian, Lorentzian and Mahan broadening as in the simulations of the  $CeM_2Al_{10}$  HAXPES spectra (Fig. 5.2) are used. The blue curve is the weighted sum of 69 %  $J = 5/2$  and 31 %  $J = 7/2$ . The experimental data of  $CeFe_2Al_{10}$  (green dots) and the corresponding final simulation (black curve) are also shown (displaced on the y-axis by an offset).

instead of a single ligand state, these contributions are weighted and contribute much less than in the fm-CI model. Nevertheless van der Laan *et al.* concluded from their Anderson impurity calculation with 3 eV broad bands and their XAS  $M$ -edge data that in intermediate valent compounds like  $CePd_3$  the  $J = 7/2$  contribution may be as high as 30 % [100].

For the  $J = 7/2$  contributions in the ground state our fm-CI calculations yield about 19 % in the case of Ru, 22 % for Os and approximately 31 % for the Fe compound. This shows nicely how the intermixing of the higher multiplet increases with increasing hybridization. Actually, the presence of a larger amount of  $J = 7/2$  in the Fe compound is also experimentally confirmed by the line shape of the Ce  $M_5$  edge as measured with soft x-ray absorption in a previous experiment [61]. The low energy peak of the  $M_5$  edge is expected to become stronger for larger contributions of  $J = 7/2$  in the ground state [100] which is in agreement with our observation (see Fig. 3 in Ref. [61] or Fig. 1(c) in Ref. [74]). However, back to the HAXPES simulations, we know that in a full band model the intermixing with the higher multiplet would be weaker than the numbers above from the fm-CI calculations may suggest. Furthermore, we know that the line shape of the Ce  $3d$   $J = 7/2$  emission multiplet differs from the  $J = 5/2$  one (see thin red and gray lines in Fig. 5.4). Hence the question arises whether the erroneous amount of  $J = 7/2$  influences the outcome of  $f^0$  contribution in the initial state.

An estimation of this error is given by Fig. 5.4, where the ionic simulations ( $f^1$  only) of

the Ce  $3d$  PES spectra of the pure  $J = 5/2$  (red curves) and  $J = 7/2$  (gray curves) states are compared. Both the underlying multiplet structure and the broadened ionic spectra are shown; here the same broadening functions as in the final fm-CI simulations of the  $\text{CeM}_2\text{Al}_{10}$  HAXPES spectra are used. The blue curve in Fig. 5.4 represents the weighted sum of the pure  $J$  spectra, using 69 % of  $J = 5/2$  and 31 % of  $J = 7/2$ . This corresponds to the mixing in the final fm-CI simulation for  $\text{CeFe}_2\text{Al}_{10}$ , which is shown in the same panel (shifted upwards by an offset) together with the experimental data. Note that in the final simulation shown in Fig. 5.2 the different  $f^n$  contributions cannot be easily separated since their multiplet lines partly overlap. Thus, a direct extraction of the  $f^1$ -only contribution is not possible. Instead, consulting the ionic simulations allows to quantitatively compare the  $J = 5/2$  and  $J = 7/2$  line shapes.

Comparing the red and the blue curve in Fig. 5.4 shows that the presence of  $J = 7/2$  has only minor effects on the spectral line shape although the  $J = 7/2$ -contribution is appreciable (31 %). The Ce  $3d_{5/2}$  feature (880 – 890 eV) in the weighted sum (blue) is nearly identical to the pure  $J = 5/2$  (red). The differences in the Ce  $3d_{3/2}$  region are only slightly larger. At most, the intensity ratio between the spin-orbit split Ce  $3d_{5/2} f^1$  and  $3d_{3/2} f^1$  multiplets is affected – the possible error amounts to about 4 %, meaning an error of less than  $\pm 0.5$  % for the  $f^0$  contribution. Here the systematic uncertainties due to background and plasmon corrections are more essential so that we conclude the error in the fm-CI model due to the overestimation of the  $J = 7/2$  multiplet in the ground state is small and in particular does not influence the result for  $f^0$ .



## References of Chapters 3 – 5

- [1] V. M. T. Thiede, T. Ebel, and W. Jeitschko. *Ternary aluminides  $\text{LnT}_2\text{Al}_{10}$  ( $\text{Ln} = \text{Y, La, Nd, Sm, Gd, Lu}$  and  $T = \text{Fe, Ru, Os}$ ) with  $\text{YbFe}_2\text{Al}_{10}$  type structure and magnetic properties of the iron-containing series.* J. Mater. Chem. **8** 125 (1998). DOI: 10.1039/A705854C.
- [2] A. I. Tursina, S. N. Nesterenko, E. V. Murashova, I. V. Chernyshev, H. Noël, and Y. D. Seropegin.  *$\text{CeRu}_2\text{Al}_{10}$  with the  $\text{YbFe}_2\text{Al}_{10}$  structure type.* Acta Crystallogr. Sect. E **61** i12 (2005). DOI: 10.1107/S1600536805000310.
- [3] A. M. Strydom. *Thermal and electronic transport in  $\text{CeRu}_2\text{Al}_{10}$ : Evidence for a metal-insulator transition.* Physica B: Condens. Matter **404** 2981 (2009). DOI: 10.1016/j.physb.2009.07.044.
- [4] T. Nishioka, Y. Kawamura, T. Takesaka, R. Kobayashi, H. Kato, M. Matsumura, K. Kodama, K. Matsubayashi, and Y. Uwatoko. *Novel Phase Transition and the Pressure Effect in  $\text{YbFe}_2\text{Al}_{10}$ -type  $\text{CeT}_2\text{Al}_{10}$  ( $T = \text{Fe, Ru, Os}$ ).* J. Phys. Soc. Jpn. **78** 123705 (2009). DOI: 10.1143/JPSJ.78.123705.
- [5] H. Tanida, D. Tanaka, M. Sera, C. Moriyoshi, Y. Kuroiwa, T. Takesaka, T. Nishioka, H. Kato, and M. Matsumura. *Existence of Fine Structure inside Spin Gap in  $\text{CeRu}_2\text{Al}_{10}$ .* J. Phys. Soc. Jpn. **79** 083701 (2010). DOI: 10.1143/JPSJ.79.083701.
- [6] K. Hanzawa. *Spin-Peierls Transition in Ce Compounds.* J. Phys. Soc. Jpn. **79** 043710 (2010). DOI: 10.1143/JPSJ.79.043710.
- [7] S. Kambe, H. Chudo, Y. Tokunaga, T. Koyama, H. Sakai, T. U. Ito, K. Ninomiya, W. Higemoto, T. Takesaka, T. Nishioka, and Y. Miyake. *Evidence for Appearance of an Internal Field in the Ordered State of  $\text{CeRu}_2\text{Al}_{10}$  by  $\mu^+$  SR.* J. Phys. Soc. Jpn. **79** 053708 (2010). DOI: 10.1143/JPSJ.79.053708.
- [8] D. D. Khalyavin, A. D. Hillier, D. T. Adroja, A. M. Strydom, P. Manuel, L. C. Chapon, P. Peratheepan, K. Knight, P. Deen, C. Ritter, Y. Muro, and T. Takabatake. *Long-range magnetic order in  $\text{CeRu}_2\text{Al}_{10}$  studied via muon spin relaxation and neutron diffraction.* Phys. Rev. B **82** 100405 (2010). DOI: 10.1103/PhysRevB.82.100405.
- [9] J. Robert, J.-M. Mignot, G. André, R. Kobayashi, T. Nishioka, M. Matsumura, H. Tanida, D. Tanaka, and M. Sera. *Long-range order and low-energy magnetic excitations in  $\text{CeRu}_2\text{Al}_{10}$  studied via neutron scattering.* Phys. Rev. B **82** 100404 (2010). DOI: 10.1103/PhysRevB.82.100404.
- [10] C. S. Lue, S. H. Yang, A. C. Abhyankar, Y. D. Hsu, H. T. Hong, and Y. K. Kuo. *Transport, thermal, and NMR characteristics of  $\text{CeRu}_2\text{Al}_{10}$ .* Phys. Rev. B **82** 045111 (2010). DOI: 10.1103/PhysRevB.82.045111.

- [11] H. Kato, R. Kobayashi, T. Takesaka, T. Nishioka, M. Matsumura, K. Kaneko, and N. Metoki. *Magnetic Structure Determination of  $CeT_2Al_{10}$  ( $T = Ru$  and  $Os$ ): Single Crystal Neutron Diffraction Studies*. J. Phys. Soc. Jpn. **80** 073701 (2011). DOI: 10.1143/JPSJ.80.073701.
- [12] M. Matsumura, H. Tanida, D. Tanaka, H. Kato, T. Nishioka, and M. Sera. *Reconciliation between NQR Spectrum and Long-Range Magnetic Order in  $CeRu_2Al_{10}$* . J. Phys. Soc. Jpn. **80** 085001 (2011). DOI: 10.1143/JPSJ.80.085001.
- [13] S.-I. Kimura, T. Iizuka, H. Miyazaki, T. Hajiri, M. Matsunami, T. Mori, A. Irizawa, Y. Muro, J. Kajino, and T. Takabatake. *Optical study of charge instability in  $CeRu_2Al_{10}$  in comparison with  $CeOs_2Al_{10}$  and  $CeFe_2Al_{10}$* . Phys. Rev. B **84** 165125 (2011). DOI: 10.1103/PhysRevB.84.165125.
- [14] S.-I. Kimura, T. Iizuka, H. Miyazaki, A. Irizawa, Y. Muro, and T. Takabatake. *Electronic-Structure-Driven Magnetic Ordering in a Kondo Semiconductor  $CeOs_2Al_{10}$* . Phys. Rev. Lett. **106** 056404 (2011). DOI: 10.1103/PhysRevLett.106.056404.
- [15] K. Yutani, Y. Muro, J. Kajino, T. J. Sato, and T. Takabatake. *Crystal-field effect on anisotropic magnetic properties of  $CeT_2Al_{10}$  ( $T = Ru$  and  $Os$ )*. J. Phys.: Conf. Ser. **391** 012070 (2012). DOI: 10.1088/1742-6596/391/1/012070.
- [16] K. Hanzawa. *Crystalline Electric Field Effects in  $CeT_2Al_{10}$  ( $T = Ru, Os$ )*. J. Phys. Soc. Jpn. **80** 023707 (2011). DOI: 10.1143/JPSJ.80.023707.
- [17] T. Nishioka, D. Hirai, Y. Kawamura, H. Kato, M. Matsumura, H. Tanida, M. Sera, K. Matsubayashi, and Y. Uwatoko. *Magnetic properties of  $CeRu_{1-x}Fe_xAl_{10}$* . J. Phys.: Conf. Ser. **273** 012046 (2011). DOI: 10.088/1742-6596/273/1/012046.
- [18] H. Tanida, D. Tanaka, Y. Nonaka, M. Sera, M. Matsumura, and T. Nishioka. *Angle-resolved  $^{27}Al$  NMR study on  $CeRu_2Al_{10}$  single crystal: Evidence of internal magnetic field and unusual spin orientation in the field-induced ordered phase*. Phys. Rev. B **84** 233202 (2011). DOI: 10.1103/PhysRevB.84.233202.
- [19] K. Hanzawa. *Resonating Valence Bond State with Antiferromagnetic Order in Ce Compounds*. J. Phys. Soc. Jpn. **80** 113701 (2011). DOI: 10.1143/JPSJ.80.113701.
- [20] A. Kondo, J. Wang, K. Kindo, T. Takesaka, Y. Ogane, Y. Kawamura, T. Nishioka, D. Tanaka, H. Tanida, and M. Sera. *Magnetization and Magnetoresistance of  $CeRu_2Al_{10}$  under High Magnetic Fields along  $c$ -Axis*. J. Phys. Soc. Jpn. **80** 013701 (2011). DOI: 10.1143/JPSJ.80.013701.
- [21] J. Goraus and A. Slebarski. J. Phys.: Condens. Matter **24** 095503 (2012). DOI: 10.1188/0953-8984/24/9/095503.
- [22] D. T. Adroja, A. D. Hillier, Y. Muro, J. Kajino, T. Takabatake, P. Peratheepan, A. M. Strydom, P. P. Deen, F. Demmel, J. R. Stewart, J. W. Taylor, R. I. Smith, S. Ramos, and M. A. Adams. *Competing  $4f$ -electron dynamics in  $Ce(Ru_{1-x}Fe_x)_2Al_{10}$  ( $0 \leq x \leq 1.0$ ): Magnetic ordering emerging from the Kondo semiconducting state*. Phys. Rev. B **87** 224415 (2013). DOI: 10.1103/PhysRevB.87.224415.
- [23] H. Ikeda and K. Miyake. *A Theory of Anisotropic Semiconductor of Heavy Fermions*. J. Phys. Soc. Jpn. **65** 1769 (1996). DOI: 10.1143/JPSJ.65.1769.

- [24] Y. Kagan, K. A. Kikoin, and A. S. Mishchenko. *Interplay between heavy fermions and crystal-field excitation in Kondo lattices: Low-temperature thermodynamics and inelastic neutron scattering spectra of CeNiSn*. Phys. Rev. B **55** 12348 (1997). DOI: 10.1103/PhysRevB.55.12348.
- [25] J. Moreno and P. Coleman. *Gap-Anisotropic Model for the Narrow-Gap Kondo Insulators*. Phys. Rev. Lett. **84** 342 (2000). DOI: 10.1103/PhysRevLett.84.342.
- [26] M. Miyazawa and K. Yamada. *Theory of the Hybridization Gap in Ce Compounds with Crystalline Electric Field Splitting*. J. Phys. Soc. Jpn. **72** 2033 (2003). DOI: 10.1143/JPSJ.72.2033.
- [27] M. Kohgi, K. Ohoyama, T. Osakabe, M. Kasaya, T. Takabatake, and H. Fujii. *Neutron scattering study of CeNiSn*. Physica B: Condens. Matter **186-188** 409 (1993). DOI: 10.1016/0921-4526(93)90588-w.
- [28] D. Adroja, B. Rainford, A. Neville, and A. Jansen. *Crossover from antiferromagnetic Kondo metal to Kondo insulator in CePt<sub>1-x</sub>Ni<sub>x</sub>Sn alloys*. Physica B: Condens. Matter **223 – 224** 275 (1996). DOI: 10.1016/0921-4526(96)00098-1.
- [29] J.-G. Park, D. T. Adroja, K. A. McEwen, Y. J. Bi, and J. Kulda. *Possible crystal-field excitation in single-crystal CeNiSn*. Phys. Rev. B **58** 3167 (1998). DOI: 10.1103/PhysRevB.58.3167.
- [30] L. Menon, D. Adroja, B. Rainford, S. Malik, and W. Yelon. *Neutron scattering studies on CeRhSb*. Solid State Commun. **112** 85 (1999). DOI: 10.1016/S0038-1098(99)00289-6.
- [31] J.-Y. So, S.-J. Oh, J.-G. Park, D. T. Adroja, K. A. McEwen, and T. Takabatake. *Inelastic neutron scattering studies of doped CeNiSn and CeRhSb: Crystal-field excitations and origin of the pseudogap*. Phys. Rev. B **71** 214441 (2005). DOI: 10.1103/PhysRevB.71.214441.
- [32] P. Hansmann, A. Severing, Z. Hu, M. W. Haverkort, C. F. Chang, S. Klein, A. Tanaka, H. H. Hsieh, H.-J. Lin, C. T. Chen, B. Fåk, P. Lejay, and L. H. Tjeng. *Determining the Crystal-Field Ground State in Rare Earth Heavy Fermion Materials Using Soft-X-Ray Absorption Spectroscopy*. Phys. Rev. Lett. **100** 066405 (2008). DOI: 10.1103/PhysRevLett.100.066405.
- [33] T. Willers, B. Fåk, N. Hollmann, P. O. Körner, Z. Hu, A. Tanaka, D. Schmitz, M. Enderle, G. Lapertot, L. H. Tjeng, and A. Severing. *Crystal-field ground state of the noncentrosymmetric superconductor CePt<sub>3</sub>Si: A combined polarized soft x-ray absorption and polarized neutron study*. Phys. Rev. B **80** 115106 (2009). DOI: 10.1103/PhysRevB.80.115106.
- [34] T. Willers, Z. Hu, N. Hollmann, P. O. Körner, J. Gegner, T. Burnus, H. Fujiwara, A. Tanaka, D. Schmitz, H. H. Hsieh, H.-J. Lin, C. T. Chen, E. D. Bauer, J. L. Sarrao, E. Goremychkin, M. Koza, L. H. Tjeng, and A. Severing. *Crystal-field and Kondo-scale investigations of CeMIn<sub>5</sub> (M = Co, Ir, and Rh): A combined x-ray absorption and inelastic neutron scattering study*. Phys. Rev. B **81** 195114 (2010). DOI: 10.1103/PhysRevB.81.195114.

- [35] T. Willers, D. T. Adroja, B. D. Rainford, Z. Hu, N. Hollmann, P. O. Körner, Y.-Y. Chin, D. Schmitz, H. H. Hsieh, H.-J. Lin, C. T. Chen, E. D. Bauer, J. L. Sarrao, K. J. McClellan, D. Byler, C. Geibel, F. Steglich, H. Aoki, P. Lejay, A. Tanaka, L. H. Tjeng, and A. Severing. *Spectroscopic determination of crystal-field levels in  $CeRh_2Si_2$  and  $CeRu_2Si_2$  and of the  $4f^0$  contributions in  $CeM_2Si_2$  ( $M=Cu, Ru, Rh, Pd, \text{ and } Au$ )*. Phys. Rev. B **85** 035117 (2012). DOI: 10.1103/PhysRevB.85.035117.
- [36] Y. Muro, J. Kajino, K. Umeo, K. Nishimoto, R. Tamura, and T. Takabatake. *Structural modification and metamagnetic anomaly in the ordered state of  $CeOs_2Al_{10}$* . Phys. Rev. B **81** 214401 (2010). DOI: 10.1103/PhysRevB.81.214401.
- [37] A. Tanaka and T. Jo. *Resonant 3d, 3p and 3s PES in Transition Metal Oxides Predicted at 2p Threshold*. J. Phys. Soc. Jpn. **63** 2788 (1994). DOI: 10.1143/JPSJ.63.2788.
- [38] M. Rotter, D. M. Le, L. G. Pascut, T. Hoffmann, M. Doerr, R. Schedler, P. F. Hoffman, S. Rotter, and M. Banks. *McPhase Manual*. 2011. URL: [http://www.cpf.s.mpg.de/~rotter/homepage\\_mcphase/manual/manual.html](http://www.cpf.s.mpg.de/~rotter/homepage_mcphase/manual/manual.html).
- [39] T. Takesaka, K. Oe, R. Kobayashi, Y. Kawamura, T. Nishioka, H. Kato, M. Matsumura, and K. Kodama. *Semiconducting behavior in  $CeFe_2Al_{10}$  and  $CeRu_2Al_{10}$  single crystals*. J. Phys.: Conf. Ser. **200** 012201 (2010). DOI: 10.1088/1742-6596/200/1/012201.
- [40] D. T. Adroja, A. D. Hillier, P. P. Deen, A. M. Strydom, Y. Muro, J. Kajino, W. A. Kockelmann, T. Takabatake, V. K. Anand, J. R. Stewart, and J. Taylor. *Long-range ordering of reduced magnetic moments in the spin-gap compound  $CeOs_2Al_{10}$  as seen via muon spin relaxation and neutron scattering*. Phys. Rev. B **82** 104405 (2010). DOI: 10.1103/PhysRevB.82.104405.
- [41] C. S. Lue, S. H. Yang, T. H. Su, and B.-L. Young. *NMR evidence for the partially gapped state in  $CeOs_2Al_{10}$* . Phys. Rev. B **82** 195129 (2010). DOI: 10.1103/PhysRevB.82.195129.
- [42] A. Kondo, J. Wang, K. Kindo, Y. Ogane, Y. Kawamura, S. Tanimoto, T. Nishioka, D. Tanaka, H. Tanida, and M. Sera. *High-field magnetization and magnetic phase transition in  $CeOs_2Al_{10}$* . Phys. Rev. B **83** 180415 (2011). DOI: 10.1103/PhysRevB.83.180415.
- [43] H. Tanida, Y. Nonaka, D. Tanaka, M. Sera, Y. Kawamura, Y. Uwatoko, T. Nishioka, and M. Matsumura. *Magnetic anisotropy of Kondo semiconductor  $CeT_2Al_{10}$  ( $T = Ru, Os$ ) in the ordered state*. Phys. Rev. B **85** 205208 (2012). DOI: 10.1103/PhysRevB.85.205208.
- [44] C. S. Lue, H. F. Liu, B. D. Ingale, J. N. Li, and Y. K. Kuo. *Transport, thermoelectric, and thermal expansion investigations of the cage structure compound  $CeOs_2Al_{10}$* . Phys. Rev. B **85** 245116 (2012). DOI: 10.1103/PhysRevB.85.245116.
- [45] J. Robert, J.-M. Mignot, S. Petit, P. Steffens, T. Nishioka, R. Kobayashi, M. Matsumura, H. Tanida, D. Tanaka, and M. Sera. *Anisotropic Spin Dynamics in the Kondo Semiconductor  $CeRu_2Al_{10}$* . Phys. Rev. Lett. **109** 267208 (2012). DOI: 10.1103/PhysRevLett.109.267208.
- [46] Y. Muro, K. Motoya, Y. Saiga, and T. Takabatake. *Formation of a Hybridization Gap in a Cage-Like Compound  $CeFe_2Al_{10}$* . J. Phys. Soc. Jpn. **78** 083707 (2009). DOI: 10.1143/JPSJ.78.083707.

- [47] Y. Muro, K. Motoya, Y. Saiga, and T. Takabatake. *Semiconducting behaviour in CeT<sub>2</sub>Al<sub>10</sub> (T = Fe and Ru)*. J. Phys.: Conf. Ser. **200** 012136 (2010). DOI: 10.1088/1742-6596/200/1/012136.
- [48] S. C. Chen and C. S. Lue. *<sup>27</sup>Al NMR study of the mixed valence compound CeFe<sub>2</sub>Al<sub>10</sub>*. Phys. Rev. B **81** 075113 (2010). DOI: 10.1103/PhysRevB.81.075113.
- [49] Y. Kawamura, S. Edamoto, T. Takesaka, T. Nishioka, H. Kato, M. Matsumura, Y. Tokunaga, S. Kambe, and H. Yasuoka. *<sup>27</sup>Al-NQR/NMR Study of Kondo Semiconductor CeFe<sub>2</sub>Al<sub>10</sub>*. J. Phys. Soc. Jpn. **79** 103701 (2010). DOI: 10.1143/JPSJ.79.103701.
- [50] S.-I. Kimura, Y. Muro, and T. Takabatake. *Anisotropic Electronic Structure of the Kondo Semiconductor CeFe<sub>2</sub>Al<sub>10</sub> Studied by Optical Conductivity*. J. Phys. Soc. Jpn. **80** 033702 (2011). DOI: 10.1143/JPSJ.80.033702.
- [51] Y. Muro, K. Yutani, J. Kajino, T. Onimaru, and T. Takabatake. *Anisotropic c-f Hybridization in the Kondo Semiconductor CeFe<sub>2</sub>Al<sub>10</sub>*. J. Korean Phys. Soc. **63** 508 (2013). DOI: 10.3938/jkps.63.508.
- [52] F. Strigari, T. Willers, Y. Muro, K. Yutani, T. Takabatake, Z. Hu, Y.-Y. Chin, S. Agrestini, H.-J. Lin, C. Chen, A. Tanaka, M. W. Haverkort, L.-H. Tjeng, and A. Severing. Phys. Rev. B **86** 081105(R) (2012). DOI: 10.1103/PhysRevB.86.081105.
- [53] J. C. Fuggle, F. U. Hillebrecht, J.-M. Esteva, R. C. Karnatak, O. Gunnarsson, and K. Schönhammer. *f-count effects in x-ray-absorption spectra of the 3d levels in Ce and its intermetallic compounds*. Phys. Rev. B **27** 4637 (1983). DOI: 10.1103/PhysRevB.27.4637.
- [54] G. Kaindl, G. Kalkowski, W. D. Brewer, B. Perscheid, and F. Holtzberg. *M-edge x-ray absorption spectroscopy of 4f instabilities in rare-earth systems*. J. Appl. Phys. **55** 1910 (1984). DOI: 10.1063/1.333517.
- [55] D. T. Adroja. Private communication (2011).
- [56] M. W. Haverkort. Private communication (2012).
- [57] S. Doniach. *The Kondo lattice and weak antiferromagnetism*. Physica B+C **91** 231 (1977). DOI: 10.1016/0378-4363(77)90190-5.
- [58] P. S. Riseborough. *Heavy Fermion Semiconductors*. Adv. Phys. **49** 257 (2000). DOI: 10.1080/000187300243345.
- [59] A. Ślebarski and J. Goraus. *Evolution from antiferromagnetic to paramagnetic Kondo insulator with increasing hybridization; XPS studies*. J. Phys.: Conf. Ser. **391** 012067 (2012). DOI: 10.1088/1742-6596/391/1/012067.
- [60] K. Kunimori, M. Nakamura, H. Nohara, H. Tanida, M. Sera, T. Nishioka, and M. Matsumura. *Unusual magnetic order in CeT<sub>2</sub>Al<sub>10</sub> (T = Ru, Os) in comparison with localized NdFe<sub>2</sub>Al<sub>10</sub>*. Phys. Rev. B **86** 245106 (2012). DOI: 10.1103/PhysRevB.86.245106.
- [61] F. Strigari, T. Willers, Y. Muro, K. Yutani, T. Takabatake, Z. Hu, S. Agrestini, C.-Y. Kuo, Y.-Y. Chin, H.-J. Lin, T. W. Pi, C. T. Chen, E. Weschke, E. Schierle, A. Tanaka, M. W. Haverkort, L. H. Tjeng, and A. Severing. Phys. Rev. B **87** 125119 (2013). DOI: 10.1103/PhysRevB.87.125119.

- [62] M. Sera, D. Tanaka, H. Tanida, C. Moriyoshi, M. Ogawa, Y. Kuroiwa, T. Nishioka, M. Matsumura, J. Kim, N. Tsuji, and M. Takata. *Crystal Structure and Anisotropic  $c$ - $f$  Hybridization in  $CeT_2Al_{10}$  ( $T = Ru, Fe$ )*. J. Phys. Soc. Jpn. **82** 024603 (2013). DOI: 10.1143/JPSJ.82.024603.
- [63] A. Kondo, K. Kindo, K. Kunimori, H. Nohara, H. Tanida, M. Sera, R. Kobayashi, T. Nishioka, and M. Matsumura. *Marked Change in the Ground State of  $CeRu_2Al_{10}$  Induced by Small Amount of Rh Substitution*. J. Phys. Soc. Jpn. **82** 054709 (2013). DOI: 10.1143/JPSJ.82.054709.
- [64] D. T. Adroja, A. D. Hillier, Y. Muro, T. Takabatake, A. M. Strydom, A. Bhattacharyya, A. Daoud-Aladin, and J. W. Taylor. *Muon-spin-relaxation and inelastic neutron scattering investigations of the caged-type Kondo semimetals*. Phys. Scr. **88** 068505 (2013). DOI: 10.1088/0031-8949/88/06/068505.
- [65] S. Hoshino and Y. Kuramoto. *Itinerant Versus Localized Heavy-Electron Magnetism*. Phys. Rev. Lett. **111** 026401 (2013). DOI: 10.1103/PhysRevLett.111.026401.
- [66] H. Tanida, D. Tanaka, Y. Nonaka, S. Kobayashi, M. Sera, T. Nishioka, and M. Matsumura. *Pressure-induced switching of magnetic anisotropy in the antiferromagnetic ordered phase in  $CeRu_2Al_{10}$* . Phys. Rev. B **88** 045135 (2013). DOI: 10.1103/PhysRevB.88.045135.
- [67] R. Kobayashi, Y. Ogane, D. Hirai, T. Nishioka, M. Matsumura, Y. Kawamura, K. Matsubayashi, Y. Uwatoko, H. Tanida, and M. Sera. *Change in Unusual Magnetic Properties by Rh Substitution in  $CeRu_2Al_{10}$* . J. Phys. Soc. Jpn. **82** 093702 (2013). DOI: 10.1143/JPSJ.82.093702.
- [68] D. D. Khalyavin, D. T. Adroja, P. Manuel, J. Kawabata, K. Umeo, T. Takabatake, and A. M. Strydom. *Change of magnetic ground state by light electron doping in  $CeOs_2Al_{10}$* . Phys. Rev. B **88** 060403 (2013). DOI: 10.1103/PhysRevB.88.060403.
- [69] H. Guo, H. Tanida, R. Kobayashi, I. Kawasaki, M. Sera, T. Nishioka, M. Matsumura, I. Watanabe, and Z.-a. Xu. *Magnetic instability induced by Rh doping in the Kondo semiconductor  $CeRu_2Al_{10}$* . Phys. Rev. B **88** 115206 (2013). DOI: 10.1103/PhysRevB.88.115206.
- [70] D. D. Khalyavin, D. T. Adroja, A. Bhattacharyya, A. D. Hillier, P. Manuel, A. M. Strydom, J. Kawabata, and T. Takabatake. *Magnetic ordering with reduced cerium moments in hole-doped  $CeOs_2Al_{10}$* . Phys. Rev. B **89** 064422 (2014). DOI: 10.1103/PhysRevB.89.064422.
- [71] J. Kawabata, T. Takabatake, K. Umeo, and Y. Muro. *Suppression of antiferromagnetic order and hybridization gap by electron and hole doping in the Kondo semiconductor  $CeOs_2Al_{10}$* . Phys. Rev. B **89** 094404 (2014). DOI: 10.1103/PhysRevB.89.094404.
- [72] Y. Zekko, Y. Yamamoto, H. Yamaoka, F. Tajima, T. Nishioka, F. Strigari, A. Severing, J.-F. Lin, N. Hiraoka, H. Ishii, K.-D. Tsuei, and J. Mizuki. *Correlation between the valence state of cerium and the magnetic transition in  $Ce(Ru_{1-x}Fe_x)_2Al_{10}$  studied by resonant x-ray emission spectroscopy*. Phys. Rev. B **89** 125108 (2014). DOI: 10.1103/PhysRevB.89.125108.

- [73] J.-M. Mignot, P. A. Alekseev, J. Robert, S. Petit, T. Nishioka, M. Matsumura, R. Kobayashi, H. Tanida, and M. Sera. *Dispersive magnetic-resonance mode in the Kondo semiconductor  $CeFe_2Al_{10}$* . Phys. Rev. B **89** 161103 (2014). DOI: 10.1103/PhysRevB.89.161103.
- [74] T. Ishiga, T. Wakita, R. Yoshida, H. Okazaki, K. Tsubota, M. Sunagawa, K. Uenaka, K. Okada, H. Kumigashira, M. Oshima, K. Yutani, Y. Muro, T. Takabatake, Y. Muraoka, and T. Yokoya. *Electronic Structures of  $CeM_2Al_{10}$  ( $M = Fe, Ru, \text{ and } Os$ ) Studied by Soft X-ray Resonant and High-Resolution Photoemission Spectroscopies*. J. Phys. Soc. Jpn. **83** 094717 (2014). DOI: 10.7566/JPSJ.83.094717.
- [75] O. Gunnarsson, K. Schönhammer, J. Allen, K. Karlsson, and O. Jepsen. *Information from photoemission spectral weights and shapes*. J. Electron Spectrosc. Relat. Phenom. **117–118** 1 (2001). DOI: 10.1016/S0368-2048(01)00241-9.
- [76] J. Allen, S. Oh, O. Gunnarsson, K. Schönhammer, M. Maple, M. Torikachvili, and I. Lindau. *Electronic structure of cerium and light rare-earth intermetallics*. Adv. Phys. **35** 275 (1986). DOI: 10.1080/00018738600101901.
- [77] S. Hüfner. *Valence band photoemission on metallic Ce systems*. Zeitschrift für Physik B Cond. Mat. **86** 241 (1992). DOI: 10.1007/BF01313831.
- [78] L. H. Tjeng, S.-J. Oh, E.-J. Cho, H.-J. Lin, C. T. Chen, G.-H. Gweon, J.-H. Park, J. W. Allen, T. Suzuki, M. S. Makivić, and D. L. Cox. *Temperature dependence of the Kondo resonance in  $YbAl_3$* . Phys. Rev. Lett. **71** 1419 (1993). DOI: 10.1103/PhysRevLett.71.1419.
- [79] C. Laubschat, E. Weschke, C. Holtz, M. Domke, O. Strebel, and G. Kaindl. *Surface-electronic structure of  $\alpha$ -like Ce compounds*. Phys. Rev. Lett. **65** 1639 (1990). DOI: 10.1103/PhysRevLett.65.1639.
- [80] A. Sekiyama, T. Iwasaki, K. Matsuda, Y. Saitoh, Y. Onuki, and S. Suga. *Probing bulk states of correlated electron systems by high-resolution resonance photoemission*. Nature **403** 396 (2000). DOI: 10.1038/35000140.
- [81] A. Yamasaki, S. Imada, H. Higashimichi, H. Fujiwara, T. Saita, T. Miyamachi, A. Sekiyama, H. Sugawara, D. Kikuchi, H. Sato, A. Higashiya, M. Yabashi, K. Tamasaku, D. Miwa, T. Ishikawa, and S. Suga. *Coexistence of Strongly Mixed-Valence and Heavy-Fermion Character in  $SmOs_4Sb_{12}$  Studied by Soft- and Hard-X-Ray Spectroscopy*. Phys. Rev. Lett. **98** 156402 (2007). DOI: 10.1103/PhysRevLett.98.156402.
- [82] L. Braicovich, N. B. Brookes, C. Dallera, M. Salvietti, and G. L. Olcese. *High-energy Ce – 3d photoemission: Bulk properties of  $CeM_2$  ( $M = Fe, Co, Ni$ ) and  $Ce_7Ni_3$* . Phys. Rev. B **56** 15047 (1997). DOI: 10.1103/PhysRevB.56.15047.
- [83] S. Tanuma, C. J. Powell, and D. R. Penn. *Calculations of electron inelastic mean free paths. IX. Data for 41 elemental solids over the 50 eV to 30 keV range*. Surf. Interface Anal. **43** 689 (2011). DOI: 10.1002/sia.3522.
- [84] D. A. Shirley. *High-Resolution X-Ray Photoemission Spectrum of the Valence Bands of Gold*. Phys. Rev. B **5** 4709 (1972). DOI: 10.1103/PhysRevB.5.4709.
- [85] S. Hüfner. *Photoelectron Spectroscopy: Principles and Applications*. Advanced Texts in Physics. Springer, Berlin - Heidelberg, 2003. DOI: 10.1007/978-3-662-09280-4.

- [86] P. W. Anderson. *Localized Magnetic States in Metals*. Phys. Rev. **124** 41 (1961). DOI: 10.1103/PhysRev.124.41.
- [87] O. Gunnarsson and K. Schönhammer. *Electron spectroscopies for Ce compounds in the impurity model*. Phys. Rev. B **28** 4315 (1983). DOI: 10.1103/PhysRevB.28.4315.
- [88] A. Kotani, T. Jo, and J. Parlebas. *Many-body effects in core-level spectroscopy of rare-earth compounds*. Adv. Phys. **37** 37 (1988). DOI: 10.1080/00018738800101359.
- [89] M. Yano, A. Sekiyama, H. Fujiwara, Y. Amano, S. Imada, T. Muro, M. Yabashi, K. Tamasaku, A. Higashiya, T. Ishikawa, Y. Ōnuki, and S. Suga. *Electronic structure of CeRu<sub>2</sub>X<sub>2</sub> (X = Si, Ge) in the paramagnetic phase studied by soft x-ray ARPES and hard x-ray photoelectron spectroscopy*. Phys. Rev. B **77** 035118 (2008). DOI: 10.1103/PhysRevB.77.035118.
- [90] J.-M. Imer and E. Wuilloud. *A simple model calculation for XPS, BIS and EELS 4f-excitations in Ce and La compounds*. Zeitschrift für Physik B Cond. Mat. **66** 153 (1987). DOI: 10.1007/BF01311650.
- [91] R. D. Cowan. *The Theory of Atomic Structure and Spectra*. University of California Press, Berkeley - Los Angeles - London, 1981.
- [92] J.-P. Rueff, S. Raymond, M. Taguchi, M. Sikora, J.-P. Itié, F. Baudalet, D. Braithwaite, G. Knebel, and D. Jaccard. *Pressure-Induced Valence Crossover in Superconducting CeCu<sub>2</sub>Si<sub>2</sub>*. Phys. Rev. Lett. **106** 186405 (2011). DOI: 10.1103/PhysRevLett.106.186405.
- [93] H. Yamaoka, Y. Zekko, A. Kotani, I. Jarrige, N. Tsujii, J.-F. Lin, J. Mizuki, H. Abe, H. Kitazawa, N. Hiraoka, H. Ishii, and K.-D. Tsuei. *Electronic transitions in CePd<sub>2</sub>Si<sub>2</sub> studied by resonant x-ray emission spectroscopy at high pressures and low temperatures*. Phys. Rev. B **86** 235131 (2012). DOI: 10.1103/PhysRevB.86.235131.
- [94] S. K. Goh, J. Paglione, M. Sutherland, E. C. T. O’Farrell, C. Bergemann, T. A. Sayles, and M. B. Maple. *Fermi-Surface Reconstruction in CeRh<sub>1-x</sub>Co<sub>x</sub>In<sub>5</sub>*. Phys. Rev. Lett. **101** 056402 (2008). DOI: 10.1103/PhysRevLett.101.056402.
- [95] I. Zerec, B. Schmidt, and P. Thalmeier. *Kondo lattice model studied with the finite-T Lanczos method*. Phys. Rev. B **73** 245108 (2006). DOI: 10.1103/PhysRevB.73.245108.
- [96] G. E. Santoro and G. F. Giuliani. *Two-impurity Anderson model: Results of a perturbative expansion in U*. Phys. Rev. B **49** 6746 (1994). DOI: 10.1103/PhysRevB.49.6746.
- [97] J. Gadzuk. *Plasmon satellites in X-ray photoemission spectra*. J. Electron Spectrosc. Relat. Phenom. **11** 355 (1977). DOI: 10.1016/0368-2048(77)80012-1.
- [98] H. Shinotsuka, T. Uwatoko, T. Konishi, and T. Fujikawa. *Theoretical Study of Plasmon Loss Peaks in Core-level Photoemission Spectra: Energy and Angular Dependence*. J. Surf. Anal. **14** 332 (2008).
- [99] Y. Kucherenko, M. Finken, S. L. Molodtsov, M. Heber, J. Boysen, C. Laubschat, and G. Behr. *Giant hybridization effects in 4f photoemission spectra of Pr and Nd transition-metal compounds*. Phys. Rev. B **65** 165119 (2002). DOI: 10.1103/PhysRevB.65.165119.
- [100] G. van der Laan, B. T. Thole, G. A. Sawatzky, J. C. Fuggle, and R. Karnatak. *Identification of the relative population of spin-orbit split states in the ground state of a solid*. J. Physics C: Solid State Phys. **19** 817 (1986). DOI: 10.1088/0022-3719/19/5/019.

# 6 Revisiting the crystal-field ground state in the Kondo semimetal CeNiSn

## 6.1 Introduction

Among the diversity of ground states in heavy-fermion systems the low-carrier Kondo insulating state gives rise to deviant magnetic, thermodynamic and transport behavior at low temperatures. The interaction of the highly localized  $f$  electrons with the sea of conduction electrons leads to a narrow hybridization gap close to the Fermi level, and depending on the detailed gap structure and the chemical potential in these systems, a Kondo insulator or semiconductor can evolve. Theoretically, Kondo insulators are regarded as highly renormalized band insulators since band structure calculations yield significantly larger gap sizes than observed in optical, magnetic or transport measurements. A more comprehensive introduction to Kondo insulators is given in Chapter 1. CeNiSn was one of the first cerium-based HF compounds to be classified as narrow-gap Kondo insulator [1, 2]. It is regarded as a special representative of this class because it has a non-cubic structure and a particularly small energy gap. Actually, a small overlap between conduction and valence band make the properties of CeNiSn rather semimetallic [3, 4].

CeNiSn has an orthorhombic  $\epsilon$ -TiNiSn-type crystal structure (space group  $Pn2_1a$ ) [5], giving rise to strong anisotropic behavior in transport, magnetic and thermal properties. Its characteristics were well studied and can be reviewed for example in Ref. [4]. The Kondo temperature is estimated to be  $T_K = 54$  K [6]. The gapped behavior and a strong gap anisotropy can be seen in resistivity, specific heat and NMR measurements [2, 7–10], as well as in tunneling spectroscopy [11]. Photoelectron spectroscopy studies were carried out to obtain a better understanding of the electronic structure [12–14], and found a finite density of state at the Fermi level and the presence of hybridization – predominantly between Ce  $4f$  and Sn  $sp$  and between Ce  $4f$  and Ni  $3d$  electrons – which leads to the (weak) intermediate valence character of CeNiSn. No signs of magnetic order were observed down to lowest temperatures [7], however, neutron scattering experiments gave proof for the existence of a temperature- and  $Q$ -dependent spin gap [15, 16]. Below the coherence temperature weak one-dimensional antiferromagnetic correlations develop, indicating the proximity of the ground state to an antiferromagnetic instability.

In the search of a theoretical description for the unusual pseudogap formation in CeNiSn, different models have been proposed, all of which either require a certain crystalline electric field (CEF) splitting or a particular crystal-field ground state symmetry. The proposed theories are nicely summarized in the work of So *et al.* [17] but still shall be briefly recapped here. Kikoin *et al.* [18] considered the so-called spin-liquid picture [19, 20], in which the interaction between the itinerant heavy fermions and the localized CEF excitations can explain the low-temperature anomalies and the formation of the pseudogap in the limit of a weak CEF splitting. Here the condition  $k_B T_K \gg \Delta E_{1,2}$  is required, where  $\Delta E_{1,2}$  are the CEF splittings between the ground state and the first/second excited Kramer's doublet and  $k_B T_K$  the energy scale given by the

Kondo temperature. Ikeda and Miyake [21] modeled the anisotropic semiconductor by taking into account the  $k$ -dependence of the hybridization between conduction and  $f$  electrons ( $c$ - $f$  hybridization), from which the CEF ground state follows to consist mainly of  $|5/2, \pm 3/2\rangle$ . The importance of the CEF symmetry was pointed out also in a similar approach [22], where a pure  $|5/2, \pm 1/2\rangle$  ground state is found. Another theory by Moreno and Coleman [23] discussed the role of Hund's interaction between the  $f$  electrons for the selection of a nodal Kondo semimetal state – and speaks in favor of a mixed- $J_z$  state with octahedral symmetry.

Since all these theories agree in explaining certain properties of CeNiSn, a direct determination of the ground-state wave function is needed to clarify which model is the most appropriate. The common technique is inelastic neutron scattering (INS) and attempts were made without obtaining a clear result [24–26]. The CEF excitations are very broad due to the presence of strong  $c$ - $f$  hybridization and, additionally, overlapping phonon peaks hamper the analysis. In Ref. [26] a very broad CEF excitation around 40 meV was reported, but the lower CEF peak could not be observed. INS has also been performed on Pt- and Cu-doped CeNiSn [17, 27], where the doping drives the system into a more localized state, leading to significantly sharper excitations: Here the crystal-field energies of CePt<sub>0.2</sub>Ni<sub>0.8</sub>Sn were found to be 18.1 meV and 32.6 meV [27], and also in CeNi<sub>0.85</sub>Cu<sub>0.15</sub>Sn two distinct magnetic excitations around 20 meV and 35 meV were observed [17]. These findings already disqualify the spin-liquid theory by Kikoin *et al.* since the CEF splittings apparently are larger than  $k_B T_K$ . On the basis of a trigonal CEF Hamiltonian a theoretical fit of the INS data of CeNi<sub>0.85</sub>Cu<sub>0.15</sub>Sn was provided in Ref. [17], yielding two possible ground-state wave functions; namely a pure  $|5/2, \pm 3/2\rangle$ , which would be in favor of the Ikeda and Miyake model, and a mixed state comprised of  $|5/2, \pm 1/2\rangle$  and  $|5/2, \mp 5/2\rangle$ , which would speak for the theory by Moreno and Coleman.

In order to complete the crystal-field picture of CeNiSn and understand the nature of its pseudogap, we have carried out linearly polarized soft x-ray absorption spectroscopy (XAS) measurements at the Ce  $M_{4,5}$  edge. Especially in  $f$  electron systems, when INS is limited due to phonon contributions or broad line widths, soft XAS has been established as complementary, highly useful and reliable technique for the determination of the CEF ground-state wave function, as explained in Sec. 2.1.3. The sensitivity to the initial state symmetry is achieved by exploiting the polarization dependence of the absorption for light polarized parallel to the different crystallographic directions. The method has been successfully applied to tetragonal and orthorhombic Ce systems, as well as to Yb compounds (see Chapters 3 and 4 and references in Sec. 2.1.3). Thus, it is most promising to study also the orthorhombic Kondo semiconductor CeNiSn by means of polarization-dependent XAS to unambiguously clarify the crystal-field ground state and thereby elucidate the mechanism behind the gap formation.

## 6.2 Experimental details

Single crystalline CeNiSn was grown by the Czochralski tri-arc technique at the University of Birmingham [26]. Small sized samples of about  $2 \times 2 \times 2 \text{ mm}^3$  were cut from an ingot and their orientation and high quality were verified by Laue x-ray diffraction, on the basis of the structure information reported in Ref. [5], and static magnetic susceptibility measurements.

The polarization-dependent XAS measurements were carried out at the European Synchrotron

Radiation Facility (ESRF) in Grenoble, France, at the undulator beamline ID08. The overall energy resolution at the Ce  $M_{4,5}$  edge ( $h\nu \approx 870 - 910$  eV) was about 0.2 eV. To ensure clean sample surfaces, the single crystals were cleaved *in situ* under ultra high vacuum conditions at a pressure of  $\sim 5 \times 10^{-10}$  mbar. The absorption spectra were recorded at normal incidence in the total electron yield (TEY) mode and were normalized to the incident photon flux as measured on the refocusing mirror. One crystal was mounted with the  $a$  axis and another one with the  $b$  axis parallel to the Poynting vector of the incoming light, such that the absorption could be investigated for light polarized parallel to all three crystallographic directions, namely  $E \parallel a$ ,  $E \parallel b$  and  $E \parallel c$ . Recording the spectra for  $E \parallel c$  on both samples allows to normalize the three polarizations to each other. The use of an undulator beamline permits an easy switching of the polarization without moving the sample, which guarantees that the same sample spot is probed. Inhomogeneities in the crystals and surface deterioration were ruled out by probing different areas on the sample and repeating the measurement for the initial temperature at the end of a temperature series.

### 6.3 Theoretical details

The Ce  $M_{4,5}$  XAS spectra were simulated using the ionic full multiplet approach as implemented in the XTLS 8.3 program [28] and as successfully applied to the orthorhombic and tetragonal cerium heavy-fermion compounds before. The atomic parameters [29] for the  $4f$ - $4f$  and  $3d$ - $4f$  Coulomb and exchange interactions and the  $3d$  and  $4f$  spin-orbit coupling are given by reduced Hartree-Fock values. From fitting the isotropic spectra the reductions were found to be approximately 40 % for the  $4f$ - $4f$  and 20 % for the  $3d$ - $4f$  interactions. The spin-orbit interactions are reduced by a few percent only. Applying an ionic approach is justified as long as the crystal-field splittings are large compared to the Kondo temperature [30]. This is the case for CeNiSn where  $k_B T_K \approx 4.7$  meV and INS experiments on Cu-doped CeNiSn [17] suggest an overall CEF splitting larger than  $\sim 18$  meV.

CeNiSn crystallizes in the orthorhombic space group  $Pn2_1a$  [5]. The true CEF symmetry is determined by the local environment of the  $\text{Ce}^{3+}$  rare earth ion, which in the case of CeNiSn is given by the monoclinic point group  $C_s$ . The spin-orbit split  $J = 5/2$  and  $J = 7/2$  multiplets divide into three and four Kramer's doublets, respectively. Considering only the low-lying  $J = 5/2$  multiplet, the general CEF Hamiltonian for monoclinic symmetry reads:

$$H_{\text{CEF}}^{\text{mono}} = B_2^0 \hat{O}_2^0 + B_2^2 \hat{O}_2^2 + B_2^{-2} \hat{O}_2^{-2} + B_4^0 \hat{O}_4^0 + B_4^2 \hat{O}_4^2 + B_4^{-2} \hat{O}_4^{-2} + B_4^4 \hat{O}_4^4 + B_4^{-4} \hat{O}_4^{-4} \quad (6.1)$$

Here  $\hat{O}_n^m$  are the Stevens operator equivalents and  $B_n^m$  the crystal-field parameters. Consequently, in order to fully describe a monoclinic CEF, eight  $B_n^m$  parameters are needed, making an unambiguous fitting of the polarization-dependent XAS data impossible. However, the monoclinic distortions in CeNiSn can be regarded as small and the local symmetry can be approximated by the trigonal point group  $D_{3d}$  [17, 25], with the threefold rotational symmetry around the crystallographic  $a$  axis. For the description of a trigonal CEF the number of parameters reduces to three and the corresponding Hamiltonian can be written as:

$$H_{\text{CEF}}^{\text{tri}} = B_2^0 \hat{O}_2^0 + B_4^0 \hat{O}_4^0 + B_4^3 \hat{O}_4^3 \quad (6.2)$$

The eigenfunctions of the three  $J = 5/2$  Kramer's doublets can be represented in the basis of  $|J_z\rangle$  and in the case of a threefold rotational symmetry these states can be a mixture of  $|J_z = \pm 1/2\rangle$  and  $|J_z = \mp 5/2\rangle$  or a pure  $|J_z = \pm 3/2\rangle$ ; therefore they can be written as

$$\begin{aligned} |2\rangle &= |\pm 3/2\rangle \\ |1\rangle &= \alpha|\pm 1/2\rangle - \beta|\mp 5/2\rangle \\ |0\rangle &= \beta|\pm 1/2\rangle + \alpha|\mp 5/2\rangle \end{aligned} \quad (6.3)$$

with  $\alpha^2 + \beta^2 = 1$ . Note that  $|0\rangle$ ,  $|1\rangle$  and  $|2\rangle$  do not refer to an energetic order here. The crystal-field parameters  $B_2^0$ ,  $B_4^0$  and  $B_4^3$  determine the mixing factor  $\alpha$  and the transition energies  $\Delta E_1$  and  $\Delta E_2$  to the first and second excited CEF doublet, and vice versa. Meaning that, as in the tetragonal case [30], the trigonal CEF scheme can be equivalently expressed either by the  $B_n^m$  or the transition energies and  $\alpha$ .

The authors of Ref. [17], who measured Cu-doped CeNiSn with INS, found two magnetic excitations at  $\Delta E_1 \approx 18$  meV and  $\Delta E_2 \approx 32$  meV and were able to describe their data with two different sets of CEF parameters, each yielding a different CEF ground state. Model 1 yields a mixed ground state of type  $|0\rangle$  and Model 2 a pure  $|\pm 3/2\rangle$  ground state. Since each pure  $|J_z\rangle$  has its own characteristic linear dichroism (LD) [30], a significant difference in the polarization dependence is expected for the two solutions. Linearly polarized XAS provides a straightforward tool to clarify which crystal-field ground state forms in CeNiSn.

## 6.4 Results

The linearly polarized XAS spectra of CeNiSn measured at  $T = 15$  K are shown in Fig. 6.1. The actual point symmetry of the cerium ion is monoclinic, hence the XAS spectrum was recorded for the polarization along each main crystallographic axis, i.e. with  $E \parallel a$ ,  $E \parallel b$  and  $E \parallel c$ . The 15 K data are representative for the ground state since there are no low-lying CEF states according to INS [17, 26] (see Sec. 6.1).

First, the general anisotropy of the XAS spectra in Fig. 6.1 shall be discussed. Both the  $M_5$  and the  $M_4$  edge show a clear polarization dependence in all three directions, as it is expected for a monoclinic crystal field. On the contrary, a trigonal crystal field (with  $a$  being the threefold rotational symmetry axis) would not give any anisotropy in the  $b$ - $c$  plane because within its dipole limits XAS is insensitive to symmetries higher than twofold, i.e. the spectra for  $E \parallel b$  and  $E \parallel c$  would look the same. This is obviously not the case and confirms that in CeNiSn monoclinic distortions are present. However, on closer inspection (especially of the  $M_5$  edge) the line shapes for  $E \parallel b$  and  $E \parallel c$  show a strong resemblance, whereas the spectrum for  $E \parallel a$  clearly features a different spectral shape. Hence, the polarization dependence confirms the proximity to trigonal symmetry. The application of a trigonal CEF model is therefore justified and also more favorable because it limits the number of crystal-field parameters. The error in the ground-state wave function made by neglecting the monoclinic distortions is regarded to be small (see discussion below).

Next, we consider the trigonal CEF models found by So *et al.* [17] with INS on Cu-doped CeNiSn and calculate the linearly polarized XAS spectra for both solutions with the full multiplet routine. The threefold  $a$  axis is chosen as quantization axis. Model 1 refers to the scenario in

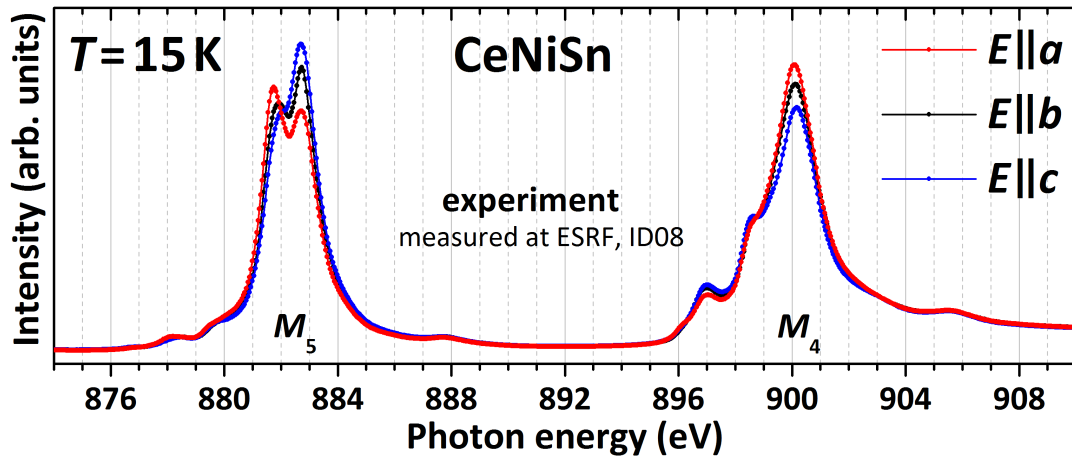


Figure 6.1: Experimental low-temperature linearly polarized soft XAS data of CeNiSn at the Ce  $M_{4,5}$  absorption edge for  $E \parallel a$ ,  $E \parallel b$  and  $E \parallel c$ . For the crystallographic orientation the structure information reported in Ref. [5] was used.

which the ground state is composed by a mixture of  $|\pm 1/2\rangle$  and  $|\mp 5/2\rangle$ . Model 2 describes the pure  $|\pm 3/2\rangle$  ground state. The mixing factor  $|\alpha|$  of the mixed ground state is slightly modified compared to the result in Ref. [17]. The resulting calculated spectra for the polarization parallel and perpendicular to the quantization axis  $a$  are shown in Fig. 6.2(a) (bottom and middle curves). Here the spectra for  $E \parallel b$  and  $E \parallel c$  are not distinguished since they are identical. In addition, the experimental data of Fig. 6.1 are replotted at the top of Fig. 6.2(a) but, for a better comparison to the trigonal calculations, the XAS spectrum for  $E \perp a$  is calculated as  $\frac{1}{2}(E \parallel b + E \parallel c)$ . In Fig. 6.2(b) the experimental LD ( $E \perp a - E \parallel a$ ) and the LD for both models is shown, enlarged by a factor of four.

The disagreement between Model 2 and the experimental data is obvious. In the simulation the difference between the absorption within the trigonal  $b$ - $c$  plane ( $E \perp a$ ) and perpendicular to it ( $E \parallel a$ ) rather shows a reversed behavior in comparison to the experimentally observed polarization dependence (see panel (b) of Fig. 6.2). In particular the line shape of the  $E \parallel a$  spectrum does not match the measurement at all. On the other hand Model 1 is in fairly good accordance with the polarized XAS measurement. By slightly varying the mixing factor from  $|\alpha| = 0.73$  (original CEF ground state solution from Ref. [17]) to  $|\alpha| = 0.77$ , the spectrum for  $E \parallel a$  can be perfectly reproduced. The calculation for  $E \perp a$ , i.e. for the in-plane polarization, also basically agrees with the data for  $E \perp a = \frac{1}{2}(E \parallel b + E \parallel c)$  – see light blue curve at the top of Fig. 6.2(a) and LD in panel (b) – indicating the closeness to trigonal symmetry. We therefore conclude the deviation from the trigonal Model 1 is small and the mixed state of predominating  $|\pm 1/2\rangle$  and  $|\mp 5/2\rangle$  contributions gives an excellent description of the CEF ground state in CeNiSn.

The nearest neighbor environment of the Ce ions from an isometric side view and a top view onto the trigonal  $b$ - $c$  plane are shown by the crystal structure in Fig. 6.3(a). The closeness to trigonal symmetry becomes clear when looking onto the  $b$ - $c$  plane. Along the  $a$ -direction

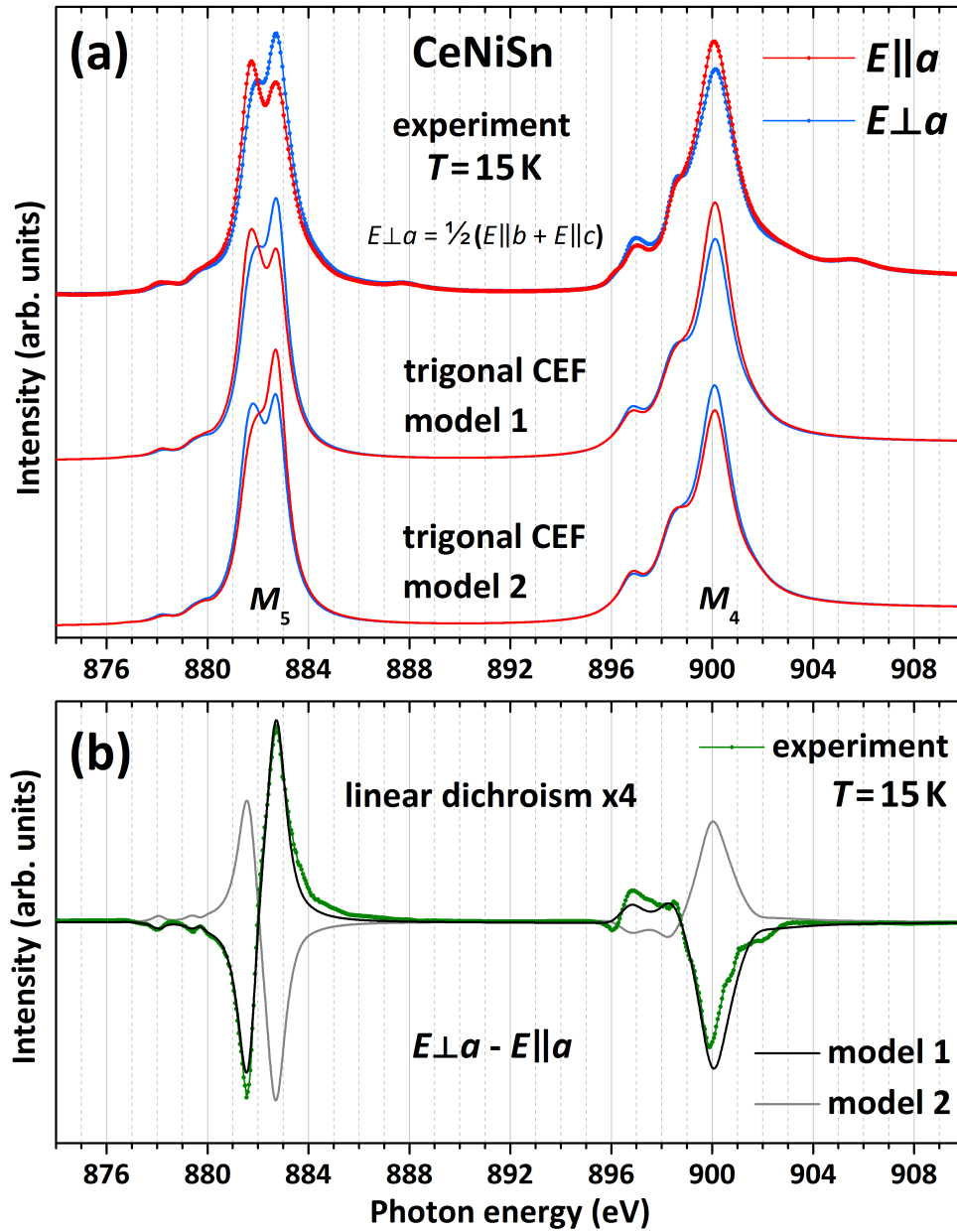


Figure 6.2: (a) The top set of spectra are the experimental data from Fig. 6.1 but with  $E_{\perp a} = \frac{1}{2}(E_{\parallel b} + E_{\parallel c})$ . The bottom and middle set of spectra for  $E_{\parallel a}$  and  $E_{\perp a}$  represent the two calculations in trigonal approximation based on the ground state solutions found in Ref. [17] (see text for details). (b) Comparison of the measured (green) LD and the LD resulting from the two model calculations (Model 1 in black, Model 2 in gray) enlarged by a factor of four.

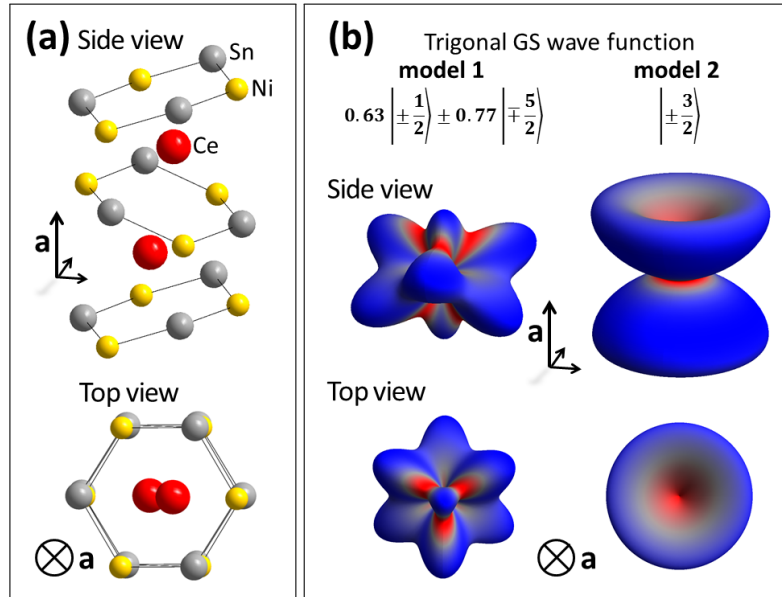


Figure 6.3: (a) Crystal structure of CeNiSn showing the nearest neighbor environment of the Ce ions. A side view and a top view onto the  $b$ - $c$  plane are shown. (b) Spatial distributions of the  $4f$  electrons as resulting from the two trigonal CEF models discussed in the text.

the crystal structure is basically comprised by hexagonal Ni-Sn rings alternating with Ce ions (see side view). In Fig. 6.3(b) the spatial distributions of the  $4f$  electrons for the two trigonal CEF models are depicted from the same perspectives. While the orbital of the pure  $|\pm 3/2\rangle$  has the well-known yo-yo shape and is isotropic within the trigonal plane, the orbital resulting from Model 1 is less extended along the quantization axis  $a$  and features a threefold rotational symmetry around this axis, as can be nicely seen in the top view representation. Considering these orbitals in the crystalline environment, the importance of the exact shape of the ground-state orbital – in particular for the hybridization with the ligand ions – becomes evident.

Information about the excited CEF states can be obtained by investigating the temperature dependence of the linear dichroism. With increasing temperature the excited Kramer's doublets are partially occupied and the contribution of the higher states modifies the polarization dependence of the absorption, so that to a certain extent the excitation energies and symmetry of the excited states can be deduced. In Fig. 6.4(a) the measured temperature-dependent XAS spectra of CeNiSn from 15 K to 250 K are shown. For a better visualization the illustration is focused on the  $M_5$  edge and as in Fig. 6.2 the spectra for  $E \parallel a$  and  $E \perp a$  are presented. In the bottom panel the respective difference spectra  $E \perp a - E \parallel a$  are shown, enlarged by a factor of four. At 50 K the LD remains unchanged compared to 15 K, and it is only faintly reduced at 100 K (magenta curve). Above 100 K a significant reduction of the LD sets in and continues until 250 K without reversing its sign. We can conclude that the excited CEF levels essentially start becoming populated above 100 K. Fig. 6.4(b) displays the theoretically expected polarization-dependent spectra for the

GS⟩	trigonal CEF Model 1		trigonal CEF Model 2
	0.63 ±1/2⟩ ± 0.77 ∓5/2⟩		±3/2⟩
$B_2^0$	<b>-0.454</b>	-0.369	-0.477
$B_4^0$	<b>-0.019</b>	-0.003	0.096
$B_4^3$	<b>-1.807</b>	-1.652	-0.001
$\Delta E_1$	<b>24</b>	18	18
$\Delta E_2$	<b>35</b>	32	32

Table 6.1: Summary of the CEF models discussed in the text. For each the ground-state wave function |GS⟩, the Stevens parameters  $B_n^m$  and the energy splittings from the ground state to the first ( $\Delta E_1$ ) and second ( $\Delta E_2$ ) excited CEF level are given (all in meV). The parameters for Model 2 are taken from Ref. [17]. The solution describing both the low-temperature data and the temperature dependence best is printed in bold.

different temperatures on the basis of Model 1, i.e. with a pure  $|\pm 3/2\rangle$  at  $\Delta E_1 = 18$  meV and  $\alpha|\pm 1/2\rangle - \sqrt{1-\alpha^2}|\mp 5/2\rangle$  with  $|\alpha| = 0.77$  at  $\Delta E_2 = 32$  meV. The simulation qualitatively agrees with the experimental observations at the  $M_5$  edge: The right peak of the  $E \parallel a$  spectrum gains spectral weight with increasing temperature, and at the same time for  $E \perp a$  the left shoulder becomes more pronounced. However, the calculation yields a faster decrease of the LD than the measurement (cf. bottom panels in Fig. 6.4); for example at 100 K a substantial reduction of LD is predicted, whereas the measurement at 100 K basically resembles the low temperature data. A closer look at the  $E \parallel a$  data reveals that here the right peak exceeds the left peak at about 200 K, whereas in the calculation this already happens at 150 K. This is indicated by the green oval in Fig. 6.4(b). These rather faint quantitative discrepancies can be corrected for by assuming larger crystal-field splittings. This is realized in Fig. 6.4(c). Here the same simulation as in (b) is shown but with the first excited CEF doublet at 24 meV and the second one at 35 meV. With these CEF splittings the right and left peak become of the same height at about 200 K (see green oval), so that the calculation now nicely reproduces the measured temperature dependence and the relative changes in the LD are well modeled.

Note that assuming the other mixed state of type  $|1\rangle$  (see equations (6.3); with  $|\alpha| = 0.77$ ) instead of a pure  $|\pm 3/2\rangle$  as first excited state, would lead to a nearly identical temperature dependence because both states exhibit a similar polarization dependence. Therefore, in the present case the symmetry of the excited CEF levels cannot be inferred from XAS and we have to rely on the previous findings. The three CEF models used for the simulations in Fig. 6.2 and 6.4 are summarized in Table 6.1. The left column gives the set of trigonal CEF parameters for the mixed ground state with  $|\alpha| = 0.77$  and the excited CEF states at 24 and 35 meV. The middle column refers to the same state with energy splittings of 18 and 32 meV, and the right column refers to the trigonal CEF Model 2 with the pure  $|\pm 3/2\rangle$  ground state. All parameters and energies are given in meV.

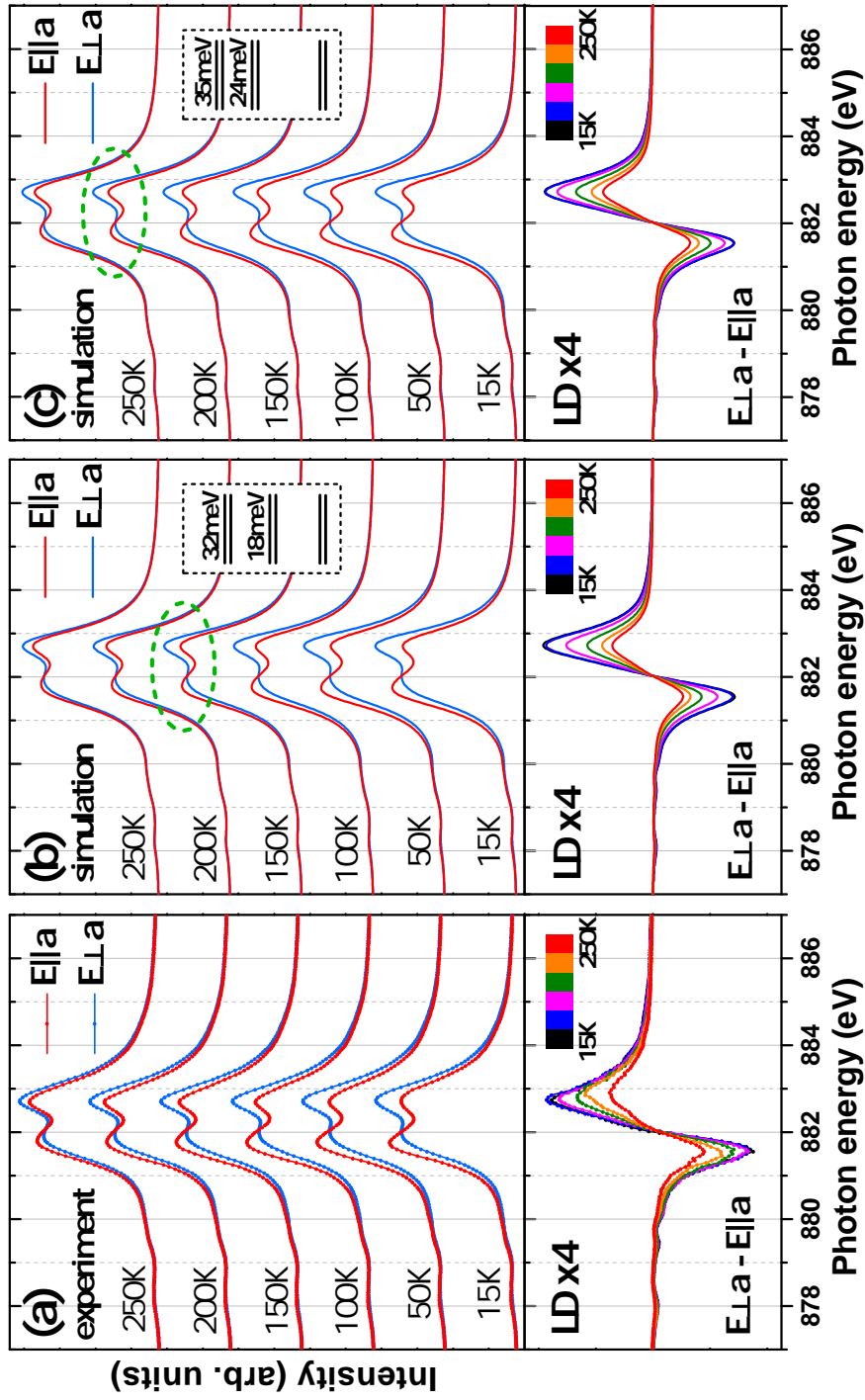


Figure 6.4: (a) Measured temperature-dependent XAS spectra of CeNiSn at the Ce  $M_5$  edge. (b) Calculation of the Ce  $M_5$  edge temperature dependence for Model 1 with crystal-field energy splittings of  $\Delta E_1 = 18$  meV and  $\Delta E_2 = 32$  meV, and (c)  $\Delta E_1 = 24$  meV and  $\Delta E_2 = 35$  meV. The bottom panels in (a) – (c) show the respective difference spectra ( $E_{\perp a} - E_{\parallel a}$ ) for each temperature, enlarged by a factor of four.

## 6.5 Discussion

From the analysis of the linearly polarized XAS data at 15 K we have clearly identified the ground-state wave function of CeNiSn in a trigonal approximation, and from the temperature dependence of the linear dichroism we further obtain an estimate for the excited CEF state energies. Here one should keep in mind that the CEF energies in Ref. [17] were determined for Cu-doped CeNiSn. Although the authors therein state that the peak position of the CEF excitations are not expected to change much upon doping at the Ni site, the actual CEF energies might be slightly different in undoped CeNiSn. With  $\Delta E_1 = 18$  meV and  $\Delta E_2 = 32$  meV the temperature dependence (Fig. 6.4b) is already reproduced quite well, nevertheless our results – in agreement with the observed broad CEF excitation at 40 meV [26] – suggest slightly higher-lying excited Kramer’s doublets. By varying the CEF energies, we were able to quantitatively model the reduction of the LD with increasing temperature with the first excited CEF doublet at  $\approx 24$  meV and the second one at  $\approx 35$  meV (Fig. 6.4c).

The resulting crystal-field scheme can be used to calculate the temperature dependence of the static susceptibility. The magnetic field operator  $\hat{H}^{\text{mag}} = \mathbf{B} \cdot (\mathbf{L} + 2\mathbf{S})$  is added to the Hamiltonian, and after diagonalization and determination of the eigenfunctions and eigenenergies the magnetization follows from the Boltzmann-weighted expectation value of the corresponding operator. In Fig. 6.5 the calculated CEF-only susceptibility  $\chi_{\text{CEF}}(T)$  is shown for  $B \parallel a$  (black line) and  $B \perp a$  (orange line) together with the experimental data  $\chi_{\text{exp}}(T)$ , taken from Ref. [31], for the three crystallographic directions (symbols). For the calculations  $B = 4.65$  T is assumed. Naturally, the trigonal CEF model again does not yield any anisotropy between the  $b$  and  $c$  axis, nevertheless  $\chi_{\text{CEF}}$  bears resemblance to the experimental observation: The easy axis  $a$  and the qualitative trend with rising temperature are nicely reproduced. In the measured susceptibility the deviation from  $\text{Ce}^{3+}$  Curie-Weiss behavior, the suppressed susceptibility along  $b$  and  $c$  and the weak temperature dependence of  $\chi_{\text{exp}}^b$  and  $\chi_{\text{exp}}^c$  indicate the influence of magnetic interactions and an anisotropic Kondo effect [1, 32], which are not accounted for in the calculation. The pronounced peak in  $\chi_{\text{exp}}^a$  is suggested to be connected to antiferromagnetic correlations of quasiparticles [1]. Thus, for a complete quantitative description, molecular and/or exchange fields and anisotropic hybridization effects between  $4f$  and conduction electrons have to be considered. Lower-lying excited CEF states would deteriorate the agreement between  $\chi_{\text{CEF}}(T)$  and the data, which can be seen as a further confirmation that the CEF energies suggested by the INS results on Cu-doped CeNiSn are too low. However, the changes in  $\chi_{\text{CEF}}(T)$  when varying  $\Delta E_{1,2}$  are small. The magnetic moments deduced from the trigonal CEF ground-state wave function  $0.63|\pm 1/2\rangle \pm 0.77|\mp 5/2\rangle$  are  $\mu_{\text{CEF}}^{\parallel a} = 1.08 \mu_B$  for the  $a$  direction and  $\mu_{\text{CEF}}^{\perp a} = 0.48 \mu_B$  perpendicular to  $a$ . Here an infinitesimal small temperature and magnetic field along the respective directions have been taken into account.

In the XAS data (Fig. 6.1) some spectral weight originating from a small  $4f^0$  contribution in the ground state reflects the delocalization of the  $4f$  electrons due to  $c$ - $f$  hybridization. This spectral weight becomes evident as weak humps on the high energy side of the  $M_5$  and  $M_4$  absorption edges at about 888 eV and 906 eV. From analyzing the integrated intensities of the  $4f^0$  humps in the isotropic spectrum (after subtraction of a linear background, cf. Ref. [33]), the  $4f^0$  weight is found to be minor ( $\lesssim 1\%$ ). Its size is comparable to the result for  $\text{CeRu}_2\text{Al}_{10}$  (Chapter 4), for which the detailed HAXPES investigation of the Ce  $3d$  core level spectrum yields a  $4f^0$

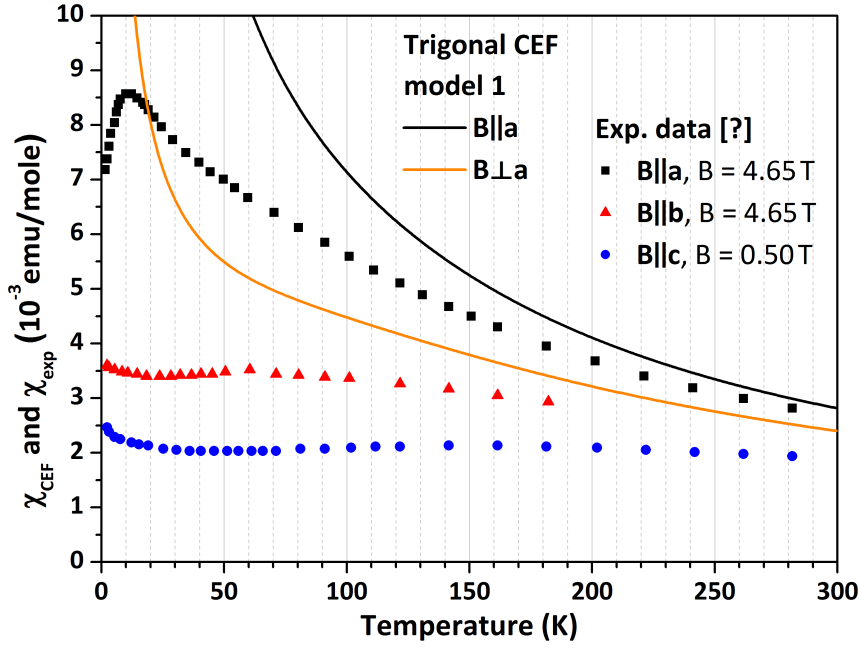


Figure 6.5: Temperature dependence of the static susceptibility adapted from Ref. [31] for the three crystallographic directions (symbols) and calculated from the trigonal CEF Model 1 (lines) with the excited CEF states at 24 and 35 meV for  $B \parallel a$  and  $B \perp a$  (see left column in Table 6.1).

contribution of approximately 6 % in the ground state (Chapter 5). Therefore, the error made by disregarding the hybridization in the calculation is negligible. Moreover, in the temperature dependence (Fig. 6.4) no significant changes are observed up to 100 K, i.e. the polarization dependence is not affected across the Kondo temperature and the energy gap opening. This is also in agreement with our previous observations for the  $\text{CeM}_2\text{Al}_{10}$  compounds (Chapter 3 and 4), where it was shown that the CEF description is applicable to Kondo semiconductors without being hampered by spin gaps or the presence of  $c$ - $f$  hybridization.

Regarding the theoretical explanations for the pseudogap formation (see Sec. 6.1 and the general introduction in Chapter 1), we can confirm the exclusion of the spin-liquid picture because in agreement with Ref. [17] the temperature-dependent XAS data rule out a low-lying CEF excitation below  $k_B T_K = 4.7$  meV. The observed LD at 15 K also clearly excludes a pure  $|\pm 3/2\rangle$  ground state and consequently the Ikeda and Miyake model. Thus, the identification of the mixed ground state speaks in favor of the model by Moreno and Coleman, so that the open question about the driving mechanism behind the gap generation in this kind of Kondo insulating materials finally might be answered.

## 6.6 Conclusion

In summary, we have carried out linearly polarized XAS measurements at the Ce  $M_{4,5}$  edge of CeNiSn and analyzed the data within a full multiplet approach. The monoclinic crystal field was approximated on the basis of a trigonal CEF Hamiltonian and the low-temperature XAS data could be reproduced by assuming a mixed ground state of the form  $0.63| \pm 1/2 \rangle \pm 0.77| \mp 5/2 \rangle$ , thereby having determined the ground-state wave function of CeNiSn. The validity of the trigonal approximation has been discussed. The temperature dependence of the linear dichroism could be qualitatively explained by thermal population of the first and second excited CEF state. Here, the energies of the excited Kramer's doublets can be estimated to be located at 24 and 35 meV. The spectroscopic investigation of the CEF ground state in CeNiSn puts forward the theoretical framework proposed by Moreno and Coleman [23].

## References of Chapter 6

- [1] T. Takabatake, F. Teshima, H. Fujii, S. Nishigori, T. Suzuki, T. Fujita, Y. Yamaguchi, J. Sakurai, and D. Jaccard. *Formation of an anisotropic energy gap in the valence-fluctuating system of CeNiSn*. Phys. Rev. B **41** 9607 (1990). DOI: 10.1103/PhysRevB.41.9607.
- [2] T. Takabatake, M. Nagasawa, H. Fujii, G. Kido, M. Nohara, S. Nishigori, T. Suzuki, T. Fujita, R. Helfrich, U. Ahlheim, K. Fraas, C. Geibel, and F. Steglich. *Anisotropic suppression of the energy gap in CeNiSn by high magnetic fields*. Phys. Rev. B **45** 5740 (1992). DOI: 10.1103/PhysRevB.45.5740.
- [3] K. Izawa, T. Suzuki, T. Fujita, T. Takabatake, G. Nakamoto, H. Fujii, and K. Maezawa. *Anomalous field dependence of specific heat of CeNiSn below 1 K*. J. Magn. Magn. Mater. **177 – 181** 395 (1998). DOI: 10.1016/S0304-8853(97)00408-3.
- [4] P. S. Riseborough. *Heavy fermion semiconductors*. Adv. Phys. **49** 257 (2000). DOI: 10.1080/000187300243345.
- [5] I. Higashi, K. Kobayashi, T. Takabatake, and M. Kasaya. *The crystal structure of CeT<sub>3</sub>Sn (T = Ni, Pd and Pt)*. J. Alloy. and Comp. **193** 300 (1993). DOI: 10.1016/0925-8388(93)90378-Z.
- [6] T. Takabatake, H. Tanaka, Y. Bando, H. Fujii, S. Nishigori, T. Suzuki, T. Fujita, and G. Kido. *Anisotropic physical properties of the Kondo semiconductor CeRhSb*. Phys. Rev. B **50** 623 (1994). DOI: 10.1103/PhysRevB.50.623.
- [7] M. Kyogaku, Y. Kitaoka, H. Nakamura, K. Asayama, T. Takabatake, F. Teshima, and H. Fujii. *NMR Investigation of Energy Gap Formation in the Valence Fluctuating Compound CeNiSn*. J. Phys. Soc. Jpn. **59** 1728 (1990). DOI: 10.1143/JPSJ.59.1728.
- [8] M. Kyogaku, Y. Kitaoka, H. Nakamura, K. Asayama, T. Takabatake, F. Teshima, and H. Fujii. *NMR study of quasiparticle gap in CeNiSn*. Physica B: Condens. Matter **171** 235 (1991). DOI: 10.1016/0921-4526(91)90521-F.
- [9] S. Nishigori, T. Suzuki, T. Fujita, H. Tanaka, T. Takabatake, and H. Fujii. *Specific heat study on the energy gap state in CeRhSb and CeNiSn*. Physica B: Condens. Matter **199–200** 473 (1994). DOI: 10.1016/0921-4526(94)91873-2.
- [10] T. Takabatake, G. Nakamoto, H. Tanaka, Y. Bando, H. Fujii, S. Nishigori, H. Goshima, T. Suzuki, T. Fujita, I. Oguro, T. Hiraoka, and S. Malik. *Coherence Kondo gap in CeNiSn and CeRhSb*. Physica B: Condens. Matter **199–200** 457 (1994). DOI: 10.1016/0921-4526(94)91868-6.
- [11] T. Ekino, T. Takabatake, H. Tanaka, and H. Fujii. *Tunneling Evidence for the Quasiparticle Gap in Kondo Semiconductors CeNiSn and CeRhSb*. Phys. Rev. Lett. **75** 4262 (1995). DOI: 10.1103/PhysRevLett.75.4262.

## References of Chapter 6

- [12] S. Nohara, H. Namatame, A. Fujimori, and T. Takabatake. *Photoemission study of CeNiSn and related compounds*. Phys. Rev. B **47** 1754 (1993). DOI: 10.1103/PhysRevB.47.1754.
- [13] A. Ślebarski, A. Jezierski, S. Mähl, M. Neumann, and G. Borstel. *Electronic structure of CeNi<sub>1-x</sub>Pd<sub>x</sub>Sn and LaMSn (M=Ni,Cu,Pd)*. Phys. Rev. B **56** 7245 (1997). DOI: 10.1103/PhysRevB.56.7245.
- [14] J.-S. Kang, C. G. Olson, Y. Inada, Y. Ōnuki, S. K. Kwon, and B. I. Min. *Valence-band photoemission study of single crystalline CeNiSn*. Phys. Rev. B **58** 4426 (1998). DOI: 10.1103/PhysRevB.58.4426.
- [15] T. E. Mason, G. Aeppli, A. P. Ramirez, K. N. Clausen, C. Broholm, N. Stücheli, E. Bucher, and T. T. M. Palstra. *Spin gap and antiferromagnetic correlations in the Kondo insulator CeNiSn*. Phys. Rev. Lett. **69** 490 (1992). DOI: 10.1103/PhysRevLett.69.490.
- [16] T. J. Sato, H. Kadowaki, H. Yoshizawa, T. Ekino, T. Takabatake, H. Fujii, L. P. Regnault, and Y. Isikawa. *Neutron scattering study of antiferromagnetic correlations in the Kondo semiconductor CeNiSn*. J. Phys.: Condens. Matter **7** 8009 (1995). DOI: 10.1088/0953-8984/7/41/010.
- [17] J.-Y. So, S.-J. Oh, J.-G. Park, D. T. Adroja, K. A. McEwen, and T. Takabatake. *Inelastic neutron scattering studies of doped CeNiSn and CeRhSb: Crystal-field excitations and origin of the pseudogap*. Phys. Rev. B **71** 214441 (2005). DOI: 10.1103/PhysRevB.71.214441.
- [18] K. A. Kikoin, M. N. Kiselev, A. S. Mishchenko, and A. de Visser. *Thermodynamics of CeNiSn at low temperatures and in weak magnetic fields*. Phys. Rev. B **59** 15070 (1999). DOI: 10.1103/PhysRevB.59.15070.
- [19] Y. Kagan, K. A. Kikoin, and N. V. Prokof'ev. *Nature of the pseudogap in the energy spectrum of CeNiSn*. JETP Lett. **57** 600 (1993).
- [20] Y. Kagan, K. A. Kikoin, and A. S. Mishchenko. *Interplay between heavy fermions and crystal-field excitation in Kondo lattices: Low-temperature thermodynamics and inelastic neutron scattering spectra of CeNiSn*. Phys. Rev. B **55** 12348 (1997). DOI: 10.1103/PhysRevB.55.12348.
- [21] H. Ikeda and K. Miyake. *A Theory of Anisotropic Semiconductor of Heavy Fermions*. J. Phys. Soc. Jpn. **65** 1769 (1996). DOI: 10.1143/JPSJ.65.1769.
- [22] M. Miyazawa and K. Yamada. *Theory of the Hybridization Gap in Ce Compounds with Crystalline Electric Field Splitting*. J. Phys. Soc. Jpn. **72** 2033 (2003). DOI: 10.1143/JPSJ.72.2033.
- [23] J. Moreno and P. Coleman. *Gap-Anisotropic Model for the Narrow-Gap Kondo Insulators*. Phys. Rev. Lett. **84** 342 (2000). DOI: 10.1103/PhysRevLett.84.342.
- [24] M. Kohgi, K. Ohoyama, T. Osakabe, M. Kasaya, T. Takabatake, and H. Fujii. *Neutron scattering study of CeNiSn*. Physica B: Condens. Matter **186-188** 409 (1993). DOI: 10.1016/0921-4526(93)90588-w.
- [25] P. A. Alekseev, E. S. Klement'ev, V. N. Lazukov, E. V. Nefedova, I. P. Sadikov, and M. N. Khlopkin. *4f Electrons and the formation of the ground state in the Kondo insulator CeNiSn*. JETP Lett. **79** 665 (1994).

- [26] J.-G. Park, D. T. Adroja, K. A. McEwen, Y. J. Bi, and J. Kulda. *Possible crystal-field excitation in single-crystal CeNiSn*. Phys. Rev. B **58** 3167 (1998). DOI: 10.1103/PhysRevB.58.3167.
- [27] D. Adroja, B. Rainford, A. Neville, and A. Jansen. *Crossover from antiferromagnetic Kondo metal to Kondo insulator in CePt<sub>1-x</sub>Ni<sub>x</sub>Sn alloys*. Physica B: Condens. Matter **223 – 224** 275 (1996). DOI: 10.1016/0921-4526(96)00098-1.
- [28] A. Tanaka and T. Jo. *Resonant 3d, 3p and 3s PES in Transition Metal Oxides Predicted at 2p Threshold*. J. Phys. Soc. Jpn. **63** 2788 (1994). DOI: 10.1143/JPSJ.63.2788.
- [29] R. D. Cowan. *The Theory of Atomic Structure and Spectra*. University of California Press, Berkeley - Los Angeles - London, 1981.
- [30] P. Hansmann, A. Severing, Z. Hu, M. W. Haverkort, C. F. Chang, S. Klein, A. Tanaka, H. H. Hsieh, H.-J. Lin, C. T. Chen, B. Fåk, P. Lejay, and L. H. Tjeng. *Determining the Crystal-Field Ground State in Rare Earth Heavy Fermion Materials Using Soft-X-Ray Absorption Spectroscopy*. Phys. Rev. Lett. **100** 066405 (2008). DOI: 10.1103/PhysRevLett.100.066405.
- [31] A. Hiess, I. Zobkalo, M. Bonnet, J. Schweizer, E. Lelièvre-Berna, F. Tasset, Y. Isikawa, and G. H. Lander. *Polarized neutron studies of CeNiSn*. J. Phys.: Condens. Matter **9** 9321 (1997). DOI: 10.1088/0953-8984/9/43/016.
- [32] F. Aliev, J. Martinez, T. Takabatake, A. Menovsky, V. Moshchalkov, and Y. Bruynseraede. *Nonlinear susceptibility as a probe for magnetic correlations in CeNiSn*. Czechoslovak J. Phys. **46** 1995 (1996). DOI: 10.1007/BF02570989.
- [33] T. Willers, D. T. Adroja, B. D. Rainford, Z. Hu, N. Hollmann, P. O. Körner, Y.-Y. Chin, D. Schmitz, H. H. Hsieh, H.-J. Lin, C. T. Chen, E. D. Bauer, J. L. Sarrao, K. J. McClellan, D. Byler, C. Geibel, F. Steglich, H. Aoki, P. Lejay, A. Tanaka, L. H. Tjeng, and A. Severing. *Spectroscopic determination of crystal-field levels in CeRh<sub>2</sub>Si<sub>2</sub> and CeRu<sub>2</sub>Si<sub>2</sub> and of the 4f<sup>0</sup> contributions in CeM<sub>2</sub>Si<sub>2</sub> (M=Cu, Ru, Rh, Pd, and Au)*. Phys. Rev. B **85** 035117 (2012). DOI: 10.1103/PhysRevB.85.035117.



## 7 Correlation between ground state and orbital anisotropy in heavy fermion materials

Proc. Natl. Acad. Sci. USA **112** (8), 2384 (2015)

*This chapter is published as Proc. Natl. Acad. Sci. USA **112** (8), 2348 (2015). A. Severing supervised the project and guided the experiment, the scientific discussion and the publication process. The research concept was designed by A. Severing and L. H. Tjeng. The single crystals were synthesized and provided by E. D. Bauer, J. L. Sarrao and J. D. Thompson. The sample preparation and the experimental planning were carried out by T. Willers and myself. V. Sessi and N. B. Brookes (the responsible beamline scientists at ESRF for the technical support during the experiment), A. Severing, T. Willers, Z. Hu and myself constituted the experimental team and performed the experiment. The program code for the data simulation was provided by A. Tanaka. The scientific discussion, the analysis/interpretation of the data and the writing of the manuscript were performed by A. Severing, T. Willers, L. H. Tjeng, S. Wirth, E. D. Bauer, J. D. Thompson and myself.*

### Abstract

The interplay of structural, orbital, charge and spin degrees of freedom is at the heart of many emergent phenomena, including superconductivity. Unraveling the underlying forces of such novel phases is a great challenge because it not only requires understanding each of these degrees of freedom, it also involves accounting for the interplay between them. Cerium-based heavy fermion compounds are an ideal playground for investigating these interdependencies, and we present evidence for a correlation between orbital anisotropy and the ground states in a representative family of materials. We have measured the  $4f$  crystal-electric field ground-state wave functions of the strongly correlated materials  $\text{CeRh}_{1-x}\text{Ir}_x\text{In}_5$  with great accuracy using linear polarization-dependent soft x-ray absorption spectroscopy. These measurements show that these wave functions correlate with the ground state properties of the substitution series, which covers long-range antiferromagnetic order, unconventional superconductivity, and coexistence of these two states.

### 7.1 Introduction

Why do many chemically and structurally highly similar compounds develop different ground states? This seemingly simple question still eludes a straightforward description despite intense research. Yet, it is specifically pressing in view of the quest for a deeper insight into unconventional superconductivity.

We here investigate heavy fermion metals, i.e. rare earth or actinide materials, in which a plethora of phenomena including antiferromagnetism and unconventional superconductivity

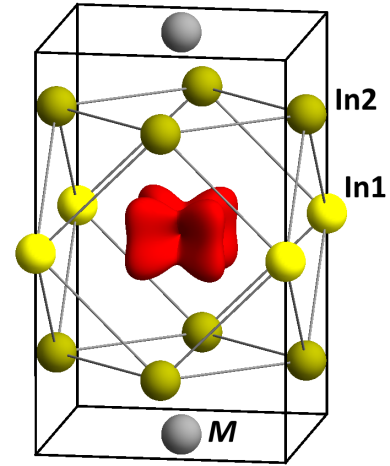


Figure 7.1: Structure of  $CeMIn_5$ . The Ce atom is represented by the angular distribution of the  $4f$  CEF ground-state orbital (red). The In1 (yellow), In2 (dark yellow) and the transition metal  $M$  (gray) are labeled in the figure.

can be observed. In these compounds, the  $f$  electrons hybridize with the conduction electrons ( $cf$ -hybridization) and, in analogy to the Kondo effect in diluted systems, the local magnetic moments can be screened in these so-called “Kondo lattices” at sufficiently low temperatures. However, the Kondo effect competes with the Ruderman-Kittel-Kasuya-Yosida (RKKY) interaction which typically favors long-range magnetic order. As a result of this competition a quantum phase transition from magnetically ordered to paramagnetic, more itinerant  $f$  electron behavior can take place. The balance of both interactions can be tuned by external parameters such as pressure, magnetic field or doping [1]. Non-Fermi liquid behavior and, of interest here, unconventional superconductivity often occurs in the vicinity of such quantum critical points. However, despite research over the last thirty years, the ability to predict conditions favorable for superconductivity has remained elusive. Here, the cerium 115 family  $CeMIn_5$  with  $M = Co, Ir,$  and  $Rh$  is ideally suited for a systematic study because ground states and changes in Fermi volumes in this family can be tuned easily by substitutions of one  $M$  element for another [2–25].

These heavy fermion compounds  $CeMIn_5$  crystallize in the tetragonal  $HoCoGa_5$ -type structure as depicted in Fig. 7.1 with In1 being the in-plane and In2 the out-of-plane indium. Figure 7.2 shows the substitution phase diagram of  $CeRhIn_5$ , where Rh is substituted by Ir or Co [5, 8–10, 12–15]. For clarity we show the magnetically ordered and superconducting regions on separate scales (up and down, respectively).  $CeCoIn_5$  and  $CeIrIn_5$  are superconductors with transition temperatures of  $T_c = 2.3$  and  $0.4$  K, [6, 7].  $CeRhIn_5$ , however, orders antiferromagnetically at  $T_N = 3.8$  K. The magnetic order of  $CeRhIn_5$  is incommensurate (IC AF) with the magnetic moments aligned in the  $ab$  plane, propagating in a spiral along the tetragonal  $c$ -axis [3]. Substituting Rh with Ir or Co tunes the ground state away from magnetic ordering towards bulk superconductivity by passing through regions where magnetic order and superconductivity coexist, and where – in the case of Ir substitution – a second commensurate magnetic phase has been observed [10]. A commensurate phase has also been observed on the Co side, but here the coexistence with the incommensurate order is still a matter of debate, possibly due to uncertainties of the samples’ stoichiometry [12–15]. We note that the Fermi surface of  $CeRhIn_5$  resembles that of  $LaRhIn_5$ , i.e. the  $4f$  electron of Ce remains localized and does not contribute to the Fermi surface volume, in contrast to the Ir and Co samples which show enlarged Fermi

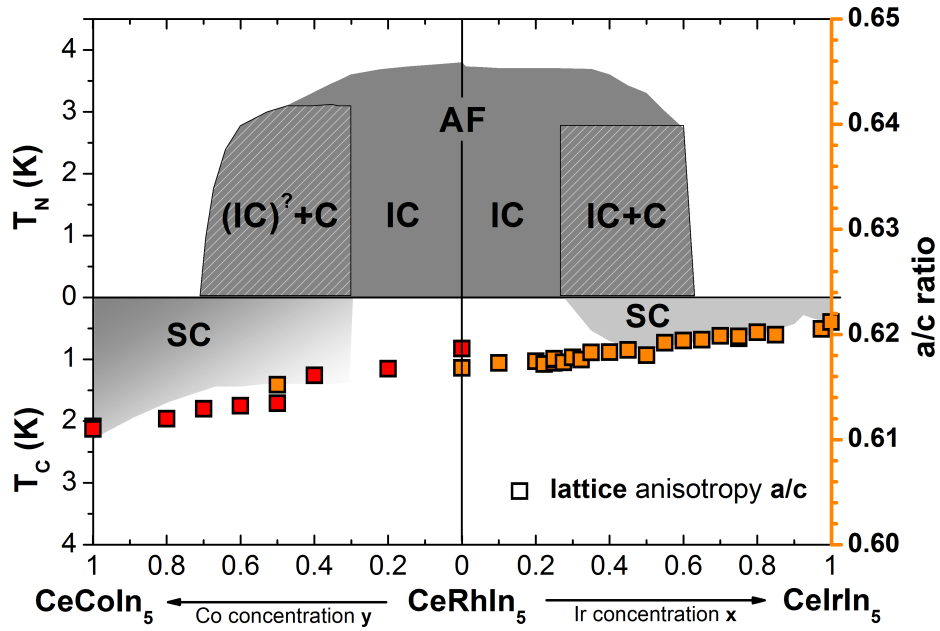


Figure 7.2: Phase diagram of  $\text{CeRh}_{1-x}\text{Ir}_x\text{In}_5$  and  $\text{CeRh}_{1-y}\text{Co}_y\text{In}_5$  as adapted from Refs. [5, 8–10, 12–15] showing the magnetically ordered and superconducting regions as function of the Ir and Co concentration. The incommensurate antiferromagnetic ordered phases (IC AF) and the commensurate ones (C AF) are colored dark gray and hatched gray, respectively, and the regions of superconductivity (SC) are marked light gray. The question mark on the Co side refers to the on-going discussion concerning the coexistence of IC and C AF order. The temperature scales of  $T_N$  and  $T_c$  are shown separately, the former one pointing up, the latter one pointing down. The colored squares show the lattice anisotropy  $a/c$  (right scale) for  $\text{CeRh}_{1-x}\text{Ir}_x\text{In}_5$  and  $\text{CeRh}_{1-y}\text{Co}_y\text{In}_5$ . The lattice constants  $a$  and  $c$  are taken from Ref. [8] (orange squares) and [5] (red squares).

surfaces volumes, implying a more itinerant  $f$  electron behavior [18–22, 25], especially in the regions of pure superconductivity [23, 24].

On the search for interdependencies of physical parameters and ground state properties Bauer *et al.* speculated about a linear relationship between lattice anisotropy  $c/a$  (here  $a$  and  $c$  are the lattice constants) and the superconducting transition temperature  $T_c$  for the superconducting plutonium and cerium 115 compounds [26]. We, however, can see from Fig. 7.2 that this relationship does not hold for almost half of the phase diagram. The colored squares in Fig. 7.2 show the lattice anisotropy  $c/a$  (or rather  $a/c$ ) on top of the  $\text{CeRh}_{1-y}\text{Co}_y\text{In}_5 - \text{CeRh}_{1-x}\text{Ir}_x\text{In}_5$  phase diagram. The  $a/c$  ratios are calculated from the values given in Ref. [8] (orange squares) and Ref. [5] (red squares) and in the following we will refer to  $a/c$  only as lattice anisotropy. Figure 7.2 shows that Bauer *et al.*'s scaling works rather well in the purely superconducting regions. However, for magnetically ordered, Rh-rich samples this linear dependency of  $T_c$  on  $a/c$

obviously breaks down. A closer inspection reveals that even in the region of phase coexistence there are significant deviations from a linear dependency (CeRh<sub>1-x</sub>Ir<sub>x</sub>In<sub>5</sub> with 0.3 ≤ x ≤ 0.45). Consequently, the lattice anisotropy has no predictive power concerning the formation of a superconducting ground state, motivating us to look further for a more fundamental parameter. In the following we concentrate on the CeRh<sub>1-x</sub>Ir<sub>x</sub>In<sub>5</sub> substitution series because the phase diagram is well defined (see Fig. 7.2).

The importance of momentum-dependent hybridization and the impact of the anisotropic crystal-electric field (CEF) ground-state wave functions has been discussed by several groups [27–31]. For the heavy fermion compound CeIrIn<sub>5</sub> Shim *et al.* have even made specific predictions on the basis of first-principle dynamical mean-field theory calculations [32]. In particular, their calculations claim that the out-of-plane hybridization with the In<sub>2</sub> ions is stronger than the in-plane one. These theoretical findings of anisotropic hybridization should be reflected in the CEF potential, implying a systematic change of the CEF wave function with hybridization and, consequently, with the ground state properties. However, such an impact of the CEF wave function on the ground state properties has never been proven experimentally, most likely due to the lack of accuracy of common methods. Here we present results of a systematic investigation of the CEF ground states and the different ground state properties of CeRh<sub>1-x</sub>Ir<sub>x</sub>In<sub>5</sub> using the soft x-ray absorption technique, which specifically targets the 4*f* ground-state wave function.

## 7.2 Materials and methods

**Samples** High-quality single crystals of CeRh<sub>1-x</sub>Ir<sub>x</sub>In<sub>5</sub> were grown by flux-growth and well characterized by magnetic susceptibility and/or heat capacity to ensure their nominal composition is in accordance with the phase diagram [8, 10]. Before the absorption experiment all crystals were aligned within 1-2° by Laue x-ray diffraction.

**Method** The linearly polarized soft XAS experiment was performed at the European Synchrotron Radiation Facility (ESRF) in Grenoble, France, at the ID08 undulator beamline. We recorded the Ce *M*-edge absorption spectra in the total electron yield mode (TEY). The energy resolution at the *M*<sub>4,5</sub> edges ( $h\nu \approx 875 - 910$  eV) was set to 0.2 eV. The samples were cleaved *in situ* in an ultra high vacuum chamber with a pressure of  $2 \times 10^{-10}$  mbar at 8 K. The *M*<sub>4,5</sub> edges were recorded for light polarized parallel ( $E \parallel c$ ) and perpendicular ( $E \perp c$ ) to the tetragonal *c* axis. Here the undulator beamline has the advantage that for normal incidence the polarization can be changed without moving the sample, so that the same sample spot is probed for both polarization directions. For each sample different spots were probed in order to rule out sample inhomogeneities. The data of CeRh<sub>1-x</sub>Ir<sub>x</sub>In<sub>5</sub> were taken at 8 K for the four Ir substitutions  $x = 0.2, 0.3, 0.5,$  and  $0.75$ . The excited CEF states are above 5 meV ( $\approx 50$  K) [33–35] so that at 8 K only the ground state is probed. The data of CeRhIn<sub>5</sub> ( $x = 0$ ), CeIrIn<sub>5</sub> ( $x = 1$ ), and also of CeCoIn<sub>5</sub> were taken in a previous experiment [35]. For the data analysis all data were normalized to the intensity of the isotropic spectra  $I_{iso} = (2I_{E \perp c} + I_{E \parallel c})/3$ .

**Analysis** The XAS data have been simulated with ionic full multiplet calculations based on the XTLS 8.3 program [36]. The atomic parameters are given by reduced Hartree-Fock values. The

reduction accounts for the configuration interaction which is not included in the Hartree-Fock calculations and is determined from fitting the isotropic spectra  $I_{iso}$ . Typical reductions are about 40% for the  $4f - 4f$  Coulomb interactions and about 20% for the  $3d - 4f$  interactions [35, 37, 38]. In the present manuscript the LD of the end members of the series were analyzed in the same manner as for the substitution series investigated here.

## 7.3 Experimental results

**Soft x-ray absorption spectroscopy and choice of samples** We recently started using soft x-ray absorption spectroscopy (XAS) at the rare earth  $M$ -edges as a method for measuring CEF ground-state wave functions in heavy fermion compounds [35, 37, 38]. Here the dipole selection rules for linearly polarized light provide the sensitivity to the ground state symmetry and allow its determination with unprecedented accuracy. The knowledge of excited CEF states is not required for the ground state analysis as long as the data are taken at low enough temperatures, nor is data statistics or background hampering the result. This is a great advantage over more conventional methods like inelastic neutron scattering and single-crystal susceptibility.

We have chosen the Ir concentrations  $x = 0, 0.2, 0.3, 0.5, 0.75$  and 1 of the  $\text{CeRh}_{1-x}\text{Ir}_x\text{In}_5$  series for the linear polarized soft XAS experiment. Here  $x = 0$  and 0.2 cover the purely incommensurate antiferromagnetic region of the phase diagram with an almost identical  $T_N$ . The region of phase coexistence, which comprises an incommensurate, a commensurate and a superconducting state, is covered with the  $x = 0.3$  and 0.5 samples. We note that in both magnetic phases the magnetic moments are aligned antiferromagnetically in the basal plane and that the region of phase coexistence has been discussed in detail in Ref. [16]. The magnetic order decays rapidly with further increasing Ir concentration so that the samples with  $x = 0.75$  and 1 are purely superconducting. By this choice we cover all phases of interest with two samples each for our systematic investigation of the orbital anisotropy.

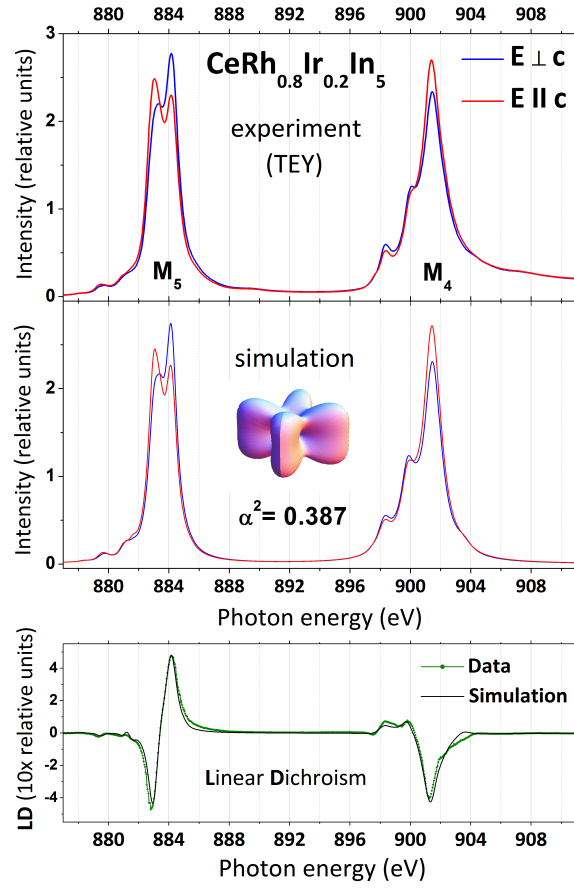
**XAS data of  $\text{CeRh}_{0.8}\text{Ir}_{0.2}\text{In}_5$**  As an example, the top of Fig. 7.3 shows the total-electron-yield (TEY) intensities of the cerium  $M_4$  and  $M_5$  edge of  $\text{CeRh}_{0.8}\text{Ir}_{0.2}\text{In}_5$  for the two polarizations  $E \perp c$  (blue) and  $E \parallel c$  (red) at  $T = 8$  K. This temperature is low enough to assure excited CEF states are not populated ( $\Delta E_1 \approx 70$  K and  $\Delta E_2 \approx 230$  K) [33–35], so that the clear difference between the two polarizations is representative for the out-of-plane anisotropy of the ground state orbital. The green dots in the bottom panel of Fig. 7.3 present the resulting linear dichroism (LD) in a tenfold enlargement. The LD is the difference of the intensities for  $E \perp c$  and  $E \parallel c$ . The data were then analyzed with an ionic full multiplet calculation (see section Analysis in Materials and Methods).

The CEF ground state in this compound family is a  $\Gamma_7$  Kramer's doublet [33–35] and can be expressed in terms of  $J_z$  as

$$\Gamma_7 = \alpha | \pm 5/2 \rangle + \sqrt{1 - \alpha^2} | \mp 3/2 \rangle.$$

The quantity  $\alpha^2$  determines the out-of-plane anisotropy where  $\alpha^2 > 1/6$  ( $\alpha^2 < 1/6$ ) corresponds to a more oblate (prolate)  $4f$  orbital. We find that a  $\Gamma_7$  ground state with  $\alpha^2 = 0.387 \pm 0.005$  describes the data (see middle panel of Fig. 7.3), and in particular the LD (see black line in the

Figure 7.3: Measured (top) and simulated (middle) linearly polarized XAS spectra of  $\text{CeRh}_{0.8}\text{Ir}_{0.2}\text{In}_5$  at the  $M_{4,5}$  edges at  $T = 8$  K. The red spectra refer to measurements and simulations with  $E \parallel c$  and the blue ones with  $E \perp c$ . The inset in the middle panel shows the corresponding  $4f$  spatial distribution. The bottom panel compares the measured (green dots) and simulated LD (black line) enlarged by a factor of ten.



bottom panel), very well. The inset visualizes the corresponding  $4f$  orbital. Note that dipole experiments like inelastic neutron scattering or soft XAS determine  $\alpha^2$ , so that the sign of  $\alpha$  cannot be determined.

**Linear dichroism of all compositions** The results for the other Ir concentrations, which were obtained in the same manner, are summarized in Fig. 7.4. In the top panels of Fig. 7.4 the measured LD of both edges is depicted for the entire series of  $\text{CeRh}_{1-x}\text{Ir}_x\text{In}_5$  from  $x = 0$  to 1. The LD is largest for the two Rh rich concentrations  $x = 0$  and 0.2 (red and orange dots). It then decreases rapidly for the intermediate Ir concentration  $x = 0.3$  (light green) and even more so for  $x = 0.5$  (dark green). The LD is smallest and almost the same on the Ir rich side ( $x = 0.75$  and 1, light and dark blue dots). The lower panels of Fig. 7.4 exhibit the corresponding simulated LD, which reproduce nicely the measured strong reduction of the LD with increasing Ir concentration. The resulting orbital anisotropies  $\alpha^2$  are listed in Table 7.1. It is important to note that the LD of the interim compositions cannot be simulated with the respective fractions of the LD of  $\text{CeRhIn}_5$  and  $\text{CeIrIn}_5$ . This is most obvious for  $\text{CeRh}_{0.5}\text{Ir}_{0.5}\text{In}_5$ , where  $0.5 \text{ LD}_{\text{CeRhIn}_5} + 0.5 \text{ LD}_{\text{CeIrIn}_5}$  would yield an  $\alpha^2 = 0.321$ , while a value of 0.284 has been observed. This change of LD indicates that the CEF ground-state wave function changes monotonically, but not linearly

sample	CeRhIn <sub>5</sub>		CeRh <sub>1-x</sub> Ir <sub>x</sub> In <sub>5</sub>			CeIrIn <sub>5</sub>	CeCoIn <sub>5</sub>
	0	0.2	0.3	0.5	0.75	1	
$\alpha^2$	0.407	0.387	0.328	0.284	0.242	0.242	0.123
Ce-In1 (Å)	3.292	-	-	-	-	3.305	3.262
Ce-In2 (Å)	3.278	-	-	-	-	3.272	3.283

Table 7.1: Out-of-plane orbital anisotropy  $\alpha^2$  ( $\Delta\alpha^2 = \pm 0.005$ ) for all measured Ir concentrations  $x$  in CeRh<sub>1-x</sub>Ir<sub>x</sub>In<sub>5</sub> and for CeCoIn<sub>5</sub> from the present analysis. Note,  $\alpha^2 = 1/6 \approx 0.166$  would correspond to a cubic-type orbital. Ce-In1 and Ce-In2 are the distances between cerium and the in-plane (In1) and out-of-plane indium (In2) as taken from Ref. [39].

with the Ir concentration, unlike the lattice anisotropy in Fig. 7.2. For completeness we also give the value for CeCoIn<sub>5</sub> in Table 7.1 [35].

## 7.4 Discussion

**Orbital anisotropy  $\alpha^2$  and phase diagram** In Fig. 7.5 the  $\alpha^2$  values are plotted as red circles along with the CeRh<sub>1-x</sub>Ir<sub>x</sub>In<sub>5</sub> phase diagram for illustrating the changes of the wave function with the Ir concentration. The size of the circles corresponds to the error bars. As shown in Fig. 7.5, we now can observe a clear trend between the value of  $\alpha^2$  and the ground state properties of CeRh<sub>1-x</sub>Ir<sub>x</sub>In<sub>5</sub>: The incommensurate antiferromagnetically ordered (IC AF) samples CeRhIn<sub>5</sub> and CeRh<sub>0.8</sub>Ir<sub>0.2</sub>In<sub>5</sub> on the Rh rich side have almost the same large LD (see also Fig. 7.4), yielding the largest  $\alpha^2$ -values within the series; the  $\alpha^2$ -value of the  $x = 0.2$  sample being only 5% smaller than the one of the pure Rh compound. In the intermediate region where the three phases coexist,  $\alpha^2$  decreases rapidly with  $x$ . On the Ir rich side of the phase diagram, in the purely superconducting region,  $\alpha^2$  is small and levels off, i.e. it is identical for CeRh<sub>0.25</sub>Ir<sub>0.75</sub>In<sub>5</sub> and CeIrIn<sub>5</sub>.

Apparently, the superconducting compositions favor the orbitals with smaller  $\alpha^2$  values. This becomes even more evident when taking into account CeCoIn<sub>5</sub>: The  $\alpha^2$  value of CeCoIn<sub>5</sub> is smallest while it has the highest  $T_c$  (Fig. 7.5). Actually, its  $\alpha^2$  value falls rather nicely onto the phase diagram when using the same scaling as for the CeRh<sub>1-x</sub>Ir<sub>x</sub>In<sub>5</sub> substitution series. This strongly supports our conjecture that  $\alpha^2$  is a parameter which correlates with the magnetic as well as the superconducting phases, in contrast to  $a/c$  which only serves the superconducting samples.

The implication of the changing  $J_z$  contribution on the spatial distribution of the  $4f$  electrons in the CEF ground state is obvious when recalling that the pure  $J_z = |\pm 5/2\rangle$  is donut shaped, while the pure  $|\pm 3/2\rangle$  is yo-yo shaped [37]. Upon going from CeRhIn<sub>5</sub> to CeIrIn<sub>5</sub> the orbital extends increasingly out-of-plane (see Fig. 7.5) such that it becomes less oblate with increasing Ir concentration. For CeCoIn<sub>5</sub> the  $4f$  orbital is prolate, i.e. has the largest extension in the  $c$  direction and CeCoIn<sub>5</sub> has the highest superconducting transition temperature. We discuss possible correlations and implications in the following.

Intuitively one would expect that the lattice anisotropy follows the orbital anisotropy, a

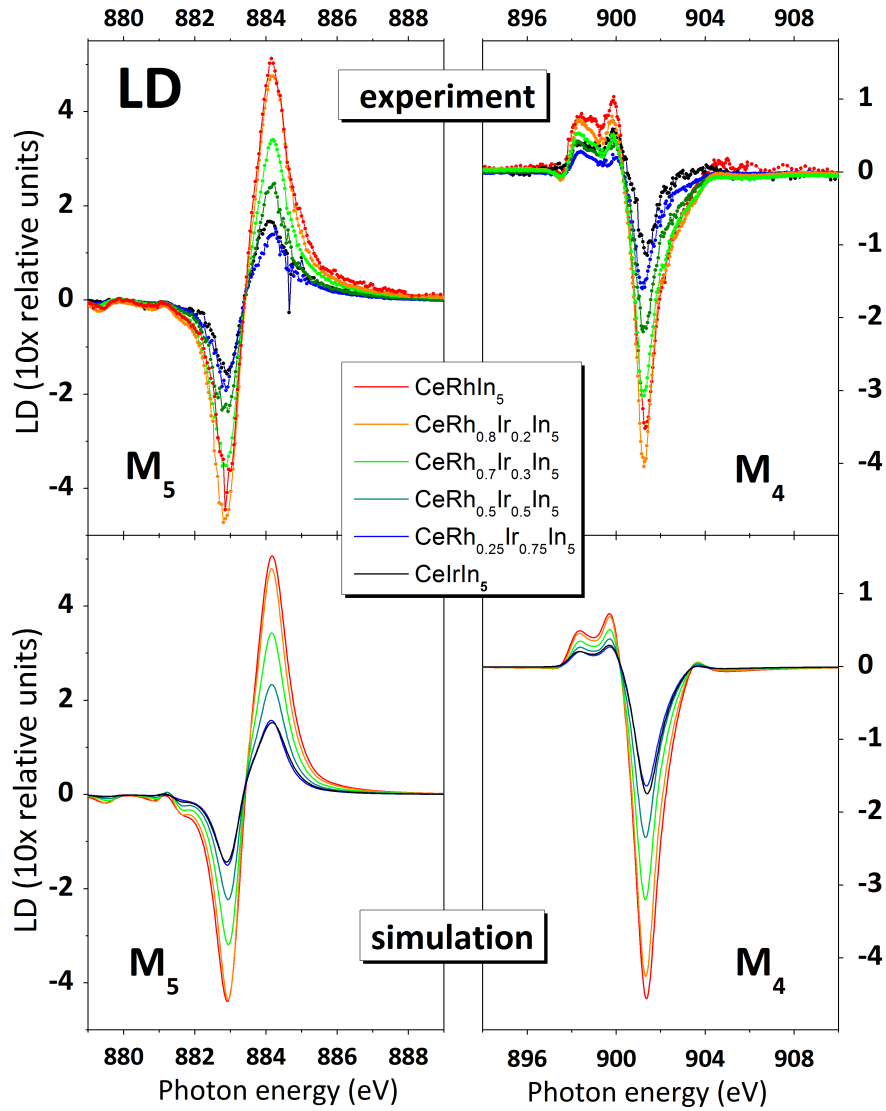


Figure 7.4: The top panels show the experimental linear dichroism (LD) at the  $M_5$  and  $M_4$  edge for the Ir substitutions  $x = 0.2, 0.3, 0.5,$  and  $0.75$  in  $\text{CeRh}_{1-x}\text{Ir}_x\text{In}_5$  at 8 K. Data for  $x = 0$  and 1 were taken in a previous experiment [35]. The bottom panels show the corresponding simulations which reproduce the data very well.

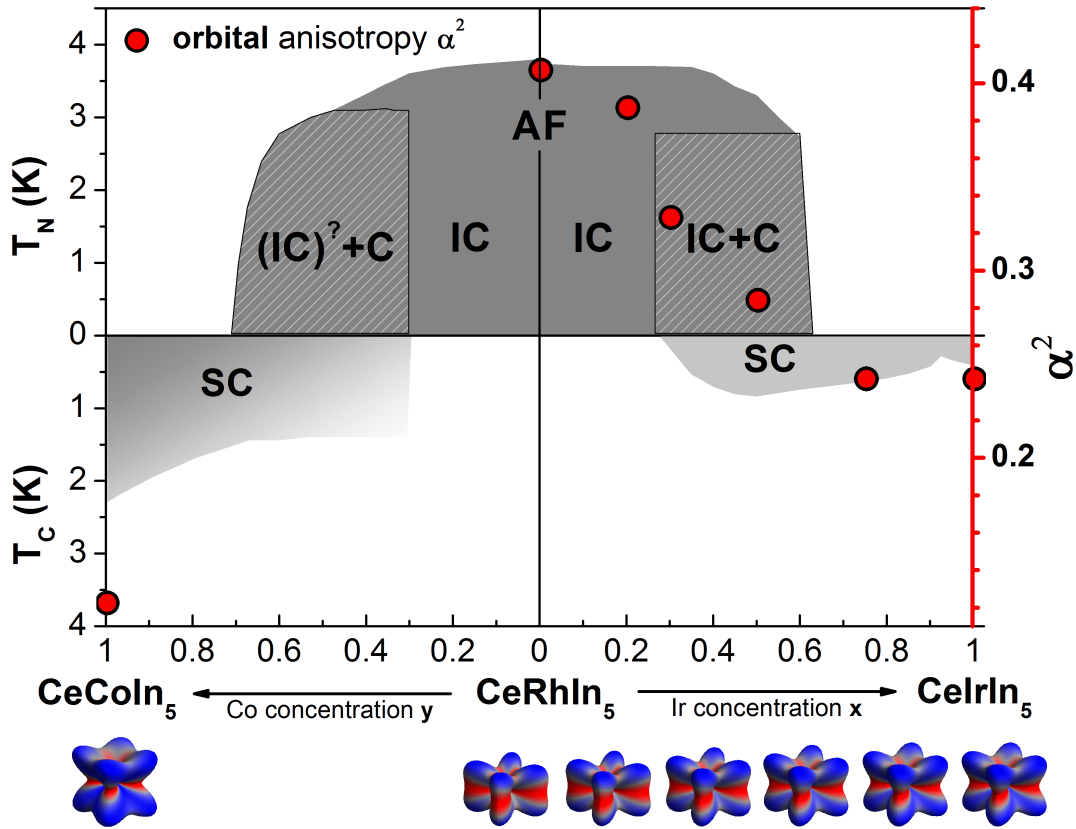


Figure 7.5: Orbital anisotropy  $\alpha^2$  on the right scale as function of  $x$  in  $\text{CeRh}_{1-x}\text{Ir}_x\text{In}_5$  and for  $\text{CeCoIn}_5$ . The evolution with  $x$  of the angular distributions of the  $4f$  CEF ground-state orbitals in  $\text{CeRh}_{1-x}\text{Ir}_x\text{In}_5$  and  $\text{CeCoIn}_5$  is shown below the phase diagram.

behavior which has been observed e.g. in the Ce-monopnictides [40]. However, in the  $\text{CeMIn}_5$  family this is obviously not the case. While the lattice constants of the  $\text{CeRh}_x\text{Ir}_{1-x}\text{In}_5$  series nicely follow Vegard's law [8], so that the *lattice* anisotropy  $a/c$  in Fig. 7.2 changes accordingly with the Ir concentration, the *orbital* anisotropy  $\alpha^2$  changes in a strongly non-linear manner (see Fig. 7.5). Furthermore, while the unit cell becomes shorter along the  $c$ -axis from Rh to Ir, the  $4f$  orbital extends increasingly out of the  $ab$  plane, suggesting an anti-correlation, rather than a correlation, between the  $4f$  wave function's *flatness* and the  $a/c$  ratio. However,  $\text{CeCoIn}_5$  indicates the opposite (i.e. correlating) behavior: in this compound, the  $4f$  orbital is the most extended one along  $c$ , while the smallest  $a/c$  ratio (largest  $c/a$ ) is observed. Apparently, there is no obvious systematics between orbital and lattice anisotropy (compare Fig. 7.2 and Fig. 7.5).

We now focus on the orbital angular distribution with respect to the degree of  $cf$ -hybridization in this compound family. We emphasize that the degree of hybridization has been measured by independent experiments. The stronger  $cf$ -hybridization of the superconducting compounds  $\text{CeIrIn}_5$  and  $\text{CeCoIn}_5$  is reflected in a larger Fermi surface [18–22, 25] and also in a larger

quasielastic line width. Inelastic neutron scattering on powder samples found a line width of  $\approx 1.4$  meV half-width at half-maximum for the magnetically ordering Rh compound and line widths at least twice as large for CeIrIn<sub>5</sub> and CeCoIn<sub>5</sub> [35]. The importance of direction-dependent hybridization is an obvious consequence when combining the two experimental findings of *cf*-hybridization strength and angular distribution of the CEF wave function. The taller orbitals are more strongly hybridized. This is in agreement with the theoretical conjecture by Shim *et al.* [32] that the out-of-plane hybridization with the In2 ions is most important despite nearly identical Ce-In bond lengths (see Table 7.1, [39]), thus providing a channel for the In2-*M* interaction to contribute significantly to the total electronic energy minimization. This yields a natural explanation for why the physical properties depend so much on the transition metal atoms: the shape of the CEF wave function, i.e. the parameter  $\alpha^2$ , marks whether a compound is more itinerant and possibly superconducting, or more localized and antiferromagnetic.

How does this relate to the observed [26] linear correlation between the lattice anisotropy  $a/c$  and  $T_c$  for the superconducting plutonium and cerium 115 compounds? We already noted that this correlation only holds for the superconducting compositions, so that the  $a/c$  ratio by itself cannot be used to predict whether or not a compound becomes superconducting. For example, the  $a/c$  ratio of CeRhIn<sub>5</sub> would indicate a finite  $T_c$  at ambient pressure, while experimentally no superconductivity has been recorded (see Fig. 7.2). Here, we infer that  $\alpha^2$  is the parameter that distinguishes superconducting from non-superconducting compounds. Once the purely superconducting region of the phase diagram has been reached,  $\alpha^2$  does not change any more and the  $a/c$  ratio seemingly tunes  $T_c$ .

## 7.5 Summary

The CEF ground-state wave functions of the CeRh<sub>1-x</sub>Ir<sub>x</sub>In<sub>5</sub> substitution series have been determined and a clear correlation between ground state properties and wave functions has been observed. These findings suggest that the shape of the cerium wave function – expressed through the parameter  $\alpha^2$  – serves as a good predictor of whether a given material becomes superconducting or magnetic. More generally, anisotropic hybridization must be a necessary component in an appropriate description of Kondo lattice materials and of the evolution of their ground states as a function of a non-thermal tuning parameter.

We thank P. Thalmeier for fruitful discussions. The wave function density plots were calculated using the CrystalFieldTheory package for Mathematica written by M. W. Haverkort. Support from the German funding agency DFG under Grant No. 583872 is gratefully acknowledged. Work at LANL was performed under the auspices of the U.S. DOE, Office of Basic Energy Sciences, Division of Materials Sciences and Engineering.

## References of Chapter 7

- [1] P. Gegenwart, Q. Si, and F. Steglich. *Quantum criticality in heavy-fermion metals*. Nature Physics **4** 186 (2008). DOI: 10.1038/nphys892.
- [2] H. Hegger, C. Petrovic, E. G. Moshopoulou, M. F. Hundley, J. L. Sarrao, Z. Fisk, and J. D. Thompson. *Pressure-Induced Superconductivity in Quasi-2D CeRhIn<sub>5</sub>*. Phys. Rev. Lett. **84** 4986 (2000). DOI: 10.1103/PhysRevLett.84.4986.
- [3] W. Bao, P. G. Pagliuso, J. L. Sarrao, J. D. Thompson, Z. Fisk, J. W. Lynn, and R. W. Erwin. *Incommensurate magnetic structure of CeRhIn<sub>5</sub>*. Phys. Rev. B **62** R14621 (2000). DOI: 10.1103/PhysRevB.62.R14621.
- [4] W. Bao, P. G. Pagliuso, J. L. Sarrao, J. D. Thompson, Z. Fisk, J. W. Lynn, and R. W. Erwin. *Erratum: Incommensurate magnetic structure of CeRhIn<sub>5</sub>*. Phys. Rev. B **67** 099903 (2003). DOI: 10.1103/PhysRevB.67.099903.
- [5] V. S. Zapf, E. J. Freeman, E. D. Bauer, J. Petricka, C. Sirvent, N. A. Frederick, R. P. Dickey, and M. B. Maple. *Coexistence of superconductivity and antiferromagnetism in CeRh<sub>1-x</sub>Co<sub>x</sub>In<sub>5</sub>*. Phys. Rev. B **65** 014506 (2001). DOI: 10.1103/PhysRevB.65.014506.
- [6] C. Petrovic, P. G. Pagliuso, M. F. Hundley, R. Movshovich, J. L. Sarrao, J. D. Thompson, Z. Fisk, and P. Monthoux. *Heavy-fermion superconductivity in CeCoIn<sub>5</sub> at 2.3 K*. J. Phys.: Condens. Matter **13** L337 (2001). DOI: 10.1088/0953-8984/13/17/103.
- [7] C. Petrovic, R. Movshovich, M. Jaime, P. G. Pagliuso, M. F. Hundley, J. L. Sarrao, Z. Fisk, and J. D. Thompson. *A new heavy-fermion superconductor CeIrIn<sub>5</sub>: A relative of the cuprates?* Europhys. Lett.) **53** 354 (2001). DOI: 10.1209/epl/i2001-00161-8.
- [8] P. G. Pagliuso, C. Petrovic, R. Movshovich, D. Hall, M. F. Hundley, J. L. Sarrao, J. D. Thompson, and Z. Fisk. *Coexistence of magnetism and superconductivity in CeRh<sub>1-x</sub>Ir<sub>x</sub>In<sub>5</sub>*. Phys. Rev. B **64** 100503 (2001). DOI: 10.1103/PhysRevB.64.100503.
- [9] P. Pagliuso, R. Movshovich, A. Bianchi, M. Nicklas, N. Moreno, J. Thompson, M. Hundley, J. Sarrao, and Z. Fisk. *Multiple phase transitions in Ce(Rh, Ir, Co)In<sub>5</sub>*. Physica B: Condens. Matter **312-313** 129 (2002). DOI: 10.1016/S0921-4526(01)01281-9.
- [10] A. Llobet, A. D. Christianson, W. Bao, J. S. Gardner, I. P. Swainson, J. W. Lynn, J.-M. Mignot, K. Prokes, P. G. Pagliuso, N. O. Moreno, J. L. Sarrao, J. D. Thompson, and A. H. Lacerda. *Novel Coexistence of Superconductivity with Two Distinct Magnetic Orders*. Phys. Rev. Lett. **95** 217002 (2005). DOI: 10.1103/PhysRevLett.95.217002.
- [11] T. Park, F. Ronning, H. Q. Yuan, M. B. Salamon, R. Movshovich, J. L. Sarrao, and J. D. Thompson. *Hidden magnetism and quantum criticality in the heavy fermion superconductor CeRhIn<sub>5</sub>*. Nature **440** 65 (2006). DOI: 10.1038/nature04571.

## References of Chapter 7

- [12] S. Ohira-Kawamura, H. Shishido, A. Yoshida, R. Okazaki, H. Kawano-Furukawa, T. Shibauchi, H. Harima, and Y. Matsuda. *Competition between unconventional superconductivity and incommensurate antiferromagnetic order in  $CeRh_{1-x}Co_xIn_5$* . Phys. Rev. B **76** 132507 (2007). DOI: 10.1103/PhysRevB.76.132507.
- [13] S. Ohira-Kawamura, H. Kawano-Furukawa, H. Shishido, R. Okazaki, T. Shibauchi, H. Harima, and Y. Matsuda. *Neutron diffraction studies on heavy fermion superconducting and antiferromagnetic compounds  $CeRh_{1-x}Co_xIn_5$* . Phys. Status Solidi A **206** 1076 (2009). DOI: 10.1002/pssa.200881222.
- [14] M. Yokoyama, N. Oyama, H. Amitsuka, S. Oinuma, I. Kawasaki, K. Tenya, M. Matsuura, K. Hirota, and T. J. Sato. *Change of antiferromagnetic structure near a quantum critical point in  $CeRh_{1-x}Co_xIn_5$* . Phys. Rev. B **77** 224501 (2008). DOI: 10.1103/PhysRevB.77.224501.
- [15] M. Yokoyama, N. Oyama, H. Amitsuka, S. Oinuma, I. Kawasaki, K. Tenya, M. Matsuura, and K. Hirota. *Polarized neutron scattering study on antiferromagnetic states in  $CeRh_{0.6}Co_{0.4}In_5$* . Physica B: Condens. Matter **403** 812 (2008). DOI: 10.1016/j.physb.2007.10.035.
- [16] J. D. Thompson and Z. Fisk. *Progress in Heavy-Fermion Superconductivity: Ce115 and Related Materials*. J. Phys. Soc. Jpn. **81** 011002 (2012). and references therein. DOI: 10.1143/JPSJ.81.011002.
- [17] P. Aynajian, E. H. da Silva Neto, A. Gyenis, R. E. Baumbach, J. D. Thompson, Z. Fisk, E. D. Bauer, and A. Yazdani. *Visualizing heavy fermions emerging in a quantum critical Kondo lattice*. Nature **486** 201 (2012). DOI: 10.1038/nature11204.
- [18] Y. Haga, Y. Inada, H. Harima, K. Oikawa, M. Murakawa, H. Nakawaki, Y. Tokiwa, D. Aoki, H. Shishido, S. Ikeda, N. Watanabe, and Y. Ōnuki. *Quasi-two-dimensional Fermi surfaces of the heavy fermion superconductor  $CeIrIn_5$* . Phys. Rev. B **63** 060503 (2001). DOI: 10.1103/PhysRevB.63.060503.
- [19] S.-i. Fujimori, T. Okane, J. Okamoto, K. Mamiya, Y. Muramatsu, A. Fujimori, H. Harima, D. Aoki, S. Ikeda, H. Shishido, Y. Tokiwa, Y. Haga, and Y. Ōnuki. *Nearly localized nature of  $f$  electrons in  $CeTIn_5$  ( $T = Rh, Ir$ )*. Phys. Rev. B **67** 144507 (2003). DOI: 10.1103/PhysRevB.67.144507.
- [20] N. Harrison, U. Alver, R. G. Goodrich, I. Vekhter, J. L. Sarrao, P. G. Pagliuso, N. O. Moreno, L. Balicas, Z. Fisk, D. Hall, R. T. Macaluso, and J. Y. Chan.  *$4f$ -Electron Localization in  $Ce_xLa_{1-x}MIn_5$  with  $M = Co, Rh, or Ir$* . Phys. Rev. Lett. **93** 186405 (2004). DOI: 10.1103/PhysRevLett.93.186405.
- [21] H. Shishido, R. Settai, H. Harima, and Y. Ōnuki. *A Drastic Change of the Fermi Surface at a Critical Pressure in  $CeRhIn_5$ : dHvA Study under Pressure*. J. Phys. Soc. Jpn. **74** 1103 (2005). DOI: 10.1143/JPSJ.74.1103.
- [22] R. Settai, T. Takeuchi, and Y. Ōnuki. *Recent Advances in Ce-Based Heavy-Fermion Superconductivity and Fermi Surface Properties*. J. Phys. Soc. Jpn. **76** 051003 (2007). DOI: 10.1143/JPSJ.76.051003.

- [23] H. Shishido, R. Settai, T. Kawai, H. Harima, and Y. Ōnuki. *de Haas–van Alphen effect of CeIr<sub>1-x</sub>Rh<sub>x</sub>In<sub>5</sub>*. J. Magn. Magn. Mater. **310** 303 (2007). DOI: 10.1016/j.jmmm.2006.10.051.
- [24] S. K. Goh, J. Paglione, M. Sutherland, E. C. T. O’Farrell, C. Bergemann, T. A. Sayles, and M. B. Maple. *Fermi-Surface Reconstruction in CeRh<sub>1-x</sub>Co<sub>x</sub>In<sub>5</sub>*. Phys. Rev. Lett. **101** 056402 (2008). DOI: 10.1103/PhysRevLett.101.056402.
- [25] M. P. Allan, F. Masee, D. K. Morr, J. V. Dyke, A. W. Rost, A. P. Mackenzie, and C. P. and J. C. Davis. *Imaging Cooper pairing of heavy fermions in CeCoIn<sub>5</sub>*. Nature Physics **9** 468 (2013). DOI: 10.1038/nphys2671.
- [26] E. D. Bauer, J. D. Thompson, J. L. Sarrao, L. A. Morales, F. Wastin, J. Rebizant, J. C. Griveau, P. Javorsky, P. Boulet, E. Colineau, G. H. Lander, and G. R. Stewart. *Structural Tuning of Unconventional Superconductivity in PuMGa<sub>5</sub> (M = Co, Rh)*. Phys. Rev. Lett. **93** 147005 (2004). DOI: 10.1103/PhysRevLett.93.147005.
- [27] P. Pagliuso, N. Curro, N. Moreno, M. Hundley, J. Thompson, J. Sarrao, and Z. Fisk. *Structurally tuned superconductivity in heavy-fermion CeMIn<sub>5</sub> (M = Co, Ir, Rh)*. Physica B: Condens. Matter **320** 370 (2002). Proceedings of the Fifth Latin American Workshop on Magnetism, Magnetic Materials and their Applications. DOI: 10.1016/S0921-4526(02)00751-2.
- [28] P. Thalmeier and G. Zwicknagl. “Unconventional Superconductivity and Magnetism in Lanthanide and Actinide Intermetallic Compounds”. In: vol. 34. Handbook on the Physics and Chemistry of Rare Earths. Elsevier, 2004, 135. DOI: 10.1016/S0168-1273(04)34002-X.
- [29] K. S. Burch, S. V. Dordevic, F. P. Mena, A. B. Kuzmenko, D. van der Marel, J. L. Sarrao, J. R. Jeffries, E. D. Bauer, M. B. Maple, and D. N. Basov. *Optical signatures of momentum-dependent hybridization of the local moments and conduction electrons in Kondo lattices*. Phys. Rev. B **75** 054523 (2007). DOI: 10.1103/PhysRevB.75.054523.
- [30] K. Haule, C.-H. Yee, and K. Kim. *Dynamical mean-field theory within the full-potential methods: Electronic structure of CeIrIn<sub>5</sub>, CeCoIn<sub>5</sub> and CeRhIn<sub>5</sub>*. Phys. Rev. B **81** 195107 (2010). DOI: 10.1103/PhysRevB.81.195107.
- [31] L. V. Pourovskii, P. Hansmann, M. Ferrero, and A. Georges. *Theoretical Prediction and Spectroscopic Fingerprints of an Orbital Transition in CeCu<sub>2</sub>Si<sub>2</sub>*. Phys. Rev. Lett. **112** 106407 (2014). DOI: 10.1103/PhysRevLett.112.106407.
- [32] J. H. Shim, K. Haule, and G. Kotliar. *Modeling the Localized-to-Itinerant Electronic Transition in the Heavy Fermion System CeIrIn<sub>5</sub>*. Science **318** 1615 (2007). DOI: 10.1126/science.1149064.
- [33] A. D. Christianson, E. D. Bauer, J. M. Lawrence, P. S. Riseborough, N. O. Moreno, P. G. Pagliuso, J. L. Sarrao, J. D. Thompson, E. A. Goremychkin, F. R. Trouw, M. P. Hehlen, and R. J. McQueeney. *Crystalline electric field effects in CeMIn<sub>5</sub> (M = Co, Rh, Ir): Superconductivity and the influence of Kondo spin fluctuations*. Phys. Rev. B **70** 134505 (2004). DOI: 10.1103/PhysRevB.70.134505.

## References of Chapter 7

- [34] A. D. Christianson, J. M. Lawrence, P. G. Pagliuso, N. O. Moreno, J. L. Sarrao, J. D. Thompson, P. S. Riseborough, S. Kern, E. A. Goremychkin, and A. H. Lacerda. *Neutron scattering study of crystal fields in CeRhIn<sub>5</sub>*. Phys. Rev. B **66** 193102 (2002). DOI: 10.1103/PhysRevB.66.193102.
- [35] T. Willers, Z. Hu, N. Hollmann, P. O. Körner, J. Gegner, T. Burnus, H. Fujiwara, A. Tanaka, D. Schmitz, H. H. Hsieh, H.-J. Lin, C. T. Chen, E. D. Bauer, J. L. Sarrao, E. Goremychkin, M. Koza, L. H. Tjeng, and A. Severing. *Crystal-field and Kondo-scale investigations of CeMIn<sub>5</sub> (M = Co, Ir, and Rh): A combined x-ray absorption and inelastic neutron scattering study*. Phys. Rev. B **81** 195114 (2010). DOI: 10.1103/PhysRevB.81.195114.
- [36] A. Tanaka and T. Jo. *Resonant 3d, 3p and 3s PES in Transition Metal Oxides Predicted at 2p Threshold*. J. Phys. Soc. Jpn. **63** 2788 (1994). DOI: 10.1143/JPSJ.63.2788.
- [37] P. Hansmann, A. Severing, Z. Hu, M. W. Haverkort, C. F. Chang, S. Klein, A. Tanaka, H. H. Hsieh, H.-J. Lin, C. T. Chen, B. Fåk, P. Lejay, and L. H. Tjeng. *Determining the Crystal-Field Ground State in Rare Earth Heavy Fermion Materials Using Soft-X-Ray Absorption Spectroscopy*. Phys. Rev. Lett. **100** 066405 (2008). DOI: 10.1103/PhysRevLett.100.066405.
- [38] F. Strigari, T. Willers, Y. Muro, K. Yutani, T. Takabatake, Z. Hu, Y.-Y. Chin, S. Agrestini, H.-J. Lin, C. Chen, A. Tanaka, M. W. Haverkort, L.-H. Tjeng, and A. Severing. Phys. Rev. B **86** 081105(R) (2012). DOI: 10.1103/PhysRevB.86.081105.
- [39] E. G. Moshopoulou, J. L. Sarrao, P. G. Pagliuso, N. O. Moreno, J. D. Thompson, Z. Fisk, and R. M. Ibberson. *Comparison of the crystal structure of the heavy-fermion materials CeCoIn<sub>5</sub>, CeRhIn<sub>5</sub> and CeIrIn<sub>5</sub>*. Appl. Phys. A **74** 895 (2002). DOI: 10.1007/s003390201673.
- [40] A. Hannan, K. Iwasa, M. Kohgi, T. Osakabe, H. Kitazawa, and T. Suzuki. *Exotic Properties of CeSb Studied by X-ray Diffraction*. J. Phys. Soc. Jpn. **73** 1881 (2004). DOI: 10.1143/JPSJ.73.1881.

## 8 Conclusions and outlook

The dense and ordered presence of Kondo impurities has striking and exceptional consequences for the (low-temperature) physics of  $f$ -electron systems. The strong interactions between the localized electrons and the conduction electrons leads to the emergence of a heavy-electron band and the formation of a (narrow) hybridization gap close to the Fermi level, as phase coherence develops between the local ‘impurities’ below  $T^* \cong T_K$ . Metal-to-insulator transitions, quantum criticality, unconventional superconductivity and unusual magnetic ordering are only some of the many phenomena arising in these strongly correlated electron systems [1]. An attribute of Kondo lattice systems is the prevalent competition between localized and itinerant behavior, which is often reflected in a non-integer valence ground state. Furthermore, intensive research on the field revealed that the anisotropic nature of the hybridization – which is strongly linked to the anisotropy of the crystal-field wave function – is of great importance for the mechanisms driving the ground-state formation.

The goal of this thesis was to provide a reliable and quantitative investigation of the hybridization and crystal-field effects in Kondo insulators by making use of the great potential of core-level spectroscopy. Especially in Kondo insulators, standard techniques for the study of the crystalline electric field (CEF), like inelastic neutron scattering (INS) and static magnetic susceptibility, turned out to encounter difficulties in the presence of hybridization, spin gaps or magnetic interactions, and yield only limited information about the CEF ground state. Here, linearly polarized x-ray absorption spectroscopy (XAS) comes into play, which was established as a complementary *spectroscopic* technique for an accurate determination of CEF ground-state wave functions [2]. Thanks to the polarization-dependent dipole selection rules, the orbital shape of the  $4f$  ground state is reflected in the linearly polarized spectra. Up to now, the method has been mostly applied to tetragonal Ce-based heavy-fermion compounds [3–5]. With regard to the issue of hybridization, the recent availability of hard x-ray photoelectron spectroscopy (HAXPES) opened up a new opportunity to probe directly and reliably the distribution of the valence states of the  $4f$  ions. High-quality data can be obtained that are representative for the bulk material.

**Impact of the presented studies** The focus of this thesis lay on one of the more recent members – namely the  $\text{Ce}M_2\text{Al}_{10}$  compound family ( $M = \text{Ru}, \text{Os}$  and  $\text{Fe}$ ) with its orthorhombic cage-like crystal structure (Chapters 3 and 4). These materials exhibit Kondo-semiconducting behavior with narrow and anisotropic hybridization gaps and soon became very prominent because of the unusual and mysterious antiferromagnetic order in  $\text{CeRu}_2\text{Al}_{10}$  and  $\text{CeOs}_2\text{Al}_{10}$ . In the isostructural  $\text{CeFe}_2\text{Al}_{10}$  magnetic ordering is absent down to lowest temperatures ( $\sim 50$  mK). The magnetic phase of the Ru and Os samples features a rather puzzling combination of properties: an unexpectedly high  $T_N$  (higher than in most other ordered Ce materials), a small ordered moment ( $\mu_{\text{ord}} \approx 0.3 - 0.4 \mu_B/\text{Ce}$ ) which is not aligned along the easy axis  $a$  but along  $c$ ,

and the presence of Kondo screening. Moreover, in all three 1-2-10 compounds the opening of a spin gap and a large anisotropy in the magnetic susceptibility is observed. The  $c$ - $f$  hybridization is suspected to play a major role for the mechanism behind the magnetic ordering, therefore a detailed investigation of the  $4f$  valence and the local electronic structure of the  $4f$  electrons was of great interest.

In Chapter 3 and 4 the XAS method has been successfully applied for the study of  $\text{CeRu}_2\text{Al}_{10}$ ,  $\text{CeOs}_2\text{Al}_{10}$  and  $\text{CeFe}_2\text{Al}_{10}$ . Ionic full multiplet calculations find two CEF ground states describing the polarization-dependent XAS data. By taking into account the anisotropy seen in magnetic susceptibility, one solution could be unambiguously identified as the  $4f$  ground-state wave function. In combination with the CEF energy splittings obtained by INS it was finally possible to give full sets of CEF parameters for all members of the  $\text{CeM}_2\text{Al}_{10}$  family. While the results for the Ru and Os samples are similar, the ground state for the non-ordering Fe compound is clearly different. The obtained ground-state wave functions, orbitals and crystal-field schemes are summarized in Fig. 8.1. The results show that linearly polarized XAS is able to determine the CEF ground-state wave function of orthorhombic Kondo insulators, and is neither hampered by the existence of spin gaps nor by the presence of strong  $c$ - $f$  hybridization. Furthermore, the CEF description validated the theoretical predictions by Hanzawa obtained within a point-charge model [6]. Most strikingly, the weak ordered moments in the Ru and Os samples are largely explained by CEF effects.

Several groups used the CEF information obtained by XAS for further studies on these materials. For instance, for  $\text{Ce}(\text{Ru,Os})_2\text{Al}_{10}$  Kunimori *et al.* [7] and Kondo *et al.* [8] performed mean-field calculations for a two-sublattice model including an anisotropic exchange interaction on the basis of the CEF ground states, and in a polarized neutron scattering study by Robert *et al.* [9], the CEF parameters of  $\text{CeRu}_2\text{Al}_{10}$  served as input in random-phase magnon simulations.

In Chapter 5 the varying degree of exchange interaction within the 1-2-10 series has been treated quantitatively by investigating the  $4f$  valence in the systems. Hard x-ray photoelectron spectroscopy on the Ce  $3d$  core levels provided a truly bulk-sensitive probe, and the spectra (including strong plasmon excitations) could be accurately reproduced by combining full multiplet calculations with a configuration interaction model. The deduced hybridization strength  $V_{\text{eff}}$  and effective  $f$  binding energy  $\Delta_f$  show that a substantial amount of Kondo screening is present in all three compounds. The exchange interaction in the Ru and Os compounds is of comparable strength (yet, slightly stronger in the Os sample), whereas in  $\text{CeFe}_2\text{Al}_{10}$  it is significantly stronger. These results undoubtedly show that a high degree of  $f$  electron delocalization persists in these systems despite their ability to develop long-range antiferromagnetic order.

The  $\text{CeM}_2\text{Al}_{10}$  compounds are the first materials with Kondo-insulating behavior showing also magnetic order, with strikingly unusual ground-state properties among the strongly correlated electron systems and a supposedly novel mechanism behind the magnetic ordering. They are ideally suited to investigate the competition ‘itinerant versus localized’ or ‘Kondo versus RKKY interaction’, however, the understanding of the 1-2-10 systems goes beyond the framework of the conventional Doniach phase diagram because of the coexistence of electronic ground states and their influence on each other. This has been explicitly addressed in literature [10, 11] by proposing a modified version of the Doniach phase diagram, in which a localized-to-itinerant transition takes place *within* the AFM phase, thereby emphasizing the influence of the Kondo

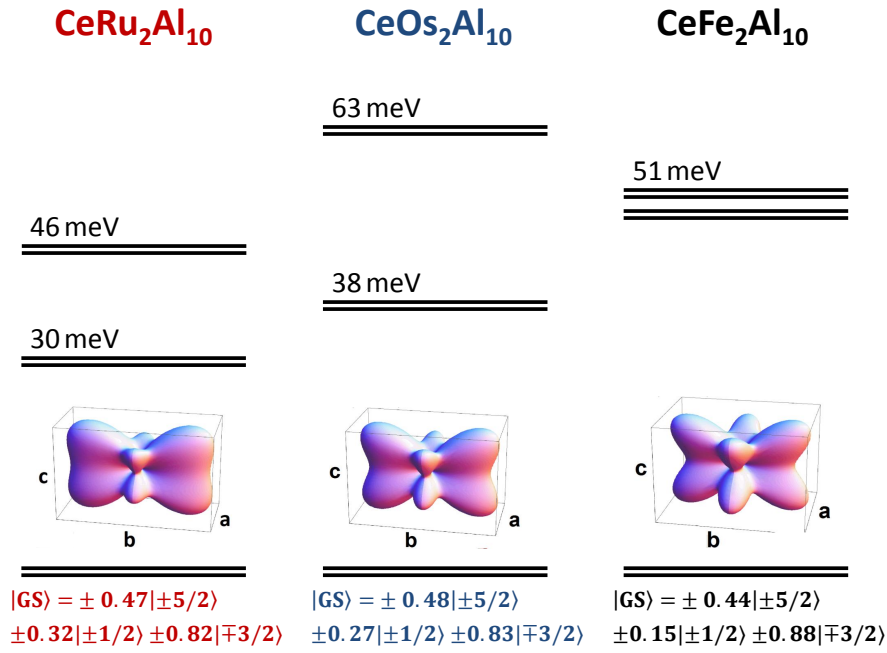


Figure 8.1: Summary of the CEF ground-state wave functions and the  $4f$  orbitals obtained by linearly polarized XAS for the members of the  $\text{CeM}_2\text{Al}_{10}$  family. The crystal-field energies that were used in Chapter 3 and 4 for the determination of the CEF parameters are also included.

effect on the magnetic order. This then might lead to a (further)<sup>1</sup> reduction of the ordered magnetic moments or determine their unusual direction along the  $c$  axis. Although the actual mechanism behind the AFM order remains an open question, our quantitative results obtained from the linearly polarized XAS and bulk-sensitive HAXPES studies are important ingredients to deepen the understanding of the Kondo-semiconducting state and to answer the question why and under which circumstances a certain ground state forms or not. Only on the basis of reliable numbers, which are now established for the crystal field and hybridization interaction of the  $\text{CeM}_2\text{Al}_{10}$  compounds, it is possible to make quantitative predictions and better understand the Kondo-insulating behavior and its consequences.

After being successful with the orthorhombic  $\text{CeM}_2\text{Al}_{10}$  Kondo insulators, we tackled the long-standing problem of the crystal-field ground state of  $\text{CeNiSn}$  (Chapter 6).  $\text{CeNiSn}$  is one of the first Ce-based Kondo insulators, which also crystallizes in an orthorhombic structure where the local environment of the Ce ion has an even lower, monoclinic symmetry (point group  $C_s$ ). No magnetic order is observed and the hybridization gap is extremely narrow ( $\approx 2.4$  meV), but particular about  $\text{CeNiSn}$  (and its relatives  $\text{CeRhSb}$  and  $\text{CeRhAs}$ ) is the ‘V’-shaped form of the electronic density of states with a small finite value at the Fermi level, making the material rather semimetallic and re-classifying the hybridization gap as ‘pseudogap’. In INS experiments

<sup>1</sup>‘Further’ is meant here with respect to the already small-sized moments due to CEF effects.

the gap formation was found to go along with a strongly Q-dependent spin gap which only emerges below the Kondo coherence temperature. Different theoretical models were proposed by independent groups [12–15] to explain the origin of the pseudogap formation, all of which set specific conditions to the crystal-field ground-state symmetry.

In Chapter 6 we have again exploited the potential of polarization-dependent XAS at the Ce  $M_{4,5}$  edge at low temperature to provide a direct experimental determination of the  $4f$  CEF ground state of CeNiSn. Reliable information about the CEF symmetry was still missing because the presence of strong hybridization and the proximity to phonon peaks hampered the analysis of INS spectra. The XAS study in Chapter 6 showed that it is justified to approximate the monoclinic symmetry by a trigonal crystal field. The measured linear dichroism ruled out the pure  $|\pm 3/2\rangle$  with the threefold rotational axis along the crystallographic  $a$  direction as a possible ground state (as it is suggested in the Ikeda and Miyake (IM) model [12]), which speaks in favor of the theoretical model proposed by Moreno and Coleman [15]. With the help of full multiplet simulations the trigonal CEF ground-state wave function  $|\psi\rangle_{\text{GS}} = 0.63|\pm 1/2\rangle \pm 0.77|\mp 5/2\rangle$  was found to nicely describe the observed polarized XAS data. Furthermore, from the temperature dependence of the linear dichroism the energies of the excited Kramer’s doublets were estimated. The final CEF ground state is in good agreement with one of the proposed solutions from INS work on Cu-doped CeNiSn [16]. Actually, since our XAS results clearly rule out one of the two possible solutions discussed by the authors of Ref. [16], we now can conjecture which one of the theoretical models is likely to be applicable to CeNiSn, namely the one of Moreno and Coleman.

More precisely, in the anisotropic semiconductor theory by IM the anomalous density of states, the anisotropic transport properties and the weak semimetallic behavior are understood within the framework of a  $\mathbf{k}$ -dependent  $c$ - $f$  hybridization matrix. In their picture the Kondo-insulating state is a consequence of nodal crystal-field states being responsible for the nodal character of the hybridization gap. However, Moreno and Coleman wondered why the particular semimetallic state is chosen from the continuum of fully-gapped CEF states and how the nodal physics can be understood in a many-body picture [17]. Their solution to that is a coupling between the Ce  $4f$  orbital shape and a many-body Weiss effective field induced by Hund’s interactions in the (valence fluctuation)  $f^2$  state. This coupling builds up an effective crystal field, which selects the nodal configurations out of the manifold of CEF ground states in order to minimize the kinetic energy of the  $f$  electrons. The quasioctahedral solution in Moreno and Coleman’s theory – according to their calculations – yields a better description of the transport/thermal properties and the ‘V’-shaped density of states in CeNiSn than the axially-symmetric IM state (which is represented by the pure  $|\pm 3/2\rangle$ ). Therefore, finding a mixed ground-state wave function, and excluding the pure  $|\pm 3/2\rangle$  state, is an important step towards a better understanding of narrow-gap Kondo insulators and motivates to further pursue the idea of an effective Weiss crystal field.

The delicate balance among the competing interactions and the question how the  $4f$  orbital degrees of freedom influence the ground state formation in an isostructural series of heavy-fermion compounds is addressed in Chapter 7. The phase diagrams of the tetragonal HF family  $\text{Ce}M\text{In}_5$  (with  $M = \text{Co}, \text{Rh}$  and  $\text{Ir}$ ) provide an ideal playground for this kind of study:  $\text{CeRhIn}_5$  orders antiferromagnetically below  $T_N = 3.8$  K, whereas in  $\text{CeIrIn}_5$  and  $\text{CeCoIn}_5$  superconductivity is observed with  $T_c = 0.4$  and  $2.3$  K, respectively. This leads to extremely rich phase diagrams of the substitution series  $\text{CeRh}_{1-x}\text{Ir}_x\text{In}_5$  and  $\text{CeRh}_{1-y}\text{Co}_y\text{In}_5$ , which comprise

antiferromagnetic regions, regions of coexisting antiferromagnetic and superconducting phases, or pure superconductivity at ambient pressure. The superconductivity in these compounds is unconventional and appears in the vicinity of magnetism. Moreover, substitution of one  $M$  element by another goes along with significant changes of the Fermi surface.

For the polarization-dependent XAS study presented in Chapter 7 the  $\text{CeRh}_{1-x}\text{Ir}_x\text{In}_5$  series was chosen. The changes in the linear dichroism  $E \perp c - E \parallel c$  were systematically studied for two AFM samples ( $x = 0$  and  $0.2$ ), two samples within the coexisting phase ( $x = 0.3$  and  $0.5$ ) and two purely superconducting samples ( $x = 0.75$  and  $1$ ). We determined the CEF ground-state wave function for each composition (which is of  $\Gamma_7$ -type, i.e.  $|\psi\rangle_{\text{GS}} = \alpha|\pm 5/2\rangle + \sqrt{1 - \alpha^2}|\mp 3/2\rangle$ ) and found a clear correlation between the CEF anisotropy – expressed by the squared mixing factor  $\alpha^2$  – and the ground-state properties. Namely, for  $4f$  orbitals with a larger spatial expansion along the tetragonal  $c$  axis, superconductivity becomes favorable. These findings fit nicely with the theoretical predictions by Shim *et al.* [18] that the interaction between the out-of-plane In and the  $M$  ion is strongest, and is in accordance with the idea of the hybridization being essential for the emergence of the superconducting state.

The importance of orbital physics is well-established in  $d$  electron systems. Our results give the spectroscopic proof that such correlations also exist in  $4f$  Kondo lattice materials and show that anisotropic hybridization has to be considered for a correct theoretical description of these systems. It is a non-trivial fact that the orbital shape of the  $4f$  electrons can be used as an indicator for whether the magnetic ground state ‘wins’ over the superconducting one or not. In fact, it might be a missing piece in the construction of a plausible model for the (non-thermal) order parameter in heavy-fermion superconductivity.

All in all, thanks to the vivid activity in the field, including our investigations on  $\text{CeM}_2\text{Al}_{10}$ ,  $\text{CeNiSn}$  and  $\text{CeMIn}_5$ , new prospects might arise from the theoretical point of view since reliable quantitative input is provided to account for hybridization and crystal-field effects. In the future still many unresolved problems in Kondo insulators, and Kondo lattice systems in general, are to be tackled both theoretically and experimentally [17]: What is the role of the Kondo effect and the heavy quasiparticles in the superconducting pairing mechanism? How can the existence of quantum critical points be understood (spin-density wave scenario vs. Kondo breakdown) and how is this connected to superconductivity and antiferromagnetic fluctuations? Do the sudden changes in the Fermi surface at a QCP go along with a loss of quasiparticle weights? How do the magnetic interactions in Kondo insulators evolve depending on the exchange interaction? When and why do they disappear at low temperatures?

**What comes next?** Having seen the impact of the orbital anisotropy in the above-mentioned Ce compounds, it is of considerable interest to analyze if similar trends can be observed in other Kondo lattice materials. Recently, electron- and hole-doping were shown to significantly alter the magnetic ground state of  $\text{CeRu}_2\text{Al}_{10}$  and  $\text{CeOs}_2\text{Al}_{10}$  already at weak doping levels [8, 19–26]: Upon substitution of Ru by Rh or Os by Ir the systems are electron-doped and it turns out that this suppresses the  $c$ - $f$  hybridization and pushes both compounds into the more localized trivalent regime. Already at around  $x = 3\%$  Rh/Ir content the direction of the ordered magnetic moment changes from  $\mu_{\text{AFM}} \parallel c$  to  $\mu_{\text{AFM}} \parallel a$ , as expected from the paramagnetic susceptibility. At the same time the ordering temperature  $T_N$  gradually decreases with increasing  $x$  and the

size of the ordered moment becomes larger. On the other hand, adding holes into the system – by using Re as substituent for Os – increases the degree of hybridization and maintains the anomalous direction of the ordered moment, favoring a delocalized non-magnetic state already for 5 % Re content. In the case of  $\text{CeRu}_2\text{Al}_{10}$  weak hole-doping (3 % Re) was found to align the ordered moment along the  $b$  direction and the size of  $\mu_{\text{AFM}}$  is further reduced compared to the undoped case.

These observations show that in the 1-2-10 compounds doping sensitively tunes the hybridization, which in turn holds a special role in the unusual antiferromagnetic order. A detailed investigation of how the CEF ground-state wave functions develop when 1) the order loses its anomalous character 2) the transition temperature changes or 3) the direction of  $\mu_{\text{AFM}}$  switches is of great interest. Corresponding measurements are in preparation.

Moreover, the young field of topological Kondo insulators promises to give new interesting perspectives. A topological insulator is insulating in the bulk but features metallic surface states which are protected by time-reversal symmetry [27]. Dzero *et al.* [28] showed that also Kondo-insulating materials – due to their strong electron-electron interactions and large spin-orbit coupling – have the potential to host a topologically nontrivial insulating state, and theoretically predicted the topological Kondo insulator (TKI). In their theory they point out that the CEF ground-state symmetry determines whether the  $k$ -dependence of the hybridization can generate a nontrivial topological structure. A narrow conduction band and a strong intermediate valence character seem to be favorable for the existence of the TKI state. In a later study the same authors explicitly calculate the topological surface modes taking into account the influence of the CEF symmetry and including it in the Anderson lattice model [29]. A lot of theoretical effort has been performed since then to strengthen the concept of TKIs [30–34]. In particular, the cubic Kondo insulator  $\text{SmB}_6$  was predicted to be a strong topological insulator [28, 30] and several experimental studies support this (see Ref. [35] for a brief review). Ce-based  $f$  electron materials – e.g.  $\text{CeNiSn}$ ,  $\text{Ce}_3\text{Bi}_4\text{Pt}_3$  and  $\text{CeRu}_4\text{Sn}_6$  – also moved into the focus of interest since they come with all necessary ingredients for the emergence of a topological state.  $\text{Ce}_3\text{Bi}_4\text{Pt}_3$  is a promising candidate because it exhibits a cubic structure, which is predicted to be advantageous for strong topological-insulating behavior [33]. A prerequisite for the insulating state in cubic symmetry is that the  $\Gamma_8$  quartet comprised of

$$\begin{aligned} |\Gamma_8^{(1)}\rangle &= \sqrt{\frac{5}{6}}|\pm 5/2\rangle + \sqrt{\frac{1}{6}}|\mp 3/2\rangle \\ |\Gamma_8^{(2)}\rangle &= |\pm 1/2\rangle \end{aligned}$$

has to be the ground state. In this context, the CEF anisotropies of the cubic uranium-based heavy-electron semiconductors  $\text{U}_3\text{T}_3\text{Sb}_4$  ( $T = \text{Ni, Pd, Pt}$ ) [36] and  $\text{UTSn}$  ( $T = \text{Ni, Pt}$ ) [37] also are worth being studied in more detail. But also in Kondo insulators with lower symmetries, such as the tetragonal  $\text{CeRu}_4\text{Sn}_6$  or the orthorhombic  $\text{CeNiSn}$ , a weak TKI state may develop [28, 35], and it depends on the detailed symmetry of the ground state whether nodes form in the hybridization gap structure or not. For the pure  $|\pm 1/2\rangle$  the hybridization gap is always open so that in the tetragonal case the  $|\pm 1/2\rangle$  ground state is favorable. It is therefore of high interest to investigate the CEF wave function in these potential TKI compounds.

## References of Chapter 8

- [1] P. S. Riseborough. *Heavy fermion semiconductors*. *Adv. Phys.* **49** 257 (2000). DOI: 10.1080/000187300243345.
- [2] P. Hansmann, A. Severing, Z. Hu, M. W. Haverkort, C. F. Chang, S. Klein, A. Tanaka, H. H. Hsieh, H.-J. Lin, C. T. Chen, B. Fåk, P. Lejay, and L. H. Tjeng. *Determining the Crystal-Field Ground State in Rare Earth Heavy Fermion Materials Using Soft-X-Ray Absorption Spectroscopy*. *Phys. Rev. Lett.* **100** 066405 (2008). DOI: 10.1103/PhysRevLett.100.066405.
- [3] T. Willers, B. Fåk, N. Hollmann, P. O. Körner, Z. Hu, A. Tanaka, D. Schmitz, M. Enderle, G. Lapertot, L. H. Tjeng, and A. Severing. *Crystal-field ground state of the noncentrosymmetric superconductor CePt<sub>3</sub>Si: A combined polarized soft x-ray absorption and polarized neutron study*. *Phys. Rev. B* **80** 115106 (2009). DOI: 10.1103/PhysRevB.80.115106.
- [4] T. Willers, Z. Hu, N. Hollmann, P. O. Körner, J. Gegner, T. Burnus, H. Fujiwara, A. Tanaka, D. Schmitz, H. H. Hsieh, H.-J. Lin, C. T. Chen, E. D. Bauer, J. L. Sarrao, E. Goremychkin, M. Koza, L. H. Tjeng, and A. Severing. *Crystal-field and Kondo-scale investigations of CeMIn<sub>5</sub> (M = Co, Ir, and Rh): A combined x-ray absorption and inelastic neutron scattering study*. *Phys. Rev. B* **81** 195114 (2010). DOI: 10.1103/PhysRevB.81.195114.
- [5] T. Willers, D. T. Adroja, B. D. Rainford, Z. Hu, N. Hollmann, P. O. Körner, Y.-Y. Chin, D. Schmitz, H. H. Hsieh, H.-J. Lin, C. T. Chen, E. D. Bauer, J. L. Sarrao, K. J. McClellan, D. Byler, C. Geibel, F. Steglich, H. Aoki, P. Lejay, A. Tanaka, L. H. Tjeng, and A. Severing. *Spectroscopic determination of crystal-field levels in CeRh<sub>2</sub>Si<sub>2</sub> and CeRu<sub>2</sub>Si<sub>2</sub> and of the 4f<sup>0</sup> contributions in CeM<sub>2</sub>Si<sub>2</sub> (M=Cu, Ru, Rh, Pd, and Au)*. *Phys. Rev. B* **85** 035117 (2012). DOI: 10.1103/PhysRevB.85.035117.
- [6] K. Hanzawa. *Crystalline Electric Field Effects in CeT<sub>2</sub>Al<sub>10</sub> (T = Ru, Os)*. *J. Phys. Soc. Jpn.* **80** 023707 (2011). DOI: 10.1143/JPSJ.80.023707.
- [7] K. Kunimori, M. Nakamura, H. Nohara, H. Tanida, M. Sera, T. Nishioka, and M. Matsumura. *Unusual magnetic order in CeT<sub>2</sub>Al<sub>10</sub> (T = Ru, Os) in comparison with localized NdFe<sub>2</sub>Al<sub>10</sub>*. *Phys. Rev. B* **86** 245106 (2012). DOI: 10.1103/PhysRevB.86.245106.
- [8] A. Kondo, K. Kindo, K. Kunimori, H. Nohara, H. Tanida, M. Sera, R. Kobayashi, T. Nishioka, and M. Matsumura. *Marked Change in the Ground State of CeRu<sub>2</sub>Al<sub>10</sub> Induced by Small Amount of Rh Substitution*. *J. Phys. Soc. Jpn.* **82** 054709 (2013). DOI: 10.1143/JPSJ.82.054709.
- [9] J. Robert, J.-M. Mignot, S. Petit, P. Steffens, T. Nishioka, R. Kobayashi, M. Matsumura, H. Tanida, D. Tanaka, and M. Sera. *Anisotropic Spin Dynamics in the Kondo Semiconductor CeRu<sub>2</sub>Al<sub>10</sub>*. *Phys. Rev. Lett.* **109** 267208 (2012). DOI: 10.1103/PhysRevLett.109.267208.

## References of Chapter 8

- [10] S. Hoshino and Y. Kuramoto. *Itinerant Versus Localized Heavy-Electron Magnetism*. Phys. Rev. Lett. **111** 026401 (2013). DOI: 10.1103/PhysRevLett.111.026401.
- [11] Y. Zekko, Y. Yamamoto, H. Yamaoka, F. Tajima, T. Nishioka, F. Strigari, A. Severing, J.-F. Lin, N. Hiraoka, H. Ishii, K.-D. Tsuei, and J. Mizuki. *Correlation between the valence state of cerium and the magnetic transition in  $Ce(Ru_{1-x}Fe_x)_2Al_{10}$  studied by resonant x-ray emission spectroscopy*. Phys. Rev. B **89** 125108 (2014). DOI: 10.1103/PhysRevB.89.125108.
- [12] H. Ikeda and K. Miyake. *A Theory of Anisotropic Semiconductor of Heavy Fermions*. J. Phys. Soc. Jpn. **65** 1769 (1996). DOI: 10.1143/JPSJ.65.1769.
- [13] K. A. Kikoin, M. N. Kiselev, A. S. Mishchenko, and A. de Visser. *Thermodynamics of  $CeNiSn$  at low temperatures and in weak magnetic fields*. Phys. Rev. B **59** 15070 (1999). DOI: 10.1103/PhysRevB.59.15070.
- [14] M. Miyazawa and K. Yamada. *Theory of the Hybridization Gap in Ce Compounds with Crystalline Electric Field Splitting*. J. Phys. Soc. Jpn. **72** 2033 (2003). DOI: 10.1143/JPSJ.72.2033.
- [15] J. Moreno and P. Coleman. *Gap-Anisotropic Model for the Narrow-Gap Kondo Insulators*. Phys. Rev. Lett. **84** 342 (2000). DOI: 10.1103/PhysRevLett.84.342.
- [16] J.-Y. So, S.-J. Oh, J.-G. Park, D. T. Adroja, K. A. McEwen, and T. Takabatake. *Inelastic neutron scattering studies of doped  $CeNiSn$  and  $CeRhSb$ : Crystal-field excitations and origin of the pseudogap*. Phys. Rev. B **71** 214441 (2005). DOI: 10.1103/PhysRevB.71.214441.
- [17] P. Coleman. *Heavy Fermions: Electrons at the Edge of Magnetism*. Handbook of Magnetism and Advanced Magnetic Materials **1** 95 (2007). DOI: 10.1002/9780470022184.
- [18] J. H. Shim, K. Haule, and G. Kotliar. *Modeling the Localized-to-Itinerant Electronic Transition in the Heavy Fermion System  $CeIrIn5$* . Science **318** 1615 (2007). DOI: 10.1126/science.1149064.
- [19] R. Kobayashi, Y. Ogane, D. Hirai, T. Nishioka, M. Matsumura, Y. Kawamura, K. Matsubayashi, Y. Uwatoko, H. Tanida, and M. Sera. *Change in Unusual Magnetic Properties by Rh Substitution in  $CeRu_2Al_{10}$* . J. Phys. Soc. Jpn. **82** 093702 (2013). DOI: 10.1143/JPSJ.82.093702.
- [20] D. D. Khalyavin, D. T. Adroja, P. Manuel, J. Kawabata, K. Umeo, T. Takabatake, and A. M. Strydom. *Change of magnetic ground state by light electron doping in  $CeOs_2Al_{10}$* . Phys. Rev. B **88** 060403 (2013). DOI: 10.1103/PhysRevB.88.060403.
- [21] H. Guo, H. Tanida, R. Kobayashi, I. Kawasaki, M. Sera, T. Nishioka, M. Matsumura, I. Watanabe, and Z.-a. Xu. *Magnetic instability induced by Rh doping in the Kondo semiconductor  $CeRu_2Al_{10}$* . Phys. Rev. B **88** 115206 (2013). DOI: 10.1103/PhysRevB.88.115206.
- [22] D. D. Khalyavin, D. T. Adroja, A. Bhattacharyya, A. D. Hillier, P. Manuel, A. M. Strydom, J. Kawabata, and T. Takabatake. *Magnetic ordering with reduced cerium moments in hole-doped  $CeOs_2Al_{10}$* . Phys. Rev. B **89** 064422 (2014). DOI: 10.1103/PhysRevB.89.064422.

- [23] J. Kawabata, T. Takabatake, K. Umeo, and Y. Muro. *Suppression of antiferromagnetic order and hybridization gap by electron and hole doping in the Kondo semiconductor  $CeOs_2Al_{10}$* . Phys. Rev. B **89** 094404 (2014). DOI: 10.1103/PhysRevB.89.094404.
- [24] A. Bhattacharyya, D. D. Khalyavin, D. T. Adroja, A. M. Strydom, A. D. Hillier, P. Manuel, T. Takabatake, J. W. Taylor, and C. Ritter. *Anomalous change of the magnetic moment direction by hole doping in  $CeRu_2Al_{10}$* . Phys. Rev. B **90** 174412 (2014). DOI: 10.1103/PhysRevB.90.174412.
- [25] A. Bhattacharyya, D. T. Adroja, A. M. Strydom, J. Kawabata, T. Takabatake, A. D. Hillier, V. G. Sakai, J. W. Taylor, and R. I. Smith. *Contrasting carrier doping effects in the Kondo insulator  $CeOs_2Al_{10}$ : The influential role of c-f hybridization in spin-gap formation*. Phys. Rev. B **90** 174422 (2014). DOI: 10.1103/PhysRevB.90.174422.
- [26] R. Kobayashi, K. Kaneko, K. Saito, J.-M. Mignot, G. André, J. Robert, S. Wakimoto, M. Matsuda, S. Chi, Y. Haga, T. D. Matsuda, E. Yamamoto, T. Nishioka, M. Matsumura, H. Tanida, and M. Sera. *Influence of Electron Doping on Magnetic Order in  $CeRu_2Al_{10}$* . J. Phys. Soc. Jpn. **83** 104707 (2014). DOI: 10.7566/JPSJ.83.104707.
- [27] M. Z. Hasan and C. L. Kane. *Colloquium: Topological insulators*. Rev. Mod. Phys. **82** 3045 (2010). DOI: 10.1103/RevModPhys.82.3045.
- [28] M. Dzero, K. Sun, V. Galitski, and P. Coleman. *Topological Kondo Insulators*. Phys. Rev. Lett. **104** 106408 (2010). DOI: 10.1103/PhysRevLett.104.106408.
- [29] M. Dzero, K. Sun, P. Coleman, and V. Galitski. *Theory of topological Kondo insulators*. Phys. Rev. B **85** 045130 (2012). DOI: 10.1103/PhysRevB.85.045130.
- [30] T. Takimoto.  *$SmB_6$ : A Promising Candidate for a Topological Insulator*. J. Phys. Soc. Jpn. **80** 123710 (2011). DOI: 10.1143/JPSJ.80.123710.
- [31] Z. Wang, X.-L. Qi, and S.-C. Zhang. *Topological invariants for interacting topological insulators with inversion symmetry*. Phys. Rev. B **85** 165126 (2012). DOI: 10.1103/PhysRevB.85.165126.
- [32] F. Lu, J. Zhao, H. Weng, Z. Fang, and X. Dai. *Correlated Topological Insulators with Mixed Valence*. Phys. Rev. Lett. **110** 096401 (2013). DOI: 10.1103/PhysRevLett.110.096401.
- [33] V. Alexandrov, M. Dzero, and P. Coleman. *Cubic Topological Kondo Insulators*. Phys. Rev. Lett. **111** 226403 (2013). DOI: 10.1103/PhysRevLett.111.226403.
- [34] J. Kim, K. Kim, C.-J. Kang, S. Kim, H. C. Choi, J.-S. Kang, J. D. Denlinger, and B. I. Min. *Termination-dependent surface in-gap states in a potential mixed-valent topological insulator:  $SmB_6$* . Phys. Rev. B **90** 075131 (2014). DOI: 10.1103/PhysRevB.90.075131.
- [35] M. Dzero and V. Galitski. *A new exotic state in an old material: a tale of  $SmB_6$* . J. Exp. Theor. Phys. **117** 499 (2013). DOI: 10.1134/S1063776113110083.
- [36] T. Takabatake, S.-i. Miyata, H. Fujii, Y. Aoki, T. Suzuki, T. Fujita, J. Sakurai, and T. Hiraoaka. *Heavy-Fermion and Semiconducting Properties of the Ternary Uranium Compounds  $U_3T_3Sn_4$  and  $U_3T_3Sb_4$  ( $T = Ni, Cu, Pd, Pt$  and  $Au$ )*. J. Phys. Soc. Jpn. **59** 4412 (1990). DOI: 10.1143/JPSJ.59.4412.

*References of Chapter 8*

- [37] T. Palstra, G. Nieuwenhuys, J. Mydosh, and K. Buschow. *Electrical transport properties of the ternary compounds  $UTSn$ ,  $UTSb$  and  $ThTSn$* . *J. Magn. Magn. Mater.* **54–57** 549 (1986).  
DOI: 10.1016/0304-8853(86)90704-3.

## Abstract

The physics of heavy-fermion materials is governed by the hybridization between itinerant conduction electrons and localized  $f$  electrons ( $c$ - $f$  hybridization). At low temperatures the Kondo effect leads to the emergence of heavy quasiparticles with a huge effective mass that can be up to 1000 times larger than the bare electron mass, giving the class of heavy fermions their name. The screening of the localized magnetic moments by the conduction electrons due to the Kondo effect competes with the indirect Ruderman-Kittel-Kasuya-Yoshida exchange, which also has its origin in the hybridization interaction and wants to drive the system into a magnetically ordered ground state. Heavy fermions are regarded as dense Kondo lattice systems, in which the balance between the two interactions is of crucial importance for the ground-state properties. Valence fluctuations, Kondo insulating and semiconducting behavior, spin and charge gaps, unconventional superconductivity, quantum criticality and non-Fermi liquid behavior are observed in these materials, with remarkable consequences for magnetic, thermodynamic and electronic properties at low temperatures.

This thesis is mainly focused on the class of Kondo insulators, which also comprises Kondo semiconductors and semimetals. When the right conditions are met – i.e. for a certain number of electrons per unit cell and for certain symmetries of the electronic structure – the interaction between the conduction and  $f$  electrons opens a narrow hybridization gap close to the Fermi level. The (anisotropic) hybridization gap is found to be responsible for many anomalous properties of Kondo insulators and several theoretical studies point out the importance of the crystalline electric field (CEF) ground-state symmetry for the gap formation.

Here we investigate the Kondo semiconductor CeNiSn, as well as the  $CeM_2Al_{10}$  compound family with  $M = Ru, Os$  and  $Fe$ . CeNiSn has an orthorhombic crystal structure, is one of the first narrow-gap Kondo semiconductors and has been intensively studied in the past. Many explanations for the low-temperature behavior have been suggested, all of which stress the significance of the  $4f$  CEF ground state, which will be investigated in the framework of this thesis. The  $CeM_2Al_{10}$  compounds belong to a fairly new class of cerium Kondo semiconductors. They also crystallize in an orthorhombic structure and order antiferromagnetically in the case of  $M = Ru$  and  $Os$  with the ordered moments being small and *not* aligned along the easy magnetic axis. In combination with the unexpectedly high ordering temperatures of  $T_N = 27$  K (Ru) and 29 K (Os), the magnetic order is of rather unusual character. The physical properties show large anisotropies and presence of  $c$ - $f$  hybridization despite the high ordering temperatures. We therefore determine the CEF wave functions in this compound family and quantify the degree of  $c$ - $f$  hybridization in order to address speculations about the impact of hybridization on the magnetic order. In addition, on the search for parameters which correlate with ground-state properties in heavy-fermion compounds, we investigate the CEF ground states of the *intermetallic* substitution series  $CeRh_{1-x}Ir_xIn_5$  since its phase diagram covers all phases of interest, from antiferromagnetic to superconducting as well as regions of phase coexistence.

To shed light on the issues above, namely the CEF ground state and the hybridization

strength, respectively, two new experimental approaches are used: polarization-dependent x-ray absorption spectroscopy (XAS) and hard x-ray photoelectron spectroscopy (HAXPES). Commonly, the CEF is investigated by inelastic neutron scattering, however, in Kondo insulators a substantial broadening of the CEF excitations and the existence of spin gaps prevent the access to the CEF. Recently, linearly polarized XAS at the Ce  $M_{4,5}$  edge has been proven to be highly useful when it comes to the determination of the  $4f$  ground-state wave function in tetragonal rare earth systems (and also in cubic compounds under the influence of an external magnetic field). In the present thesis the same technique is applied to the above-mentioned materials, demonstrating that linearly polarized XAS can be employed to obtain an unambiguous and reliable picture of the CEF ground state even in Kondo-insulating systems and even for symmetries lower than tetragonal. In addition to that, HAXPES measurements on the  $CeM_2Al_{10}$  series are presented. A common technique for studying hybridization effects in rare earths, and their electronic structure in general, is photoelectron spectroscopy in the soft x-ray range ( $h\nu \leq 1.5$  keV). However, in this energy region surface effects are known to matter so that the picture about the hybridization interaction might be distorted with respect to the bulk. The use of hard x-rays ( $h\nu = 5-10$  keV) guarantees a sufficiently large probing depth for obtaining information about the actual bulk electronic structure. In a detailed quantitative analysis of HAXPES  $3d$  core level spectra – using a combination of full multiplet calculations and a configuration interaction model (fm-CI model) – the hybridization strength can be quantified.

The XAS results show that the CEF ground states of  $CeRu_2Al_{10}$  and  $CeOs_2Al_{10}$  are very similar, while it is clearly different for the non-ordering system  $CeFe_2Al_{10}$ . The CEF description nicely explains the magnetic anisotropy observed in susceptibility data and to a large extent the small ordered moments along the  $c$  axis. We provide a reliable quantitative description of the CEF ground state of the  $CeM_2Al_{10}$  compounds which now serves as input for further studies. Furthermore, the analysis of the HAXPES data in the fm-CI model allows to quantify the intermediate  $4f$  valence and establishes that the exchange interaction increases within the series from Ru to Os to Fe. A substantial amount of Kondo screening is shown to be present even in the magnetically ordered Ru and Os compounds.

The polarized XAS study on  $CeNiSn$  demonstrates that the monoclinic CEF is well described in a trigonal approximation, and the determined  $4f$  ground-state wave function is consistent with results from inelastic neutron scattering for Cu-doped  $CeNiSn$ . Thanks to this first successful direct experimental detection of the  $4f$  ground state in  $CeNiSn$ , an important step is made towards a better understanding of the mechanism behind the gap formation in this archetype Kondo insulator.

Moreover, the systematic investigation of the  $CeRh_{1-x}Ir_xIn_5$  substitution series by means of polarization-dependent XAS for the first time reveals a correlation between the CEF anisotropy and the formation of an antiferromagnetic, superconducting or coexisting (antiferromagnetism plus superconductivity) ground state. This discovery shows that the anisotropy of the  $4f$  ground-state wave function is a good predictor for when these materials are magnetic or superconducting.

## Kurzzusammenfassung

Maßgeblich für die Physik von Schwere-Fermionen-Materialien ist die Hybridisierung zwischen itineranten Leitungselektronen und lokalisierten  $f$ -Elektronen ( $c$ - $f$ -Hybridisierung). Bei tiefen Temperaturen führt der Kondo-Effekt zur Bildung von schweren Quasiteilchen mit einer sehr großen effektiven Masse, die bis zu 1000 Mal größer sein kann als die freie Elektronenmasse und der die Klasse der Schwere Fermionen ihren Namen verdankt. Die Abschirmung der lokalisierten magnetischen Momente durch die Leitungselektronen aufgrund der Kondo-Wechselwirkung konkurriert mit der indirekten Ruderman-Kittel-Kasuya-Yoshida-Austauschwechselwirkung, die ebenfalls in der Delokalisierung der  $f$ -Elektronen begründet liegt und einen magnetisch geordneten Grundzustand favorisiert. Schwere Fermionen werden als dicht-gepackte Kondo-Gitter verstanden, in denen das Gleichgewicht zwischen den zwei Wechselwirkungen von entscheidender Bedeutung für die Grundzustandseigenschaften ist. In diesen Materialien werden unter anderem Valenzfluktuationen, die Ausbildung von Kondo-Isolatoren und -Halbleitern, die Entstehung von Spin- und Ladungslücken, unkonventionelle Supraleitung, Quantenkritikalität und das Auftreten von Nicht-Fermi-Flüssigkeitsverhalten beobachtet, was zu außergewöhnlichen magnetischen, thermodynamischen und elektronischen Eigenschaften bei tiefen Temperaturen führt.

Die vorliegende Arbeit beschäftigt sich hauptsächlich mit der Klasse der Kondo-Isolatoren, die auch Kondo-Halbleiter und -Halbmetalle umfasst. Unter bestimmten Bedingungen – d.h. für eine gewisse Anzahl an Elektronen pro Einheitszelle und für gewisse Symmetrien der elektronischen Struktur – öffnet die Wechselwirkung zwischen Leitungs- und  $f$ -Elektronen eine enge Hybridisierungs-Bandlücke in der Nähe des Fermi-Niveaus. Die (anisotrope) Hybridisierungslücke zeigt sich verantwortlich für viele ungewöhnliche Eigenschaften von Kondo-Isolatoren und eine Vielzahl theoretischer Studien betont die Wichtigkeit der Symmetrie des Kristallfeld-(CEF-)Grundzustandes für die Entstehung der Lücke.

Hier untersuchen wir den Kondo-Halbleiter CeNiSn sowie die Familie der  $CeM_2Al_{10}$ -Systeme mit  $M = Ru, Os$  und  $Fe$ . CeNiSn hat eine orthorhombische Kristallstruktur, gehört zu einem der ersten Kondo-Halbleiter mit enger Bandlücke und wurde in der Vergangenheit intensiv untersucht. Mehrere Konzepte zur Beschreibung des Tieftemperaturverhaltens wurden entwickelt, von denen alle die Wichtigkeit des  $4f$  CEF-Grundzustandes hervorheben, der im Rahmen der vorliegenden Arbeit untersucht wird. Die  $CeM_2Al_{10}$ -Verbindungen wurden erst vor Kurzem als Kondo-Halbleiter klassifiziert und kristallisieren ebenfalls in einer orthorhombischen Struktur. Im Falle von  $M = Ru$  und  $Os$  tritt antiferromagnetische Ordnung auf, wobei die geordneten Momente klein und *nicht* entlang der magnetischen *easy axis* ausgerichtet sind. In Kombination mit den unerwartet hohen Ordnungstemperaturen von  $T_N = 27$  K (Ru) und 29 K (Os) wird die magnetische Ordnung als sehr unüblich angesehen. Die physikalischen Eigenschaften zeigen stark anisotropes Verhalten und weisen auf die Existenz von  $c$ - $f$ -Hybridisierung trotz hoher Ordnungstemperaturen hin. Wir bestimmen daher die CEF-Wellenfunktion dieser Verbindungen und quantifizieren den Grad der  $c$ - $f$ -Hybridisierung, um damit Spekulationen über den

Einfluss der Hybridisierung auf die magnetische Ordnung nachzugehen. Auf der Suche nach Parametern, die mit den Grundzustandseigenschaften in Schwere-Fermionen-Verbindungen korrelieren, werden die Kristallfeld-Grundzustände der *intermetallischen* Substitutionsreihe  $\text{CeRh}_{1-x}\text{Ir}_x\text{In}_5$  untersucht, da hier im Phasendiagramm alle Phasen von Interesse auftreten, von antiferromagnetisch bis supraleitend sowie auch Bereiche von Phasen-Koexistenz.

Um die oben genannten Problematiken des Kristallfeld-Grundzustandes und der Hybridisierungs-Stärke anzugehen, werden zwei neue experimentelle Ansätze verwendet: polarisationsabhängige Röntgenabsorptions-Spektroskopie (XAS) und Photoelektronen-Spektroskopie mit harter Röntgenstrahlung (HAXPES). Das Kristallfeld wird üblicherweise mittels inelastischer Neutronenstreuung untersucht, jedoch tritt in Kondo-Isolatoren das Problem auf, dass die Kristallfeld-Anregungen stark verbreitert sind und Spin-Lücken auftreten, so dass Informationen über das Kristallfeld nicht zugänglich sind. In der jüngsten Vergangenheit hat sich polarisationsabhängige XAS an der Ce  $M_{4,5}$ -Kante als eine höchst nützliche Methode zur Bestimmung der  $4f$ -Grundzustands-Wellenfunktion in tetragonalen Selten-Erd-Systemen etabliert (sowie auch in kubischen Verbindungen, wenn ein externes Magnetfeld angelegt wird). In dieser Arbeit wird dasselbe Verfahren auf die oben genannten Materialien angewandt. Es zeigt sich, dass linear-polarisierte Röntgenabsorption verwendet werden kann, um eine eindeutige und zuverlässige Charakterisierung des CEF-Grundzustandes zu erhalten, und das sogar in Kondo-isolierenden Systemen und für niedrigere als tetragonale Symmetrien. Zusätzlich dazu werden HAXPES-Messungen an den  $\text{CeM}_2\text{Al}_{10}$ -Verbindungen präsentiert. Die übliche Methode zur Untersuchung von Hybridisierungs-Effekten in Selten-Erd-Materialien, und deren elektronischer Struktur im Allgemeinen, ist Photoelektronen-Spektroskopie mit weicher Röntgenstrahlung ( $h\nu \leq 1.5$  keV). Jedoch sind in diesem Energiebereich Oberflächen-Effekte von nicht-vernachlässigbarer Bedeutung, so dass die Ergebnisse nicht die tatsächliche Volumen-(Bulk-)Hybridisierung widerspiegeln. Hier garantiert die Verwendung von harter Röntgenstrahlung ( $h\nu = 5-10$  keV) eine ausreichend hohe Eindringtiefe um Informationen über die tatsächliche elektronische Struktur im Bulk zu erhalten. Eine detaillierte quantitative Analyse von HAXPES  $3d$ -Kern-Niveau-Spektren – anhand eines kombinierten *full-multiplet-configuration-interaction*-Modells (fm-CI) – ermöglicht es, die Stärke der Hybridisierung zu quantifizieren.

Die XAS-Ergebnisse zeigen, dass die CEF-Grundzustände von  $\text{CeRu}_2\text{Al}_{10}$  und  $\text{CeOs}_2\text{Al}_{10}$  sehr ähnlich sind, wohingegen der CEF-Grundzustand des nicht-ordnenden Systems  $\text{CeFe}_2\text{Al}_{10}$  sich eindeutig davon unterscheidet. Die Kristallfeld-Beschreibung erklärt die magnetische Anisotropie, wie sie in der Suszeptibilität zu beobachten ist, und größtenteils das kleine geordnete Moment entlang der  $c$ -Richtung. Damit ist eine zuverlässige quantitative Beschreibung des CEF-Grundzustandes der  $\text{CeM}_2\text{Al}_{10}$ -Verbindungen erbracht, die nun als Input für weiterführende Studien verwendet werden kann. Darüber hinaus erlaubt die Analyse der HAXPES-Daten anhand des fm-CI-Modells, quantitative Werte für die (nicht ganzzahlige) Ce  $4f$ -Valenz zu geben, und weist nach, dass die Austausch-Wechselwirkung von Ru über Os zum Fe hin zunimmt. Es zeigt sich, dass sogar in den magnetisch ordnenden Ru- und Os-Verbindungen ein beträchtliches Maß an Kondo-Abschirmung existiert.

Die polarisationsabhängige XAS-Studie an  $\text{CeNiSn}$  demonstriert, dass das monokline CEF in guter Näherung als trigonal angesehen werden kann, und die erhaltenen  $4f$  Grundzustands-Wellenfunktion ist konsistent mit Ergebnissen aus inelastischer Neutronenstreuung für Cu-dotiertes  $\text{CeNiSn}$ . Diese erste erfolgreiche direkte experimentelle Bestimmung des  $4f$ -Grundzu-

standes in CeNiSn ist ein wichtiger Schritt auf dem Weg zu einem besseren Verständnis des treibenden Mechanismus hinter der Entstehung der Hybridisierungslücke in diesem Archetyp-Kondo-Isolator.

Außerdem enthüllt die systematische Untersuchung der  $\text{CeRh}_{1-x}\text{Ir}_x\text{In}_5$  Substitutions-Reihe durch polarisierte Röntgenabsorption zum ersten Mal Korrelationen zwischen der CEF-Anisotropie und der Ausbildung eines antiferromagnetischen, supraleitenden oder gemischt antiferromagnetisch-supraleitenden Grundzustandes. Diese Entdeckung zeigt, dass die Anisotropie der  $4f$  Grundzustands-Wellenfunktion ein geeigneter Indikator dafür ist, wann diese Materialien magnetisch ordnen oder supraleitend werden.



## Acknowledgment

A physicist works never alone! The studies of this thesis would have not been realized without the enormous effort of many many people. At this point it is time to express my gratitude to everyone who contributed to the projects and supported me throughout the years of my PhD.

First, my sincere thanks go to Hao Tjeng. I started as a diploma student in your group, working on thin films, and soon enjoyed being part of your research team. You supported me when I continued as a PhD, and even after you moved to Dresden you took the time whenever possible for fruitful discussions, illustrative ‘private lectures’ and helpful advice. It was fascinating to learn from you how complex physical problems can be tackled by combining experiments and theory. Your ambition was always motivating and encouraging – I will never forget a sentence you wrote in an email on one of my first beamtimes: "...you are at the edge of what is possible experimentally!" Thank you for all the challenging tasks and your confidence over all these years.

Many thanks to Paul van Loosdrecht, who agreed to be my primary supervisor not long after beginning his work in Cologne. It was interesting to participate in your group meetings and gain insight into a different field of research, and on the other hand it was nice to present my results also to people from outside the field.

I also would like to thank Ladislav Bohatý for having agreed to being the chairman of the committee.

My deepest thanks go to Andrea Severing, who gave me the opportunity to join her project and guided me through the jungle of heavy fermions. Andrea, your door was always open when I had questions or problems, and even trivial questions you answered patiently. Thank you for sharing all your knowledge and expertise, and the constantly positive working atmosphere over all these years. There are probably not many PhD students out there experiencing the same high degree of mentoring through their time of research as I did. You initiated the numerous beamtimes and several international conferences, so that I had the pleasure to travel all over the world and experience a great deal of scientific exchange as well as many different cultures. Thank you for your trust when putting me in charge of the experiments, or sending me to conferences to represent our small research team by presenting our results. You made sure that we see more from the foreign countries than its synchrotron facilities and the corresponding guest house, and I also very much enjoyed the ‘off-topic’ conversations during meals or when having a break during beamtime. And of course thanks a lot for the many cycles of proofreading, all your suggestions, remarks and your support especially in the last weeks.

The next person to thank is Thomas Willers. You finished your PhD soon after I started mine, and nevertheless you managed to teach me how to thoroughly prepare an experiment and all about sample preparation. Your enthusiasm confirmed me that I made the right choice when entering the field of Kondo systems, and especially at the beginning it was great to be able just to ask ‘across the desk’ if anything was unclear. I learned a lot from your experience and your way of solving problems. I very much appreciated to go on beamtime (and doing the night

## Acknowledgment

shifts) with you, and it was great fun to discover Tokyo, enjoy a Japanese beer or check out the variety of Taiwanese food together.

Furthermore, many thanks go to Martin Sundermann. You started as a master student in our group and very quickly found your way into the topic. You implemented the model for the analysis of the HAXPES data, so that I could present the very nice results on the  $CeM_2Al_{10}$  compounds. Your practical and theoretical understanding was also of great help during beamtimes, and I am sure that you will have a successful time as a PhD student in Dresden.

Collaborating with the Max Planck Institute in Dresden had the great consequence that I got the opportunity to work with Maurits Haverkort. Thank you a lot, Maurits, for your extremely valuable Mathematica package, that you took all the time to help me with the AIM simulations (although they did not become part of the publication) and for your theoretical input in general, either during meetings in Dresden or via phone and email. Your widespread knowledge and your ability to theoretically capture experimental results are highly impressive.

Every co-author of the publications presented in this thesis provided an essential piece of work to the respective studies. Thank you all for your effort and for all the valuable remarks and suggestions during the publication process. Steffen Wirth struggled hard with us to finally get the manuscript on the Ce115 systems published. Thank you very much, Steffen, for your important contributions to the paper. A special thank also goes to Joe D. Thompson and Eric D. Bauer for their help with the Ce115 paper. Furthermore, an extra thank to Peter Thalmeier for his theoretical input to the discussion in the HAXPES study on the  $CeM_2Al_{10}$  series.

Performing an experiment at a synchrotron is a 24 hours job and only possible with many helping hands. A big thank you to the Dresden people who joined our experiments and significantly contributed to their successful outcome; these are Zhiwei Hu, Stefano Agrestini, Chang-Yang Kuo and Yi-Ying Chin.

In this context special thanks go to Zhiwei Hu, who certainly can be regarded as the world champion on the field of x-ray absorption. Your incredible knowledge and your experience always were extremely impressive and invaluable during beamtime (as well as afterwards via phone or when meeting in Dresden) – and in addition to that you always took care that we enjoyed the best food for lunch and dinner.

Also special thanks to Stefano Agrestini, who participated in our experiments particularly often, although he had to organize a bunch of own beamtimes. It was fun discovering Hiroshima with you and it was always very nice to have someone to chat with in Italian. *Grazie mille!*

All the experiments of course would not have been possible without the high-quality single crystals provided from several sample makers all over the world. Many thanks go to Yuji Muro, Keisuke Yutani and Toshiro Takabatake in Hiroshima, Japan; Eric D. Bauer, John L. Sarrao and Joe D. Thompson in Los Alamos, USA; and David Fort in Birmingham, UK.

Equally important are all the beamline scientists at the synchrotron light sources, who were responsible for the experimental endstations and ensured that the experiments run as smoothly as possible, which often meant that they had to stay late or come in at the weekends. For all their efforts I would like to thank Hong-Ji Lin, Fan-Hsiu Chang, C. T. Chen and T. W. Pi from the beamlines at the NSRRC in Taiwan; Enrico Schierle and Eugen Weschke from beamline UE-46 at BESSY in Berlin; Violetta Sessi, Kurt Kummer and Nick B. Brookes from the former

beamline ID08 at the ESRF in Grenoble; and Ku-Ding Tsuei and Yen Fa Liao from the HAXPES beamline at SPring-8 in Japan.

After my short residence in room 318, I returned to the famous room 317, and in both cases I benefited from the pleasant working atmosphere. Therefore, many thanks to Jonas Weinen, Thomas Willers, Nils Hollmann, Marcel Buchholz, Simone Altendorf, Siegurt Skoda, Martin Sundermann and Paul Rosenberger, and of course to all the other former and temporary members of our office, and the whole Tjeng group in general. A big thank you also to the van Loosdrecht group for the updates on free time activities like barbecue, paintball or making liquid nitrogen ice cream. Thanks also to Matteo Montagnese for organizing the (very important) supply of coffee on the yellow floor.

A big special thank goes to my direct desk neighbor Jonas Weinen. You probably had to deal most with my ups and downs, and with all my computer-related problems. Thank you for all the chats, the good and bad jokes, and the musical intermezzi – we still can pursue the idea of forming a (non-carnival-related) band. Many thanks also for your help with my questions concerning HAXPES, for the proofreading, for the figures and the perfect TeX-template you provided for my thesis, and for the nice day trips in Japan on one of our few mutual beamtimes.

In general, my thanks go to all colleagues from the II. Physical Institute and to the members of the Max-Planck group. Everyone was extremely helpful in case of questions or problems, and the secretaries Carmen Handels, Britta Schulz and Andrea Helldörfer always provided the important organizational support. Extra thanks to Ralf for supplying our office with sparkling water, to Sandra for the nice selection of ice cream during summer time, and Siegurt for the IT support. Thanks also to Thomas Lorenz for putting me in charge of the specific heat experiment for the students' lab course and all the nice discussions about it, from which I learned a lot (especially to be patient if something does not work the way it should).

Working at many different beamlines required many different types of sample holder, which were accurately manufactured by the mechanical workshop of the II. Physical Institute. Thanks a lot for that.

Scientific as well as private exchange are the basis for one's personal development. In over 20 beamtimes and at several conferences I had the pleasure to learn from and work together with a plethora of excellent scientists, both within own projects and as a helping hand for other projects. And the conferences provided an ideal platform to get to know the people 'behind the literature'. Hence, in addition to the people already mentioned I want to thank Nils Hollmann, Chun-Fu (Roger) Chang, Anna Efimenko, Nozomu Hiraoka, Hitoshi Yamaoka, Jun'ichiro Mizuki, Arata Tanaka, Jean-Pascal Rueff, James Ablett, Philippe Ohresser, Fadi Choueikani, Toshiro Takabatake, Yuji Muro, Silke Paschen, Hannes Winkler and Devashibhai Adroja.

The list has become quite long and I probably have forgotten several names, so I would like to thank everyone I missed to mention!

At the end, my warmest thanks go to my parents, my brother and my friends, who took care of me in the world outside physics and guaranteed that there were always welcome distractions around. *Grazie ai miei genitori, per esser stati un costante sostegno durante tutto questo tempo – e per tutto il vostro aiuto nei compiti di vita.* I would also like to thank my *Pausen-Crew* Fanny, Nina, Hanno and Patrick for the funny breaks and the recreational walks around the institute.

And I do not know where I would be today without my Caro... Thank you for everything!



## Publications

Publications of the cumulative part of the dissertation:

- *Crystal-field ground state of the orthorhombic Kondo insulator  $CeRu_2Al_{10}$*   
F. Strigari, T. Willers, Y. Muro, K. Yutani, T. Takabatake, Z. Hu, Y.-Y. Chin, S. Agrestini, H.-J. Lin, C. T. Chen, A. Tanaka, M. W. Haverkort, L. H. Tjeng, and A. Severing  
Physical Review B **86**, 081105(R) (2012)
- *Crystal-field ground state of the orthorhombic Kondo semiconductors  $CeOs_2Al_{10}$  &  $CeFe_2Al_{10}$*   
F. Strigari, T. Willers, Y. Muro, K. Yutani, T. Takabatake, Z. Hu, S. Agrestini, C.-Y. Kuo, Y.-Y. Chin, H.-J. Lin, T. W. Pi, C. T. Chen, E. Weschke, E. Schierle, A. Tanaka, M. W. Haverkort, L. H. Tjeng, and A. Severing  
Physical Review B **87**, 125119 (2013)
- *Quantitative study of valence and configuration interaction parameters of the Kondo semiconductors  $CeM_2Al_{10}$  ( $M = Ru, Os$  and  $Fe$ ) by means of bulk-sensitive hard x-ray photoelectron spectroscopy*  
F. Strigari, M. Sundermann, Y. Muro, K. Yutani, T. Takabatake, K.-D. Tsuei, Y. F. Liao, A. Tanaka, P. Thalmeier, M. W. Haverkort, L. H. Tjeng, and A. Severing  
Journal of Electron Spectroscopy and Related Phenomena **199**, 56 (2015)
- *Correlation between ground state and orbital anisotropy in heavy fermion materials*  
T. Willers, F. Strigari, Z. Hu, V. Sessi, N. B. Brookes, E. D. Bauer, J. L. Sarrao, J. D. Thompson, A. Tanaka, S. Wirth, L. H. Tjeng, and A. Severing  
Proceedings of the National Academy of Sciences of the USA **112** (8), 2348 (2015)

Publications as a co-author:

- *Strain-dependent transport properties of the ultra-thin correlated metal,  $LaNiO_3$*   
E. J. Moon, B. A. Gray, M. Kareev, J. Liu, S. G. Altendorf, F. Strigari, L. H. Tjeng, J. W. Freeland, and J. Chakhalian  
New Journal of Physics **13**, 073037 (2011)
- *Asymmetric Orbital-Lattice Interactions in Ultrathin Correlated Oxide Films*  
J. Chakhalian, J. M. Rondinelli, J. Liu, B. A. Gray, M. Kareev, E. J. Moon, N. Prasai, J. L. Cohn, M. Varela, I. C. Tung, M. J. Bedzyk, S. G. Altendorf, F. Strigari, B. Dabrowski, L. H. Tjeng, P. J. Ryan, and J. W. Freeland  
Physical Review Letters **107**, 116805 (2011)

## Publications

- *Magnetic Field Induced Orbital Polarization in Cubic YbInNi<sub>4</sub>: Determining the Quartet Ground State Using X-Ray Linear Dichroism*  
T. Willers, J. C. Cezar, N. B. Brookes, Z. Hu, F. Strigari, P. Körner, N. Hollmann, D. Schmitz, A. Bianchi, Z. Fisk, A. Tanaka, L. H. Tjeng, and A. Severing  
Physical Review Letters **107**, 236402 (2011)
- *Determining the In-Plane Orientation of the Ground-State Orbital of CeCu<sub>2</sub>Si<sub>2</sub>*  
T. Willers, F. Strigari, N. Hiraoka, Y. Q. Cai, M. W. Haverkort, K.-D. Tsuei, Y. F. Liao, S. Seiro, C. Geibel, F. Steglich, L. H. Tjeng, and A. Severing  
Physical Review Letters **109**, 046401 (2012)
- *Correlation between the valence state of cerium and the magnetic transition in Ce(Ru<sub>1-x</sub>Fe<sub>x</sub>)<sub>2</sub>Al<sub>10</sub> studied by resonant x-ray emission spectroscopy*  
Y. Zekko, Y. Yamamoto, H. Yamaoka, F. Tajima, T. Nishioka, F. Strigari, A. Severing, J.-F. Lin, N. Hiraoka, H. Ishii, K.-D. Tsuei, and J. Mizuki  
Physical Review B **89**, 125108 (2014)
- *Polarization dependent hard X-ray photoemission experiments for solids: Efficiency and limits for unraveling the orbital character of the valence band*  
J. Weinen, T. C. Koethe, C. F. Chang, S. Agrestini, D. Kasinathana, Y. F. Liao, H. Fujiwara, C. Schüßler-Langeheine, F. Strigari, T. Haupricht, G. Panaccione, F. Offie, G. Monaco, S. Huotarif, K.-D. Tsuei and L. H. Tjeng  
Journal of Electron Spectroscopy and Related Phenomena **198**, 6 (2015)

## Eigene Beteiligung an den Veröffentlichungen des kumulativen Teils der Dissertation

Die auf Seite 149 (in der oberen Aufzählung) genannten Veröffentlichungen bilden den kumulativen Teil der vorliegenden Dissertation (Kapitel 3, 4, 5 und 7). Die Beiträge der einzelnen Autoren sind am Anfang des jeweiligen Kapitels aufgeführt. Die folgende Tabelle fasst meine eigene Beteiligung an den jeweiligen Studien zusammen.

Kapitel 3: Phys. Rev. B <b>86</b> , 081105(R) (2012)	Vorbereitung und Durchführung des Experiments; Auswertung, Simulation und Darstellung der Messergebnisse; Verfassen des Manuskripts. Eigener Anteil an der Veröffentlichung $\approx 80-90\%$
Kapitel 4: Phys. Rev. B <b>87</b> , 125119 (2013)	Vorbereitung und Durchführung des Experiments; Auswertung, Simulation und Darstellung der Messergebnisse; Verfassen des Manuskripts. Eigener Anteil an der Veröffentlichung $\approx 80-90\%$
Kapitel 5: J. Electr. Spectr. Rel. Phenom. <b>199</b> , 56 (2015)	Vorbereitung des Experiments; Auswertung, Simulation und Darstellung der Messergebnisse; Verfassen des Manuskripts. Eigener Anteil an der Veröffentlichung $\approx 80-90\%$
Kapitel 7: Proc. Natl. Acad. Sci. USA <b>112</b> (8), 2348 (2015)	Vorbereitung und Durchführung des Experiments; Auswertung, Simulation und Darstellung der Messergebnisse; Verfassen des Manuskripts. Eigener Anteil an der Veröffentlichung $\approx 60-70\%$

Im Falle von Kapitel 7 liegt die Zweitautorschchaft darin begründet, dass das Experiment und dessen Auswertung unter der Anleitung von Dr. Thomas Willers (Erstautor) begonnen wurde und ich diese Arbeiten dann zu Ende geführt habe.



## Erklärung

Ich versichere, dass ich die von mir vorgelegte Dissertation selbständig angefertigt, die benutzten Quellen und Hilfsmittel vollständig angegeben und die Stellen der Arbeit einschließlich Tabellen, Karten und Abbildungen, die anderen Werken im Wortlaut oder dem Sinn nach entnommen sind, in jedem Einzelfall als Entlehnung kenntlich gemacht habe; dass diese Dissertation noch keiner anderen Fakultät oder Universität zur Prüfung vorgelegen hat; dass sie abgesehen von oben angegebenen Teilpublikationen noch nicht veröffentlicht worden ist, sowie, dass ich eine solche Veröffentlichung vor Abschluss des Promotionsverfahrens nicht vornehmen werde. Die Bestimmungen der Promotionsordnung sind mir bekannt. Die von mir vorgelegte Dissertation ist von Prof. Dr. Paul H. M. van Loosdrecht und Prof. Dr. L. H. Tjeng betreut worden.

Köln, den 18.02.2015

Fabio Strigari